

Ultrafast Dynamics of Spin-Crossover Complexes with Photochromic Ligands Investigated by Time-Resolved Electronic Absorption Spectroscopy

Dissertation

zur Erlangung des Doktorgrades

Dr. rer. nat.

der Mathematisch-Naturwissenschaftlichen Fakultät

der Christian-Albrechts-Universität zu Kiel

vorgelegt von

SEBASTIAN MEGOW

geboren am 25. März 1990 in Buxtehude

Institut für Physikalische Chemie

Kiel, 2022

Erster Gutachter: Prof. Dr. Friedrich Temps
Zweiter Gutachter: Prof. Dr. Felix Tucek

Tag der mündlichen Prüfung: 21. April 2022
Zum Druck genehmigt: 21. April 2022

Eidestattliche Erklärung

Hiermit erkläre ich, dass die vorliegende Abhandlung - abgesehen von der Beratung durch meinen Betreuer Prof. Dr. Friedrich Temps - nach Inhalt und Form meine eigene Arbeit ist. Diese Arbeit hat weder in Auszügen noch in ganzer Form einer anderen Stelle im Rahmen eines Prüfungsverfahrens vorgelegen. Sie wurde in ihrer Gesamtheit nicht veröffentlicht und auch nicht zur Veröffentlichung eingereicht. Teile dieser Arbeit wurden in fachwissenschaftlichen Zeitschriften veröffentlicht oder zur Veröffentlichung eingereicht. Dies bezieht sich auf die folgenden Kapitel:

KAPITEL 3

S. Megow, J. Bahrenburg, M. Dittner, B. Kohly, J. Gripp, M. Dommaschk, C. Schütt, R. Herges, F. Temps, Ultrafast Dynamics of a Bi-stable Azopyridine Ni-porphyrin Spin Switch after Photoexcitation in the Porphyrin B-bands, EPJ Web of Conferences, 2019, 205, 05019

KAPITEL 5

S. Megow, H.-L. Fitschen, F. Tuczek, F. Temps, Ultrafast Photodynamics of an Azopyridine-Functionalized Iron(II) Complex: Implications on the Concept of Ligand-Driven Light-Induced Spin Change, J. Phys. Chem. Lett. 2019, 10, 6048-6054

KAPITEL 6

L. Mewes, R.A. Ingle, S. Megow, H. Böhnke, E. Baranoff, F. Temps and M. Chergui, Ultrafast Intersystem Crossing and Structural Dynamics of [Pt(ppy)](μ -^tBu₂pz)]₂, Inorg. Chem. 2020, 59, 14643-14653

Zusätzlich wurden folgende Kapitel zur Veröffentlichung vorbereitet:

KAPITEL 4

S. Megow, M. Dommaschk, B. Behr, J. Gripp, R. Herges and F. Temps, On the ultrafast photo-induced dynamics and the spin crossover mechanism of the magnetically bi-stable azopyridine nickel(II) porphyrin complex, Prepared for submission

KAPITEL 7

S. Megow, O. Hüter, S. Schatz, and F. Temps, A Setup for Multiscale Pump-Supercontinuum Probe Spectroscopy: Full Photocycle of 7-Hydroxyquinoline-8-Carbaldehyde, Manuscript

Die Arbeit ist unter Einhaltung der Regeln guter wissenschaftlicher Praxis der Deutschen Forschungsgemeinschaft entstanden. Ein akademischer Grad wurde mir nicht entzogen.

Kiel, Januar 2022

Sebastian Megow

Für meine Familie

Abstract

The primary goal of this Thesis was the investigation of the ultrafast photodynamics of transition-metal complexes that were designed to undergo photo-induced spin crossover (SCO) in solution and at room temperature. These complexes have been functionalized with photochromic molecular switches in order to achieve control over and bi-stability of the two spin states. Although the investigated complexes were designed with the same goal and make use of phenylazopyridines (PAPs) as photoswitches, the underlying SCO concepts exhibit principal differences. In the azopyridine nickel(II) porphyrin (azoNiPor), also called record player, the attached PAP acts as an axial ligand in the *cis*-configuration, while it is detached in the *trans*-configuration. This molecule was designed according to the concept of light-driven coordination-induced spin-state switching (LD-CISSS). It can be reversibly switched between the diamagnetic low-spin (LS) form and the paramagnetic high-spin (HS) form upon irradiation. As evidenced by femtosecond time-resolved electronic absorption spectroscopy (fs-TEAS), excitation of the porphyrin states of each azoNiPor isomer induces efficient SCO in <1 ps. However, the product of this light-induced SCO is metastable and recovers to the ground state in ~ 500 ps, since the configuration of the PAP ligand is preserved and no (de)coordination can take place. The (de)coordination-induced SCO leading to the formation of the stable products occurs exclusively upon direct excitation and subsequent isomerization of the PAP unit, which is the reason for the low quantum yields determined for the spin switch. In the novel complex $[\text{Fe}(\text{3AzoN4Py})(\text{MeCN})](\text{BF}_4)_2$ the iron(II) ion is surrounded by a photoisomerizable pentadentate azo-tetrapyridylamino ligand with the aim to realize a photoswitchable SCO on the basis of the concept of ligand-driven light-induced spin change (LD-LISC). The results of fs-TEAS performed on the LS form of this complex show that initial excitation of the $\pi\pi^*$ state of the azopyridine unit is followed by ultrafast energy transfer to the metastable HS state, from which the LS ground state is recovered within ~ 3 ns. This process is in competition with the relaxation dynamics involving purely ligand-centered states and therefore diminishes the intended photoisomerization of the azopyridine. From the obtained results, implications on the SCO concepts and suggestions for a more rational design of such compounds were made. Furthermore, as the investigated systems exhibit photodynamics that are not restricted to ultrafast timescales, a broadband TEAS experiment that relies on a pair of coupled Ti:Sa amplifiers was developed, allowing for the observation of the photodynamics on timescales of several picoseconds up to a millisecond.

Kurzzusammenfassung

Im Rahmen der vorliegenden Dissertation wurde die ultraschnelle Photodynamik von Übergangsmetallkomplexen untersucht, die zur Realisierung eines licht-steuerbaren Spin-Crossover (SCO) in Lösung und bei Zimmertemperatur entworfen wurden. Dazu wurden sie mit lichtempfindlichen Liganden funktionalisiert, die die Kontrolle über den Spinzustand und Bistabilität ermöglichen sollen. Obwohl die untersuchten Verbindungen mit demselben Ziel entworfen wurden und dafür auf Phenylazopyridin (PAP) Liganden zurückgreifen, unterscheiden sich die zugrundeliegenden SCO-Konzepte. In dem Azopyridin-Nickel(II)-Porphyrin (azoNiPor), auch Plattenspieler-Molekül genannt, stellt das PAP im *cis*-Zustand einen axialen Liganden dar, während es im *trans*-Zustand dekoordiniert vorliegt. Es wurde auf Grundlage der licht-getriebenen koordinations-induzierten Spin-Zustandsschaltung (LD-CISSS, engl.) entwickelt und kann durch Belichtung reversibel zwischen dem Low-Spin (LS) und dem High-Spin (HS) Zustand geschaltet werden. Mittels Femtosekunden-zeitaufgelöster elektronischer Absorptionsspektroskopie (fs-TEAS, engl.) wurde gezeigt, dass die Anregung des Porphyrins der jeweiligen azoNiPor Spezies einen effizienten SCO in <1 ps zur Folge hat. Da so die Konfiguration des PAP unverändert bleibt und keine (De-)Koordination stattfinden kann, ist dieser Zustand metastabil, was in einer vollständigen Wiederbevölkerung des Grundzustandes innerhalb von ~ 500 ps resultiert. Das stabile Produkt wird nur gebildet, wenn eine direkte Anregung in die Zustände des PAP und die darauffolgende Isomerisierung stattfindet. Dies ist der Grund für die ermittelten niedrigen Quantenausbeuten der Spinschaltung. In dem Komplex $[\text{Fe}(\text{3AzoN4Py})(\text{MeCN})](\text{BF}_4)_2$ ist das Eisen(II)-Ion von einem photoschaltbaren pentadentaten Azo-Tetrapyrroldiamino-Liganden umgeben, der einen licht-steuerbaren SCO auf Grundlage der liganden-getriebenen licht-induzierten Spinänderung (LD-LISC, engl.) ermöglichen soll. Mittels fs-TEAS wurde gezeigt, dass die LS-Form des Komplexes nach Anregung in den $\pi\pi^*$ -Zustand des Azo-Liganden durch schnellen Energietransfer in den metastabilen HS-Zustand gelangt, von dem aus der Grundzustand innerhalb von ~ 3 ns wiederbevölkert wird. Dieser Prozess konkurriert mit den Relaxationsprozessen innerhalb des Azo-Liganden und folglich mit dessen angestrebter Isomerisierung. Auf Basis der erhaltenen Ergebnisse werden die Auswirkungen auf die SCO-Konzepte diskutiert. Da die untersuchten Verbindungen auch Photodynamik außerhalb der Zeitskalen der fs-TEAS zeigen, wurde eine Methode entwickelt, die durch Kopplung zweier Ti:Sa-Verstärker die lückenlose TEAS bis zu einer Millisekunde ermöglicht.

Contents

1	Introduction	1
1.1	General Photophysics and Photochemistry	4
1.2	Photophysics and Photochemistry of Transition-Metal Complexes	10
1.3	Spin Crossover in Transition-Metal Complexes	11
1.3.1	Ligand-Driven Light-Induced Spin Change	12
1.3.2	Light-Driven Coordination-Induced Spin-State Switching	13
1.4	Photophysical and Photochemical Properties of (Metal)Porphyrins	16
1.5	Photophysical and Photochemical Properties of Metal Polypyridyls	23
1.6	Azobenzenes as Molecular Photoswitches	26
	References	33
2	Experimental Methods	45
2.1	Femtosecond Time-Resolved Electronic Absorption Spectroscopy	46
2.1.1	Experimental Setup	47
2.1.2	Data Preparation and Analysis	51
2.2	Femtosecond Time-Resolved Fluorescence Spectroscopy	57
2.2.1	Experimental Setup	58
2.2.2	Data Analysis	59
	References	61
3	Ultrafast Dynamics of a Bi-stable Azopyridine Ni-porphyrin	65
3.1	Introduction	67
3.2	Experimental Details	67
3.3	Results and Discussion	67
	References	71
4	Spin-Crossover Mechanism of an Azopyridine Ni(II) Porphyrin	73
4.1	Introduction	75
4.2	Experimental Section	78
4.2.1	Static UV–vis Absorption Spectroscopy	78
4.2.2	Photostationary States and Quantum Yields	78
4.2.3	Femtosecond Electronic Absorption Spectroscopy	80
4.2.4	Nanosecond Electronic Absorption Spectroscopy	80
4.3	Results	81
4.3.1	Static UV–vis Absorption Spectra	81
4.3.2	Fractions of <i>cis</i> -azoNiPor(HS) in the Photostationary States	81
4.3.3	Quantum Yields	82

4.3.4	Femtosecond Time-Resolved Electronic Absorption Spectra	84
4.3.5	Nanosecond Time-Resolved Electronic Absorption Spectra	89
4.4	Discussion	89
4.4.1	UV–vis Absorption Spectroscopy and Quantum Yields .	90
4.4.2	Time-Resolved Electronic Absorption Spectroscopy . . .	91
4.5	Conclusion	95
	References	99
	Supporting Information	105
	Additional Results	115
5	Ultrafast Photodynamics of an Fe(II) Azopolypyridyl	125
5.1	Reprint of the Publication	127
	References	137
	Supporting Information	141
	Additional Results	145
6	Intersystem Crossing and Dynamics of a Diplatinum Complex	157
6.1	Introduction	159
6.2	Experimental Section	163
6.3	Results and Discussion	166
6.4	Conclusion	176
	References	177
7	Multi-Timescale Pump-Probe Absorption Spectroscopy	183
7.1	Introduction	185
7.2	Experimental Setup	187
7.2.1	Femtosecond Transient Electronic Absorption Spectroscopy	187
7.2.2	Nanosecond Transient Electronic Absorption Spectroscopy	188
7.2.3	Measurement Schemes	190
7.3	Results for 7-Hydroxyquinoline-8-Carbaldehyde	191
7.3.1	Static UV–vis Absorption Spectroscopy	191
7.3.2	Time-Resolved Electronic Absorption Spectroscopy . . .	191
7.4	Conclusion	195
	References	197
8	Conclusion and Outlook	199
8.1	Photodynamics of Azo-Porphyrin Nickel(II)	199
8.2	Photodynamics of Azo-N4Py Iron(II)	202
8.3	Multiscale Pump-Probe Spectroscopy	205

1 Introduction

Photochemistry, the conversion of light into chemical energy, has been the source of life on our planet ever since the beginning. Starting from the formation of small organic molecules up to the emergence of molecular assemblies of growing complexity, chemical and physical processes triggered by sunlight have shaped us and our environment. A series of photochemical events referred to as photosynthesis is used by plants and algae as well as some bacteria to store solar energy by synthesizing energy rich carbohydrates from energy poor species water and carbon dioxide. These carbohydrates and the additionally released by-product oxygen further serve as fuels for all organisms not capable of performing photosynthesis, which makes this process essential for almost all life on Earth. The pigment chlorophyll whose chemical structure is displayed in Figure 1.1a, is of pivotal importance for the process of photosynthesis. In green plants and algae chlorophyll molecules are organized in pigment protein antennas, known as light-harvesting complexes (LHCs). These antennas capture the sunlight and effectively funnel the solar energy to the photosynthetic reaction centers with almost no loss due to heat dissipation.^[1] Besides that some prokaryotic bacteria use non-chlorophyll based pathways to harvest light energy by exploiting the photochemistry of retinal proteins (opsins). These photo-sensory proteins are also found in the photoreceptor cells of higher animals enabling them to visually perceive their environment. In all visual opsins, light absorption triggers a series of structural changes in the protein, which activate signal transduction cascades resulting in the conversion of light into an electrical signal.^[2]

These examples can be viewed as role models of photochemical reactions as they have prevailed due to their remarkably high efficiency. This high efficiency, in turn, is associated with fast timescales of the photo-initiated reactions such that unwanted side reactions are minimized. In most cases the outcome is determined by the initial events after the absorption of the photon. These events most likely involve movement of the atoms along only few molecular degrees of freedom, which takes place exceedingly fast within femtoseconds (10^{-15} s). Apparently, observation of these processes is quite challenging. The development of ultrafast laser systems in combination with pump-probe spectroscopic techniques has proven a great tool to study the photodynamics on this ultrashort timescales. The investigation of the photochemical processes in biologically relevant systems can be viewed as a major driving force in the field of femtochemistry and femtobiology.^[3] A. H. Zewail is one of the pioneers in this field and was awarded the Nobel Prize in Chemistry in 1999.^[4]

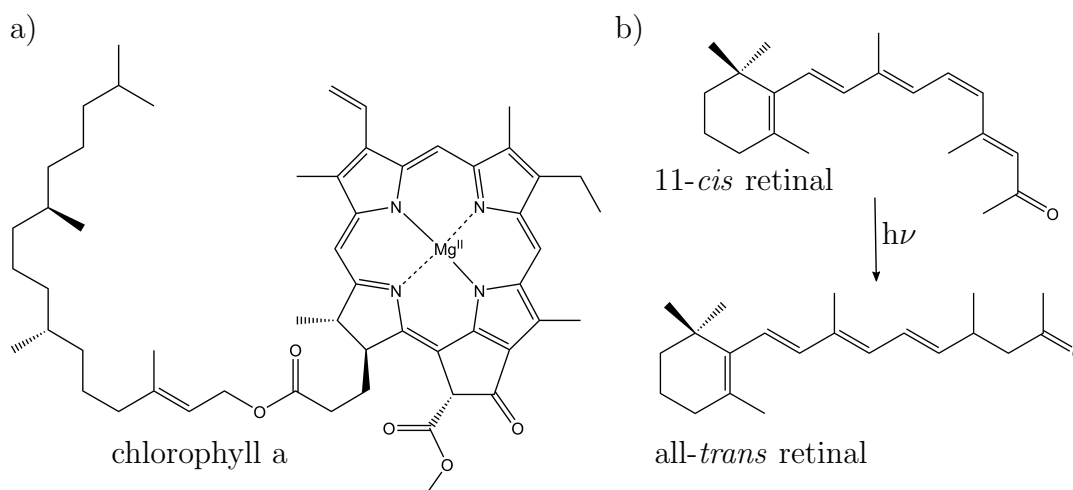


Figure 1.1: Chemical structures of (a) the pigment chlorophyll a that plays a major role in photosynthesis of green plants and algae and (b) retinal that is the chromophore of the photo-sensitive opsin proteins. The photoisomerization of 11-*cis* to all-*trans* retinal triggers a signal transduction cascade in the visual cycle of higher animals.

Using femtosecond time-resolved spectroscopic techniques it was demonstrated that quantum coherences play an important role for the efficient transfer of the solar energy captured by the LHCs to the photosynthetic reaction centers.^[1,5,6] The studies of opsins revealed that the primary event following light absorption is the ultrafast geometric change called *cis*–*trans* isomerization of the retinal chromophore^[7,8] (Figure 1.1b) around a specific C=C stretching bond, leading to a highly distorted, spectrally red-shifted photoproduct.^[2] The speed and efficiency of this process is strongly promoted by the protein environment as the free retinal chromophore in solution displays longer excited-state lifetimes,^[9–11] lower quantum yields^[12] and poor selectivity of the photoreaction.^[2]

Inspired by these natural systems, the design of artificial materials mimicking these functions became paramount objective for generations of scientists in different research fields. Light is a particularly good stimulus to trigger certain processes since it allows for high spacial and temporal control. For the rational design of such materials knowledge of the key structural features and their photochemical and physical properties is a prerequisite. As chlorophyll in photosynthesis, molecular compounds consisting of organic ligands coordinated to metal centers gained special attention as they also carry out other crucial functions in some of nature’s most fundamental processes. Hemoproteins such as hemoglobin, myoglobin and cytochromes are important for oxygen transport and electron-transfer processes in living organisms. Their central structural element, the heme prosthetic group, is structurally similar to chlorophyll, but contains an iron ion instead of a magnesium ion which is complexed by a porphyrin-like ligand. Furthermore, non-heme metalloproteins containing iron and molybde-

num are of outstanding importance in the process of nitrogen fixation in living organism.^[13–15] The possibility to exist in different oxidation states gives rise to this multifarious reactivity and is the reason why metal complexes are employed in various major research fields such as solar energy conversion,^[16] photoredox catalysis^[17] and photodynamic therapy.^[18] Moreover, if these complexes are formed with transition metals, the degenerate d-orbitals are only partially filled which results in a variety of states with different spin multiplicity and thus different molecular magnetic moments. By applying an external stimulus, *e.g.* light, it is possible to induce transitions between these states which is referred to as spin crossover (SCO).^[19] This phenomenon bears huge application potential^[20] as it can be used to encode binary information which is interesting in terms of high-density optical data storage.^[21] In order to built reliable memory devices on the basis of SCO complexes it is desired that the information can be erased, rewritten and stored over a long period of time under ambient conditions. For this and many other applications, however, it is required that the system is stable in both electronic states. In reality, unfortunately, only one of the states is thermodynamically favored while the other one is metastable. In this context the application of photochromic molecular switches becomes particularly interesting. These compounds can undergo a reversible photo-induced transformation between two isomeric forms with distinct physical and chemical properties. These transformations can include electrocyclic ring opening and ring closure, proton transfer or isomerization reactions. The *cis–trans* isomerization in opsins is just one example of a blueprint molecular photoswitch in nature, which occurs in a rather complex protein environment. However, there are also small organic prototype systems that are able to perform reversible photoisomerization reactions. Among these, azobenzene derivatives represent one of the most extensively studied and widely used class of photoswitches. The selective addressing of both isomers with light, low degree of photochemical fatigue and high thermal stability make it a popular choice for applications in molecular machines,^[22–24] holographic recording devices,^[25–27] and other photoresponsive materials.^[28–32] Successful applications are countless. Thus, the combination of transition-metal complexes and molecular photoswitches seems to be a promising approach to built systems that can be reversibly switched between two stable magnetic states. For that, the understanding of photophysical and -chemical reaction pathways driving the specific reactivity of transition-metal coordination compounds and molecular photochromic switches is mandatory in order to optimize those systems for successful applications.

The present Thesis deals primarily with the investigation of the ultrafast photodynamics of transition-metal complexes with isomerizable ligands using femtosecond time-resolved spectroscopic techniques. These techniques are introduced in Chapter 2. In Chapters 3 and 4 the photodynamics of a magnetically bi-stable azopyridine nickel(II) porphyrin are presented. Conclusions on the mechanism of the spin switch are drawn from the results of time-resolved

spectroscopy as well as static quantum yield measurements. For a deeper understanding of the observed photodynamics of this complex, a detailed investigation of the photophysics of its molecular sub-units was required. These results are presented in the Additional Results of Chapter 4. In Chapter 5 the photo-induced dynamics of an azopyridine-functionalized iron(II) SCO complex were investigated. The nature of the energy-transfer processes observed in the iron complex that diminishes the efficiency of *trans*–*cis* isomerization of the attached azopyridine is rationalized by investigation of the zinc(II) analogue and quantum chemical calculations. These results are outlined in the Additional Results of Chapter 5. Chapter 6 deals with the interplay of electronic and structural dynamics in a d^8 – d^8 diplatinum complex and their influence on intersystem crossing (ISC) rates in such compounds. Femtosecond time-resolved absorption and emission spectroscopy as well as quantum chemical calculations were used to unambiguously identify the observed relaxation processes. Furthermore, most of the presented results demonstrate that the photodynamics of such compounds can exhibit a multiscale distribution of time constants. Therefore, a new experiment was developed that relies on the coupling of two Ti:Sa amplifiers each seeded by a free-running oscillator and allows for the seamless tracking of the photodynamics from femto- to micro- and even milliseconds. The description of the experimental setup and the first data obtained for the proposed excited-state proton-transfer switch 7-hydroxyquinoline-8-carbaldehyde are presented in Chapter 7. Concluding remarks and a brief outlook is given in Chapter 8.

A general picture of the photophysical processes and timescales that holds for most organic molecules is presented in the following Section. This helps to understand the photochemical properties of the mostly organic ligands. A detailed description of photophysical and photochemical processes as well as quantum mechanical and group theoretical aspects of electronic transitions can be found in numerous textbooks.^[33,34]

1.1 General Photophysics and Photochemistry

The interaction of polyatomic molecules with light can trigger a series of events of both nonradiative as well as radiative decay processes, which involve luminescence, electron or energy transfer and spin change that are often driven and accompanied by structural rearrangements. While photophysical processes do not alter the chemical structure of original molecule, photochemical processes lead to the formation of photoproducts, which possess chemical structures that are significantly different from those of the reactants.^[35] The primary photophysical events that occur after electronic excitation can be illustrated in a so-called Jablonski diagram.^[36] An example of such a diagram, which should apply to almost any organic molecule, is given in Figure 1.2. Since most organic molecules have a closed-shell electron configuration, the electronic ground state S_0 is a singlet state and the one electron excited-state configurations occur in pairs of

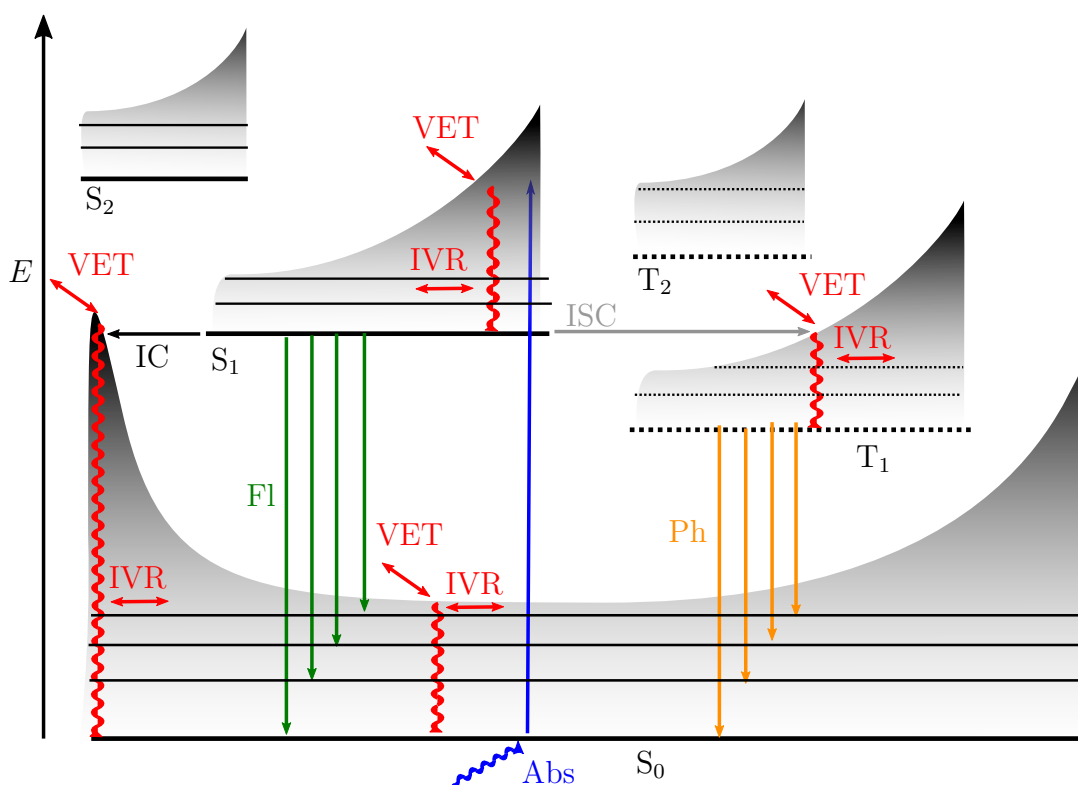


Figure 1.2: Jablonski diagram illustrating the primary photophysical processes after electronic excitation of an organic molecule with closed-shell electron configuration. Photophysical processes are displayed by arrows. Abs: Absorption; IC: Internal conversion; IVR: Intramolecular vibrational energy redistribution, ISC: Intersystem crossing; Fl: Fluorescence; Ph: Phosphorescence; VET: Intermolecular vibrational energy transfer. Shading indicates increasing density of vibrational states.

singlet and triplet states (S_1 and T_1 , S_2 and T_2) that belong to the same electron configuration, with the triplet state being lower in energy. Due to strict spin selection rules, initial absorption of a photon from the ground state leads to the population of an electronically excited state of the same multiplicity, which in this case is given by the S_1 state. From Heisenberg's uncertainty relation^[37] absorption can be estimated to occur on a timescale of 10^{-17} s, which is orders of magnitude faster than the fastest nuclear motions that have frequencies of $10^{12} - 10^{15}$ Hz. Thus, electronic movement proceeds instantaneously compared to nuclear motions. Since the excited state usually possesses a different equilibrium geometry than the ground state, it will be populated in a high vibrational energy level, by virtue of the Franck-Condon principle.^[38,39] This vibrationally "hot" species now dissipates its excess energy by collisions with its environment (intermolecular vibrational energy transfer, VET, also called vibrational relaxation, VR) and/or redistribution among others of its vibrational modes (intramolecular vibrational energy redistribution, IVR) leading to the

formation of a thermalized species within the respective electronic state. With typical collision rates in solution being in the order of 10^{13} Hz, VET takes place on a picosecond timescale.^[33,34] The rate of IVR, *i.e.* the molecule acts as its own heat bath, spans $10^{-13} - 10^{-9}$ s depending on the size of the molecule and the density of vibrational states.^[33,34] Further relaxation can now occur by transitions to different electronic states as either nonradiative or radiative processes. Nonradiative processes are transitions to an isoenergetic highly excited vibrational level of a lower lying electronic state that subsequently can again undergo vibrational thermalization. Such transitions can occur between states of the same spin multiplicity ($S_1 \rightarrow S_0$) which is referred to as internal conversion (IC), and to states of different spin multiplicity ($S_1 \rightarrow T_1$) which is referred to as intersystem crossing (ISC). The rate $k_{i \rightarrow f}$ of each process can be calculated according to Fermi's golden rule^[40]

$$k_{i \rightarrow f} = \left(\frac{2\pi}{\hbar} \right) \langle \phi_i S_i | \hat{H}'_{\text{nr}} | \phi_f S_f \rangle^2 \sum_n \langle \chi_i | \chi_f \rangle^2 \rho_f \quad (1.1)$$

with \hat{H}'_{nr} being the operator of the perturbation responsible for the nonradiative transition, ϕ the spatial and S the spin wavefunction of the initial and final state.^[34] The term $\langle \chi_i | \chi_f \rangle^2$ is the Franck-Condon factor representing the overlap of the vibrational wavefunctions and the factor ρ_f is the density of vibrational states in the final state that matches the energy of the initial state. In order to fulfill the conditions for an allowed transition, the integrand of $\langle \phi_i | \hat{H}'_{\text{nr}} | \phi_f \rangle$ has to be totally symmetric. Since, in case of IC the operator of the perturbation \hat{H}'_{IC} transforms totally symmetric, this case is fulfilled if ϕ_i and ϕ_f belong to the same irreducible representation.^[34] These selection rules can be lifted for molecules with many different types of vibrational modes by vibronic coupling.^[34] In contrast, for ISC the perturbation \hat{H}'_{ISC} is not totally symmetric, which means that the spatial wavefunctions ϕ must not belong to the same irreducible representation.^[34] The demand that ISC can only occur between orbitals of different spacial symmetry gives rise to the so-called El-Sayed rules.^[41] Since ISC is *per se* spin-forbidden, its rate is usually much slower and can thus not compete with that of IC processes ($10^{-12} - 10^{-6}$ s).^[33,34] However, spin-forbidden transitions can become more allowed if spin-orbit coupling (SOC) increases which is the case in the presence of heavy atoms, usually not contained in most organic molecules. Moreover, the molecule can loose its excitation energy by spontaneous emission of a photon. The rate of such radiative processes in a two-level system is described by the Einstein coefficient

$$A_{21} = \left(\frac{64\pi^4 \nu_{21}^3}{3hc^3} \right) \langle \Psi_2 | \hat{\mu} | \Psi_1 \rangle^2 \quad (1.2)$$

depending on the cube of the transition frequency ν_{21} between the two states and the square of the transition moment $\langle \Psi_2 | \hat{\mu} | \Psi_1 \rangle$.^[34] This process can occur

as fluorescence between singlet states ($S_1 \rightarrow S_0$) or as phosphorescence from a triplet to a singlet state ($T_1 \rightarrow S_0$).^[34] Typical timescales of fluorescence are in the range of $10^{-9} - 10^{-8}$ s, while phosphorescence, because of its spin-forbidden nature, occurs on timescales of $10^{-6} - 10^{-3}$ s but can extend to several seconds or even hours.^[33,34] Since the rates of radiative processes cannot compete with those of fast nonradiative processes such as VR and IC, luminescence is most likely observed from the lowest excited state of the respective multiplicity. This is referred to as Kasha’s rule.^[42] Again, the described photophysical deactivation processes cause no change in the chemical structure, even if some excited state might have a distorted geometry compared to the ground state. However, the difference in electronic structure might result in a higher reactivity. Thus, the molecule also has the possibility to deactivate to the ground state by a number of different chemical processes that can alter the chemical composition (decomposition) or retain it (isomerization). These processes are not contained in the Jablonski diagram and shall be discussed in the following.^[33,34]

Primary photochemical reactions are often visualized on their potential energy surfaces (PES). These are derived from the Born-Oppenheimer (BO) approximation which is based on the assumption that the electrons can adapt to a change of nuclear positions “instantaneously” (adiabatically).^[43] Starting from the molecular Schrödinger equation

$$\hat{H}\Psi^{(k)}(\mathbf{q}, \mathbf{Q}) = \epsilon_k \Psi^{(k)}(\mathbf{q}, \mathbf{Q}) \quad (1.3)$$

with the eigenenergies ϵ_k and the molecular Hamilton operator given by

$$\hat{H} = \hat{H}_{el} + \hat{T}_Q \quad (1.4)$$

where \hat{H}_{el} is called the electronic Hamilton operator and \hat{T}_Q is the operator of the kinetic energy of the nuclei.^[44] Based on the BO approximation, the total molecular wavefunction $\Psi^{(k)}(\mathbf{q}, \mathbf{Q})$ is factorized

$$\Psi^{(k)}(\mathbf{q}, \mathbf{Q}) = \sum_{n=1}^{\infty} \phi^{(n)}(\mathbf{q}, \mathbf{Q}) \chi^{(n,k)}(\mathbf{Q}) \quad (1.5)$$

in a nuclear wavefunction $\chi^{(n,k)}(\mathbf{Q})$ and an electronic wavefunction $\phi^{(n)}(\mathbf{q}, \mathbf{Q})$ which implicitly depends on the electron coordinates \mathbf{q} but only parametrically depends on the positions of the nuclei \mathbf{Q} and not on their movement anymore.^[44] This way, Equation 1.1 can be separated into an electronic part which can be solved for each value of \mathbf{Q} according to

$$\hat{H}_{el}\phi^{(n)}(\mathbf{q}, \mathbf{Q}) = E_n(\mathbf{Q})\phi^{(n)}(\mathbf{q}, \mathbf{Q}) \quad (1.6)$$

and a system of coupled nuclear Schrödinger equations

$$[\hat{T}_Q + E_m(\mathbf{Q})]\chi^{(m,k)}(\mathbf{Q}) + \sum_n [2\hat{T}'_{mn}(\mathbf{Q}) + \hat{T}''_{mn}(\mathbf{Q})]\chi^{(n,k)}(\mathbf{Q}) = \epsilon_k \chi^{(m,k)}(\mathbf{Q}) \quad (1.7)$$

where the eigenvalues of the electronic part $E_m(\mathbf{Q})$ emerge in form of the PES.^[44] By neglecting the non-adiabatic (diabatic) couplings

$$\hat{T}'_{mn}(\mathbf{Q}) = -\frac{\hbar}{2M} \langle \Psi^{(m)} | \nabla_Q | \Psi_{(n)} \rangle \quad (1.8)$$

and

$$\hat{T}''_{mn}(\mathbf{Q}) = -\frac{\hbar}{2M} \langle \Psi^{(m)} | \nabla_Q^2 | \Psi_{(n)} \rangle \quad (1.9)$$

the Schrödinger equation for the nuclei can be solved for an isolated electronic state m .^[44] Thus, photochemical reactions can be displayed as the movement of the excited wavepacket in the $(3N - 6)$ -dimensional space of internal nuclear coordinates.^[33] The PES are characterized by local minima and maxima that can be far apart from each other but also can approach each other closely and even cross at a particular nuclear coordinate. The crossing of states, however, can only occur if these states do not interact with each other, which is the case when they are of different symmetry or multiplicity. Otherwise the interaction will lead to a perturbation of the states that results in an avoided crossing and the original adiabatic PES are substituted by diabatic PES.^[34] At sufficiently low velocities of the nuclei (flat gradient of the PES) the wavepacket follows a single adiabatic PES.^[34] However, in molecules with many vibrational modes it is likely that at some point in the multidimensional space the wavefunction of two energetically close-lying adiabatic states are degenerate and a transition between these states is possible.^[34] These points are referred to as conical intersections and often serve as ultrafast relaxation channels in photochemical reaction. At a conical intersection (CI), the diabatic couplings caused by pseudo-Jahn-Teller distortions can no longer be neglected which results in the breakdown of the BO approximation.^[34] Initial absorption most likely places the wavepacket on an elevated point of the excited-state PES in the Franck-Condon region, from where it rapidly deactivates to a local (spectroscopic) minimum, where the previously discussed photophysical processes can occur.^[33]

For a photochemical reaction to take place with a sufficient efficiency it has to be fast in order to compete with photophysical processes, which means that low activation barriers of the reaction are required. A classification of photoreactions established by Förster^[45] is displayed in Figure 1.3. In reactions of class I deexcitation occurs in the reactant (A). The electronically excited reactant species (A^*) undergoes IC to a vibrationally excited level of the electronic ground state (A^{hot}). Such hot ground-state (or quasi-thermal) reactions can be theoretically treated as excess energy driven unimolecular reactions using the model of Rice-Ramsperger-Kassel-Marcus (RRKM) and its variants.^[46,47] Since

in solution VR is fast compared to the chemical change, these types of reaction preferentially take place in the gas phase. In reactions of class II the structural change proceeds entirely on the excited-state PES which is why they are referred to as adiabatic reactions. The deexcitation occurs from an excited state of the product (B^*), which might be identified by some luminescence. Such reactions are not unusual for triplet states, where ISC processes are slow and there is enough time to surpass a substantial potential energy barrier. In singlet states, however, the reaction needs to be fast and thus no significant structural changes can be expected, which is the case for valence isomerization and proton-transfer reactions.^[33] If deexcitation occurs somewhere between species A^* and B the reactions is referred to as diabatic (class III). The direct conversion between the excited reactant and the product proceeds via a geometry at which the energies of the involved PES are degenerate (CI) or almost degenerate (avoided crossing).^[34] If a CI is involved, the reactions are very fast (sub-picosecond) and deactivation is efficient.

The efficiency of any photochemical process is described by the quantum yield (Φ_i) according to

$$\Phi_i = \frac{N_i}{N_{\text{Ph,abs}}} \quad (1.10)$$

where N_i is the number of molecules formed by the respective process and $N_{\text{Ph,abs}}$ is the number of absorbed photons.^[35] The quantum yield is an important measure for photochromic molecular switches, which are a subject of this Thesis and should be high for a desired process. The quantum yield is strongly influenced by the rates of all competing photophysical and photochemical processes discussed above for organic molecules.

However, looking at transition-metal coordination compounds, the picture of the accessible electronic states gets more complicated and the timescales of the associated dynamical processes can be drastically altered. In the following Section the general picture will be adapted with respect to transition-metal coordination compounds.

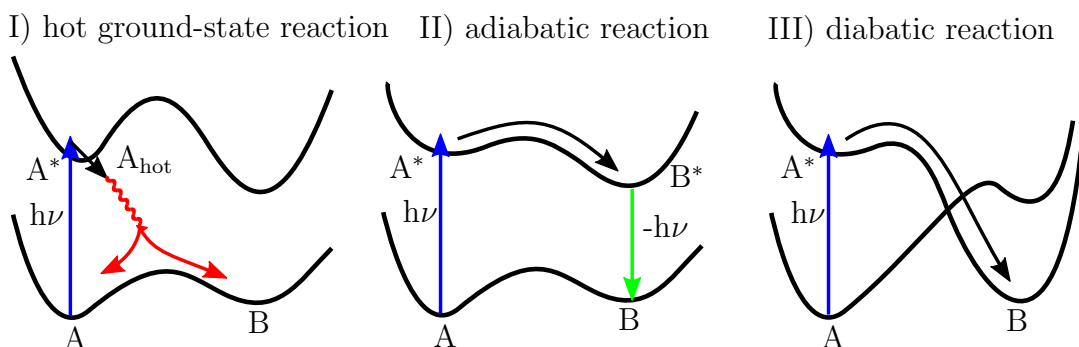


Figure 1.3: Three classes of photoreactions established by Förster^[45]: hot ground-state reaction (I), adiabatic reaction (II), diabatic reaction (III).

1.2 Photophysics and Photochemistry of Transition-Metal Complexes

Transition-metal complexes consisting of d-block elements with coordinated ligands can be neutral or carry a charge. In contrast to most organic molecules, their ground-state electron configurations can contain degenerate orbitals that are not fully occupied, which gives rise to a multiplicity higher than one.^[34] Furthermore, most organic molecules do not contain such “heavy” atoms and thus show only a small degree of SOC. As a consequence, the incorporation of d-block elements introduces noticeable amounts of SOC.^[34] Thus, ISC processes are significantly accelerated and can become compatible with or even exceed the fastest initial photophysical processes. The combination of transition-metal centers with organic ligands also results in a variety of electronic states of different origin occasionally lying in a narrow energy range.^[48] Those include states where the excited electron is located on the ligand (ligand-centered, LC) or the metal (metal-centered, MC) as well as charge transfer (CT) states, where an electron is excited from metal-to-ligand (MLCT), from ligand-to-metal (LMCT), or from ligand-to-ligand (LLCT).^[48] However, it has to be pointed out that the classification of the electronic states based on the principal localized electronic configuration is only an approximation.^[34] Besides the origin of those states other factors like spin, geometry and character strongly influence their accessibility among optical excitation from the ground state and from subsequent relaxation processes.^[48] Transitions within the metal center are usually of weak intensity ($\epsilon \approx 1$ to 10^3 L mol⁻¹ cm⁻¹) since they most likely occur between d-orbitals which have the same parity.^[49] The conservation of parity of an electronic transition is forbidden according to the Laporte rule, but it can become weakly allowed if symmetry is broken by Jahn-Teller distortions or coupling to asymmetric vibrations. Although they are harder to access directly upon excitation from the ground state, MC states can be populated by subsequent nonradiative processes effectively.^[34] In contrast, CT states do not underlie these symmetry restrictions, which results in a usually strong radiative coupling to the ground state, giving rise to transitions with absorption coefficients of $\epsilon \approx 10^3 - 10^6$ L mol⁻¹ cm⁻¹.^[49] Since the photochemical reactivity of a molecule is in principle determined by its electron distribution, this rich variety of quantum states offers a broad spectrum of possible applications of transition-metal coordination compounds.^[34] However, the fact that these states lie in a narrow energy range can also make it hard to access and control the desired reactivity. While MC or ligand-field states play an important role for applications as molecular magnets, the CT states, since they originate from an intramolecular oxidation-reduction reaction between metal and ligand, are important in the fields of sensing and catalysis.^[34] As this Thesis deals with complexes that were designed to achieve magnetic bi-stability, the focus here will be on the processes leading to the formation of long-lived MC states.

1.3 Spin Crossover in Transition-Metal Complexes

According to crystal field theory the degeneracy of the metal d-orbitals in a non-centrosymmetric ligand field is lifted due to their different electrostatic interaction with the ligand orbitals.^[50] As displayed in Figure 1.4 the interaction of the metal ion with an octahedral ligand field leads to a splitting of the d-orbitals into a t_{2g} set containing the d_{xy} -, d_{yz} - and d_{zx} -orbitals, which is lower in energy, and the e_g set containing the $d_{x^2-y^2}$ - and d_{z^2} -orbitals, which are raised in energy due to their stronger repulsion with the ligands. If the transition-metal central ion possesses a d^4 - d^7 electron configuration, it can in principle exist in two ground states of different spin multiplicity. The stability of each configuration is determined by two parameters: the spin pairing energy E_{sp} and the ligand-field splitting energy Δ . If $E_{sp} > \Delta$ the orbitals are filled with electrons in a way that the overall spin is maximized (Hund's first rule); this is referred to as the high-spin (HS) configuration. If $E_{sp} < \Delta$ the lower set of orbitals is first filled completely with electrons; this is referred to as the low-spin (LS) configuration. For tetrahedral complexes the splitting of the orbitals is opposite compared to that of octahedral ones. Thus, in principle, tetrahedral complexes with metal ions of d^3 - d^6 should also be able to exist in a LS and a HS state. Practically, however, tetrahedral complexes are almost exceptionally present in their HS form, due to the weaker splitting of the ligand field ($\Delta_t = \frac{4}{9}\Delta_o$), with only few exceptions known.^[51-53] Besides the tetraeder, the four ligands could also be arranged quadratically around the metal center. This rather special case offers metals with d^8 configuration, which often show such a geometry, the possibility to exist in either of the two spin states. However, the strong repulsion of the $d_{x^2-y^2}$ -orbitals with all four ligands leads to a strong splitting, which is why this orbital is usually vacant and the complexes are exceptionally stable in the LS configuration.

Furthermore, it is possible to induce transitions between the two electron configuration by applying an external stimulus.^[19,54] This phenomenon, called spin crossover (SCO), bears huge application potential in research on high-density magnetic data storage and medicine. The process of SCO can be triggered by different stimuli such as pressure, temperature or light.^[21] For most applications light is a particularly interesting tool since it offers good spatio-temporal control and high selectivity. However, since the thus generated electronic state is usually metastable, an actual bi-stability between the two spin states used to be restricted to solids at very low temperatures by virtue of the light-induced excited spin-state trapping (LIESST) effect.^[55-57] In order to carry the LIESST effect to ambient temperatures and solution different concepts were developed which are sketched in the following.

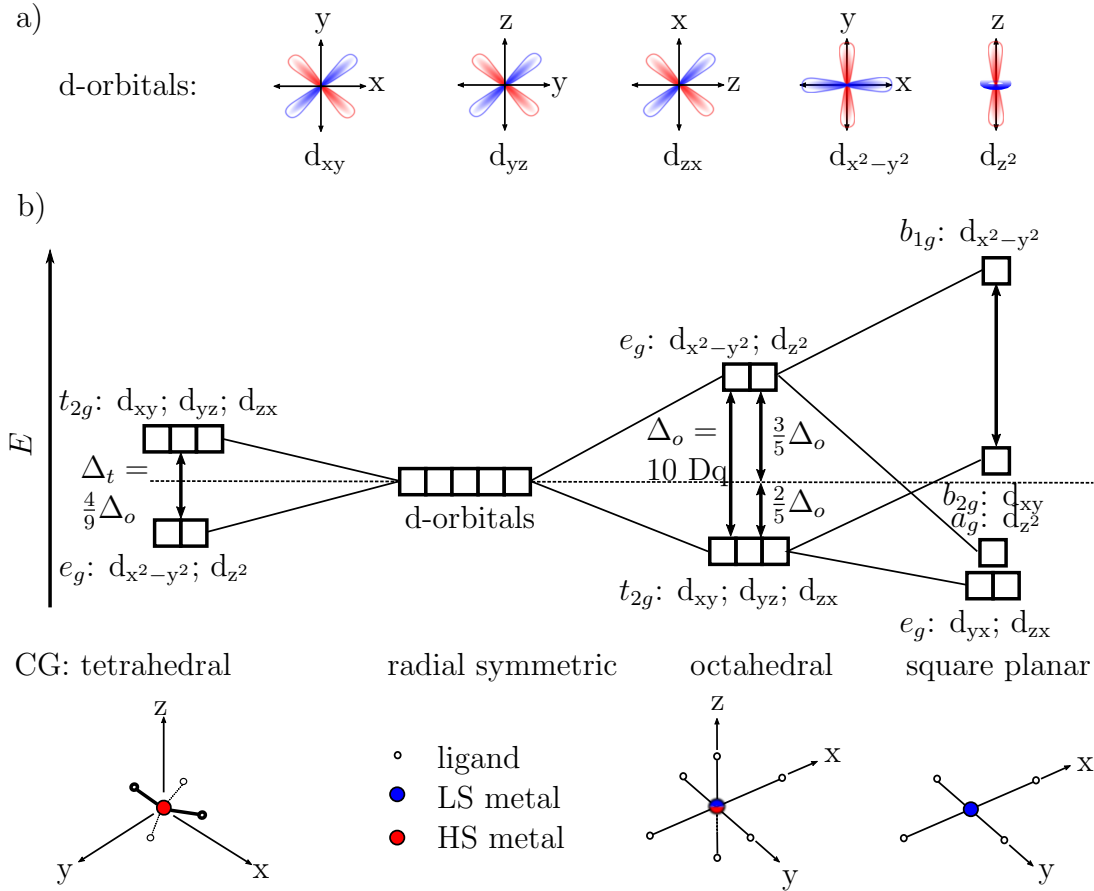


Figure 1.4: Basics of ligand-field theory: orientations of the d-orbitals (a) and ligand-field splitting for different complex geometries (CG, b).

1.3.1 Ligand-Driven Light-Induced Spin Change

The concept of ligand-driven light-induced spin change (LD-LISC) was first proposed by Zarembowitch and co-worker.^[58] Their strategy to achieve a reversible and sustainable spin change in a transition-metal coordination compound was based on the idea of “varying the ligand-field strength under the effect of an electromagnetic radiation”.^[59] They proposed that a reversible intramolecular photochemical reaction of one or more ligands can change the ligand-field splitting Δ in a way that promotes the SCO process. The principle is illustrated in Figure 1.5. The transition-metal complex C_A with the ligand isomer L_A exhibits a thermally-induced SCO can be seen from the evolution of the fraction of the HS compound (γ_{HS}) as a function of temperature (T). Furthermore, a slight variation of the ligand-field strength should also be sufficient to induce the SCO. The complex C_B formed with the ligand isomer L_B should possess a SCO temperature significantly different from that of C_A .^[59] In order for the spin change to be observed under the most favorable conditions, C_A and C_B should meet the requirements of having similar geometries of the coordination cores,

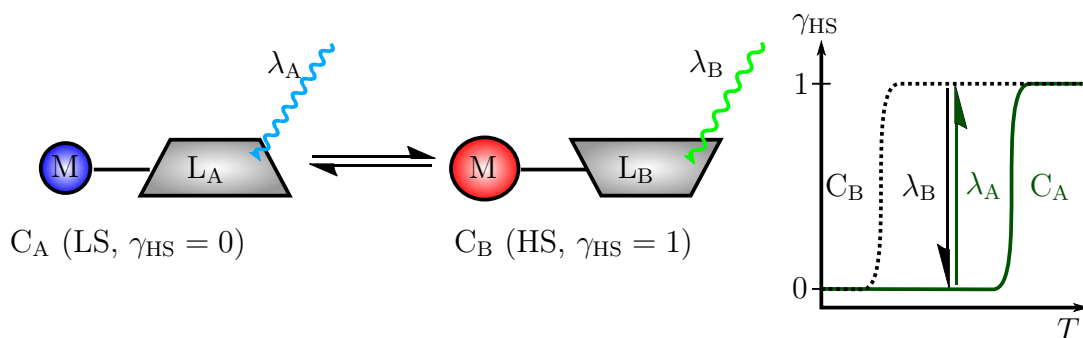


Figure 1.5: Principle of ligand-driven light-induced spin change (LD-LISC). Reproduced from Ref. 62.

different spin states in a rather wide temperature range and high quantum yields for ligand photoisomerization.^[59] First successful attempts used Fe(II) centers in combination with 4-styrylpyridine (stpy) ligands in cellulose acetate films at 140 K.^[60] These ligands can undergo a reversible *trans-cis* photoisomerization reaction upon irradiation with ultraviolet (UV) light. It was argued, that the loss in π -conjugation, triggered by the *trans-to-cis* isomerization is accompanied by a reduction of π -backbonding, resulting in a weaker ligand field. Eventually, LD-LISC at room temperature was achieved.^[61] Henceforth, further adoptions of the LD-LISC scheme have been reported, underscoring its importance for realizing the spin-state switching of transition-metal complexes in solution.^[62,63] A very successful example was presented by Khusniyarov and co-workers, who used the cyclization/photocycloreversion reaction of a diarylethane derived ligand to induce the SCO in an iron complex in acetonitrile solution at room temperature. They reported turnover efficiencies of 40% and thermal half-life times of 18 d.^[64] Hitherto, however, no case of quantitative and reversible bi-stability has been achieved.

1.3.2 Light-Driven Coordination-Induced Spin-State Switching

Another promising concept to achieve bi-stable spin switching in solution and at room temperature was developed by Herges and co-workers.^[65–70] Their approach is based on the fact that several transition-metal ions possess oxidation states (*e.g.*, Mn(III), Fe(II), Fe(III), Co(II), Co(III) and Ni(II)) which can exist in different spin states depending on the coordination number (N). They chose Ni(II) which, despite its small attainable spin change ($\Delta S = 1$) compared to, *e.g.*, Fe(II) ($\Delta S = 2$) offers the advantage of facile synthesis and handling due to its oxidation stability and reliable predictability through quantumchemical calculations.^[68,69] As basic complex structure, a tetradentate porphyrin ligand was used to form a square planar nickel porphyrin complex (N = 4). Since Ni(II) has a d^8 electron configuration, in the square-planar environment of the

porphyrin the $d_{x^2-y^2}$ is very high in energy and remains unoccupied, giving rise to the diamagnetic LS ($S = 0$) complex. However, nickel porphyrins properly designed with respect for the association constant of axial coordination are able to form square-pyramidal ($N = 5$) or octahedral ($N = 6$) complexes by binding one or two axial ligands. The association constant strongly depends on the nucleophilicity of the solvent and the acidity of the nickel center. In piperidine, which is a strong nitrogen donor, 90% of NiTPP molecules are bis-ligated,^[71] whereas pyridine only binds at high concentrations.^[72] Concomitantly, increasing the electron deficiency of the porphyrin and thus the acidity of the nickel center also leads to an increased binding strength.^[65] This can be achieved by electron withdrawing substituents in the *meso*-positions, as demonstrated for nickel dodecaphenylporphyrin (NiDPP) which forms octahedral complexes with neither piperidine nor pyridine, while for (NiF₂₀DPP) a ligation of 80% and 65%, respectively, is observed.^[73] Furthermore, structural factors concerning the porphyrin as well as the ligands strongly influence the axial reactivity.^[74] The axial coordination lifts the doubly occupied d_{z^2} -orbital in energy, which eventually results in the promotion of an electron to the $d_{x^2-y^2}$ -orbital, giving rise to paramagnetic HS ($S = 1$) complexes. The increased size of the HS Ni(II) ion leads to an elongation in Ni–N bond length which induces a flattening of the porphyrin ring that possesses a ruffled conformation when the nickel is 4-coordinate. Large substituents in the *meso*-positions, however, can impede this increase in planarity and thus hinder axial coordination.^[65] The occurrence of 5-coordinate nickel porphyrin species is rare since the ligand exchange is fast and the association constant for the binding of the first ligand (K_{1S}) is usually much smaller than that for the second one (K_2). Thus, the 5-coordinate species will only exist in small concentrations and will rapidly be converted into the 6-coordinate complex.^[75] The control over the coordination number was achieved by two different approaches that are shown in Figure 1.6. On the one hand, the steric hindrance can be switched in order to control the coordination number by using photodissociable ligands (PDLs). This approach was successfully demonstrated by the use of azopyridine derivatives. Azopyridines can undergo a reversible photo-induced *trans-cis*-isomerization reaction. The azopyridines used as PDLs can bind in the *trans*-configuration but suffer from dissociation due to steric hindrance when switched to the *cis*-configuration.^[65,66,68,69] On the other hand, nickel porphyrins with an azopyridine covalently attached to the porphyrin were designed. In this so-called “record player” molecule, the orientation of the azopyridine in the *trans*-configuration prevents it from axial coordination, while the *cis*-azopyridine has the perfect geometry for binding to the nickel center. As a result, record player spin switches show exceptional turnover efficiencies between the LS and HS form of almost 100%, high thermal stability and no photochemical fatigue.^[67,69,70] The unprecedented properties of molecules based on this design make them interesting candidates for applications as, *e.g.*, photoswitchable contrast agents in magnetic resonance imaging

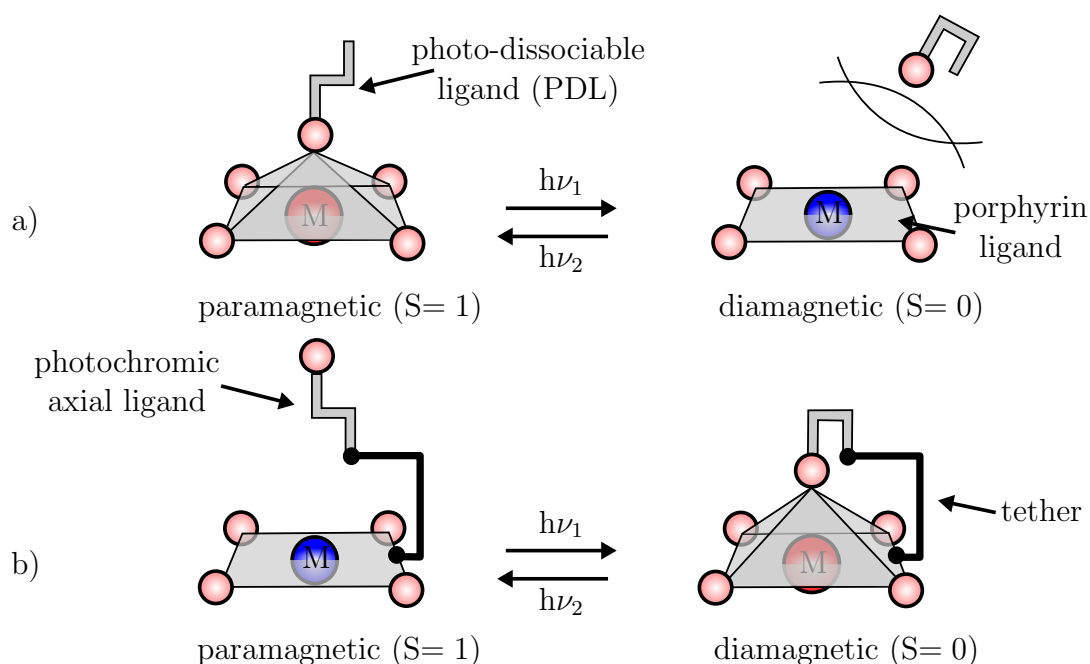


Figure 1.6: Principle of light-driven coordination-induced spin-state switching (LD-CISSS) using photo-dissociable ligands (PDLs, a) and the “record player” design (b). Reproduced from Ref. 68.

(MRI).^[67,69,70] However, the underlying mechanism of the photo-induced spin-state switching remained unclear.

One major aim of this Thesis is to study the photophysical and photochemical properties and driving forces of the molecular dynamics of compounds that were designed on the basis of the previously presented concepts and help to develop a strategy to improve and foster a more rational design of such molecules. In Chapter 3 and 4, the photodynamics of a bi-stable azopyridine nickel porphyrin (record player) designed on the basis of the LD-CISSS concept are investigated by time-resolved electronic absorption spectroscopy and stationary spectroscopic techniques. A general picture of the photodynamics of nickel porphyrins is outlined here in Section 1.4.

In Chapter 5, the photodynamics of a novel azopyridine-functionalized iron polypyridyl complex, designed on the basis of the LD-LISC concept, is investigated by time-resolved electronic absorption spectroscopy. Fundamental aspects of the photodynamics of structurally related iron polypyridyl systems are briefly discussed in Section 1.5.

Further, since in both cases azopyridines are used as ligands that should induce the SCO or stabilize the respective spin states in order to achieve bi-stability, the general photochemistry of azo compounds is discussed in Section 1.6.

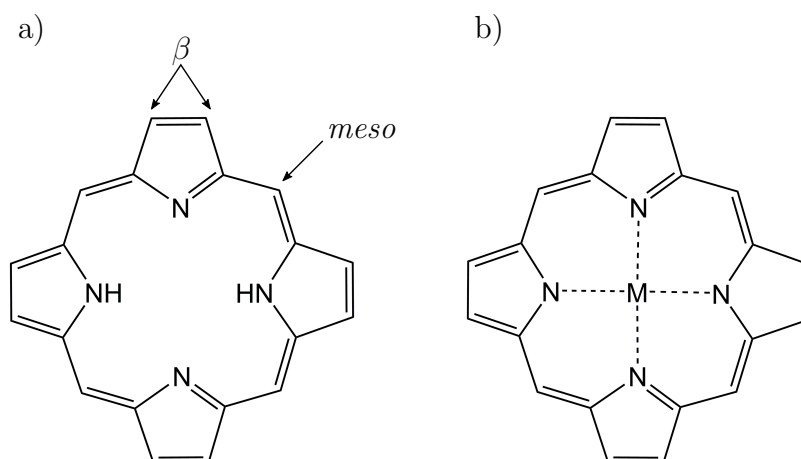


Figure 1.7: Chemical structure of free-base porphine (a) and porphine with an incorporated metal ion (b).

1.4 Photophysical and Photochemical Properties of (Metallo)Porphyrins

As (metallo)porphyrins are naturally occurring chromophores that play major roles in many important biological processes, they have been subject to intense research for decades.^[76–79] As prosthetic groups in hemoproteins, *i.e.* hemoglobin, myoglobin and cytochrome c, they are responsible for the oxygen transport in vertebrates as well as cellular respiration. In the form of chlorophyll, they take part in photosynthesis in green plants and algae. Many of their fascinating functions are initiated by the absorption of light. Their high oscillator strength and photostability makes them particularly interesting for applications in fields of solar energy conversion^[80,81] and medicine.^[18]

The basic porphyrin skeleton is the free-base porphine (Figure 1.7a) that consists of four pyrrole units that are covalently linked by methine bridges to form an aromatic macrocycle. Derivatives of this molecule can be obtained upon functionalization at the *meso*- and β -positions as highlighted in Figure 1.7a. Furthermore, this molecule can act as a tetradentate chelating ligand to metal ions (Figure 1.7b). Depending on the nature of the incorporated ion and the substitution of the macrocycle, the ground- as well as excited-state reactivities of the complex can be changed systematically. First, a general picture of the electronic states and transitions in (metallo)porphyrins is presented. Second, an overview over the photodynamics of (metallo)porphyrins is given with focus on nickel porphyrins in particular.

Electronic States and Transitions in Porphyrins

The electronic absorption spectra of porphyrins usually feature two distinct sets of absorption bands arising from $\pi^* \leftarrow \pi$ transitions, an intense ($\epsilon \approx 10^5 \text{ L mol}^{-1}$

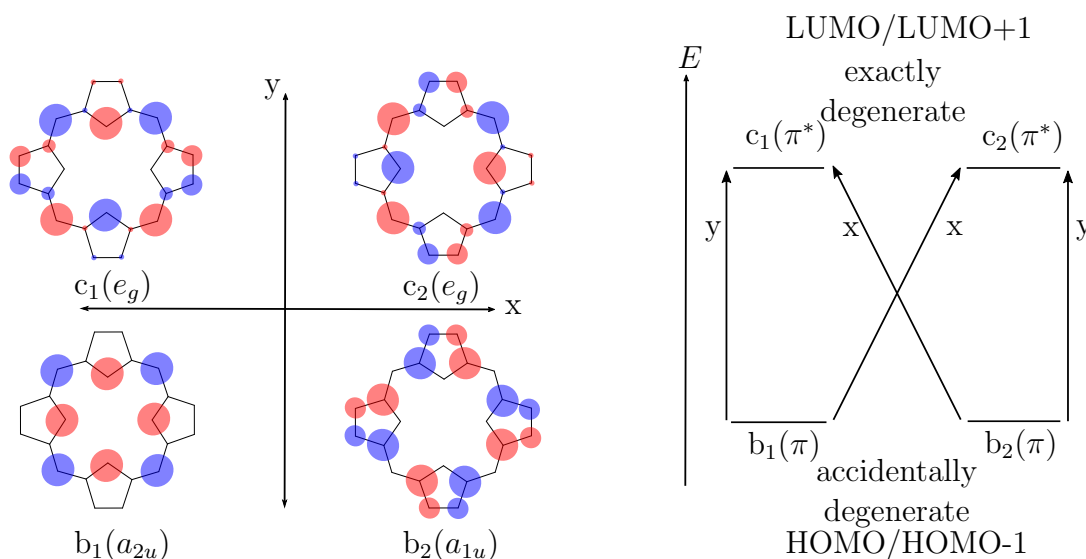


Figure 1.8: Schematic depiction of the HOMOs and LUMOs of a D_{4h} porphyrin that form the basis of the four-orbital model by Gouterman (a). Transitions resulting in the pairwise degenerate one-electron excited-state configurations together with their respective polarizations (b).

cm^{-1}) band in the ultraviolet (UV) and a less intense set of bands in the visible (vis) region of the spectrum. Traditionally, these transitions are rationalized in the four-orbital model developed by Gouterman.^[76,82] It is derived from previous theoretical works by Longuet-Higgins and Simpson that described metal porphyrins as 16-membered cyclic polyenes based on a Hückel model.^[83,84] As depicted in Figure 1.8, within the D_{4h} point group, the two highest occupied molecular orbitals (HOMOs) b_1 and b_2 show a_{2u} - and a_{1u} -symmetry, respectively, while the two lowest unoccupied molecular orbitals (LUMOs) c_1 and c_2 are of e_g -symmetry. However, in contrast to the naive molecular orbital (MO) calculations for cyclic polyenes it is necessary to assume that in porphyrins the HOMOs are accidentally degenerate, while the LUMOs are exactly degenerate. The pairwise degenerate one-electron excited states (Figure 1.8) generated from transitions $b_1 \rightarrow c_1, c_2$ and $b_2 \rightarrow c_1, c_2$ both transform as E_u . These states can mix by configuration interaction, because they are of same symmetry and close in energy. The two possible linear combinations of their wavefunctions result in the S_1 and S_2 state. While the dipole moments of the $S_2 \leftarrow S_0$ transition reinforce each other, the dipole moments of the $S_1 \leftarrow S_0$ transition almost cancel out.^[85] A schematic depiction of the resulting states and corresponding absorption spectra is given in Figure 1.9a. The intense absorption bands in the UV are referred to as B or Soret bands, while the less intense vis bands are referred to as quasi-allowed bands or in short Q bands. Since the central metal ion only influences the energetics of the b_1 orbital, as the metal ion becomes more electro-positive the Q bands will undergo a bathochromic shift and intensify.^[76] The observed splitting of the Q bands into the Q(0,0)

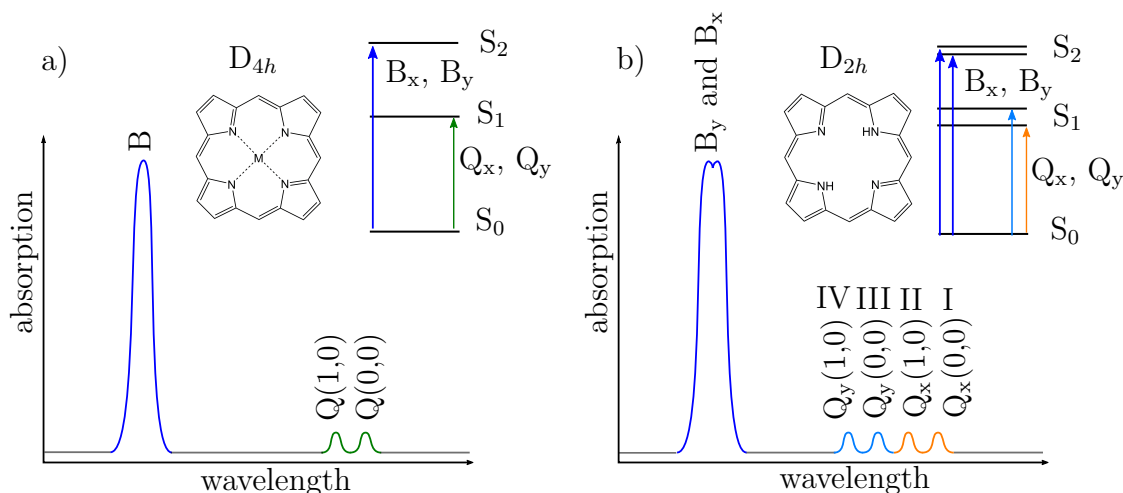


Figure 1.9: Generic picture of the possible electronic transitions and resulting spectra of a metal porphyrin with D_{4h} symmetry (a) and the corresponding free-base porphine with D_{2h} symmetry (b) derived from the four-orbital model.

and $Q(1,0)$ components is ascribed to a vibrational progression due to vibronic coupling with the Soret band. Going from the metal-salt back to the free-base porphine a further splitting of the Q bands is observed which is displayed in Figure 1.9b. The two opposite protons stabilize a 18-membered ring, while lowering the symmetry to D_{2h} . Now the HOMOs b_1 and b_2 exhibit a_u and b_{1u} symmetry while the LUMOs c_1 and c_2 transform as b_{2g} and b_{3g} . Of the four resulting one-electron excited-state configurations two transform as B_{3u} while the other two transform as B_{2u} . The transitions to the B_{3u} states are polarized along the x-axis while transitions to the B_{2u} states are polarized perpendicularly along the y-axis. Since the opposite pyrrole protons lift the degeneracy of the x- and y-axis, the transitions split into B_x , B_y , Q_x and Q_y .^[76,85,86] The effect of this splitting is much stronger on the Q than on the B bands.^[85–87] The different polarizations of the transitions was demonstrated in fluorescence depolarization experiments by Weigl.^[88] Moreover, the effect of substitution of the porphyrin macrocycle can be explained by the four-orbital model. Introduction of substituents on the β -positions for example affects the energies of the orbitals b_2 , c_1 and c_2 . Depending on the relative energies of the orbitals to each other, the intensities of the Q bands I–IV vary strongly, which can explain the occurrence of *etio*-, *phyllo*- and *rhodo*-type porphyrin spectra.^[76,89] For *etio*-type porphyrins the relative intensities are such that $IV > III > II > I$, which is the case if six or more of the β -positions are occupied with groups that do not possess π -electrons. In contrast, attached carbonyl or vinyl groups in the β -positions change the intensity sequence to $III > IV > II > I$, which is referred to as *rhodo*-type, as they also introduce a red-shift to the spectra. When $IV > II > III > I$, the porphyrin belongs to the *phyllo*-type, which is obtained by *meso*-substitution.^[90] Furthermore, *meso*-substituted metalloporphyrins show a

merging of the Q bands.^[91]

Ultrafast Photodynamics of (Metallo)Porphyrins

(Metallo)Porphyrins have been subject to various time-resolved studies within the past decades. Tetraphenylporphyrin (TPP) is among the most extensively studied derivatives. Studies on the free-base TPP (H₂TPP) found that excitation in the Soret band ($S_2 \leftarrow S_0$ transition) is followed by an ultrafast IC that generates the lowest-lying singlet $^1(\pi, \pi^*)$ state (Q_x) within ≤ 100 fs. Most previous reports assume a consecutive scheme in which relaxation from the B state to the Q_x state occurs via the Q_y state. However, the time constants of the decay processes have been assigned differently. Akimoto *et al.* studied a structurally similar free-base porphyrin using femtosecond fluorescence up-conversion.^[92] They assigned a 90 fs fluorescence component to the conversion from the Q_y to the Q_x state, while estimating <40 fs for the initial decay of the Soret state. In contrast, Zewail and co-workers interpreted the 100–200 fs component obtained from transient absorption and fluorescence up-conversion experiments as an IVR process leading to the thermal equilibration of the Q_x state.^[93] They suggest time scales of ≤ 50 fs for $B \rightarrow Q_y$ and ≤ 100 fs for $Q_y \rightarrow Q_x$ IC. Kim and co-workers established a value of 68 fs for the fluorescence lifetime of the B state.^[94] More recent studies, carried out with high time resolution propose a competition between a direct conversion from B to Q_x and the sequential pathway via Q_y , inferred from coherent nuclear wavepacket motion in both states that can be observed by a modulation in fluorescence intensity.^[95] In any case, the decay of the B state and formation of the Q_x state is completed in ≤ 100 –200 fs. The ultrafast IC from the Q state was theoretically examined by Falahati *et al.* using electronic structure studies and on-the-fly surface-hopping nonadiabatic dynamics.^[96] They claim that dark states within the elusive N band effectively mediate the $B \rightarrow Q$ conversion. The N band arises from non-Gouterman transitions under participation of orbitals not considered in the four-orbital model, *i.e.*, the HOMO–2 (b_{3g}) and HOMO–3 (b_{1u}).^[96–98] Solvent-induced vibrational relaxation within the Q_x state is observed with time constants of 1.4 ps and 10–20 ps.^[93] Deexcitation to the electronic ground state is a slow process. The lifetime of the Q_x state in H₂TPP was determined to ~ 13 ns^[99–101] and assigned to either ISC^[93,102] to the triplet $^3(\pi, \pi^*)$ state that decays on the micro- to millisecond timescale^[103,104] or to ground-state recovery.^[92] Relaxation times to the ground state were shown to be accelerated when the porphyrin gains flexibility by a decrease of the planarity of the skeleton. This can be achieved by steric crowding of peripheral substituents or incorporation of transition-metal ions.^[102]

The two extremely weakly acidic protons of the free-base porphine ($pK_a = 16$) can be substituted by various metal ions.^[33] Among many possible metalloporphyrins, those with an incorporated Zn(II) ion are the most extensively studied systems. Due to the closed-shell d^{10} electron configuration interactions between

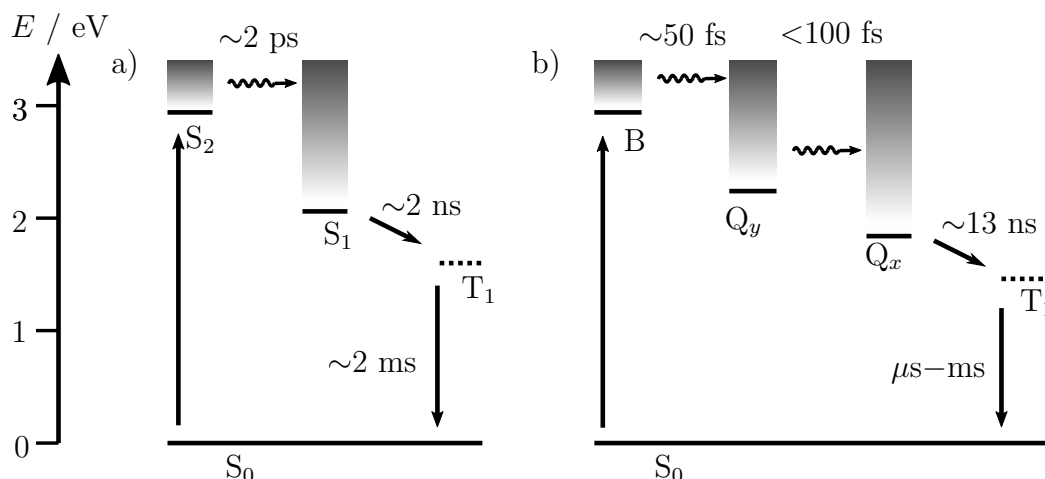


Figure 1.10: Schematic diagram of the energy levels and relaxation processes of a) ZnTPP in toluene and b) H_2TPP in benzene. Reproduced from Refs. 33 and 93.

the porphyrin and the metal are small and relaxation after photoexcitation will occur most likely, and exceptionally under involvement of porphyrin states.^[105] This makes Zn(II) porphyrin perfectly suited for studying the effects of increased symmetry of the macrocycle on the photodynamics. Time-resolved fluorescence experiments upon excitation of the Soret band revealed a significant slowing down of the IC from the S_2 to the S_1 state, which is no longer distinguished in Q_x and Q_y , to ~ 2 ps in ZnTPP.^[100,106–108] Subsequently, efficient ISC to the triplet state occurs within 1–2 ns.^[109–111] As the sum of the quantum yield of fluorescence from the S_1 state ($\Phi_F = 0.033$) and triplet formation ($\Phi_T = 0.88$) is > 0.9 , $S_1 \rightarrow S_0$ IC is not considered a major deactivation pathway.^[78,112] The efficient triplet-state formation and the long (millisecond)^[111] triplet-state lifetimes make zinc porphyrins particularly useful as photosensitizers.^[113–116] The general photodynamics and timescales for the paradigmatic free-base and zinc porphyrins systems H_2TPP and ZnTPP are summarized in Figure 1.10.

However, the situation drastically changes when going from Zn(II) to Ni(II) which possesses d^8 electron configuration. The incomplete occupation of the d-orbitals enables rapid relaxation of the initially excited $\pi\pi^*$ states of the macrocycle via the formation of MC states. Indications for that are the low quantum yields for luminescence of these complexes, which usually possess emissive singlet or triplet $^1,^3(\pi, \pi^*)$ states.^[117–119] Furthermore, as already mentioned in Section 1.3, nickel porphyrins can be present in different complex geometries and can form 4-, 5- or 6-coordinate complexes, depending on the solvent and the substitution of the macrocycle, and therefore allow for the investigation of their (de-)coordination dynamics. The photodynamics of 4-coordinate nickel porphyrins in non-coordinating solvents have been studied to a high extent.^[119–127]

In the square-planar ($N = 4$) ligand field of the porphyrin, the $d_{x^2-y^2}$ orbital

of the d^8 nickel(II) ion remains empty. Deexcitation of the initially excited $S_1(\pi, \pi^*)$ or the $S_2(\pi, \pi^*)$ state of the porphyrin occurs in less than one picosecond through energy transfer to the metal center. As a consequence of the energy transfer, an electron is promoted from the doubly occupied d_{z^2} orbital to the $d_{x^2-y^2}$ orbital to form the (d,d) state. Whether the energy-transfer process is due to ISC to the paramagnetic $^3(d,d)$ or IC to the diamagnetic $^1(d,d)$ state is debated elsewhere.^[128] Since this state is formed with an high excess of vibrational energy, it subsequently undergoes vibrational and conformational relaxation within several picoseconds, with the precise value depending on the solvent.^[122,123] For the relaxed (d,d) state lifetimes of hundreds of picoseconds are reported. Although 4-coordinate nickel porphyrins have been subject to time-resolved studies for several decades, some controversy remains. In general, similar photodynamics are observed independent of whether the B or Q bands are excited. Consequently, it is assumed that, similar to free-base and zinc porphyrins, the S_2 state relaxes within the experimental time resolution via the S_1 state. However, the nature of the first observed transient is interpreted differently. Mostly, the broad and featureless initially observed transient is assigned to the lowest excited singlet $^1(\pi, \pi^*)$ state of the porphyrin and thus the fastest (<1 ps) time component to the energy-transfer process forming the metal centered (d,d) state.^[119–123,127,128] However, Eom *et al.* studied NiTPP and nickel octaethylporphyrin (NiOEP) in different solvents.^[129] From the lack of stimulated emission and the broad and featureless shape of the spectrum, they derive that neither the porphyrin $S_2(\pi, \pi^*)$ nor the $S_1(\pi, \pi^*)$ state but a vibrationally highly excited (d,d) state of the metal is present immediately after photoexcitation. The reported decay time constants of $\tau_1 = 0.7–3.5$ ps, $\tau_2 = 4–30$ ps and $\tau_3 = 350$ ps are consequently assigned to inter- and intramolecular vibrational relaxation and conversion to the ground state, respectively. Zhang *et al.* further question the sequential $S_2 \rightarrow S_1 \rightarrow (d,d)$ relaxation scheme, by proposing that direct $S_2 \rightarrow (d,d)$ ISC is faster than $S_2 \rightarrow S_1$ IC and consequently different relaxation pathways follow S_2 and S_1 excitation.^[124] This is derived from the finding that stimulated emission from the S_1 state is only observed if this state is directly excited whereas it is absent following excitation to the S_2 state. They conclude that $S_2 \rightarrow (d,d)$ ISC happens within the experimental time resolution and find time constants of 0.2–0.4 ps for $S_1 \rightarrow (d,d)$ ISC, 2 ps and 6–20 ps for IVR and VC within the (d,d) state and 100–200 ps for recovery of the ground state. In summary, independent of whether the $S_2(\pi, \pi^*)$ or $S_1(\pi, \pi^*)$ state of the macrocycle is initially excited, the (d,d) state is reached in less than a picosecond. There is a general agreement that triplet $^3(\pi, \pi^*)$ as well as LMCT (π, d) and MLCT (d, π^*) states play no role in the relaxation dynamics since the associated near infrared (NIR) absorption features are absent in all studies.^[125,126] The relaxation of the (d,d) state to the ground state of the molecule takes hundreds of picoseconds. In the presence of coordination partners such as nitrogenous bases, however, the lifetime of this state can be drastically in-

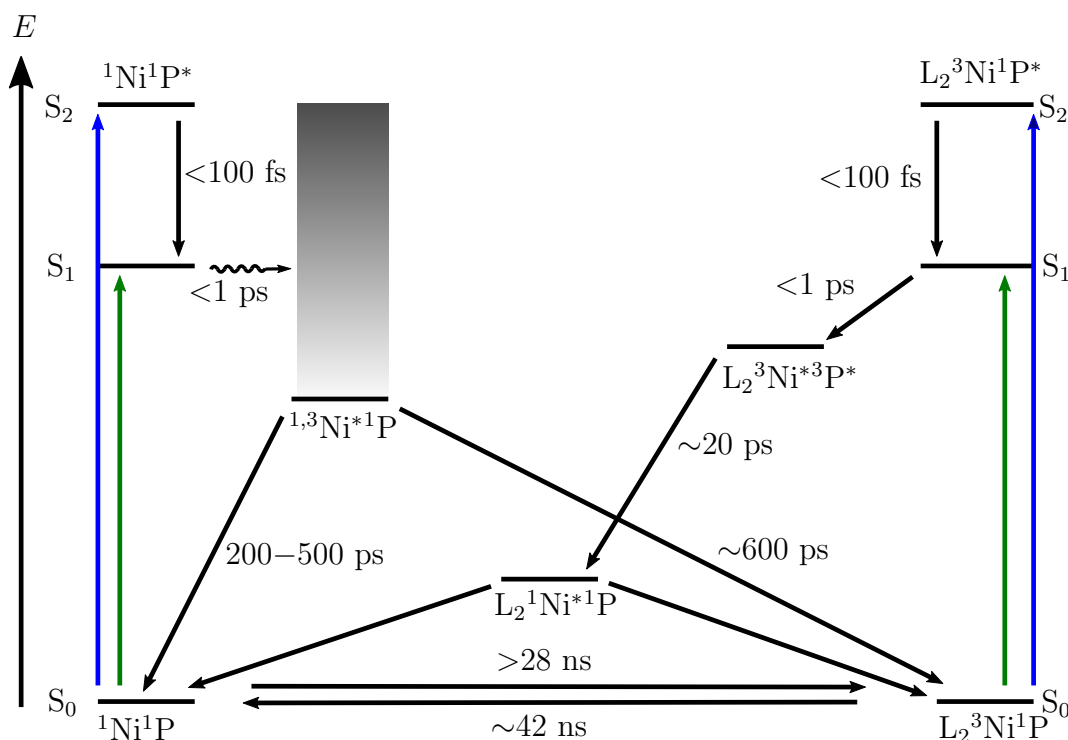


Figure 1.11: Illustration of the key processes and general timescales of the relaxation of nickel porphyrins with and without axial ligands (L) after photoexcitation adapted from Ref. 73. The preceding superscripts denote the spin multiplicity at the nickel (Ni) and the porphyrin (P). The asterisk denotes the excited species.

creased since its electron configuration is attractive towards axial ligation.^[89,130] The excited-state coordination dynamics of nickel porphyrins have been extensively studied by Holten and co-workers.^[89,130] They report an increase of the lifetime of the (d,d) state from 450 ps of the uncomplexed species to >20 ns when complexed by two pyridines. More recent studies by Chen *et al.* reported an elongation of the lifetime of the (d,d) state of nickel tetramesitylporphyrin (NiTMP) from 200 ps to 42 ns when pyridine ligation takes place.^[131,132] As discussed in Section 1.3, nickel porphyrins can also bind two axial ligands to form octahedral complexes with the nickel being 6-coordinate in its ground state. In the octahedral ($N = 6$) environment, the d_{z^2} - and $d_{x^2-y^2}$ -orbitals of nickel are both singly occupied, giving rise to the paramagnetic $^3(d,d)$ ground state. Photoexcitation of the $^1(\pi, \pi^*)$ state of the porphyrin now leads to the formation of a MC excited state with $(d_{z^2})^2$ configuration. This $(d)^2$ state acts repulsive towards axial ligands causing their release which generates the 4-coordinate complex.^[73,89,119,129,130,133,134] The deactivation cascade leading to the formation of the diamagnetic $^1(d)^2$ state occurs via several intermediates, of which one probably involves a porphyrin triplet $^3(\pi, \pi^*)$ state that conserves the spin mul-

tiplicity of the photo-produced state.^[119,135] Ultimately, rebinding of the ligands and recovery of the (d,d) ground state occurs in tens of nanoseconds.^[133,134] The key photophysical processes and (de-)coordination dynamics together with the general timescales are summarized in Figure 1.11. Although 5-coordinate species are proposed as intermediates in the (de-)coordination dynamics following photoexcitation of 4- and 6-coordinate nickel porphyrins^[73] studies regarding their photodynamics are barely present since they cannot be isolated for the reasons mentioned in Section 1.3.

The ultrafast photodynamics of the bi-stable azopyridine nickel porphyrin spin switch dubbed record player (RP), the reference complex NiTPPF₂₀ and the free-base porphyrin H₂TPPF₂₀ are subject to the studies presented in Chapter 3 and 4 of this Thesis. Upon irradiation the coordination number of the nickel(II) ion in RP can be reversibly switched between the 4-coordinate complex with the diamagnetic ¹(d)² ground state and the 5-coordinate complex with the paramagnetic ³(d,d) ground state. The results obtained for RP, NiTPPF₂₀ and H₂TPPF₂₀ are embedded in the context of this Section.

1.5 Photophysical and Photochemical Properties of Metal Polypyridyls

Metal polypyridyls are a large class of molecules that have played major roles in a variety of applications that make use of the excited-state chemistry of transition-metal complexes. Therefore, the understanding of the photophysics and photochemistry of these compounds has become a pivotal challenge in the development of solar cells,^[16] photoredox catalysts^[17] and photodynamic therapy agents.^[18] Among these compounds, tris(2,2'-bipyridine)ruthenium(II) ([Ru(bpy)₃]²⁺ (Figure 1.12a) is one of the most extensively studied molecules during the past decades and can be viewed as a prototype for this class of complexes. Although [Ru(bpy)₃]²⁺ nominally possesses a D₃-symmetry, to a first approximation it can be considered an octahedral complex. The Ru(II) has a d⁶ LS configuration and thus its ground state is a singlet state with the t_{2g}-orbital as the HOMO. Since Ru(II) is easy to oxidize and hard to reduce, while bpy is hard to oxidize and easy to reduce, LMCT states are high in energy and MLCT states are expected at low energies.^[33] Furthermore, the strong ligand-field splitting in 4d- and 5d-metals causes the e_g orbitals to be energetically above the ligand π* orbitals. Consequently, as illustrated in Figure 1.12b, the lowest-lying excited state is not of MC but of MLCT character, giving rise to an intense visible absorption band (λ_{max} = 452 nm; ε_{λ_{max}} ≈ 13000 L mol⁻¹ cm⁻¹ in acetonitrile).^[136] A Jablonski diagram summarizing the relaxation processes after photoexcitation of [Ru(bpy)₃]²⁺ is depicted in Figure 1.12c. Excitation at this absorption band initially produces the singlet ¹MLCT state, however, the heavy metal ruthenium enables rapid ISC to the triplet ³MLCT state, which is formed with unity quan-

tum yield.^[137] Femtosecond time-resolved absorption spectroscopy established a timescale of ~ 300 fs until the population of the $^3\text{MLCT}$ state is completed after photoexcitation.^[138] Fluorescence up-conversion experiments revealed time constants of <50 fs for the decay of the $^1\text{MLCT}$ emission.^[139–141] In this state the Ru-N distances are only weakly elongated, which in combination with the large energy gap between the $^3\text{MLCT}$ state and the ground state, favors a radiative deexcitation pathway. This relaxation path competes with the nonradiative deactivation through the MC $^3\text{T}_1$ state. However, as this state is slightly higher in potential energy and significantly distorted along the Ru-N coordinate, a certain barrier has to be surmounted. This results in a long lifetime of the $^3\text{MLCT}$ state that was determined by time-resolved emission experiments to range from 500–1000 ns depending on solvent, temperature and oxygen concentration and a decent quantum yield of luminescence ($\Phi = 0.045$).^[136,142–144] Furthermore, the spacial redistribution of electron density in this state causes an enhanced reactivity compared to the ground state.^[136] These properties make $[\text{Ru}(\text{bpy})_3]^{2+}$ a popular choice as a photosensitizer for the initially mentioned applications.

However, on a larger scale, it is desired to achieve similar photochemical properties using more inexpensive, environmentally benign and potentially nontoxic metals.^[145,146] In this context, iron-based complexes seem promising candidates, as iron is the fourth most abundant element in the Earth’s crust and in the same group of the periodic table as ruthenium.^[147] However, Fe(II) polypyridine complexes possess a drastically different excited-state chemistry compared to the Ru(II) analogues, which shall be demonstrated on the example of the archetypical complex $[\text{Fe}(\text{bpy})_3]^{2+}$ which is depicted in Figure 1.12d. The radial distribution of the six 3d electrons of Fe(II) is closer to the metal than that of the 4d electron in Ru(II) giving rise to a weaker ligand-field splitting.^[144] As a consequence, the e_g orbitals are energetically lower than the ligand π^* orbitals and the MC $^5\text{T}_{2g}$ state becomes the lowest-lying excited state, while the MLCT states are basically left unaffected (Figure 1.12e).^[148] This enables the photo-produced $^1\text{MLCT}$ state to deactivate in a barrierless fashion to the lowest ligand-field state, manifesting itself in an absence of notable luminescence in iron complexes. Early experiments by McCusker and co-workers revealed that the population of the $^5\text{T}_2$ state is completed in <1 ps, followed by a slower 2–3 ps step which was assigned to vibrational cooling within this state.^[149] Subsequent recovery of the $^1\text{A}_1$ ground state takes about 650 ps.^[150] Further studies were carried out with the goal to resolve the intermediate events of the $^1\text{MLCT} \rightarrow ^5\text{T}_2$ transition. Chergui and co-workers concluded from broadband fluorescence up-conversion experiments that the photo-produced $^1\text{MLCT}$ state is depopulated within <20 fs, which is in accordance with the observations made for $[\text{Ru}(\text{bpy})_3]^{2+}$. They were also able to identify the $^3\text{MLCT}$ by its emission with a decay time of <150 fs. Additional transient absorption spectroscopy demonstrates that the absorption features of the $^5\text{T}_2$ state arrive within 960 fs consistent with the previous results.^[151] In a subsequently performed X-ray near-

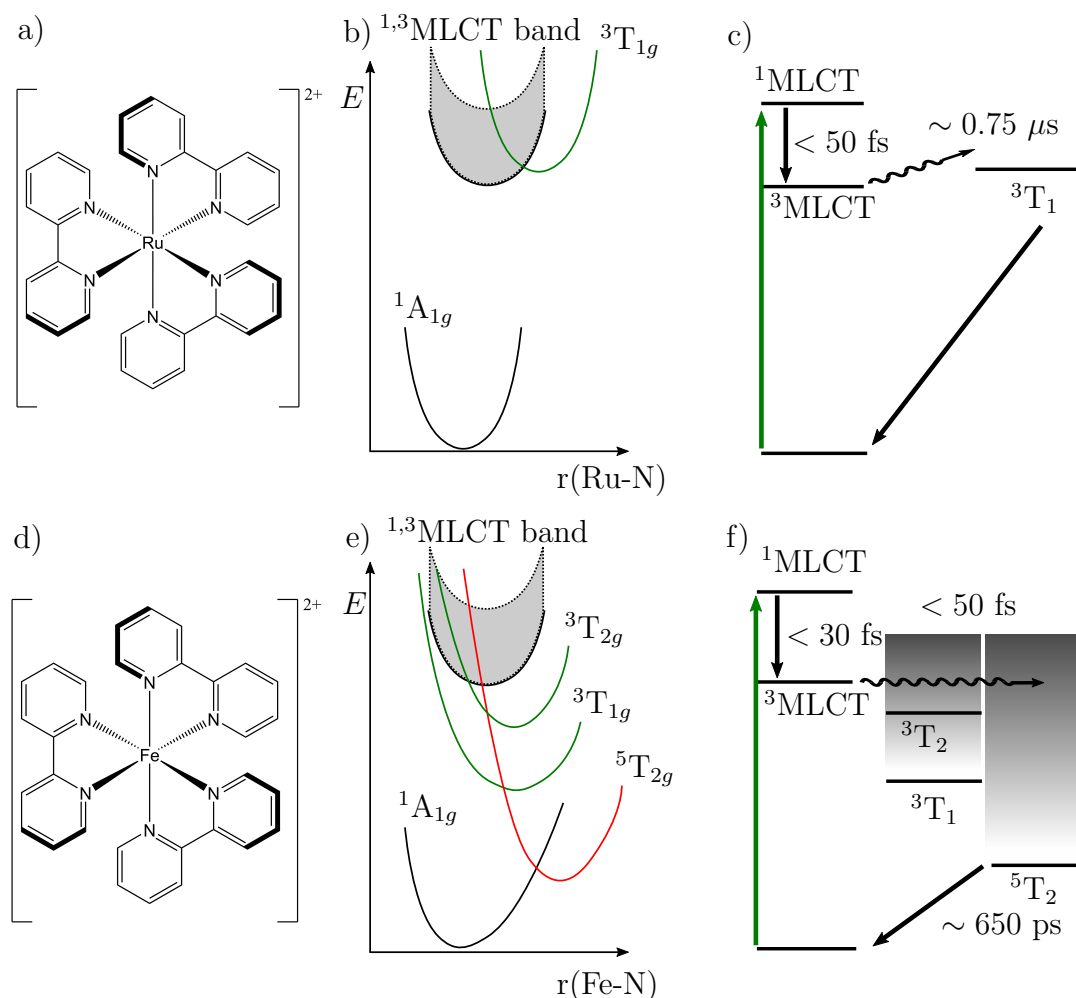


Figure 1.12: Chemical structures, electronic states and Jablonski diagrams of $[\text{Ru}(\text{bpy})_3]^{2+}$ (a–c) and $[\text{Fe}(\text{bpy})_3]^{2+}$ (d–f). Reproduced from Refs. 144, 148 and 33.

edge absorption spectroscopy (XANES) study the 120 fs decay of the $^3\text{MLCT}$ state was directly related to the rise time of the $^5\text{T}_2$ absorption.^[152] Direct probing of the UV absorption of the quintet state further revealed the appearance of vibrational wavepackets on the $^5\text{T}_2$ surface with oscillation periods of 254 fs.^[153] On the basis of these results Chergui and co-workers claim a direct $^3\text{MLCT} \rightarrow ^5\text{T}_2$ ISC, bypassing the MC triplet $^3\text{T}_2$ and $^3\text{T}_1$ states.^[152–154] This is in contrast to other experimental and theoretical works suggesting a weak SOC constant between the $^{1,3}\text{MLCT}$ and $^5\text{T}_2$ and a more favorable relaxation path involving IC to the $^3\text{T}_2$ and $^3\text{T}_1$ states.^[155] However, those findings are contradictory to the fact that direct excitation of the ^3T states populate the $^1\text{A}_1$ and the $^5\text{T}_2$ state at a ratio of 1:4,^[156] while the $^5\text{T}_2$ state is populated from the $^1\text{MLCT}$ state with unity quantum yield.^[157] In the most recent study Auböck *et al.* impressively demonstrated that the $\text{MLCT} \rightarrow ^5\text{T}_2$ transition even occurs in

less than 50 fs, leaving extremely little time for the population of intermediate ligand-field states.^[158] These results are summarized in the Jablonski diagram in Figure 1.12f. Similarly fast ISC dynamics are observed in structurally related iron polypyridyl complexes.^[149,150,159–164] Thus, if a photochemical properties resembling those of $[\text{Ru}(\text{bpy})_3]^{2+}$ are desired with iron, the lifetime of the luminescent $^3\text{MLCT}$ state have to be increased by several orders of magnitude. This can be achieved by either stabilizing the $^3\text{MLCT}$ state or pushing the MC states to higher energies. The six key concepts developed by different workgroups that are working towards this goal are summarized by Wenger.^[144] A record lifetime of 26 ps was reported Gros *et al.*^[145] However, the nonluminescent HS $^5\text{T}_2$ state that is formed after photoexcitation of iron polypyridyl complexes can be exploited in other photochemical contexts. Since this state is of quintet multiplicity ($S = 2$) its formation from the singlet $^1\text{A}_1$ ground state ($S = 0$) is a two-electron transition with an overall spin change of $\Delta S = 2$. The fact that the $^5\text{T}_2$ state is formed with unity quantum efficiency and is fairly long-lived make iron polypyridyl complexes interesting candidates for the SCO application mentioned in Section 1.3.^[144,158]

In Chapter 5 the ultrafast photodynamics of the novel SCO complex $[\text{Fe}(\text{3Az-N4Py})(\text{MeCN})](\text{BF}_4)_2$ and the reference complex $[\text{Fe}(\text{N4Py})(\text{MeCN})](\text{BF}_4)_2$ are studied. Since the structures of the two complexes resemble that of previously studied iron polypyridyls, the results obtained are discussed in the context of this Section.

1.6 Azobenzenes as Molecular Photoswitches

This Thesis deals with the ultrafast photodynamics of transition-metal complexes that undergo photo-induced SCO. These compounds were designed to be magnetically bi-stable at room temperature. Bi-stability as well as reliable switching between the two spin states are essential prerequisites for SCO-based devices. Thus, large molecule-intrinsic potential energy barriers are required. Concepts to accomplish this goal were presented in Section 1.3. The molecules that were studied in this Thesis were designed on the basis of these concepts. Furthermore, selective addressing of each species and high quantum yields for the photoreaction are desired. In order to meet these demands, the investigated systems exploit the photoisomerization reaction of azopyridine derivatives, which are used instead of azobenzene, since the ring nitrogen atom facilitates coordination to metal centers. These compounds are structurally similar to azobenzenes that represent one of the most extensively studied classes of photochromic molecular switches during the past decades. The photochemical properties and ultrafast photodynamics of azopyridine will therefore be discussed in the context of azobenzene based compounds.

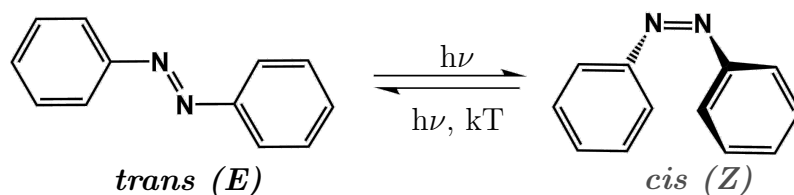


Figure 1.13: Chemical structure and reversible isomerization of azobenzene (AB).

Photophysical and Photochemical Properties of Azobenzene

As displayed in Figure 1.13, azobenzene (AB) based compounds can undergo a *trans-cis*-isomerization reaction that can be triggered by irradiation at an appropriate wavelength, as well as by mechanical stress or electrostatic stimulation.^[165] The conformational change from the *trans*- to the *cis*-isomer reduces the length of the molecule by ~ 3 Å and is accompanied by an increase in dipole moment from ~ 0 D for the *trans*- to ~ 3 D for the *cis*-isomer.^[166,167] As can be seen from the electronic absorption spectrum in Figure 1.14, the *trans*-isomer exhibits an intense ($\epsilon \approx 25 \cdot 10^3 \text{ L mol}^{-1} \text{ cm}^{-1}$) absorption feature in the UV around 330 nm originating from the $\pi\pi^*$ transitions and a less intense ($\epsilon \approx 0.5 \cdot 10^3 \text{ L mol}^{-1} \text{ cm}^{-1}$) absorption band in the vis region centered around 440 nm originating from the $n\pi^*$ transition. The electronic origin of the $n\pi^*$ transition has been determined precisely to $E_0(n\pi^*) = 18471.7 \text{ cm}^{-1}$ ($\lambda = 541.36 \text{ nm}$) in the gas phase.^[168] When switched to the *cis*-isomer, the $n\pi^*$ absorption band increases in oscillator strength as the symmetry of the system decreases from nominally C_{2h} to C_2 .^[169] The loss in planarity also causes the $\pi\pi^*$ absorption band to vanish and shift further into the UV. Excitation at either of the transitions in both isomers will lead to $\text{trans} \rightleftharpoons \text{cis}$ interconversion. However, looking at the UV–vis absorption spectra it seems obvious that continuous irradiation at $\lambda_{\text{irrad}} \approx 340 \text{ nm}$ effectively produces the *cis*-isomer in excess, while at $\lambda_{\text{irrad}} \approx 450 \text{ nm}$ a photostationary state (PSS) consisting predominately of the *trans*-isomer is reached. Furthermore, since the *trans*-isomer is lower in energy by 0.6 eV and *cis*→*trans* isomerization in the ground state has a potential energy barrier of $\approx 95 \text{ kJ mol}^{-1}$, thermal conversion of *cis*-AB occurs spontaneously in the dark with a half-life of 2 days.^[165,170] This process can be strongly influenced by substitution of the aromatic rings.^[171] Push-pull ABs, for example are substituted with an electron donating and an electron withdrawing group on the opposite phenyl rings, inducing a strong CT character to the $\pi\pi^*$ transition. Since the $S_2(\pi\pi^*)$ and the $S_1(n\pi^*)$ state become almost degenerate in push-pull ABs, these molecules are also referred to as pseudostilbenes. This manifests itself in a pronounced solvent-dependent red-shift of the absorption band and a drastic reduction of the isomerization energy barrier. Thus, thermal isomerization is accelerated to the millisecond-to-second timescale.^[165,172] In contrast, bulky substituents lead to a decrease in the rates of thermal back-isomerization by introducing attractive London dispersion interactions that stabilize the *cis*-isomer.^[173] The possibility

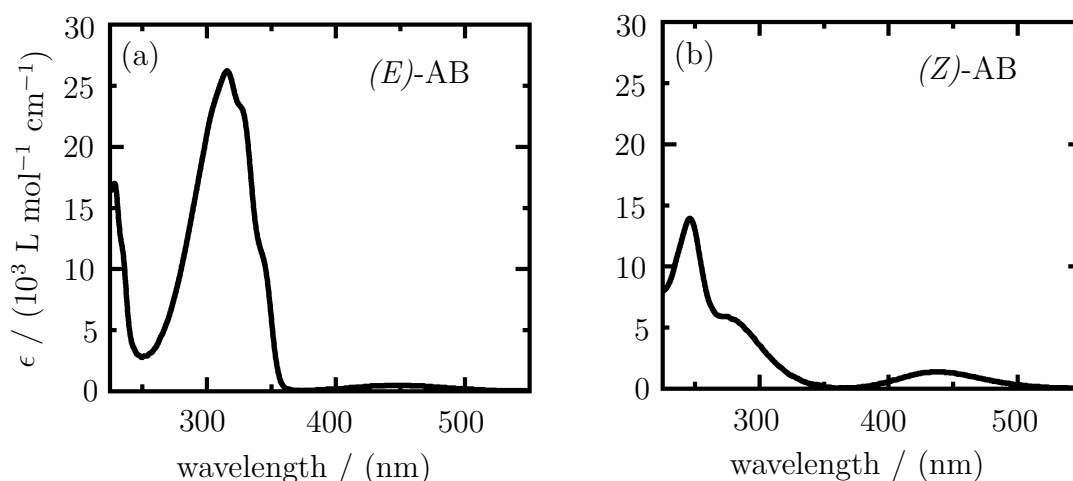


Figure 1.14: UV–vis absorption spectra of (a) the (*E*)- and (b) the (*Z*)-isomer of azobenzene (AB) in acetonitrile.

of selectively addressing both isomers with light, high photochemical fatigue and the preservation of its photochemical properties even under environmental constraints as well as the vast possibilities for tuning its photochemical properties make AB perfectly suited to build tailored photochromic materials. Examples of its successful application are countless.^[174–177] However, questions regarding the isomerization mechanism have been debated in length. Although in practice the manipulation of the isomerization QYs and thermal rates is sufficient, a detailed mechanistic understanding is mandatory for the design of AB-systems that execute a specific task.

In principle, five different mechanisms that depend on the photo-produced state, the substitution of the AB and environmental effects are proposed in the literature. These are the torsion, inversion, concerted inversion, inversion-assisted rotation and the hula-twist. The torsion mechanism is based on the alteration of the C-N-N-C dihedral angle at constant N-N-C angles. In contrast, for inversion/concerted inversion to occur the C-N-N-C dihedral angle remain constant while one/two N-N-C angles become 180°. Since the concerted inversion mechanism occurs over a linear transition state which was determined to be energetically unfavorable for free AB, it is generally not considered.^[178] In the inversion-assisted torsion mechanism all angles around the double bond are altered significantly. The recently suggested hula-twist can be viewed as pedal-like concerted motion of the nitrogen atoms and the phenyl rings.

Zimmerman *et al.* were the first to show that the isomerization QY following S_n excitation is $\sim 50\%$ lower than that following S_1 excitation, which is a violation of Kasha’s rule and hints at different molecular motions associated with the relaxation dynamics.^[179] Rau and co-workers investigated azobenzophanes, for which inversion is the only isomerization pathway and found isomerization QYs independent of the excitation wavelength.^[178] In a subsequent study on

sterically-hindered azobenzenes they proposed that “normal” azo compounds follow the inversion pathway in the lowest excited state and the torsion pathway in higher excited states.^[180] The most recently redetermined values of the isomerization QYs are given in Refs. 181 and 182. Based on these findings several ultrafast time-resolved studies as well as quantumchemical calculation were carried out to decipher the isomerization mechanism. A detailed summary of the research conducted on the photodynamics of azobenzene in solution can be found in Ref. 183. A brief overview shall be given in the next Section.

Ultrafast Photodynamics of Azobenzene

In early femtosecond time-resolved electronic absorption spectroscopy studies of *trans*-AB in different solvents by Moore and coworkers, it was stated that the photo-produced $\pi\pi^*$ state decays within <1 ps to a bottleneck state where IC to the ground state (and possibly IVR) takes place within ~ 15 ps.^[184] A follow-up study investigating the excitation wavelength dependence revealed an additional <200 fs component following $\pi\pi^*$ excitation which was attributed to motion along the rotational coordinate. In contrast, excitation to the $n\pi^*$ state close to the electronic origin showed an monoexponential decay with 2.5 ps which was attributed to motion along the inversion coordinate. An additional <600 fs component showed up when the $n\pi^*$ state was excited with some excess energy.^[185] Similar conclusions were drawn from the results obtained by Zinth and co-workers. They further investigated *cis*-azobenzene upon excitation to the $n\pi^*$ state and observed a fast photoreaction with 170 fs and 2 ps and a ~ 10 ps component that was assigned to vibrational cooling in the ground state.^[186,187] The assignment of the long time component was supported by subsequent measurements by Satzger *et al.* and time-resolved Raman studies by Tahara and co-workers.^[188–190] However, in meticulous studies by Ernsting and co-workers, this time component was also found in the ground-state recovery and thus re-assigned to the isomerization process which was found to be in line with the hula-twist rather than the inversion mechanism. Furthermore, in contrast to Tahara and co-workers, who concluded that upon $\pi\pi^*$ excitation all of the population passes through the same region of the S_1 state as upon $n\pi^*$ excitation, they concluded that 50% of the population deactivates through another region of the S_1 state.^[191] Most recently, Nenov *et al.* were able to resolve the lifetime of the $\pi\pi^*$ state of *trans*-AB using transient absorption spectroscopy with sub-20 fs time resolution.^[192] They observed the buildup of the $n\pi^*$ population within ≈ 50 fs and further identified an ultrafast (0.45 ps) nonproductive deactivation pathway through a “CNN-bending” channel that is inaccessible upon direct $n\pi^*$ excitation. For the *cis*-isomer to be formed IVR into the torsion modes is required, which takes orders of magnitude longer (2–4 ps) and proceeds analogously for $\pi\pi^*$ and $n\pi^*$ excitation. This additional channel reduces the QY for *trans*→*cis* isomerization and is thus responsible for the violation of Kasha’s rule.

A simplified picture summarizing the general photodynamics and timescales of azobenzene based on these studies is given in Figure 1.15.

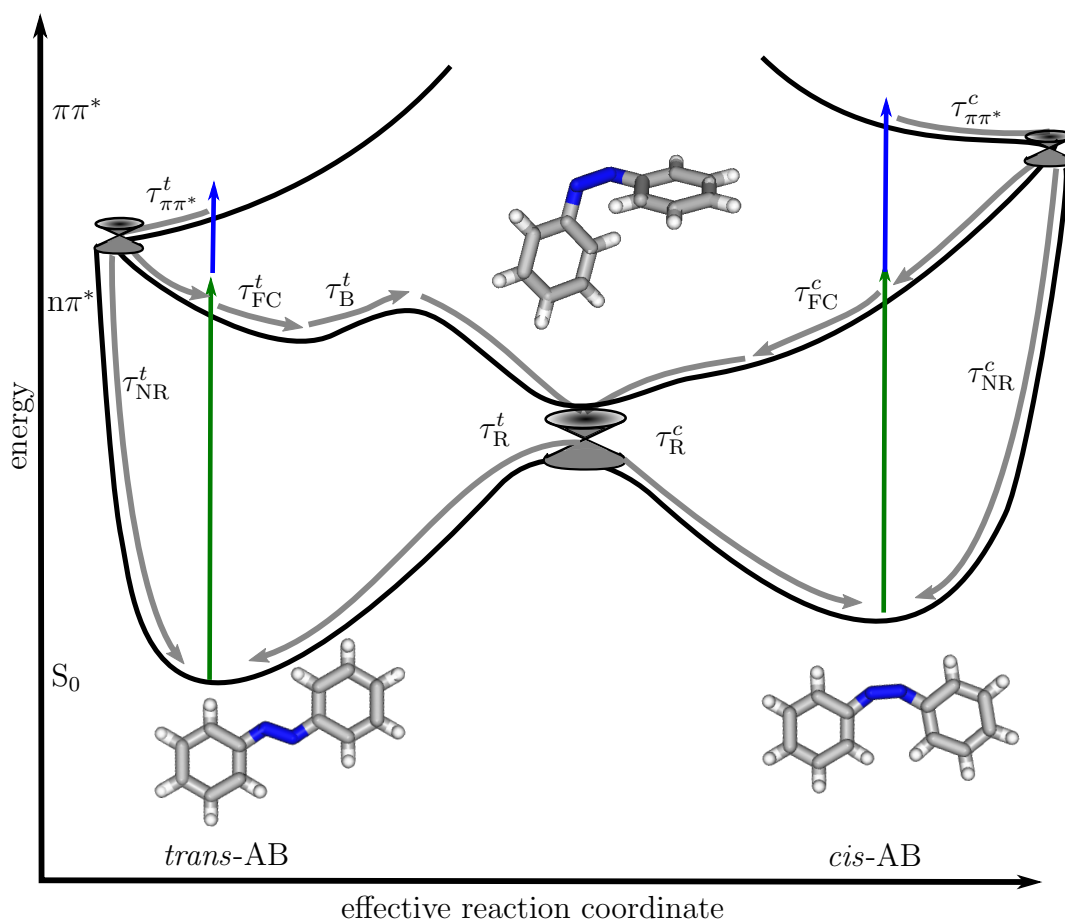


Figure 1.15: Schematic depiction illustrating the key photodynamics observed for AB following $\pi\pi^*$ and $n\pi^*$ excitation of the *trans*- and *cis*-isomer, respectively. Upon $n\pi^*$ excitation of *trans*-AB the wavepacket evolves from the Franck-Condon region with $\tau_{\text{FC}}^t \approx 0.3$ ps, overcomes a barrier with $\tau_{\text{B}}^t \approx 3$ ps and finally relaxes to the ground state S_0 with $\tau_{\text{R}}^t \approx 16$ ps. For *cis*-AB upon $n\pi^*$ excitation a barrierless initial relaxation from the Franck-Condon region with $\tau_{\text{FC}}^c \approx 0.1$ ps and subsequent repopulation of the ground state with $\tau_{\text{R}}^c \approx 1.1$ ps is observed.^[191] Upon $\pi\pi^*$ excitation of the *trans*-isomer the $n\pi^*$ state is populated within $\tau_{\pi\pi^*}^t < 50$ fs in a region that is not accessed by direct excitation. This opens up a non-reactive decay channel through which 50% of the molecules repopulate the ground state within $\tau_{\text{NR}}^t \approx 0.45$ ps, which explains the observed violation of Kasha's rule.^[192] For *cis*-AB, excitation of the $\pi\pi^*$ state 30% of the molecules isomerize to *trans*-AB while 70% relax back to the ground state via an region of the $n\pi^*$ state not accessible upon direct excitation.^[191]

Given the similarity in chemical structure and the virtually identical electronic absorption spectrum, this picture is adapted for the interpretation of the photodynamics of azopyridines. The SCO complexes that were investigated in this Thesis were designed on the basis of the concepts presented in Section 1.3. These molecules are functionalized with azopyridine ligands to achieve control over the spin states, but also to achieve bi-stability of these states by introducing the conformation of the azopyridine as an additional degree of freedom. Therefore, it is in principle required that the azopyridine ligands preserve their photochemical properties upon complexation. However, as discussed in Section 1.2, in practice, coordination of aromatic molecules to transition-metal centers can lead to fundamental changes of the photophysics and the associated photodynamical processes. Thus, the timescales for the formation of photoproducts can strongly be altered or even driven towards completely new relaxation channels, which substantially affects the QYs. In order to understand the impact of the coordination to the transition-metal center on the azopyridine, the free azopyridine ligand is measured in addition as a reference to the complex. The results of these measurements are also presented in Chapters 4 and 5 where they are to be discussed in the context of this Section.

References

- [1] Sarovar, M.; Ishizaki, A.; Fleming, G. R.; Whaley, K. B. *Nat. Phys.* **2010**, *6*, 462–467.
- [2] Polli, D.; Rivalta, I.; Nenov, A.; Weingart, O.; Garavelli, M.; Cerullo, G. *Photochem. Photobiol. Sci.* **2015**, *14*, 213–228.
- [3] Sundström, V. *Annu. Rev. Phys. Chem.* **2008**, *59*, 53–77.
- [4] Zewail, A. H. *Angew. Chem. Int. Ed. English* **2000**, *39*, 2586–2631.
- [5] Brixner, T.; Stegner, J.; Vaswani, H. M.; Cho, M.; Blankenship, R. E.; Fleming, G. R. *Nature* **2005**, *446*, 782.
- [6] Engel, G. S.; Calhoun, T. R.; Read, E. L.; Ahn, T. K.; Mančal, T.; Cheng, Y. C.; Blankenship, R. E.; Fleming, G. R. *Nature* **2007**, *446*, 782–786.
- [7] Shank, C. V.; Mathies, R. A.; Cruz, C. H. B.; Pollard, W. T. *Science* **1988**, *240*, 777–779.
- [8] Schoenlein, R. W.; Peteanu, L. A.; Mathies, R. A.; Shank, C. V. *Science* **1991**, *254*, 412–415.
- [9] Kandori, H.; Sasabe, H.; Katsuta, Y.; Ito, M. *J. Am. Chem. Soc.* **1995**, *117*, 2669–2670.
- [10] Logunov, S. L.; Song, L.; El-Sayed, M. A. *J. Phys. Chem.* **1996**, *100*, 18586–18591.
- [11] Hamm, P.; Zurek, M.; Röschinger, T.; Patzelt, H.; Oesterhelt, D.; Zinth, W. *Chem. Phys. Lett.* **1997**, *268*, 180–186.
- [12] Becker, R. S.; Freedman, K. *J. Am. Chem. Soc.* **1985**, *107*, 1477–1485.
- [13] Burgess, B. K.; Lowe, D. J. *Chem. Rev.* **1996**, *96*, 2983–3011.
- [14] Howard, J. B.; Rees, D. C. *Chem. Rev.* **1996**, *96*, 2965–2982.
- [15] Eady, R. R. *Chem. Rev.* **1996**, *96*, 3013–3030.
- [16] Grätzel, M.; Kalyanasundaram, K. *Curr. Sci.* **1994**, *66*, 706–714.

- [17] Kalyanasundaram, K.; Grätzel, M. *Photosensitization and Photocatalysis Using Inorganic and Organometallic Compounds*, 1st ed.; Springer, Dordrecht, 1993.
- [18] Szacilowski, K.; Macyk, W.; Drzewiecka-Matuszek, A.; Brindell, M.; Stochel, G. *Chem. Rev.* **2005**, *105*, 2647–2694.
- [19] Cambi, L.; Szegő, L. *Chem. Ber. Dtsch. Ges.* **1931**, *64*, 2591–2598.
- [20] Bousseksou, A.; Molnár, G.; Salmon, L.; Nicolazzi, W. *Chem. Soc. Rev.* **2011**, *40*, 3313–3335.
- [21] Kahn, O. *Science*. **1998**, *279*, 44–48.
- [22] Murakami, H.; Kawabuchi, A.; Kotoo, K.; Kunitake, M.; Nakashima, N. **1997**, *119*, 7605–7606.
- [23] Norikane, Y.; Tamaoki, N. *Org. Lett.* **2004**, *6*, 2595–2598.
- [24] Muraoka, T.; Kinbara, K.; Aida, T. *Nature* **2006**, *440*, 512–515.
- [25] Alasfar, S.; Ishikawa, M.; Kawata, Y.; Egami, C.; Sugihara, O.; Okamoto, N.; Tsuchimori, M.; Watanabe, O. *Appl. Opt.* **1999**, *38*, 6201.
- [26] Gindre, D.; Boeglin, A.; Fort, A.; Mager, L.; Dorkenoo, K. D. *Opt. Exp.* **2006**, *14*, 9896.
- [27] Sobolewska, A.; Bartkiewicz, S.; Mysliwiec, J.; Singer, K. D. *J. Mater. Chem. C* **2014**, *2*, 1409–1412.
- [28] Van den Mooter, G.; Samyn, C.; Kinget, R. *Int. J. Pharm.* **1992**, *87*, 37–46.
- [29] Ikeda, T.; Tsutsumi, O. *Science* **1995**, *268*, 1873–1875.
- [30] Puntoriero, F.; Ceroni, P.; Balzani, V.; Bergamini, G.; Vögtle, F. *J. Am. Chem. Soc.* **2007**, *129*, 10714–10719.
- [31] Lee, W.; Kim, D.; Lim, J.; Kim, G.; Kim, I.; Kim, S.; Kim, J. *Sensors Actuators, B Chem.* **2018**, *266*, 724–729.
- [32] Mutruc, D.; Goulet-Hanssens, A.; Fairman, S.; Wahl, S.; Zimathies, A.; Knie, C.; Hecht, S. *Angew. Chem.* **2019**, *131*, 12994–12999.
- [33] Klan, P.; Wirz, J. *Photochemistry of Organic Compounds: From Concepts to Practice*; John Wiley & Sons, 2009; Chapter 2, pp 25–72.
- [34] Balzani, V.; Ceroni, P.; Juris, A. *Photochemistry and Photophysics: Concepts, Research, Applications*, 1st ed.; Wiley-VCH Verlag GmbH & Co. KGaA., 2014.

- [35] Braslavsky, S. E. *Pure Appl. Chem.* **2007**, *79*, 293–465.
- [36] Jabłonski, A. *Zeitschrift für Physik* **1935**, *94*, 38–46.
- [37] Heisenberg, W. *Zeitschrift für Phys.* **1927**, *43*, 172–198.
- [38] Franck, J. *Trans. Faraday Soc.* **1926**, *21*.
- [39] Condon, E. *Phys. Rev.* **1926**, *28*, 1182–1201.
- [40] Dirac, P. A. M. *Proc. R. Soc. London, Ser. A* **1927**, *114*, 243–265.
- [41] El-Sayed, M. A. *Acc. Chem. Res.* **1968**, *1*, 8–16.
- [42] Kasha, M. *Discuss. Faraday Soc* **1950**, *9*, 14–19.
- [43] Born, M.; Oppenheimer, R. *Ann. Phys.* **1927**, *389*, 457–484.
- [44] Fischer, G. *Vibronic Coupling: The Interaction between the Electronic and Nuclear Motions*; Academic Press: London, 1984; p 28ff.
- [45] Förster, T. *Pure Appl. Chem.* **1970**, *24*, 443–450.
- [46] Steinfeld, J. I.; Francisco, J. S.; Hase, W. L. *Chemical Kinetics and Dynamics*; Prentice Hall: Englewood Cliffs, NJ, 1989.
- [47] Holbrook, K. A.; Pilling, M. J.; Robertson, S. H. *Unimolecular Reactions*; John Wiley & Sons: Chichester, 1996.
- [48] Sousa, C.; Alías, M.; Domingo, A.; De Graaf, C. *Chem. Eur. J.* **2019**, *25*, 1152–1164.
- [49] Adamson, A. W.; Waltz, W. L.; Zinato, E.; Watts, D. W.; Fleischer, P. D.; Lindholm, R. D. *Chemical Reviews* **1968**, *68*, 541–585.
- [50] Griffith, B. J. S.; Orgel, L. E. *Q. Rev. Chem. Soc.* **1957**, *11*, 381–393.
- [51] Bower, B. K.; Tennent, H. G. *J. Am. Chem. Soc.* **1972**, *94*, 2512–2514.
- [52] Byrne, E. K.; Richeson, D. S.; Theopold, K. H. *J. Chem. Soc. - Ser. Chem. Commun.* **1986**, *930*, 1491–1492.
- [53] Byrne, E. K.; Theopold, K. H. *J. Am. Chem. Soc.* **1989**, *111*, 3887–3896.
- [54] Cambi, L.; Szegő, L. *Ber. dtsch. Chem. Ges.* **1933**, *66*, 656–661.
- [55] Gütlich, P.; Hauser, A. *Coord. Chem. Rev.* **1990**, *97*, 1–22.
- [56] Hauser, A. *J. Chem. Phys.* **1991**, *94*, 2741–2748.
- [57] Létard, J.-F. *J. Mater. Chem.* **2006**, *16*, 2550–2559.

- [58] Zarembowitch, J.; Roux, C.; Boillot, M. L.; Claude, R.; Itie, J. P.; Polian, A.; Bolte, M. *Mol. Cryst. Liq. Cryst. Sci. Technol. Sect. A. Mol. Cryst. Liq. Cryst.* **1993**, *234*, 247–254.
- [59] Roux, C.; Zarembowitch, J.; Gailois, B.; Granier, T.; Claude, R. *Inorg. Chem.* **1994**, *33*, 2273–2279.
- [60] Boillot, M.-L.; Roux, C.; Audi re, J.-P.; Dausse, A.; Zarembowitch, J. *Inorg. Chem.* **1996**, *35*, 3975–3980.
- [61] Boillot, M. L.; Chantraine, S.; Zarembowitch, J.; Lallemand, J. Y.; Prunet, J. *New J. Chem.* **1999**, *23*, 179–183.
- [62] Boillot, M.-L.; Zarembowitch, J.; Sour, A. *Spin Crossover in Transition Metal Compounds II*; Springer Berlin Heidelberg: Berlin, Heidelberg, 2004; pp 261–276.
- [63] Bannwarth, A.; Schmidt, S. O.; Peters, G.; S nnichsen, F. D.; Thimm, W.; Herges, R.; Tuczek, F. *Eur. J. Inorg. Chem.* **2012**, 2776–2783.
- [64] Milek, M.; Heinemann, F. W.; Khusniyarov, M. M. *Inorg. Chem.* **2013**, *52*, 11585–11592.
- [65] Thies, S.; Bornholdt, C.; K hler, F.; S nnichsen, F. D.; N ther, C.; Tuczek, F.; Herges, R. *Chem. Eur. J.* **2010**, *16*, 10074–10083.
- [66] Thies, S.; Sell, H.; Sch tt, C.; Bornholdt, C.; N ther, C.; Tuczek, F.; Herges, R. *J. Am. Chem. Soc.* **2011**, *133*, 16243–16250.
- [67] Venkataramani, S.; Jana, U.; Dommaschk, M.; S nnichsen, F. D.; Tuczek, F.; Herges, R. *Science* **2011**, *331*, 445–449.
- [68] Thies, S.; Sell, H.; Bornholdt, C.; Sch tt, C.; K hler, F.; Tuczek, F.; Herges, R. *Chem. Eur. J.* **2012**, *18*, 16358–16368.
- [69] Dommaschk, M.; Sch tt, C.; Venkataramani, S.; Jana, U.; N ther, C.; S nnichsen, F. D.; Herges, R. *Dalt. Trans.* **2014**, *43*, 17395–17405.
- [70] Dommaschk, M.; Peters, M.; Gutzeit, F.; Sch tt, C.; N ther, C.; S nnichsen, F. D.; Tiwari, S.; Riedel, C.; Boretius, S.; Herges, R. *J. Am. Chem. Soc.* **2015**, *137*, 7552–7555.
- [71] Jia, S. L.; Jentzen, W.; Shang, M.; Song, X. Z.; Ma, J. G.; Robert Scheldt, W.; Shelnutt, J. A. *Inorg. Chem.* **1998**, *37*, 4402–4412.
- [72] Cole, S. J.; Curthoys, G. C.; Magnusson, E. A.; Phillips, J. N. *Inorg. Chem.* **1972**, *11*, 1024–1028.

- [73] Retsek, J. L.; Drain, C. M.; Kirmaier, C.; Nurco, D. J.; Medforth, C. J.; Smith, K. M.; Sazanovich, I. V.; Chirvony, V. S.; Fajer, J.; Holten, D. *J. Am. Chem. Soc.* **2003**, *125*, 9787–800.
- [74] Walker, F. A.; Hui, E.; Walker, J. M. *J. Am. Chem. Soc.* **1975**, *97*, 2390–2397.
- [75] Gutzeit, F.; Dommaschk, M.; Levin, N.; Buchholz, A.; Schaub, E.; Plass, W.; Näther, C.; Herges, R. *Inorg. Chem.* **2019**, *58*, 12542–12546.
- [76] Bajema, L.; Gouterman, M.; Meyer, B. *J. Mol. Spectrosc.* **1961**, *27*, 225–235.
- [77] Gouterman, M. In *The Porphyrins*; Dolphin, D., Ed.; Academic Press: New York, 1978; Vol. 3.
- [78] Kalyanasundaram, K. *Photochemistry of Polypyridine and Porphyrin Complexes*; Academic Press: London, 1992.
- [79] Kadish, K. M.; Smith, K. M.; Guillard, R. *Handbook of Porphyrin Science: With Applications to Chemistry, Physics, Materials Science, Engineering, Biology and Medicine*; World Scientific Publishing Co. Pt. Ltd., 2012; Vol. 16–20.
- [80] Whitten, D. G. *Acc. Chem. Res.* **1980**, *13*, 83–90.
- [81] Darwent, J. R.; Douglas, P.; Harriman, A.; Porter, G.; Richoux, M. C. *Coord. Chem. Rev.* **1982**, *44*, 83–126.
- [82] Gouterman, M.; Wagnière, G. H.; Snyder, L. C. *J. Mol. Spectrosc.* **1963**, *11*, 108–127.
- [83] Longuet-Higgins, H. C.; Rector, C. W.; Platt, J. R. *J. Chem. Phys.* **1950**, *18*, 1174.
- [84] Simpson, W. T. *J. Chem. Phys.* **1949**, *17*, 1218.
- [85] Gouterman, M. *J. Chem. Phys.* **1959**, *30*, 1139–1161.
- [86] Hirao, K. *J. Phys. Chem. A* **1999**, *103*, 1894–1904.
- [87] Rimington, C.; Mason, S. F.; Kennard, O. *Spectrochim. Acta* **1958**, *12*, 65–77.
- [88] Weigl, J. W. *J. Mol. Spectrosc.* **1957**, *1*, 133–138.
- [89] Kim, D.; Kirmaier, C.; Holten, D. *Chem. Phys.* **1983**, *75*, 305–322.
- [90] Giovannetti, R. *Macro Nano Spectrosc.* **2012**, 87–108.

- [91] Suslick, K.; Watson, R. *New. J. Chem* **1992**, *16*, 633–642.
- [92] Akimoto, S.; Yamazaki, T.; Yamazaki, I.; Osuka, A. *Chem. Phys. Lett.* **1999**, *309*, 177–182.
- [93] Baskin, J. S.; Yu, H. Z.; Zewail, A. H. *J. Phys. Chem. A* **2002**, *106*, 9837–9844.
- [94] Yeon, K. Y.; Jeong, D.; Kim, S. K. *Chem. Commun.* **2010**, *46*, 5572–5574.
- [95] Kim, S. Y.; Joo, T. *J. Phys. Chem. Lett.* **2015**, *6*, 2993–2998.
- [96] Falahati, K.; Hamerla, C.; Huix-Rotllant, M.; Burghardt, I. *Phys. Chem. Chem. Phys.* **2018**, *20*, 12483–12492.
- [97] Sundholm, D. *Phys. Chem. Chem. Phys.* **2000**, *2*, 2275–2281.
- [98] Cai, Z.-L.; Crossley, M. J.; Reimers, J. R.; Kobayashi, R.; Amos, R. D. *J. Phys. Chem. B* **2006**, *110*, 15624–15632.
- [99] Osuka, A.; li Liu, B.; Maruyama, K. *J. Org. Chem.* **1993**, *58*, 3582–3585.
- [100] Yu, H. Z.; Baskin, J. S.; Steiger, B.; Wan, C. Z.; Anson, F. C.; Zewail, A. H. *Chem. Phys. Lett.* **1998**, *293*, 1–8.
- [101] Yang, S. I.; Lammi, R. K.; Seth, J.; Riggs, J. A.; Arai, T.; Kim, D.; Bocian, D. F.; Holten, D.; Lindsey, J. S. *J. Phys. Chem. B* **1998**, *102*, 9426–9436.
- [102] Retsek, J. L.; Gentemann, S.; Medforth, C. J.; Smith, K. M.; Chirvony, V. S.; Fajer, J.; Holten, D. *J. Phys. Chem. B* **2000**, *104*, 6690–6693.
- [103] Pekkarinen, L.; Linschitz, H. *J. Am. Chem. Soc.* **1960**, *82*, 2407–2411.
- [104] Gratz, H.; Penzkofer, A. *Chem. Phys.* **2000**, *254*, 363–374.
- [105] Okhrimenko, A. N.; Rodgers, M. A. J.; Smith, S. L.; Ogawa, M. Y.; Kinstle, T. H. Ultrafast Excited State Relaxation Dynamics of Electron Deficient Porphyrins : Conformational and Electronic Factors. Dissertation, 2005.
- [106] Gurzadyan, G. G.; Tran-Thi, T. H.; Gustavsson, T. *J. Chem. Phys.* **1998**, *108*, 385–388.
- [107] Mataga, N.; Shibata, Y.; Chosrowjan, H.; Yoshida, N.; Osuka, A. *J. Phys. Chem. B* **2000**, *104*, 4003–4004.
- [108] Bräm, O.; Cannizzo, A.; Chergui, M. *J. Phys. Chem. A* **2019**, *123*, 1461–1468.

- [109] Even, U.; Jortner, J.; Friedman, J. *J. Phys. Chem.* **1982**, *86*, 2273–2276.
- [110] Kalyanasundaram, K.; Neumann-Spallart, M. *J. Phys. Chem.* **1982**, *86*, 5163–5169.
- [111] Ohno, O.; Kaizu, Y.; Kobayashi, H. *J. Chem. Phys.* **1984**, *82*, 1779–1787.
- [112] Seybold, P. G.; Gouterman, M. *J. Mol. Spectrosc.* **1969**, *31*, 1–13.
- [113] Zhang, P.; Wang, M.; Li, C.; Li, X.; Dong, J.; Sun, L. *Chem. Commun.* **2010**, *46*, 8806–8808.
- [114] Yuan, Y. J.; Chen, D.; Zhong, J.; Yang, L. X.; Wang, J. J.; Yu, Z. T.; Zou, Z. G. *J. Phys. Chem. C* **2017**, *121*, 24452–24462.
- [115] Martini, L. A.; Moore, G. F.; Milot, R. L.; Cai, L. Z.; Sheehan, S. W.; Schmuttenmaer, C. A.; Brudvig, G. W.; Crabtree, R. H. *J. Phys. Chem. C* **2013**, *117*, 14526–14533.
- [116] Pavani, C.; Uchoa, A. F.; Oliveira, C. S.; Iamamoto, Y.; Baptista, M. S. *Photochem. Photobiol. Sci.* **2009**, *8*, 233–240.
- [117] Eastwood, D. L.; Gouterman, M. *J. Mol. Spectrosc.* **1970**, *35*, 359–375.
- [118] Antipas, A.; Gouterman, M. *J. Am. Chem. Soc.* **1983**, *105*, 4896–4901.
- [119] Musewald, C.; Hartwich, G.; Lossau, H.; Gilch, P.; Pöllinger-Dammer, F.; Scheer, H.; Michel-Beyerle, M. E. *J. Phys. Chem. B* **1999**, *103*, 7055–7060.
- [120] Zamyatin, A. V.; Soldatova, A. V.; Rodgers, M. A. *Inorg. Chim. Acta* **2007**, *360*, 857–868.
- [121] Zamyatin, A. V.; Gusev, A. V.; Rodgers, M. A. J. *J. Am. Chem. Soc.* **2004**, *126*, 15934–15935.
- [122] Drain, C. M.; Kirmaier, C.; Medforth, C. J.; Nurco, D. J.; Smith, K. M.; Holten, D. *J. Phys. Chem.* **1996**, *100*, 11984–11993.
- [123] Drain, C. M.; Gentemann, S.; Roberts, J. A.; Nelson, N. Y.; Medforth, C. J.; Jia, S.; Simpson, M. C.; Smith, K. M.; Fajer, J.; Shelnutt, J. A.; Holten, D. *J. Am. Chem. Soc.* **1998**, *120*, 3781–3791.
- [124] Zhang, X.; Wasinger, E. C.; Muresan, A. Z.; Attenkofer, K.; Jennings, G.; Lindsey, J. S.; Chen, L. X. *J. Phys. Chem. A* **2007**, *111*, 11736–11742.
- [125] Rodriguez, J.; Kirmaier, C.; Holten, D. *J. Am. Chem. Soc.* **1989**, *111*, 6500–6506.
- [126] Rodriguez, J.; Holten, D. *J. Chem. Phys.* **1989**, *91*, 3525.

- [127] Chen, L. X.; Zhang, X.; Wasinger, E. C.; Attenkofer, K.; Jennings, G.; Muresan, A. Z.; Lindsey, J. S. *J. Am. Chem. Soc.* **2007**, *129*, 9616–9618.
- [128] Ryland, E. S.; Zhang, K.; Vura-Weis, J. *J. Phys. Chem. A* **2019**, *123*.
- [129] Eom, H. S.; Jeoung, S. C.; Kim, D.; Ha, J. H.; Kim, Y. R. *J. Phys. Chem. A* **1997**, *101*, 3661–3669.
- [130] Kim, D.; Holten, D. *Chem. Phys. Lett.* **1983**, *98*, 584–589.
- [131] Shelby, M. L.; Mara, M. W.; Chen, L. X. *Coord. Chem. Rev.* **2014**, *277*, 291–299.
- [132] Chen, L. X.; Zhang, X.; Wasinger, E. C.; Lockard, J. V.; Stickrath, A. B.; Mara, M. W.; Attenkofer, K.; Jennings, G.; Smolentsev, G.; Soldatov, A. *Chem. Sci.* **2010**, *1*, 642.
- [133] Chen, L. X.; Zhang, X.; Lockard, J. V.; Stickrath, A. B.; Attenkofer, K.; Jennings, G.; Liu, D. J. *Acta Crystallogr. Sect. A Found. Crystallogr.* **2010**, *66*, 240–251.
- [134] Chen, L. X.; Zhang, X.; Jäger, W. J. H.; Jennings, G.; Gosztola, D. J.; Munkholm, A.; Hessler, J. P. *Science* **2001**, *292*.
- [135] Rodriguez, J.; Holten, D. *J. Chem. Phys.* **1990**, *92*, 5944.
- [136] Arias-Rotondo, D. M.; McCusker, J. K. *Chem. Soc. Rev.* **2016**, *45*, 5803–5820.
- [137] Sutin, N.; Creutz, C. *Pure Appl. Chem.* **1980**, *52*, 2717–2738.
- [138] Damrauer, N. H.; Cerullo, G.; Yeh, A.; Boussie, T. R.; Shank, C. V.; McCusker, J. K. *Chemtracts* **1997**, *11*, 621–625.
- [139] Okada, T.; Nakashima, S.; Suzuki, M.; Achikanath C. Bhasikuttan, *J. Am. Chem. Soc.* **2002**, *124*, 8398–8405.
- [140] Cannizzo, A.; Van Mourik, F.; Gawelda, W.; Zgrablic, G.; Bressler, C.; Chergui, M. *Angew. Chem. Int. Ed.* **2006**, *45*, 3174–3176.
- [141] Chergui, M. *Acc. Chem. Res.* **2015**, *48*, 801–808.
- [142] Juris, A.; Balzani, V.; Barigelletti, F.; Campagna, S.; Belser, P.; von Zelewsky, A. *Coord* **1988**, *84*, 85–277.
- [143] Medlycott, E. A.; Hanan, G. S. *Chem. Soc. Rev.* **2005**, *34*, 133–142.
- [144] Wenger, O. S. *Chem. Eur. J.* **2019**, *25*, 6043–6052.

- [145] Liu, L.; Duchanois, T.; Etienne, T.; Monari, A.; Beley, M.; Assfeld, X.; Haacke, S.; Gros, P. C. *Phys. Chem. Chem. Phys.* **2016**, *18*, 12550–12556.
- [146] Zimmer, P.; Burkhardt, L.; Friedrich, A.; Steube, J.; Neuba, A.; Schep-
per, R.; Müller, P.; Flörke, U.; Huber, M.; Lochbrunner, S.; Bauer, M.
Inorg. Chem. **2018**, *57*, 360–373.
- [147] Frey, P. A.; Reed, G. H. *ACS Chem. Biol.* **2012**, *7*, 1477–1481.
- [148] De Graaf, C.; Sousa, C. *Chem. Eur. J.* **2010**, *16*, 4550–4556.
- [149] McCusker, J. K.; Walda, K. N.; Dunn, R. C.; Simon, J. D.; Magde, D.;
Hendrickson, D. N. *J. Am. Chem. Soc.* **1993**, *115*, 298–307.
- [150] McCusker, J. K.; Rheingold, A. L.; Hendrickson, D. N. *Inorg. Chem.* **1996**,
35, 2100–2112.
- [151] Gawelda, W.; Cannizzo, A.; Pham, V. T.; Van Mourik, F.; Bressler, C.;
Chergui, M. *J. Am. Chem. Soc.* **2007**, *129*, 8199–8206.
- [152] Bressler, C. Milne, C. Pham, V. ElNahhas, a. E. A. *Science* **2009**, *323*,
489–492.
- [153] Consani, C.; Prémont-Schwarz, M.; Elnahhas, A.; Bressler, C.; Van
Mourik, F.; Cannizzo, A.; Chergui, M. *Angew. Chem. Int. Ed.* **2009**, *48*,
7184–7187.
- [154] Cannizzo, A.; Milne, C. J.; Consani, C.; Gawelda, W.; Bressler, C.; van
Mourik, F.; Chergui, M. *Coord. Chem. Rev.* **2010**, *254*, 2677–2686.
- [155] Sousa, C.; De Graaf, C.; Rudavskyi, A.; Broer, R.; Tatchen, J.;
Etinski, M.; Marian, C. M. *Chem. Eur. J.* **2013**, *19*, 17541–17551.
- [156] Hauser, A. *Chem. Phys. Lett.* **1990**, *173*, 507–512.
- [157] Bergkamp, M. A.; Chang, C. K.; Netzel, T. L. *J. Phys. Chem.* **1983**, *87*,
4441–4446.
- [158] Auböck, G.; Chergui, M. *Nat. Chem.* **2015**, *7*, 629–633.
- [159] Monat, J. E.; McCusker, J. K. *J. Am. Chem. Soc.* **2000**, *122*, 4092–4097.
- [160] Brady, C.; Callaghan, P. L.; Ciunik, Z.; Coates, C. G.; Døssing, A.;
Hazell, A.; McGarvey, J. J.; Schenker, S.; Toftlund, H.; Trautwein, A. X.;
Winkler, H.; Wolny, J. A. *Inorg. Chem.* **2004**, *43*, 4289–4299.
- [161] Smeigh, A. L.; Creelman, M.; Mathies, R. A.; McCusker, J. K. *J. Am.*
Chem. Soc. **2008**, 14105–14107.

- [162] Huse, N.; Cho, H.; Hong, K.; Jamula, L.; De Groot, F. M. F.; Kim, T. K.; McCusker, J. K.; Schoenlein, R. W. *J. Phys. Chem. Lett.* **2011**, *2*, 880–884.
- [163] Tribollet, J.; Galle, G.; Jonusauskas, G.; Deldicque, D.; Tondusson, M.; Letard, J. F.; Freysz, E. *Chem. Phys. Lett.* **2011**, *513*, 42–47.
- [164] Sousa, C.; De Graaf, C.; Rudavskiy, A.; Broer, R. *J. Phys. Chem. A* **2017**, *121*, 9720–9727.
- [165] Bandara, H. M.; Burdette, S. C. *Chem. Soc. Rev.* **2012**, *41*, 1809–1825.
- [166] Füchsel, G.; Klamroth, T.; Dokić, J.; Saalfrank, P. *J. Phys. Chem. B* **2006**, *110*, 16337–16345.
- [167] Bahrenburg, J. Ultrafast Photochemical Dynamics of Azobenzenes Affected by Intra- and Intermolecular Interactions and of a Proton Transfer Switch. Ph.D. Thesis, Christian-Albrechts-Universität zu Kiel, 2014.
- [168] Tan, E. M.; Amirjalayer, S.; Smolarek, S.; Vdovin, A.; Zerbetto, F.; Buma, W. J. *Nat. Commun.* **2015**, *6*.
- [169] Crecca, C. R.; Roitberg, A. E. *J. Phys. Chem. A* **2006**, *110*, 8188–8203.
- [170] Tiago, M. L.; Ismail-Beigi, S.; Louie, S. G. *J. Chem. Phys.* **2005**, *122*.
- [171] Dokić, J.; Gothe, M.; Wirth, J.; Peters, M. V.; Schwarz, J.; Hecht, S.; Saalfrank, P. *J. Phys. Chem. A* **2009**, *113*, 6763–6773.
- [172] Poprawa-Smoluch, M.; Baggerman, J.; Zhang, H.; Maas, H. P.; De Cola, L.; Brouwer, A. M. *J. Phys. Chem. A* **2006**, *110*, 11926–11937.
- [173] Schweighauser, L.; Strauss, M. A.; Bellotto, S.; Wegner, H. A. *Angew. Chem. Int. Ed.* **2015**, *54*, 13436–13439.
- [174] Mahimwalla, Z.; Yager, K. G.; Mamiya, J. I.; Shishido, A.; Priimagi, A.; Barrett, C. J. *Polym. Bull.* **2012**, *69*, 967–1006.
- [175] bo Wei, Y.; Tang, Q.; Gong, C. B.; Lam, M. H. W. *Anal. Chim. Acta* **2015**, *900*, 10–20.
- [176] Dong, L.; Feng, Y.; Wang, L.; Feng, W. *Chem. Soc. Rev.* **2018**, *47*, 7339–7368.
- [177] Li, S.; Wang, H.; Fang, J.; Liu, Q.; Wang, J.; Guo, S. *J. Therm. Sci.* **2020**, *29*, 280–297.
- [178] Rau, H.; Lüddecke, E. *J. Am. Chem. Soc.* **1982**, *104*, 1616–1620.

- [179] Zimmerman, G.; yung Chow, L.; jin Paik, U. *J. Am. Chem. Soc.* **1958**, *80*, 3528–3531.
- [180] Rau, H.; Yu-Quan, S. *J. Photochem. Photobiol. A Chem.* **1988**, *42*, 321–327.
- [181] Ladányi, V.; Dvořák, P.; Al Anshori, J.; Vetráková, u.; Wirz, J.; Heger, D. *Photochem. Photobiol. Sci.* **2017**, *16*, 1757–1761.
- [182] Vetráková, u.; Ladányi, V.; Al Anshori, J.; Dvořák, P.; Wirz, J.; Heger, D. *Photochem. Photobiol. Sci.* **2017**, *16*, 1749–1756.
- [183] Kumpulainen, T.; Lang, B.; Rosspeintner, A.; Vauthey, E. *Chem. Rev.* **2017**, *117*, 10826–10939.
- [184] Lednev, I. K.; Ye, T.-Q.; Hester, R. E.; Moore, J. N. *J. Phys. Chem.* **1996**, *100*, 13338–13341.
- [185] Lednev, I. K.; Ye, T. Q.; Matousek, P.; Towrie, M.; Foggi, P.; Neuwahl, F. V.; Umapathy, S.; Hester, R. E.; Moore, J. N. *Chem. Phys. Lett.* **1998**, *290*, 68–74.
- [186] Nägele, T.; Hoche, R.; Zinth, W.; Wachtveitl, J. *Chem. Phys. Lett.* **1997**, *272*, 489–495.
- [187] Hamm, P.; Ohline, S. M.; Zinth, W. *J. Chem. Phys.* **1997**, *106*, 519–529.
- [188] Satzger, H.; Root, C.; Braun, M. *J. Phys. Chem. A* **2004**, *108*, 6265–6271.
- [189] Satzger, H.; Spörlein, S.; Root, C.; Wachtveitl, J.; Zinth, W.; Gilch, P. *Chem. Phys. Lett.* **2003**, *372*, 216–223.
- [190] Fujino, T.; Arzhantsev, S. Y.; Tahara, T. *Bull. Chem. Soc. Jpn.* **2002**, *75*, 1031–1040.
- [191] Quick, M.; Dobryakov, A. L.; Gerecke, M.; Richter, C.; Berndt, F.; Ioffe, I. N.; Granovsky, A. A.; Mahrwald, R.; Ernsting, N. P.; Kovalenko, S. A. *J. Phys. Chem. B* **2014**, *118*, 8756–8771.
- [192] Nenov, A.; Borrego-Varillas, R.; Oriana, A.; Ganzer, L.; Segatta, F.; Conti, I.; Segarra-Martí, J.; Omachi, J.; Dapor, M.; Taioli, S.; Manzoni, C.; Mukamel, S.; Cerullo, G.; Garavelli, M. *J. Phys. Chem. Lett.* **2018**, *9*, 1534–1541.

2 Experimental Methods

Intersystem crossing processes in transition-metal complexes as well as isomerization reaction of azo compounds occur on ultrafast timescales. These processes are triggered by electronic excitation of the molecules and are therefore accompanied by changes in their electronic absorption properties. Furthermore, some of the transient intermediates can exhibit fluorescence. In order to monitor the molecular dynamics after photoexcitation the employed methods need high temporal resolution while at the same time allowing for discrimination between distinct excited-state as well as ground-state species. The combination of different femtosecond time-resolved spectroscopic techniques meets those demands.

Femtosecond time-resolved spectroscopic techniques make use of ultrashort laser pulses. Nonlinear optics form the basis for the generation and conversion of such pulses. A detailed description of the underlying nonlinear optical processes is omitted at this point since it can be found in a number of textbooks.^[1–4] Working with ultrashort pulses, in turn, requires detection methods that are fast enough to record on such small time intervals. However, the response times of most direct electronic detection methods are restricted to a few nanoseconds. Therefore, ultrafast spectroscopic techniques are based on the pump-probe principle, which is illustrated in Figure 2.1 and will be briefly explained in the following.

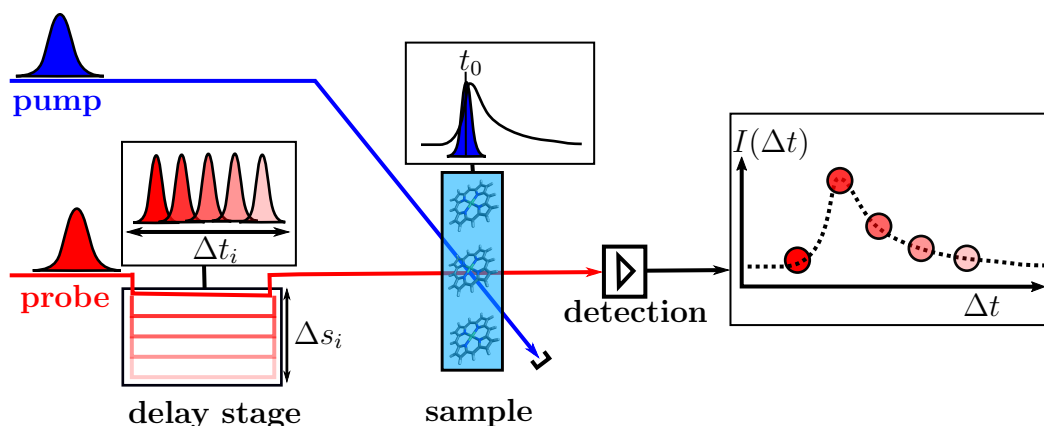


Figure 2.1: Schematic depiction of the pump-probe principle for femtosecond time-resolved spectroscopy. An ultrashort pump pulse excites the sample molecules at a given time t_0 . The molecular response is monitored by the probe pulse at a distinct delay time Δt that is varied by a delay stage.

An ultrashort laser pulse, referred to as pump pulse, is used to generate an excited-state population in the ensemble of sample molecules at a given time t_0 . The molecular response is monitored by another pulse, referred to as probe pulse, at distinct delay times Δt_i with respect to the pump pulse. The temporal delay can be realized by gradually adding small distances Δs_i to the optical path of the probe pulse using an adjustable delay stage. In this way, it is possible to scan the dynamical evolution of the system following photoexcitation with a time resolution that becomes ultimately limited by the duration of the employed laser pulses.

The pump-probe method can be integrated in a variety of different spectroscopic techniques by tailoring the laser pulses and the detectors depending on the nature of the sample and the molecular properties of interest. Thus, it is possible to detect, *e.g.*, fluorescence, scattering or absorption in the UV–vis and IR spectral range on ultrafast timescales. The by far largest part of the work presented in this Thesis was accomplished using femtosecond time-resolved electronic absorption spectroscopy (TEAS). The basic principles of the method as well as the specific experimental setup and data evaluation procedure are the subject of Section 2.2. Another smaller proportion was contributed by fluorescence up-conversion spectroscopy (FIUPS) which is briefly explained in Section 2.3.

The basis of both experiments is a Clark MXR CPA 2001 Ti:Sa regenerative amplifier with 1 W output performance that supplies pulses at a center wavelength of 775 nm with 150 fs (sech^2) duration (full width at half maximum, FWHM) at a repetition rate of 1013 Hz. Further details about the laser system and can be found in preceding Ph.D.^[5–7] and Master or Diploma^[8] theses of the Temps workgroup.

Furthermore, a variant of TEAS allowing for the observation of photodynamics on the picosecond-to-millisecond timescale, that is based on the coupling of two Ti:Sa amplifiers and was developed in the course of this Thesis, will be described separately in Chapter 7.

2.1 Femtosecond Time-Resolved Electronic Absorption Spectroscopy

In time-resolved electronic absorption spectroscopy (TEAS) an ultrashort and spectrally narrow pump pulse allows the excitation of a distinct electronic state of the sample molecules, whereas broadband probe pulses are used to detect the induced electronic absorption changes over a wide spectral range. In analogy to static UV–vis spectroscopy, where the absorption of the sample molecules in the ground state is measured against a solvent reference, in TEAS the absorption of the molecules in the excited state is compared to the absorption of the molecules in their ground state. This gives rise to an absorbance difference spectrum

containing positive as well as negative contributions to the detected signals that shall be discussed in the following.

Molecular Contributions to TEAS Signals

First, absorption of the pump pulse transfers a large fraction of the sample molecules to an electronically excited state, diminishing the number of molecules in the electronic ground state (S_0). This ground-state bleaching (GSB) makes the excited sample more transparent at the positions of the ground state absorption bands, which gives rise to negative signals at the corresponding energies. The decay of GSB signal contains information on the timescales and the extent of ground-state recovery (GSR). Second, the probe pulse can induce stimulated emission (SE), if an optically bright state is populated. Since the additional photons are emitted in the same direction as the probe photons, the increased intensity that reaches the detector will result in a negative absorption signal. Third, excited states populated by the pump pulse or subsequent relaxation processes can absorb probe photons to form higher-lying excited states S_n . This excited-state absorption (ESA) manifests itself in additional positive absorption features. The decay of ESA as well as SE can be related to the lifetimes of the excited states. Once back in the electronic ground state, vibrationally hot levels of the reactant or the eventually formed photoproducts can be accessed giving rise to positive hot ground-state absorption (HGSA) or hot product absorption (HPA) features. Furthermore, product absorption (PA) can occur from the relaxed species. The molecular contributions to the absorbance difference spectrum are summarized in Figure 2.2.

2.1.1 Experimental Setup

The TEAS experiment can be divided in four major parts: generation of the pump pulses, generation of the probe pulses, detection and signal processing. A sketch of the experimental setup is depicted in Figure 2.3. More details can be found in Refs. 9–14.

Optical Pathway for the Pump Pulses

For the generation of the pump pulses a fraction of 300 μJ of the Ti:Sa fundamental is used to operate a non-collinear optical parametric amplifier (NOPA). For that the beam is sent on an optical wedge, where a small fraction of 20 μJ is attenuated and focused by a fused silica lens into a 2 mm thick sapphire plate to generate a white-light supercontinuum. The supercontinuum is collimated and focused into a $\beta\text{-BaB}_2\text{O}_4$ (BBO) crystal ($d = 2$ mm, $\theta = 31.2^\circ$, $\phi = 90^\circ$), where it serves as seed for the NOPA process. The major part of the Ti:Sa fundamental passing the wedge is directed along an optical delay line and into another BBO crystal ($d = 2$ mm, $\theta = 29.2^\circ$, $\phi = 90^\circ$), where second harmonic

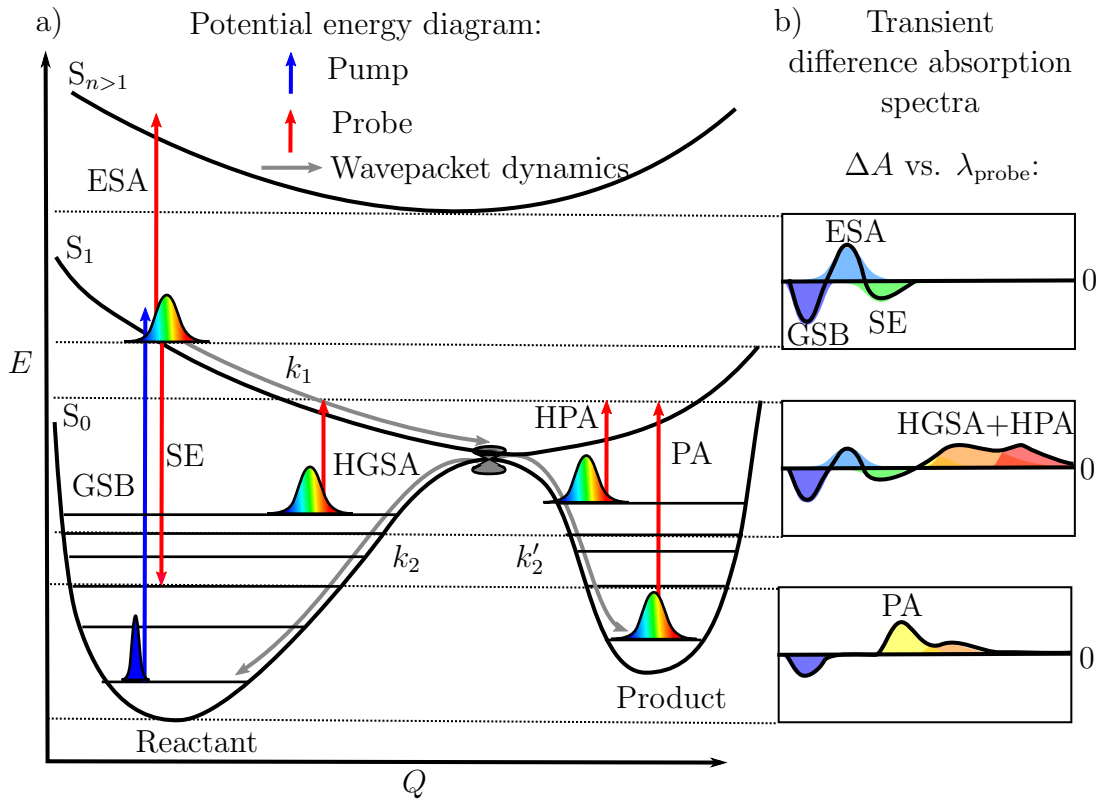


Figure 2.2: Schematic potential energy surfaces (a) and corresponding difference absorption spectra (b) of a photoreaction tracked by transient electronic absorption spectroscopy to illustrate the molecular contributions observed signals. GSB: ground-state bleaching; ESA: excited-state absorption; SE: stimulated emission; HGSA: hot ground-state absorption; HPA: hot product absorption; PA: product absorption.

generation (SHG) takes place with an efficiency of about 35 %. This part supplies the energy required for the NOPA process. For that it is focused into the same BBO crystal as the supercontinuum seed under an angle of $\theta = 6.3^\circ$ with respect to the seed beam. By adjusting the tilt angle of the BBO crystal and the pump-seed delay it is possible to amplify a certain part of the supercontinuum. A prism compressor consisting of two SF10 prisms at a distance of ~ 30 cm is used to temporally compress the NOPA output. If excitation pulses in the UV are required, the pulses can subsequently be frequency doubled in another BBO crystal. A Berek compensator is introduced into the beam path to set its polarization to the magic angle (54.7°) with respect to the probe polarization.

Optical Pathway for the Probe Pulses

Broadband probe pulses are obtained from the Ti:Sa fundamental by supercontinuum generation in CaF_2 . Before entering the 2 mm thick CaF_2 plate, the

beam passes a computer-controlled delay line with a mounted retroreflector, a $\lambda/2$ waveplate, a polarizer and a set of neutral density filters. About $2 \mu\text{J}$ of the fundamental are focused for supercontinuum generation by a moveable lens. To reduce optical damage by F-center formation and to ensure the stability of the supercontinuum, the CaF_2 plate is kept in permanent translational motion. The resulting supercontinuum in the range from $320 \text{ nm} \leq \lambda_{\text{probe}} \leq 750 \text{ nm}$ is strongly influenced by the position of the focus in the plate and by the intensity. Precise tunability of the intensity is achieved by rotation of the $\lambda/2$ waveplate in combination with the polarizer. An etalon splits the generated pulses horizontally into probe and reference.

Detection

All beams are focused into the sample flow cell. The pump is spatially overlapped with the probe beam under a small angle. After passing the cell, it is removed by a mirror and reflected to a photodiode. The strong IR part of the probe beams is attenuated by a BG38 filter. The horizontal separation between probe and reference is transferred to a vertical separation using a periscope. Both beams get spectrally dispersed in a prism and are detected with two FFT-CCD cameras, which are read out by a *LabVIEW*^[15] routine programmed by Falk Renth.

Signal processing

A 10-blade chopper operating at a quarter of the laser repetition rate f_0 is introduced in the pump beam path allowing for two consecutive pump pulses to pass while blocking the next two. Additionally, every second probe pulse is blocked by another chopper operated at half of the laser repetition rate. This gives rise to the four pulse sequences (I–IV) displayed in Figure 2.4. Sequence I allows one to detect the signal of the excited-state molecules that is corrected for eventual contributions from scattered pump light given by sequence II, while sequence III detects the absorption of the ground-state sample molecules corrected by the ambient background detected in sequence IV.

The transient changes in optical density $\Delta\text{OD}(\lambda, \Delta t)$, *i.e.*, the transient difference absorbance $\Delta A(\lambda, \Delta t)$, follows from the difference of the transient absorbance of the excited-state ($A^*(\lambda, \Delta t)$) and the ground-state ($A^0(\lambda, \Delta t)$) sample molecules:

$$\Delta A(\lambda, \Delta t) = A^*(\lambda, \Delta t) - A^0(\lambda, \Delta t) = -\log T^*(\lambda, \Delta t) - (-\log T^0(\lambda, \Delta t)) \quad (2.1)$$

The respective transient transmissions $T^*(\lambda, \Delta t)$ and $T^0(\lambda, \Delta t)$ can be calculated from the intensities of the probe beam in the presence of the pump beam (I_{pro}^*) and in the absence of the pump beam (I_{pro}^0) according to Lambert-Beer's

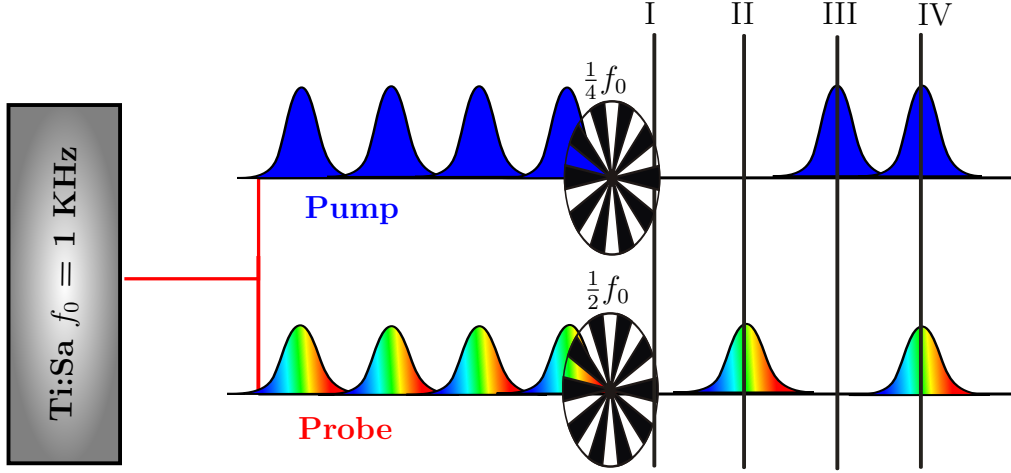


Figure 2.4: Schematic depiction of the four different pump-probe pulse sequences (I-IV) generated by the choppers running with quarter of the experimental repetition rate (f_0) in the pump path and half the repetition rate in the probe path, respectively, that are used to calculate the transient absorption signal.

law:

$$\Delta A(\lambda, \Delta t) = -\log \frac{I_{\text{pro.}}^*(\lambda, \Delta t)}{I_{\text{pro.}}^0(\lambda, \Delta t)}. \quad (2.2)$$

To improve the sensitivity and to account for fluctuations of the laser output the probe intensities are further normalized by the respective intensities of the reference beam ($I_{\text{ref.}}$) that is generated from the back reflection at the etalon giving:

$$\Delta A(\lambda, \Delta t) = -\log \frac{I_{\text{pro.}}^*(\lambda, \Delta t) I_{\text{ref.}}^0(\lambda, \Delta t)}{I_{\text{pro.}}^0(\lambda, \Delta t) I_{\text{ref.}}^*(\lambda, \Delta t)} \quad (2.3)$$

Applying the four pulse sequence from Figure 2.4 gives:

$$\Delta A(\lambda, \Delta t) = -\log \frac{[I_{\text{pro.}}^{\text{I}}(\lambda, \Delta t) - I_{\text{pro.}}^{\text{II}}(\lambda, \Delta t)][I_{\text{ref.}}^{\text{III}}(\lambda, \Delta t) - I_{\text{ref.}}^{\text{IV}}(\lambda, \Delta t)]}{[I_{\text{ref.}}^{\text{I}}(\lambda, \Delta t) - I_{\text{ref.}}^{\text{II}}(\lambda, \Delta t)][I_{\text{pro.}}^{\text{III}}(\lambda, \Delta t) - I_{\text{pro.}}^{\text{IV}}(\lambda, \Delta t)]} \quad (2.4)$$

2.1.2 Data Preparation and Analysis

Further, the data have to be prepared for subsequent analysis. The procedures of data preprocessing and analysis are performed using *MATHEMATICA*^[16] notebooks mostly written by Ron Siewertsen and Falk Renth that were established and described in several preceding theses^[9,10,13,14,17] and publications^[18-20] of the workgroup. First of all, in order to transfer the spectral information to the wavelength domain, each camera pixel has to be assigned to a certain probe

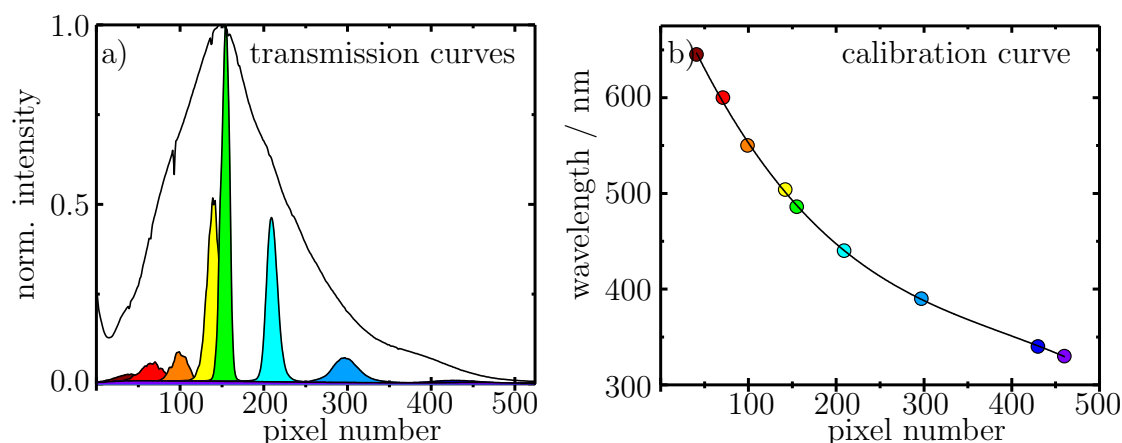


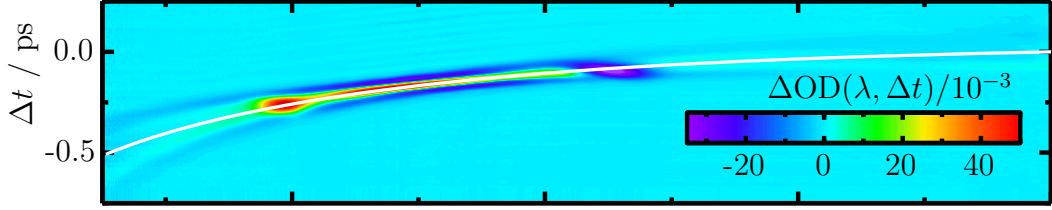
Figure 2.5: Transmission curves of the probe beam (black) and of the interference filters (colored) detected by the CCD camera (a). Plot of the wavelength of the respective filter against the pixel number detecting the transmission together with the resulting calibration curve (b). Reproduced from Ref. 10.

wavelength, which is done by placing different narrow-bandpass interference filters that transmit at a defined wavelength (see Figure 2.5a) in front of the CCD camera. The wavelength of the filter is subsequently plotted against the transmission maximum at the respective camera pixel and the fitted curve (Figure 2.5b) is used to calibrate the probe spectrum.

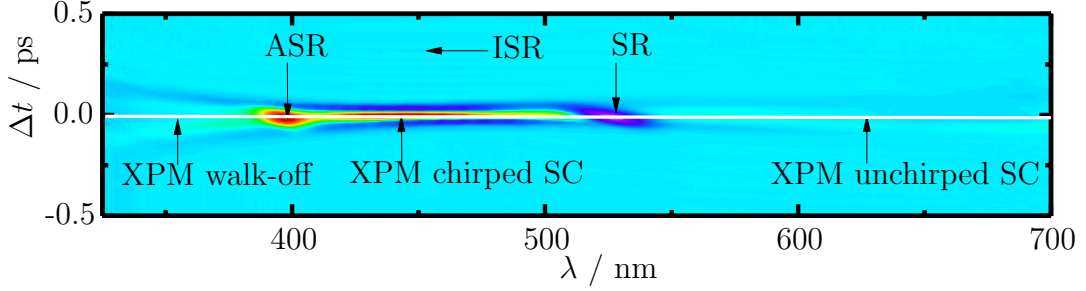
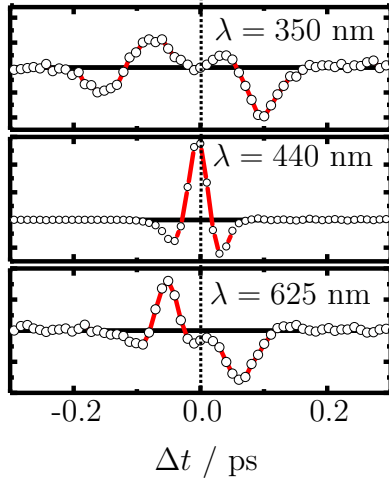
Coherent Artifacts and Time-Zero Correction

The high power densities of the ultrashort pump pulses of $10\text{--}500\text{ GW cm}^{-2}$ can introduce processes in the sample cell windows and solvent. These are two photon absorption (TPA), stimulated Raman scattering (SRS), and temporal modulation of the refractive index which in combination with a chirped supercontinuum probe pulse leads to a redistribution of probe wavelength along the pulse envelope, called cross-phase modulation (XPM).^[21–23] These phenomena only occur when both pump and probe pulse are present and they inevitably cause signals that can be summarized as coherent artifacts. Coherent artifacts have to be carefully distinguished from the molecular contributions to the transient absorption signals. By taking an auxiliary solvent-only measurement, coherent artifacts can be taken into account in the data analysis. Since these signals arise from the simultaneous interaction of the pump and probe pulse in the cell volume, their appearance is restricted to the duration of the pump probe cross-correlation. Thus, they can provide valuable information about the experimental time resolution and the wavelength-dependent time-zero (t_0). In Figure 2.6 the two-dimensional spectro-temporal absorption map showing the change in optical density ($\Delta\text{OD}(\lambda, \Delta t)$) as a function of probe wavelength and pump-probe delay time of pure cyclohexane in a flow cell with 1 mm optical

a) uncorrected data matrix



b) time-zero corrected data matrix

c) XPM time traces t_0 

d) Raman time traces

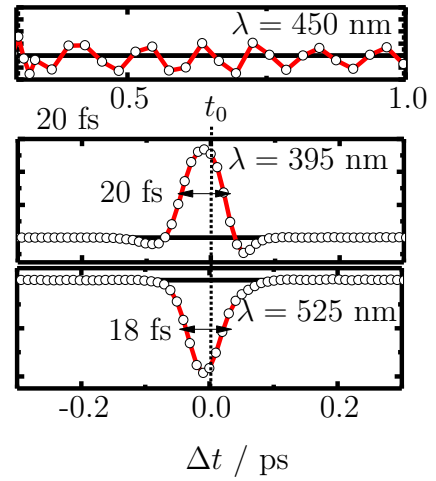


Figure 2.6: Uncorrected (a) and time-zero corrected (b) two-dimensional time-resolved electronic absorption maps obtained from the interaction of a pump pulse at $\lambda_{\text{pump}} = 455$ nm and a supercontinuum probe pulse in the range of $325 \text{ nm} < \lambda_{\text{probe}} < 700$ nm in cyclohexane in a sample cell of 1 mm optical path length and 0.2 mm thick quartz windows. The white line marks the wavelength dependent time-zero of the experiment. The difference absorption time traces at selected probe wavelength display the temporal shape of the XPM (c) and the Raman (d) signals. Reproduced from Ref. 9.

path length and 0.2 mm thick quartz windows upon excitation with a pump pulse of $\lambda_{\text{pump}} = 455$ nm is displayed.

Since the supercontinuum probe pulses in the range of $325 \text{ nm} < \lambda_{\text{probe}} <$

700 nm have a positive chirp with the blue wavelengths at the trailing edge of the pulse, a gradual increase of the pump-probe delay time will first lead to a temporal overlap with the blue end of the probe spectrum. Consequently, the XPM signal starts in the blue part of the spectrum and marches on to the red end. A vertical cut along the time axis at wavelengths of $405 \text{ nm} < \lambda_{\text{probe}} < 500 \text{ nm}$ reveals the shape of the XPM signal consisting of a maximum flanked by two minima. Such a W-shape is expected for a linearly chirped probe pulse with the maximum marking the t_0 at this wavelength.^[21] For wavelengths $< 400 \text{ nm}$ and $> 550 \text{ nm}$ the difference between the group velocities of pump and probe increases significantly causing a temporal spread of the XPM signal and a distorted shape. This so called walk-off diminishes the temporal resolution of the experiment in this region and the determination of the experimental t_0 becomes ambiguous.^[22,23] For wavelengths $> 620 \text{ nm}$ the XPM signal likely develops into an S-shape which can be explained by the decreased chirp of the supercontinuum. In this case, t_0 is marked by the zero-crossing point.^[21] The SRS signals of the solvent can be observed at probe wavelengths located close to the excitation wavelength. They arise when a pump and a probe photon are coupled through a virtual state of the solvent. The emission of a third photon can take place when the energy difference of the two incident photons is resonant with a normal mode of the solvent (ω_{vib}). If the coupling to the virtual state is provided by a probe photon ($\omega_{\text{probe}} = \omega_{\text{pump}} + \omega_{\text{vib}}$), the scattered photons will follow the pump beam path which results in a reduced intensity on the detector and thus gives a positive absorption-like ΔOD blue-shifted to the pump wavelength. If an initially absorbed pump photon provides the coupling to the virtual state, additional photons will be scattered into the probe beam path at $\omega_{\text{probe}} = \omega_{\text{pump}} - \omega_{\text{vib}}$, resulting in an increased intensity at the detector giving a negative emission-like blue-shifted ΔOD . In the case presented in Figure 2.6 the Anti-Stokes-Raman (ASR) absorption signal can be observed at 395 nm and the Stokes-Raman (SR) emission signal at 525 nm. Further, if the pump pulse duration is shorter than a single oscillation cycle of a low frequency Raman-active mode of the solvent, it can exert an impulsive driving force on the vibrational mode.^[24–26] The initiated coherent vibrational oscillation modulates the refractive index of the material and provides a transient grating through which the variably delayed probe photons are scattered.^[24,27,28] The mode frequency appears as quantum beats of the diffraction efficiency^[24] in the range of $425 \text{ nm} < \lambda_{\text{probe}} < 475 \text{ nm}$ in Figure 2.6.

Determination of t_0 from the solvent artifacts at a number of probe wavelengths, enables one to create a model fit function that is subsequently applied to correct the measurement of the sample molecules. The wavelength dependent time-zero is indicated by the white curve in the uncorrected data matrix in Figure 2.6a that afterwards results in the straight line in the corrected matrix (Figure 2.6b). The same correction function is subsequently applied to the data matrix of the sample molecule.

Solvent Correction

In the last step, the pure sample contribution to the transient absorption is obtained by subtraction of the scaled data matrix obtained by the auxiliary solvent-only measurement. Since all these coherent artifacts show a linear dependence on pump intensity, the artifact-free signal S_c can be obtained according to

$$S_c = S - S_r \frac{E_r}{E_s} f, \quad (2.5)$$

where S_r is the solvent signal measured at the pump intensity E_r and E_s denotes the pump intensity from which the signal was measured.^[23] The scaling factor f accounts for the decrease in mean excitation energy due to the sample absorption, which can be described by

$$f = \frac{1 - 10^{-A}}{2.3A} \quad (2.6)$$

where A denotes the absorbance of the sample at the pump wavelength.^[23] In the next step the complete time-zero and solvent corrected data matrix is subjected to a global analysis to get a quantitative picture of the underlying kinetics and molecular species involved in the relaxation process.

Singular Value Decomposition Based Global Analysis

The transient difference absorption data matrix \mathbf{A} consists of n_{λ_i} (number of camera pixels) columns and $m_{\Delta t_j}$ (number of measured delays) rows. Each element A_{ij} of this matrix can be described according to Lambert-Beer's law and the addition of some stochastic disturbance $\xi(\lambda_i, \Delta t_j)$

$$\Delta A(\lambda_i, \Delta t_j) = d \sum_{l=1}^{n_s} \epsilon_l(\lambda_i) c_l(\Delta t_j) + \xi(\lambda_i, \Delta t_j) = A_{ij} \quad (2.7)$$

Here, n_s is the number of species in the system, $\epsilon_l(\lambda_i)$ the absorption coefficient of species number l at the wavelength λ_i , $c_l(\Delta t_j)$ the concentration of species number l at the delay time Δt_j and d the sample thickness.^[29] Using the matrix notation this can also be written as

$$\mathbf{A} = d\mathbf{C}\mathbf{E}^T + \Xi. \quad (2.8)$$

In the hypothetical case of noise-free ($\Xi = 0$) data and if there are no linear dependencies between the columns of \mathbf{E} and \mathbf{C} , respectively, both matrices are of full rank and their rank is equal to the number of species n_s .^[29] Consequently, $\mathbf{C}\mathbf{E}^T$ is also of rank n_s . Thus, in order to determine the number of species in our experimental data the rank of \mathbf{A} has to be determined. Using the singular value decomposition (SVD) the $(m_{\Delta t} \times n_{\lambda})$ -matrix \mathbf{A} is decomposed into three

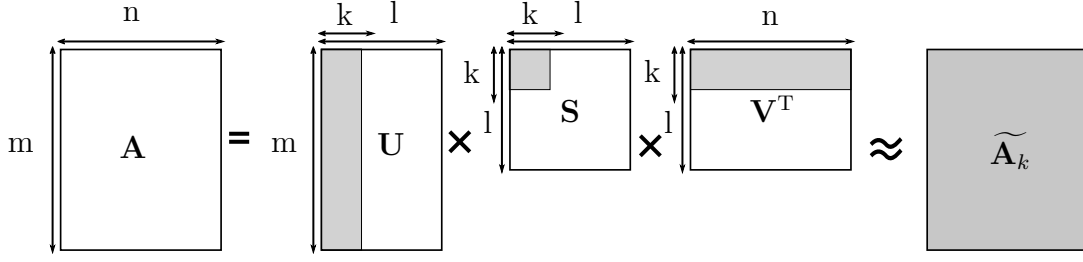


Figure 2.7: Singular value decomposition of the matrix \mathbf{A} and its approximation by the reduced matrix $\widetilde{\mathbf{A}}_k$. Adapted from Ref. 17.

matrices

$$\mathbf{A} = \mathbf{U}\mathbf{S}\mathbf{V}^T \quad (2.9)$$

where the $(m_{\Delta t} \times l)$ -matrix \mathbf{U} and the $(l \times n_{\lambda})$ -matrix \mathbf{V} are orthogonal and contain the left and right singular vectors.^[29] The $(l \times l)$ -matrix \mathbf{S} is diagonal and contains the singular values s_l in a decreasing fashion ($s_1 \geq s_2 \geq \dots \geq s_l \geq 0$).^[14] In the noise-free case and with n_s species the matrix would contain exactly $l = n_s$ significant singular values. However the additional Ξ term alters the singular values and perturbs the singular vector pairs, so that $n_s < l \leq n_{\lambda}$.^[29] In a so-called scree plot^[30] it is possible to identify the relevant number of singular values n_k , significantly different from noise and based on that build an accurate approximation to the matrix \mathbf{A} by using only subset of representative linear combinations of the singular vectors represented by the reduced matrices

$$\widetilde{\mathbf{A}}_k = \widetilde{\mathbf{U}}_k \widetilde{\mathbf{S}}_k \widetilde{\mathbf{V}}_k^T = \widetilde{\mathbf{C}}_k(t) \widetilde{\mathbf{V}}_k^T. \quad (2.10)$$

This procedure is illustrated in Figure 2.7. Subsequently, a global lifetime analysis (GLA) is performed by least-square fitting of the n_k time traces weighted by the respective singular value contained in matrix $\widetilde{\mathbf{C}}_k(t)$:

$$\widetilde{\mathbf{C}}_k(t) = \sum_{l=1}^{n_k} b_l \cdot \exp\left(\frac{-t}{\tau_l}\right) \quad (2.11)$$

Additional to the relaxation times τ_l the matrix \mathbf{B} contains the amplitudes b_l . From this the decay-associated difference spectra (DADS), representing the loss or gain of absorption associated with a certain lifetime,^[29] are obtained as follows:

$$\text{DADS}_k = \mathbf{B}^T \widetilde{\mathbf{V}}_k^T \quad (2.12)$$

By applying a certain kinetic model these spectra can also be transformed into the physically more meaningful evolution-associated difference spectra (EADS) representing the spectral evolution. For sequential kinetics with increasing lifetimes the EADS represent true species and are thus referred to as species-associated difference spectra (SADS).^[29]

2.2 Femtosecond Time-Resolved Fluorescence Up-Conversion Spectroscopy

The multiple positive and negative contributions of the transient species in TEAS can overlap and an unambiguous assignment can often be challenging. Therefore, additional detection of the fluorescence decay can be useful, as this method is specific for the identification of excited-state intermediates. Long-lived fluorescence can be recorded by time-correlated single photon counting (TCSPC) using the PicoQuant FluoTime 200 modular fluorescence lifetime spectrometer available in the Temps workgroup. For short-lived fluorescent species single-color fluorescence up-conversion spectroscopy (FIUPS) has proven as a powerful tool. Since FIUPS measurements contributed only a minor part to this Thesis, the method will only be described briefly in this Section. As depicted in Figure 2.8 an ultrashort and spectrally narrow pump pulse is used for the electronic excitation of the sample molecules. The emitted fluorescence photons of the initially excited — or any other bright state that emerges in the evolution of the population — are up-converted with a probe pulse, referred to as gate, in a material with second order nonlinear optical susceptibility ($\chi^{(2)}$). The temporal decay of the fluorescence can be scanned by detecting the intensity of the sum-frequency generation (I_{SFG}) in dependence of the delay (Δt) between pump and gate pulse.

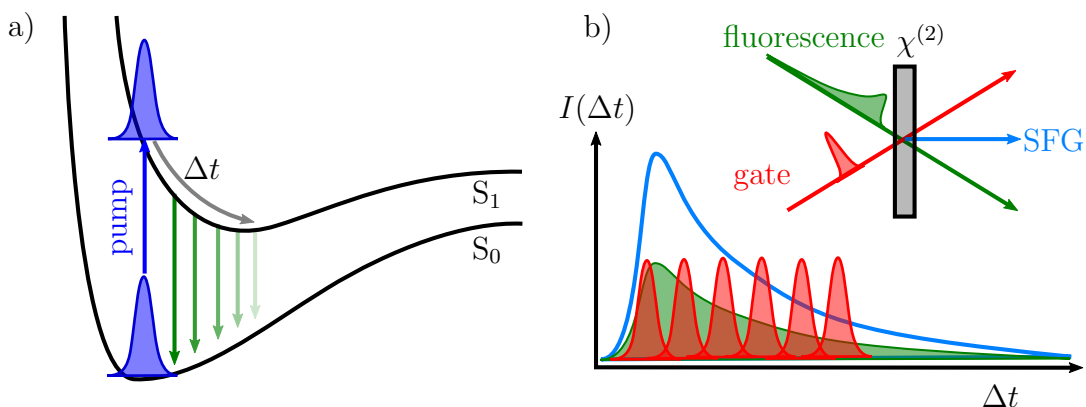


Figure 2.8: Illustration of the gating process in fluorescence up-conversion spectroscopy (FIUPS). Absorption of the pump pulse leads to the population of the S_1 state (a). The emitted fluorescence is up-converted with a gate pulse by sum-frequency generation (SFG) at different delay times Δt (b). The intensity of up-converted signal decreases as the population moves out of the Franck-Condon region.

2.2.1 Experimental Setup

A schematic depiction of the single-color fluorescence up-conversion setup is given in Figure 2.9. The setup is divided in three major parts: the optical pathway of the pump pulses, the optical pathway of the probe pulses and the up-conversion and detection part. A brief description is given in the following, more details can be found in preceding theses.^[10–12,31]

Optical Pathway for the Pump Pulses

Analogous to the TEAS experiment, pump pulses are delivered by the compressed output of a home-built NOPA and are used either directly for excitation in the visible spectral region or frequency-doubled when excitation in the UV is required. The pump beam is focused into a flow cell with 1 mm optical path length that contains the sample solution. A beam stop in combination with a suitable bandpass filter is used to remove scattered pump light from the subsequent experiment while allowing for the transmission of the fluorescence. To avoid fluorescence depolarization effects the polarization of the pump beam is set to magic angle with respect to the detected up-conversion signal using a Berek compensator. A pair of off-axis parabolic mirrors is used to collect the emission of the sample and to focus it into the BBO crystal.

Optical Pathway for the Probe Pulses

A portion of $\sim 65 \mu\text{J}$ of the Ti:Sa fundamental is used directly as probe. After passing an optical delay stage with mounted retroreflector, this beam is also focused into the BBO crystal where it is spacially overlapped with the sample fluorescence under a small angle. Depending on whether a BBO crystal for type I or type II phase-matching is used, the polarization of the probe beam can be adjusted by a $\lambda/2$ plate.

Fluorescence Up-conversion and Detection

The up-conversion of the fluorescence photons takes place by type I or type II sum frequency generation (SFG) in a BBO crystal. If the rotation angle of the BBO crystal meets the phase-matching conditions for SFG between the probe and the desired fluorescence wavelength the up-converted signal emerges spatially between the two beams. A pair of lenses directs the up-converted photons through a double monochromator. A photomultiplier connected to a preamplifier and gated photon counter are used for subsequent detection and are read out by a *LabVIEW*^[15] routine programmed by Dennis Bank.

2.2.2 Data Analysis

The obtained single-color fluorescence time profiles were analyzed without any further preprocessing steps. The time constants of the fluorescence decay were obtained from fitting a sum of exponential decay curves with time constants τ_i and amplitudes A_i to the data

$$F(\Delta t) = \sum A_i \cdot \exp\left(\frac{-\Delta t}{\tau_i}\right). \quad (2.13)$$

The limited experimental time-resolution owing to the finite duration of the pump and probe pulses is accounted for by a Gaussian-shaped instrument response function (IRF)

$$G(\Delta t) = \frac{1}{\sigma\sqrt{2\pi}} \cdot \exp\left[-\frac{\Delta t^2}{2\sigma^2}\right] \quad (2.14)$$

with the standard deviation of the Gaussian σ that is related to the FWHM by

$$\text{FWHM} = \sqrt{8\ln 2} \cdot \sigma. \quad (2.15)$$

For an accurate description of the experimentally observed fluorescence time profiles $I(\Delta t)$ the functions $F(\Delta t)$ and $G(\Delta t)$ are convoluted according to

$$I(\Delta t) = [F * G](\Delta t) \equiv \int_{-\infty}^{+\infty} F(\Delta t') G(\Delta t - \Delta t') d\Delta t' \quad (2.16)$$

which eventually results in the expression

$$I(\Delta t) = B + \sum A_i \cdot \exp\left[\frac{\sigma^2}{2\tau_i^2} - \frac{-\Delta t}{\tau_i}\right] \cdot \left(1 + \operatorname{erf}\left[\frac{\Delta t(\tau_i - \sigma^2)}{\sqrt{2} \cdot \sigma \cdot \tau_i}\right]\right). \quad (2.17)$$

Here, a constant term B has been added to account for possible background.^[31]

References

- [1] Demtröder, W. *Laserspektroskopie: Grundlagen und Techniken*; Springer, Berlin, 2007.
- [2] Boyd, R. W. *Nonlinear Optics*; Elsevier Inc., Amsterdam, 2008.
- [3] Meschede, D. *Optik, Licht und Laser*; Teubner, Wiesbaden, 2008.
- [4] Mukamel, S. *Principles of Nonlinear Optical Spectroscopy*; Oxford University Press, New York, 1995.
- [5] Pancur, T. Untersuchung der Isomerisierungsdynamik von Azobenzolen und der strahlungslosen Desaktivierung von Nukleobasen mit Hilfe der Femtosekunden-Fluoreszenzspektroskopie. Ph. D. Thesis, Christian-Albrechts-Universität zu Kiel, 2004.
- [6] Foca, M. Investigations of Ultrafast Photoisomerization of Photochromic Molecular Switches by fs-Time-Resolved Transient Absorption Spectroscopy. Ph. D. Thesis, Christian-Albrechts-Universität zu Kiel, 2005.
- [7] Studzinski, H. Ultrafast Radiationless Dynamics of Selected Electronically Excited Aromatic Molecules by Femtosecond Time-Resolved Mass Spectrometry and Photoelectron Imaging. Ph. D. Thesis, Christian-Albrechts-Universität zu Kiel, 2007.
- [8] Studzinski, H. Aufbau und Charakterisierung eines nicht-kollinearen optisch-parametrischen Verstärkers. Diploma Thesis, Christian-Albrechts-Universität zu Kiel, 2002.
- [9] Siewertsen, R. Ultrafast Photochromic Reactions of Structurally Modified Furylfulgides and a Bridged Azobenzene. Ph. D. Thesis, Christian-Albrechts Universität zu Kiel, 2011.
- [10] Röttger, K. Ultrafast Deactivation Dynamics of Structurally Modified and Hydrogen-Bonded DNA and RNA Building Blocks. Ph. D. Thesis, Christian-Albrechts Universität zu Kiel, 2013.
- [11] Stuhldreier, M. C. Electronic Deactivation Dynamics of DNA Model Systems and Solvation Dynamics of a Natural Antioxidant by Femtosecond Fluorescence and Absorption Spectroscopy. Ph. D. Thesis, Christian-Albrechts Universität zu Kiel, 2013.

- [12] Bahrenburg, J. Ultrafast Photochemical Dynamics of Azobenzenes Affected by Intra- and Intermolecular Interactions and of a Proton Transfer Switch. Ph. D. Thesis, Christian-Albrechts-Universität zu Kiel, 2014.
- [13] Wang, S. Ultrafast Photoisomerization Dynamics of Photochromic Molecular Switches Affected by Their Environment and Ultrafast Energy Transfer. Ph. D. Thesis, Christian-Albrechts-Universität zu Kiel, 2018.
- [14] Stange, U. C. Electronic Dynamics of Monomers , Dimers and Oligomers of Purine Nucleobases Studied by Femtosecond Time-Resolved Spectroscopy. Ph. D. Thesis, Christian-Albrechts-Universität zu Kiel, 2018.
- [15] National Instruments, C. LabVIEW. 2012.
- [16] Wolfram Research, I. Mathematica. 2016.
- [17] Marschan, R. Globale Analyse von femtosekunden-zeitaufgelösten transienten Absorptionsdaten in MATLAB mittels Singulärwertzerlegung. Master Thesis, Christian-Albrechts-Universität zu Kiel, 2015.
- [18] Renth, F.; Siewertsen, R.; Strübe, F.; Mattay, J.; Temps, F. *Phys. Chem. Chem. Phys.* **2014**, *16*, 19556–19563.
- [19] Wang, S.; Schatz, S.; Stuhldreier, M. C.; Böhnke, H.; Wiese, J.; Schröder, C.; Raeker, T.; Hartke, B.; Keppler, J. K.; Schwarz, K.; Renth, F.; Temps, F. *Phys. Chem. Chem. Phys.* **2017**, *19*, 30683–30694.
- [20] Wang, S.; Bohnsack, M.; Megow, S.; Renth, F.; Temps, F. *Phys. Chem. Chem. Phys.* **2019**, *21*, 2080–2092.
- [21] Kovalenko, S. A.; Dobryakov, A. L.; Ruthmann, J.; Ernsting, N. P. *Phys. Rev. A - At. Mol. Opt. Phys.* **1999**, *59*, 2369–2384.
- [22] Ekvall, K.; Van Der Meulen, P.; Dhollande, C.; Berg, L. E.; Pommeret, S.; Naskrecki, R.; Mialocq, J. C. *J. Appl. Phys.* **2000**, *87*, 2340–2352.
- [23] Lorenc, M.; Ziolek, M.; Naskrecki, R.; Karolczak, J.; Kubicki, J.; Maciejewski, A. *Appl. Phys. B Lasers Opt.* **2002**, *74*, 19–27.
- [24] Chesnoy, J.; Mokhtari, A. *Phys. Rev. A* **1988**, *38*, 3566–3576.
- [25] Ruhman, S.; Joly, A. G.; Nelson, K. A. *IEEE J. Quantum Electron.* **1988**, *24*, 460–469.
- [26] Weiner, A. M.; Wiederrecht, G. P.; Nelson, K. A.; Leaird, D. E. *J. Opt. Soc. Am. B* **1991**, *8*, 1264.
- [27] Wahlstrand, J. K.; Merlin, R.; Li, X.; Cundiff, S. T.; Martinez, O. E. *Opt. Lett.* **2005**, *30*, 926.

- [28] Merlin, R. *Solid State Commun.* **1997**, *102*, 207–220.
- [29] Van Stokkum, I. H.; Larsen, D. S.; Van Grondelle, R. *Biochim. Biophys. Acta - Bioenerg.* **2004**, *1657*, 82–104.
- [30] Cattell, R. B. *Multivariate Behav. Res.* **1966**, *1*, 245–276.
- [31] Schwalb, N. K. Ultrafast Electronic Deactivation Dynamics in DNA Model Systems by Femtosecond UV Fluorescence Spectroscopy. Ph. D. Thesis, Christian-Albrechts-Universität zu Kiel, 2009.

3 Ultrafast dynamics of a bi-stable azopyridine Ni-porphyrin spin switch after photoexcitation in the porphyrin B-bands

Sebastian Megow,¹ Julia Bahrenburg,¹ Mark Dittner,¹ Birthe Kohly,¹ Joachim Gripp,¹ Marcel Dommaschk,² Christian Schütt,² Rainer Herges² and Friedrich Temps^{1,}*

¹Institute of Physical Chemistry, Christian-Albrechts-University Kiel,
Max-Eyth-Str. 1, 24098 Kiel, Germany

²Otto Diels-Institute of Organic Chemistry, Christian-Albrechts-University
Kiel, Otto-Hahn-Platz 4, 24098 Kiel, Germany

EPJ Web of Conferences, 2019, 205, 05019

OWN CONTRIBUTIONS TO THIS MANUSCRIPT:

- Femtosecond time-resolved electronic absorption spectroscopy (TEAS),
- Analysis of experimental TEAS data,
- Writing of the manuscript.

*To whom correspondence should be addressed. Email: temps@phc.uni-kiel.de

Abstract

Femtosecond time-resolved absorption measurements of a magnetically bi-stable azopyridine Ni-porphyrin in solution at room temperature show that the photo-induced dynamics are dominated by transient low-spin \rightleftharpoons high-spin interconversion involving Ni (d^2) and (d,d) states.

3.1 Introduction

Metal porphyrins are naturally occurring chromophores that play central roles in a multitude of biological processes such as photosynthesis, redox reactions or oxygen transport.^[1] Many of their fascinating functions are initiated by absorption of light. An extraordinary example is the recently designed nickel porphyrin spin-state switch (azoNiPor) with an azopyridine unit attached to the porphyrin ring (Fig. 1a), which shows magnetic bi-stability in solution at room temperature and thereby carries potential as photoswitchable contrast agent for magnetic resonance imaging (MRI).^[2,3] As illustrated in Fig. 1 (b–d), the central Ni(II) ion can be converted almost quantitatively from the diamagnetic singlet low-spin (*LS*) to the paramagnetic triplet high-spin (*HS*) state by irradiation with green light at $\lambda = 505$ nm. In this process, the pyridine nitrogen coordinates axially to the Ni centre, when the azo arm is switched from the *trans* to *cis* configuration. The spin-state transition is reversed upon irradiation with blue light at $\lambda = 435$ nm. Here, we report on a study of the ultrafast photo-induced dynamics of the azoNiPor switch in its *LS-trans* and *HS-cis* states following excitation in the B (Soret) bands of the porphyrin by means of femtosecond time-resolved transient absorption spectroscopy to shed light onto the spectro-temporal processes and physical mechanisms behind the spin-state switching.

3.2 Experimental details

The femtosecond transient absorption measurements were performed in solution in cyclohexane in flow cells of 0.1 and 1 mm optical path length.^[4] The samples were excited by pump pulses at $\lambda = 406$ nm (*LS-trans*) and 420 nm (*HS-cis*), respectively, and interrogated by supercontinuum probe pulses from 350 – 700 nm.

3.3 Results and discussion

The observed transient spectra of the *LS-trans* azoNiPor isomer in Fig. 2 exhibit a pronounced negative band in the 400 – 425 nm region reflecting the ground-state bleach (GSB) and a strong positive excited-state absorption (ESA) from

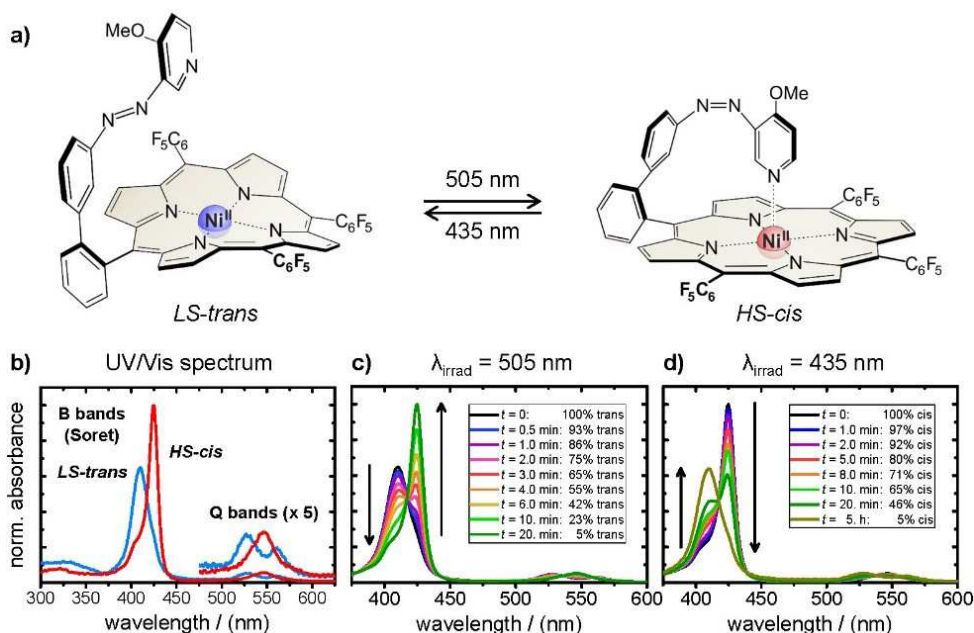


Figure 1: a) Structures of the azoNiPor spin switch in its *LS-trans* and *HS-cis* forms; b) static UV-Vis spectra; c) conversion of the *LS-trans* to the *HS-cis* form by cw irradiation at $\lambda = 505$ nm (12.4 mW, 30 nm bandwidth); d) conversion of the *HS-cis* to the *LS-trans* form by cw irradiation at $\lambda = 435$ nm (0.066 mW, 5 nm bandwidth).

425 – 450 nm. In the quadratic-planar ligand field of the *LS* state, the d^8 Ni(II) ion adopts its $^1(d_{z^2})^2$ electron configuration with an empty $d_{x^2-y^2}$ orbital. The pronounced ESA thus arises from the Ni $^3(d_{z^2}, d_{x^2-y^2})$ state. The apparent first derivative-like transient band shape that is typical for these dynamics^[5] is fully established after $\Delta t \sim 3$ ps (cf. Fig. 2c). The optically excited S_2 ($^1\pi\pi^*$) state of the porphyrin evidently undergoes ultrafast intersystem crossing (ISC) in < 100 fs. The high vibrational energy dumped into the molecule by the accompanying Ni $^1(d_{z^2})^2 \rightarrow ^3(d_{z^2}, d_{x^2-y^2})$ transition explains the initially very broad ESA up to ~ 550 nm, but the band rapidly blue-shifts and narrows by vibrational cooling on a time scale of $\tau \sim 1$ ps. All transient spectral features eventually decay, indicating a virtually complete ground state recovery (GSR) with $\tau \sim 350$ ps (Fig. 2d).

The axial azopyridine in the *HS-cis* isomer raises the energy of the Ni (d_{z^2}) orbital such that the Ni electron configuration switches to $^3(d_{x^2-y^2}, d_{z^2})$ and the porphyrin S_2 ($^1\pi\pi^*$) band red-shifts to 420 nm. The transient spectra after 420 nm excitation in Fig. 2 display second derivative-like band shapes due to the characteristic transient absorption by the *LS* state around 406 nm. After the initial optical excitation to the Por(S_2)–Ni $^3(d_{x^2-y^2}, d_{z^2})$ state, the system thus reverts at least partially to a Por–Ni $^1(d_{z^2})$ state, which repels the axial azo ligand. At $\Delta t \sim 11.9$ ps, the absorbance at 406 nm indicates a transient

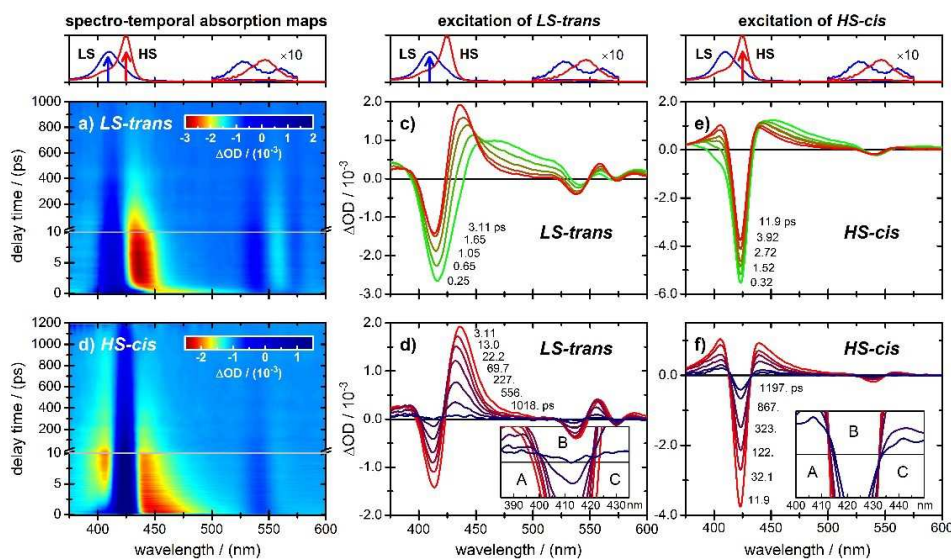


Figure 2: Measured spectro-temporal transient absorption maps of the change in optical density ΔOD after fs excitation of azoNiPor in its *LS-trans* (a) and *HS-cis* forms (b) and selected transient spectra at different delay times (c-f).

LS state yield of $\sim 20\%$. Subsequent relaxation processes, however, lead to recapture of the azo ligand and efficient *HS-cis* GSR. The slow ($\tau \sim 600$ ps) temporal decay asymptotically extrapolates to an *LS* yield of $\sim 6\%$ as upper limit. Actinometric quantum yield measurements at 425 – 435 nm established a value of $2.2 \pm 0.2\%$.

Additional femtosecond measurements are in progress to shed light on the photo-induced dynamics after excitation of both of the azoNiPor isomers in the Q bands and in the mysterious 450 – 500 nm window, where *LS*-to-*HS* conversion takes place (Fig. 1b). We speculate that spin-state switching at 500 nm is mediated by transfer from the "hot" $^3[\text{Por-Ni}(\text{d}^2/\text{d},\text{d})]$ state right after excitation to the azopyridine triplet, where *trans-cis* isomerization is easily feasible. The measured *LS*-to-*HS* quantum yield at 500 nm is very low ($\sim 0.5\%$). Direct excitation of the weak azo ($n\pi^*$) band could also contribute to this quantum yield. Despite the low quantum yields, the azoNiPor system stands out for the almost quantitative $LS \rightleftharpoons HS$ interconversion. The excellent overall spin-state switching efficiency is mediated by the huge absorption coefficients of the porphyrin.

Acknowledgements

The authors acknowledge the support of this work by the Collaborative Research Centre (SFB) 677.

References

- [1] Bajema, L.; Gouterman, M.; Meyer, B. *J. Mol. Spectrosc.* **1961**, *27*, 225–235.
- [2] Venkataramani, S.; Jana, U.; Dommaschk, M.; Sönnichsen, F. D.; Tuczek, F.; Herges, R. *Science* **2011**, *331*, 445–449.
- [3] Dommaschk, M.; Peters, M.; Gutzeit, F.; Schütt, C.; Näther, C.; Sönnichsen, F. D.; Tiwari, S.; Riedel, C.; Boretius, S.; Herges, R. *J. Am. Chem. Soc.* **2015**, *137*, 7552–7555.
- [4] Röttger, K.; Siewertsen, R.; Temps, F. *Chem. Phys. Lett.* **2012**, *536*, 140–146.
- [5] Zhang, X.; Wasinger, E. C.; Muresan, A. Z.; Attenkofer, K.; Jennings, G.; Lindsey, J. S.; Chen, L. X. *J. Phys. Chem. A* **2007**, *111*, 11736–11742.

4 On the ultrafast photo-induced dynamics and the spin crossover mechanism of the magnetically bi-stable azopyridine nickel(II) porphyrin complex

*Sebastian Megow,^a Marcel Dommaschk,^b Birthe Behr,^a Joachim Gripp,^a
Rainer Herges^b and Friedrich Temps^b*

^aInstitut für Physikalische Chemie, Christian-Albrechts-Universität,
Olshausenstrasse 40, 24098 Kiel, Germany

^bOtto Diels Institut für Organische Chemie, Christian-Albrechts-Universität,
Olshausenstrasse 40, 24098 Kiel, Germany

Manuscript

OWN CONTRIBUTIONS TO THIS MANUSCRIPT:

- Static UV–vis absorption spectroscopy,
- Femtosecond time-resolved electronic absorption spectroscopy (TEAS),
- Analysis of experimental TEAS data,
- Writing of the manuscript.

Abstract

We report on the ultrafast photo-induced dynamics and the spin crossover (SCO) mechanism of the phenylazopyridine nickel porphyrin complex azoNi-Por developed by Herges and co-workers [Science **2011**, *120*, 445], the first molecule showing magnetic bi-stability in homogeneous solution at room temperature. Results of static absorption spectroscopy and chemical actinometry demonstrate that, although the low-spin (LS) and high-spin (HS) forms of this compound can be interconverted into to each other almost quantitatively, the quantum yields for each process are generally smaller than 2 %. As evidenced by femtosecond time-resolved electronic absorption spectroscopy (TEAS), excitation of the porphyrin states of the four-coordinate LS complex with the phenylazopyridine (PAP) ligand in the *trans*-configuration rapidly produces the desired high-spin (HS) electron configuration at the Ni(II) center. However, as this state cannot be trapped by intramolecular coordination with the *trans*-PAP ligand, the LS ground state quickly recovers by efficient intersystem crossing. Congruently, excitation of the porphyrin chromophore of the five-coordinate HS complex with the PAP ligand in its *cis* form that coordinates to the Ni(II) in the ground state results in the generation of a Ni-centered excited state with LS electron configuration. The LS electron configuration at the Ni(II) center usually is repulsive towards axial ligands, but in this case is unable to expel the coordinated *cis*-PAP unit within the short lifetime of the excited state, causing efficient recovery of the HS form. However, measurements at wavelengths allowing for (weak) direct excitation and isomerization of the PAP moiety indicate formation of the stable SCO product, which is beyond the time scales of ultrafast spectroscopy. These results suggest that the SCO mechanism is indeed driven by the photodynamics of the PAP unit rather than the Ni porphyrin, in accordance with the proposed concept of light-driven coordination-induced spin-state switching (LD-CISSS).

4.1 Introduction

Metal porphyrins are naturally occurring chromophores which play central roles in numerous biological processes, including photosynthesis, reduction–oxidation reactions and oxygen transport.^[1] Many of these processes are initiated by absorption of light. With their high absorption coefficients and excellent photostabilities, porphyrins thus attract attention for a wide variety of applications in biology, medicine, chemistry, physics, materials science and engineering.^[2–10] An extraordinary example is the recently designed spin-state switch azoNiPor developed by Herges and co-workers based on a nickel porphyrin with an attached phenylazopyridine (PAP) unit as depicted in Fig. 1.^[11–14] This molecule is the first to show magnetic bi-stability in homogeneous solution at room temperature^[11] and therefore possesses unique application potential as photoswitchable

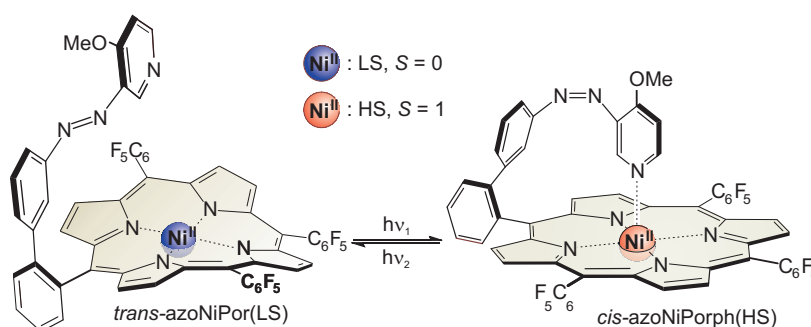


Figure 1: Sketch of the structures and reversible photoswitching processes of azoNiPor in the *trans*-low spin and *cis*-high spin states.

contrast agent in magnetic resonance imaging (MRI).^[13] As illustrated in Fig. 1, the spin state of the Ni(II) ion can be reversibly switched between the MRI silent diamagnetic low-spin (LS, $S = 0$, *i.e.* singlet) state and the MRI active paramagnetic high-spin (HS, $S = 1$, *i.e.* triplet) state. This process is connected with the *trans*–to–*cis* isomerization of the attached PAP unit that acts as an axial ligand to the Ni(II) center in the *cis*-configuration, while it is detached in the *trans*-form. Due to the similar appearance, the azoNiPor complex has been nick-named as “record player” molecule (RP).

In a series of meticulous studies, the azoNiPor system has been optimized in the Herges group with respect to the equilibrium constant for the coordination of the axial *cis*-azo ligand to the Ni.^[12,13] The attachment of the azopyridine arm in *meta*-position to the phenyl tether to the porphyrin platform was chosen to avoid electronic conjugation between the two chromophores.^[12] The pentafluorophenyl substituents at the porphyrin in *meso*-position diminish the electron density at the Ni(II) center making it more acidic and thus more attractive towards coordination of nitrogeneous bases. The intramolecular coordination was further improved by introduction of electron donating groups in *para*-position to the nitrogen atom of the pyridine. Eventually, the azoNiPor derivative chosen for an ultrafast time-resolved spectroscopic study in the present work carried a methoxy group, leading to a practically quantitative yield of the paramagnetic HS *cis*-isomer in the photostationary state (PSS) upon irradiation of the diamagnetic LS *trans*-species with light at $\lambda = 495 - 520$ nm, while the back-reaction from the HS *cis*- to the stable LS *trans*-isomer is completed upon irradiation at $\lambda = 400 - 435$ nm.^[13]

Despite its excellent operational functionality, however, the actual spin-state switching mechanism in azoNiPor is not yet understood at all to date. The fact that the *cis*-azoNiPor(HS) state is obtained from the stable *trans*-azoNiPor(LS) molecule upon irradiation in the 495 – 520 nm wavelength region is surprising, since this happens at energies just a little above the porphyrin Q band origin and thus at much lower energies than the $^1\pi\pi^*$ excited state on the PAP ligand (= S_2 in free PAP^[15]), which yields the highest amount of *cis*-isomer for free PAP

upon excitation in the near-UV. Further, the 400 – 435 nm region, where *cis* (HS)–to–*trans* (LS) isomerization in the azoNiPor title compound is induced, is obscured by the predominant absorption in the Soret (= B) band of the porphyrin macrocycle. This seems counterintuitive considering the originally proposed mechanism of **light-driven coordination-induced spin-state switching** (LD-CISSS)^[11] for which the spin crossover (SCO) is initiated by photoisomerization of the PAP unit. On the other hand, the electronic origin of the $^1n\pi^*$ transition in the parent azobenzene (AB) molecule (= S_1 in free AB)^[15] has been located at 18 471.7 cm⁻¹ (541.3 nm) in the gas phase, and the threshold energy for the *trans*–to–*cis* photoisomerization of AB is believed to lie no more than 750 – 1000 cm⁻¹ higher, *i.e.* between 513 and 520 nm.^[16] The respective energies in the PAP derivative of interest here are supposed to be quite similar. Thus, the LD-CISSS mechanism has been called into question.^[14,17]

Considering the observed efficient photoswitching of azoNiPor, it has instead been suggested that the dynamics of the Ni porphyrin may be crucial for the intramolecular coordination/de-coordination of the PAP ligand,^[11–14,17] especially since Ni(II) porphyrin itself shows light-induced SCO even in the absence of further coordination partners.^[18] The optically bright excited states of the porphyrin chromophore of interest are of $^1\pi\pi^*$ character and give rise to the Q (= S_1) and B (= S_2) bands in the UV–vis spectrum of the free porphine base and the Ni(II) porphyrin complex, which are traditionally rationalized in terms of the four-orbital model of Gouterman.^[19] Occurring in < 50 – 100 fs, the electronic relaxation from the B to the Q state(s) is known to be ultrafast,^[20] and possibly involves the recently proposed optically dark N state.^[21] The Q states are significantly longer-lived. The photo-induced dynamics of four-coordinate LS Ni(II) porphyrins have been studied in some detail.^[22–29] Accordingly, the initially excited $^1\pi\pi^*$ state(s) of the macrocycle decay(s) back to the electronic ground state (GS) under involvement of the metal d-excited states, to which the porphyrin $\pi\pi^*$ states are strongly coupled. In the square-planar ligand field of the porphyrin, the $d_{x^2-y^2}$ orbital of the d⁸ Ni(II) ion remains empty. Photoexcitation of either the $S_1(\pi\pi^*)$ or the $S_2(\pi\pi^*)$ state of the porphyrin is thus followed by the promotion of an electron from the doubly occupied d_{z^2} orbital to the $d_{x^2-y^2}$ orbital of the Ni to form a vibrationally highly excited $^{1,3}(d,d)^{hot}$ state (where the ^{1,3}superscripts indicate singlet or triplet) that subsequently undergoes vibrational and conformational relaxation within several picoseconds depending on the solvent.^[24,25] The resulting relaxed $^3(d,d)$ state has a lifetime of a few hundred picoseconds and is known to be attractive towards axial coordination of a nucleophilic ligand such as a nitrogenous base.^[30–36]

Moreover, depending on the macrocycle as well as the solvent, Ni(II) porphyrins can also bind two axial ligands to form octahedral complexes in the GS. In the six-coordinate environment, the Ni(II) d_{z^2} and $d_{x^2-y^2}$ are both singly occupied. Photoexcitation of the porphyrin now leads to the formation of a metal centered excited state with $(d_{z^2})^2$ configuration from which both axial ligands

are rapidly released.^[30–33,35,37] That state is probably reached via a $^3\pi\pi^*$ state of the porphyrin macrocycle.^[38]

Five-coordinate Ni porphyrins as the *cis*-azoNiPor(HS) complex in the present study (cf. Fig. 1) now come into play as intermediates in the coordination/de-coordination dynamics after excitation of four- and six-coordinate Ni porphyrins. Studies of the photodynamics of five-coordinate Ni porphyrins have, however, been rare. In the present work, we aim to shed light on the ensuing SCO mechanism in the azoNiPor spin switch by disentangling the photo-induced dynamical processes in the Ni porphyrin and the PAP units of the molecule and exploring their mutual interactions. Towards these ends, we use femtosecond transient electronic absorption spectroscopy (TEAS) to study the ultrafast photodynamics of the title molecules *trans*-azoNiPor(LS) and *cis*-azoNiPor(HS) and their building blocks, the nickel porphyrin NiTPPF₂₀, and the free porphine H₂TPPF₂₀ at excitation wavelengths between $300\text{ nm} \leq \lambda_{\text{pump}} \leq 560\text{ nm}$. Further insight is obtained by static electronic absorption measurements, including an investigation of the apparent excitation wavelength dependent photostationary states in the UV–vis region, by quantum yield measurements, and by nanosecond TEAS.

4.2 Experimental section

4.2.1 Static UV–vis absorption spectroscopy

Static UV–vis absorption spectra of azoNiPor in the *trans*-LS and *cis*-HS forms and its constituents, the PAP ligand, the Ni porphyrin NiTPPF₂₀, as well as the Ni-free porphine H₂TPPF₂₀, were measured in spectroscopic grade cyclohexane using a Shimadzu UV-2410 desktop spectrometer.

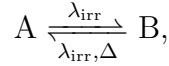
4.2.2 Photostationary states and quantum yields

The relative concentrations of the reactants and products in steady-state measurements at different irradiation wavelengths λ_{irr} as function of time t and in the resulting photostationary states PSS(λ_{irr}) at time $t \rightarrow \infty$ were measured in a setup designed after that of Megerle et al.^[39] with some added experimental options. A sketch of the setup can be found in Fig. S1 in the ESI.† The employed light sources were either selected high-power light emitting diodes (LEDs, Luxeon III Star) for broadband irradiation ($\Delta\lambda = 20 - 30\text{ nm}$) or a Xe arc lamp (75 W, 180 – 2500 nm bandwidth) coupled to a 200 mm ($f/4$) monochromator (Horiba Scientific) for narrow band irradiation ($\Delta\lambda = 1 - 5\text{ nm}$ depending on slit width). The excitation light was collimated through a camera lens (Nikkor AF-S 50/1.4 D) and directed through the cuvettes containing the sample or a reference solution, which were mixed thoroughly during exposure by magnetic stirrers (Thermo Scientific, Variomag Mini). Absolute ir-

radiation intensities were measured behind the cuvettes with a calibrated power meter (Coherent PS19Q) or a calibrated solar cell (Conrad YH-46X76) following Megerle et al.^[39], or by ferrioxalate chemical actinometry ($\lambda < 500$ nm) following Hatchard and Parker.^[40]

The concentrations of *cis*-azoNiPor(HS) resp. *trans*-azoNiPor(LS) in the irradiated solutions after time t and in the eventual photostationary states were determined from recorded UV–vis spectra (see results below) using a calibration curve constructed using the absorption coefficients of pure *trans*-(LS) and *cis*-(HS) solutions. The optical pathlengths in the static measurements were $d = 10$ mm.

The quantum yields Φ_i for the photoreactions, defined as the mole number of product molecules n_i divided by the mole number of absorbed photons $n_{\text{ph,abs}}$,^[41] were determined as function of λ_{irr} following the methods of Maafi and Brown^[42] and Corrie et al.^[43] For a reversible photoreaction initiated at wavelength λ_{irr} between two species A and B,



the time-dependent concentrations c_A and c_B of A and B are described by the differential equation^[42,44]

$$\begin{aligned} \frac{dc_A(t)}{dt} = - \frac{dc_B(t)}{dt} = & \Phi_{A \rightarrow B} \epsilon_A c_A(t) \times I_0 \times F(t) \\ & + \Phi_{B \rightarrow A} \epsilon_B c_B(t) \times I_0 \times F(t) + k_{\text{th}} \times c_B(t) \end{aligned} \quad (4.1)$$

with the irradiance I_0 at λ_{irr} in units of Einstein/(cm² s) = mol_{photons}/(cm² s), the concentrations $c_A(t)$ and $c_B(t)$ (related by $c_A(t) + c_B(t) = c_0$, where c_0 is the initial input concentration), the decadic molar absorption coefficients ϵ_A and ϵ_B at λ_{irr} , the quantum yields $\Phi_{A \rightarrow B}$ and $\Phi_{B \rightarrow A}$ of the photoreactions at λ_{irr} in the A \rightarrow B and B \rightarrow A directions, the rate constant k_{th} for the thermal back-reaction of B, and the photokinetic factor at λ_{irr}

$$F(t) = (1 - 10^{-E})/E \text{ with } E = (\epsilon_A c_A(t) + \epsilon_B c_B(t))d. \quad (4.2)$$

In the case of azoNiPor, $c_A(t)$ and $c_B(t)$ are the time-dependent concentrations of *trans*-azoNiPor(LS) and *cis*-azoNiPor(HS), respectively, ϵ_A and ϵ_B are known from the UV–vis absorption spectra of the pure *trans*-(LS) and *cis*-(HS) isomers, and $k_{\text{th}} = 0$ at room temperature. Thus, starting at $t = 0$ from either $c_A(0) = c_0$ and $c_B(0) = 0$ or from $c_A(0) = 0$ and $c_B(0) = c_0$, the above differential equations are easily solved for the values of $\Phi_{A \rightarrow B}$ resp. $\Phi_{B \rightarrow A}$ by numerical integration as function of irradiation time t . Towards these ends, we used the ParametricNDSolve routine implemented in Mathematica^[45] and least-squared fitting to the measured concentrations $c_B(t)$ and $c_A(t)$ at the selected detection wavelengths λ .

Further measurements for the quantum yield $\Phi_{B \rightarrow A}$ in the *cis*-(HS) \rightarrow *trans*-(LS) direction were carried out following the method of Corrie et al.^[43] using the xenon arc lamp with monochromator as light source to allow for irradiation with narrower spectral bandwidths compared to the LEDs. Due to the low irradiation intensity, the ferrioxalate chemical actinometer of Hatchard and Parker was used to measure the absorbed light intensities directly behind the sample and reference cuvettes.^[40] At small conversion yields, as detailed by Corrie et al.,^[43] the product yields $\Delta n(t_{\text{irr}})$ as function of irradiation time t_{irr} can be described by straight lines with slopes m , giving $\Phi_{B \rightarrow A}$ according to

$$\Phi_{B \rightarrow A} = \frac{m_B}{m_{\text{Fe}^{2+}, \text{ref}} - m_{\text{Fe}^{2+}, \text{sample}}} \times \Phi_{\text{Fe}^{2+}}. \quad (4.3)$$

The quantities m_B , $m_{\text{Fe}^{2+}, \text{ref}}$ and $m_{\text{Fe}^{2+}, \text{sample}}$, respectively, are the slopes of the regression lines to the B product yields in the sample solution and the Fe^{2+} product yields in the ferrioxalate actinometer with and without sample, while $\Phi_{\text{Fe}^{2+}}$ is the (known)^[40] quantum yield in the photolysis of ferrioxalate.

4.2.3 Femtosecond time-resolved electronic absorption spectroscopy

The femtosecond transient absorption measurements were performed in cyclohexane (Sigma Aldrich, spectroscopic grade) using a flow cell with 1 mm optical pathlength. The transient absorption set-up consists of a Ti:Sa regenerative amplifier (Clark MXR CPA 2001) that delivers 120 fs fwhm (full width at half maximum) pulses with 1 kHz repetition rate at a center wavelength of $\lambda = 775$ nm. Most of the 775 nm beam is used to run a home-built non-collinear optical parametric amplifier (NOPA) with a subsequent prism pulse compressor. Femtosecond pulses in the UV were obtained by second-harmonic generation (SHG). The difficult pump wavelengths in the 350 – 450 nm range were accessed by a two-staged NOPA with intermediate white-light generation to achieve tunable pulses in the 700 – 900 nm region and subsequent SHG as described in Ref. 46. For broadband detection, a small fraction of the laser fundamental was sent through a CaF_2 plate. The resulting supercontinuum white light pulses were subsequently split into probe and reference beams, sent into the sample cell and then dispersed in a prism spectrograph and detected using fast frame-transfer CCD cameras. The setup has been described in some detail before.^[47–49]

4.2.4 Nanosecond time-resolved electronic absorption spectroscopy

Tentative broadband nanosecond transient absorption spectra were taken in the same sample cell by coupling a fraction of the fundamental of a second, technically identical Ti:Sa regenerative amplifier (Clark MXR CPA 2011) into

the probe beam path of the transient electronic absorption setup to generate delayed supercontinuum pulses as probe. The temporal phase relation between the two laser systems was controlled by using the first Ti:Sa amplifier to trigger the amplifier of the second laser. Owing to the deviations in the repetition rates of the free-running oscillators of both systems, the probe pulses have a 58 ns temporal jitter with respect to the pump pulse that limits the temporal resolution of this experiment. The obtained probe spectra thus have to be viewed as averages over 58 ns windows, *i.e.* data points are obtained at $\Delta t = 0 - 58$ ns, $58 - 116$, $116 - 174$ etc., ns. The pulse timings were monitored with two fast photodetectors (Thorlabs PDA10A2) connected to a digital oscilloscope (Tektronix TDS3054). The respective delay times were electronically controlled by a digital delay generator (Stanford Research Systems, DG535). Despite the 58 ns temporal uncertainty, this method allows us to observe spectral changes on a much longer than femtosecond time scale. In particular, as will be seen, the slow attachment of the *cis*-PAP arm to the Ni(II) center can be observed.

4.3 Results

4.3.1 Static UV–vis absorption spectra

The static UV–vis spectra of both azoNiPor isomers in cyclohexane are given in Figure 2. The respective spectra of its constituents, the PAP ligand, the nickel porphyrin NiTPPF₂₀ and the free porphine H₂TPPF₂₀ can be found in Figs. S2 and S3 in the supporting information (SI).[†] The black dots represent the mole fractions of *cis*-azoNiPor(HS) that are obtained in the PSS upon irradiation with high-power LEDs at the respective wavelengths. As typical for porphyrins, the spectra of azoNiPor feature two distinct sets of bands, whose origin can be explained by Goutermans four-orbital model.^[1,19] The intense B or Soret bands around $375 \text{ nm} < \lambda_B < 450 \text{ nm}$ and the less intense Q bands around $500 \text{ nm} < \lambda_Q < 575 \text{ nm}$ both originate from $\pi\pi^*$ transitions of the porphyrin macrocycle. For *trans*-azoNiPor(LS), the B band maximum is located at 410 nm. The maxima of the associated Q(1,0) and Q(0,0) band are located at 527 nm and 561 nm, respectively. *cis*-azoNiPor(HS) shows a somewhat different structure due to its paramagnetic triplet ground state. In the five-coordinate complex, the accidental degeneracy of the porphyrin HOMOs is lifted, causing a red-shift in the B band maximum to 424 nm compared to *trans*-azoNiPor(LS). Instead of two separated Q bands, one sees only one broadened band with a maximum at 547 nm.

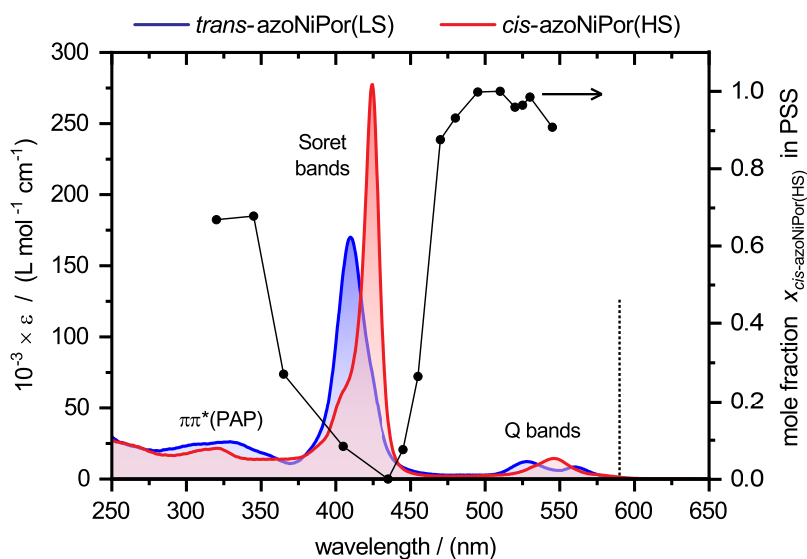


Figure 2: Static UV–vis absorption spectra of *trans*-azoNiPor(LS) (solid blue line) and *cis*-azoNiPor(HS) (solid red line). The black dots display the fractions of *cis*-azoNiPor(HS) in the photostationary states (PSS) upon irradiation with an LED of the respective wavelength. For LED wavelengths ≥ 590 nm (vertical dashed line), no photostationary equilibrium could be reached.

4.3.2 Fractions of *cis*-azoNiPor(HS) in the photostationary states

Looking at the PSS ratios obtained by irradiation with high-power LEDs, azoNiPor is present as a mixture of *trans*-azoNiPor(LS) and *cis*-azoNiPor(HS) for PSSs in the range of 320–365 nm. At irradiation wavelength in the range of 405–455 nm the PSS contains almost 100% *trans*-azoNiPor(LS). This value drops down to $\sim 0\%$ for irradiation wavelength > 470 nm, where *cis*-azoNiPor(HS) becomes almost exceptionally present. Finally, at LED wavelengths ≥ 590 nm, no photostationary equilibrium could be reached any more because the photon energies were too low to drive the *trans*–to–*cis* photoisomerization reaction. The static UV–vis spectra and *trans/cis* ratios of the free PAP are displayed in Figure S2. As can be seen, the free PAP data differ significantly from those of the PAP ligand in azoNiPor for PSS wavelengths > 470 nm, where the *trans*-isomer is present to $\sim 80\%$. Furthermore, comparing the static absorption coefficients of azoNiPor to those of the free PAP ligand it becomes clear that the porphyrin absorption exceeds the absorption of the azo chromophore at wavelengths > 350 nm, making a direct excitation of the PAP unit in this range unlikely. However, there is a chance to excite the $\pi\pi^*$ transition of PAP that contributes to the absorption spectrum of azoNiPor at wavelengths < 350 nm.

The above results were important for the choice of the excitation wavelengths in the time-resolved electronic absorption experiments below.

4.3.3 Quantum yields

The quantum yields for the spin switching process were determined for irradiation wavelength of $\lambda_{\text{irr}} = 435$ nm and $\lambda_{\text{irr}} = 505$ nm, where an almost quantitative interconversion between the *trans*-azoNiPor(LS) and the *cis*-azoNiPor(HS) form takes place. Preliminary results were reported before.^[14]

Recorded UV–vis spectra showing the conversion from *trans*-azoNiPor(LS) to *cis*-azoNiPor(HS) upon irradiation with a high-power LED at $\lambda_{\text{irr}} = 505$ nm are depicted in Figure 3(a). The reverse conversion from *cis*-azoNiPor(HS) to *trans*-azoNiPor(LS) upon irradiation with a high-power LED at $\lambda_{\text{irr}} = 435$ nm in Figure 3(c). The fit results from the numeric solution of the differential equation (1) are given in Figure 3 by the red (b) and blue (d) curves and give quantum yields of $\Phi_{LS \rightarrow HS}(505 \text{ nm}) = 0.016$ and $\Phi_{HS \rightarrow LS}(435 \text{ nm}) = 0.025$. Further, provided that the conversion to the photoproduct and its absorption at the irradiation wavelength is small, the photo-induced back-reaction can be neglected and the quantum yield can be calculated from

$$\Phi_i = \frac{n_i}{n_{\text{ph,abs}}} = N_A h c \frac{c_P V_{\text{irr}}}{P_{\text{abs.}} \Delta t \lambda_{\text{irr}}} \quad (4.4)$$

according to Megerle *et al.*^[39] Here, N_A is Avogadro's constant, h Planck's constant, c the speed of light, c_P the product concentration, V the sample volume, $P_{\text{abs.}}$ the absorbed power, and Δt the irradiation time. In this case, a linear regression to the initial part of the conversion reaction (black lines in (b) and (d)) gives the slope $m = c_P / \Delta t$. By applying this procedure, quantum yields of $\Phi_{LS \rightarrow HS}(505 \text{ nm}) = 0.005 \pm 0.001$ and $\Phi_{HS \rightarrow LS}(435 \text{ nm}) = 0.023 \pm 0.003$ were established.

As the quantum yield is most informative for irradiation with monochromatic light, further measurements were carried out using the xenon arc lamp equipped with a monochromator for narrowband irradiation and the ferrioxalate actinometer for detection of the irradiation intensity. The UV–vis absorption spectra showing the conversion from *cis*-azoNiPor(HS) to *trans*-azoNiPor(LS) upon irradiation at $\lambda_{\text{irr}} = 436$ nm at a bandwidth of $\Delta\lambda = 5$ nm and 1 nm are displayed in Figs. 4(a) and 4(c), respectively. Due to the small conversion yields, the time dependent *trans*-azoNiPor(LS) product concentrations (black) were described with straight lines. The respective product concentrations formed in the actinometer cuvette with either the reference cuvette (red) or the sample cuvette (blue) being present are given in Figs. 4(b) and 4(d). Evaluation of the slopes at bandwidths of $\Delta\lambda = 5$ nm and 1 nm, using Eq. 3 yielded values of $\Phi_{HS \rightarrow LS}(436 \text{ nm}) = 0.022 \pm 0.003$ for $\Delta\lambda = 5$ nm and of $\Phi_{HS \rightarrow LS}(436 \text{ nm}) = 0.021 \pm 0.003$ for $\Delta\lambda = 1$ nm. Unfortunately, the quantum yield $\Phi_{LS \rightarrow HS}(505 \text{ nm})$ could not be determined with this method since no adequate amount of photoproduct could be generated. This has several reasons: First, the quantum yield of the actinometer itself is very low at $\lambda > 500$ nm. Second, the irradiation

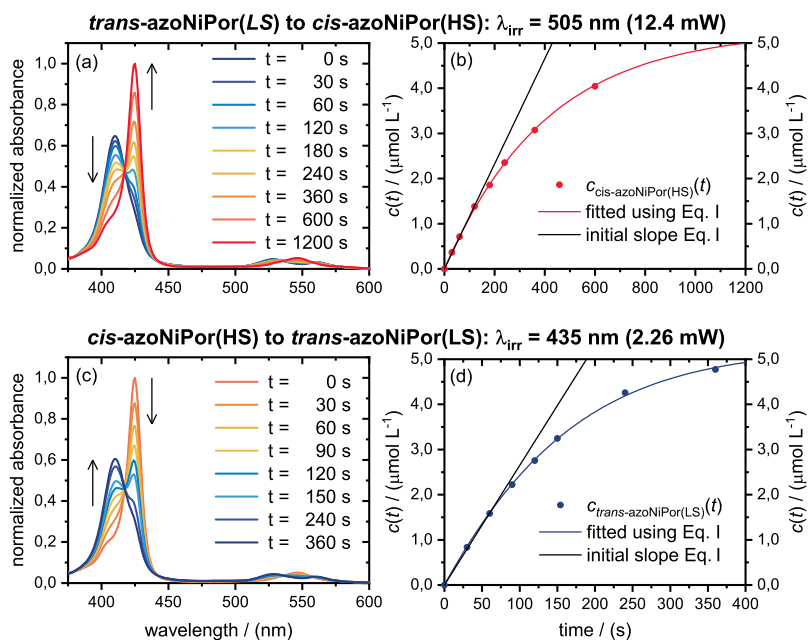


Figure 3: Static UV–vis spectra and product concentration vs. irradiation time profiles together with the fit results from the numeric solution of the differential equation and linear fits to the initial slopes showing the conversion of a $5 \mu\text{M}$ solution of *trans*-azoNiPor(LS) to *cis*-azoNiPor(HS) upon irradiation with an LED at $\lambda_{\text{irr}} = 505 \text{ nm}$ ($P_0 = 12.4 \text{ mW}$) (a,b) and the conversion of *cis*-azoNiPor(HS) to *trans*-azoNiPor(LS) upon irradiation with an LED at $\lambda_{\text{irr}} = 435 \text{ nm}$ ($P_0 = 2.26 \text{ mW}$) (c,d).

power of the xenon lamp is very small at this wavelength. Third, the quantum yield $\Phi_{LS \rightarrow HS}(505 \text{ nm})$ determined before is even smaller than 2%, leading to very little conversion yields within reasonable irradiation times.

4.3.4 Femtosecond time-resolved electronic absorption spectra

Recorded femtosecond time-resolved electronic absorption spectra provided a detailed picture of the ultrafast photodynamics of both azoNiPor isomers. Pump pulses at $\lambda_{\text{pump}} = 405 \text{ nm}$ and 420 nm were used to excite the porphyrin B bands, pulses at $\lambda_{\text{pump}} = 525 \text{ nm}$, 545 nm and 560 nm to excite the porphyrin Q bands. Furthermore, pulses at $\lambda_{\text{pump}} = 325 \text{ nm}$ and 456 nm were employed with the aim to directly excite the $\pi\pi^*$ and the $n\pi^*$ transitions of the PAP chromophore. The two-dimensional spectro-temporal absorption maps and spectra showing the change in optical density (ΔOD) as a function of probe wavelength (λ_{probe}) and pump-probe delay time (Δt) of *trans*-azoNiPor(LS) and *cis*-azoNiPor(HS) recorded after photoexcitation at $\lambda_{\text{pump}} = 545 \text{ nm}$ are displayed in Figures 5(a)–(c) and 5(d)–(f), respectively. A summary comparing the transient data

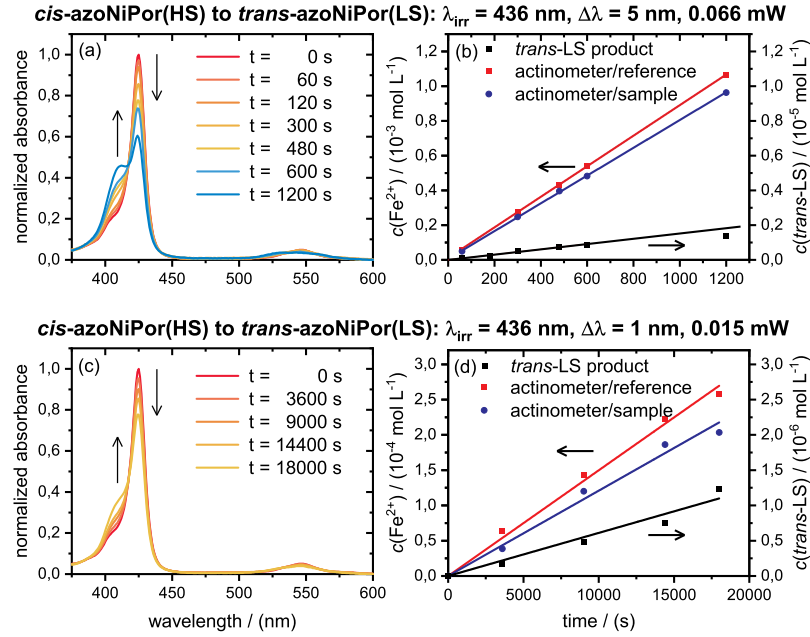


Figure 4: Static UV–vis spectra and product concentration vs. irradiation time profiles together with the respective linear regression lines showing the conversion from *cis*-azoNiPor(HS) to *trans*-azoNiPor(LS) of a 3.5 μM solution upon irradiation with a xenon lamp at $\lambda_{\text{irr}} = 436 \text{ nm}$ with a bandwidth of $\Delta\lambda = 5 \text{ nm}$ ($P_0 = 0.066 \text{ mW}$) (a,b) and of a 4.0 μM solution at the same wavelength with a bandwidth of $\Delta\lambda = 1 \text{ nm}$ ($P_0 = 0.015 \text{ mW}$) (c,d).

obtained at all the different pump wavelength is provided in Figs. S5 and S6 in the SI.† Additional measurements for $\text{H}_2\text{TTPF}_{20}$ and NiTTPF_{20} are provided in Fig. S4. At first glance the transient absorption data obtained for each azoNiPor species exhibit virtual identical photodynamics independent of the excitation wavelength. Thus, it is sufficient to proceed with the analysis of one representative data set per azoNiPor isomer as it facilitates getting to a general understanding of the underlying dynamical processes following photoexcitation of the porphyrin macrocycle.

The first observable transient of *trans*-azoNiPor(LS) (Figure 5(b)) shows the bleach of the Soret and the Q band as well as a broad excited-state absorption (ESA) covering almost all the spectral range. This diffuse ESA evolves within $\Delta t \sim 5 \text{ ps}$ into a spectrum resembling the shape of a Gaussian derivative with a sharp absorption maximum at $\lambda_{\text{probe}} = 420 \text{ nm}$. The build-up of this feature is accompanied by a significant recovery of the ground-state bleach (GSB) signals. The transient spectra observed in this initial conversion process exhibit non-zero isosbestic points at $\lambda_{\text{probe}} = 380 \text{ nm}$ and $\lambda_{\text{probe}} = 440 \text{ nm}$. During the second phase of temporal evolution ($\Delta t > 5 \text{ ps}$, Figure 5(c)) the amplitudes of all transient absorption features decay. The apparent isosbestic points emerging at zero absorption clearly indicate ground-state recovery (GSR), which is

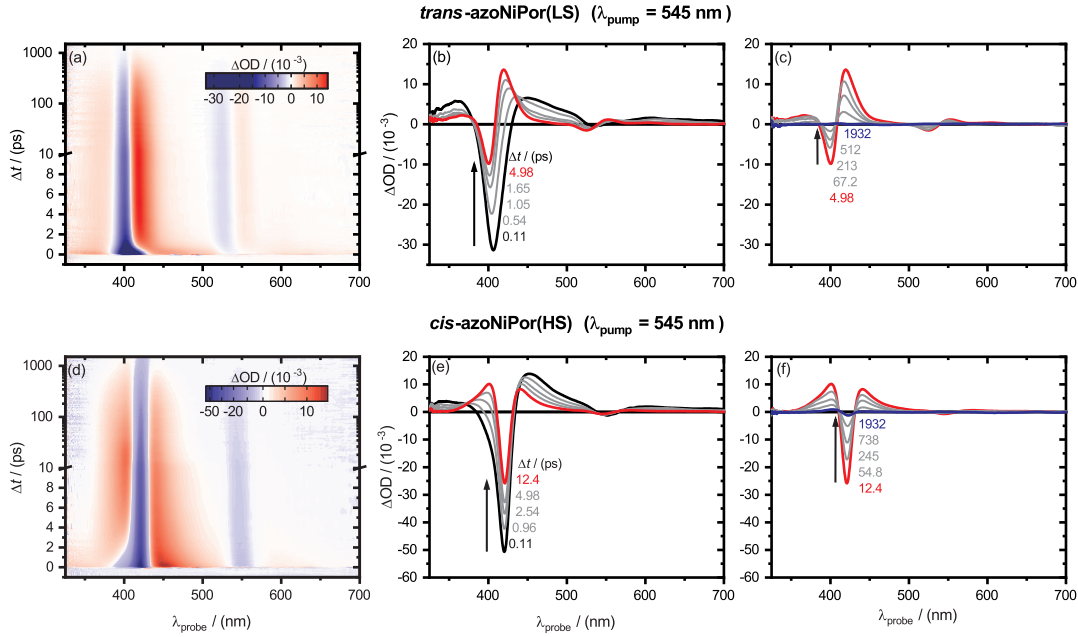


Figure 5: Femtosecond time-resolved electronic absorption maps and spectra of *trans*-azoNiPor(LS) (a–c) and *cis*-azoNiPor(HS) (d–f) recorded in cyclohexane after photoexcitation at $\lambda_{\text{pump}} = 545$ nm.

completed after $\Delta t \sim 1$ ns.

The first observable transient after photoexcitation of *cis*-azoNiPor(HS) also possesses a broad ESA band with a diffuse spectral shape (Figure 5(e)). This transient is similar to that initially observed for *trans*-azoNiPor(LS) and only differs in the slightly different positions of the superimposed GSB features. Analogously, the decay of this ESA is accompanied by the rise of a sharp positive absorption feature at $\lambda_{\text{probe}} = 400$ nm that reaches its maximum at $\Delta t \sim 12.4$ ps. In this phase of temporal evolution a significant GSR occurs and non-zero isosbestic points can be observed at $\lambda_{\text{probe}} = 370$ nm and $\lambda_{\text{probe}} = 440$ nm. The resulting transient spectrum resembles the shape of a second derivative Gaussian. In the time window ($\Delta t > 12.4$ ps, Figure 5(f)) the amplitudes of all transient absorption features decay. The clearly visible isosbestic points at zero absorption again reveal the GSR process.

The quantitative temporal development of the transient absorption features is represented by the transient absorption vs. delay time graphs in Figure 6(a) and 6(c). The time traces were integrated over the specified spectral ranges using the isosbestic points as integration limits and evaluated by simultaneous least-square fitting using a sum of exponentials convoluted with a Gaussian instrument response function (IRF). For both azoNiPor species the black and gray curves were chosen since they reflect the dynamics of the initially observed

diffuse ESA band. The red curves represent the temporal dynamics of the subsequently formed sharp ESA and the blue curves the bleach recovery.

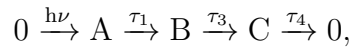
For *trans*-azoNiPor(LS) the integrated time traces in Figure 6(a) can be described by three exponentials with decay time constants $\tau_1 = 0.73 \pm 0.01$ ps, $\tau_3 = 11 \pm 2$ ps and $\tau_4 = 360 \pm 9$ ps. In the case of *cis*-azoNiPor(HS) (Figure 6(c)) four exponential functions were required with decay times of $\tau_1 = 0.65 \pm 0.04$ ps, $\tau_2 = 4.6 \pm 0.2$ ps, $\tau_3 = 19 \pm 1$ ps and $\tau_4 = 524 \pm 11$ ps.

To obtain further quantitative insight into the relaxation dynamics the complete time zero and solvent corrected data matrices, were evaluated by a singular value decomposition (SVD) based global analysis. After identifying the number n of relevant SVD components using a scree plot, the optimal global decay time constants and corresponding decay-associated difference spectra (DADS) were extracted by simultaneous non-linear least-square fitting of the SVD time traces with a sum of n exponentials convoluted with the instrument response function (IRF).^[50–52] To understand the encoded photodynamics in more detail and obtain information on the species involved in the relaxation process, subsequently, the DADS are transformed into the physically meaningful evolution-associated difference spectra (EADS) by applying a sequential kinetic model.

Table 1: Summary of the global time constants τ_i of *trans*-azoNiPor(LS) and *cis*-azoNiPor(HS) obtained from from band-integrated global fitting (BIF) and singular value decomposition (SVD) based analysis.

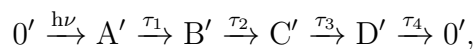
time constant	<i>trans</i> -azoNiPor(LS)		<i>cis</i> -azoNiPor(HS)	
	BIF	SVD	BIF	SVD
τ_1 / ps	0.73(1)	0.70(2)	0.65(4)	0.70(2)
τ_2 / ps	-	-	4.6(2)	5(1)
τ_3 / ps	11(2)	9(1)	19(1)	21(3)
τ_4 / ps	360(9)	360(13)	524(11)	600(30)

The data matrix of *trans*-azoNiPor(LS) can be reconstructed using three individual SVD components associated with global decay time constants of $\tau_1 = 0.70 \pm 0.02$ ps, $\tau_3 = 9 \pm 1$ ps and $\tau_4 = 360 \pm 13$ ps. Applying a kinetic scheme of the type



where 0 labels the ground state of *trans*-azoNiPor(LS) yields the EADS displayed in Figure 6b. The black EADS A shows the same diffuse shape as the initially observed transient, while EADS B and C resemble the derivative-shaped transient spectra observed after ~ 5 ps, with EADS B (red) being slightly broadened and red-shifted compared to EADS C (blue). In accordance with the results of the band-integrated fitting, four individual SVD components were required for satisfactorily modelling of the *cis*-azoNiPor(HS) data. The associated global decay time constants $\tau_1 = 0.70 \pm 0.02$ ps, $\tau_2 = 5 \pm 1$ ps, $\tau_3 = 21 \pm 3$ ps and

$\tau_4 = 600 \pm 30$ ps were applied to a kinetic scheme of the type



where $0'$ labels the ground state of *cis*-azoNiPor(HS) which results in the EADS displayed in Figure 6d. EADS A' (black) and B' (gray) resemble the shape of the earliest transient spectrum and show similarity to EADS A obtained from *trans*-azoNiPor(LS). EADS C' (red) and D' (blue) exhibit the second derivative Gaussian shape observed in the late transient spectra.

For both azoNiPor species the decay times extracted by the SVD based analysis are in good agreement with those obtained by the band integrated fitting procedure. These results are summarized in Table 1. For *trans*-azoNiPor(LS) the time constant $\tau_4 = 360$ is associated with a complete refilling of the ground state independent of the applied excitation wavelength (cf. Figure S5). As the progression of the deexcitation of *cis*-azoNiPor(HS) with an extracted time constant of $\tau_4 = 600$ ps is significantly slowed down compared to the *trans*-LS isomer, no complete recovery is observed within the recorded 2 ns time frame of femtosecond TEAS experiments (cf. Figure S6). In order to examine whether the incomplete recovery of the GSB is associated with the formation of the stable photoproduct, the temporal evolution of the bleach signals at different excitation wavelength were analyzed in more detail. These results are displayed in Figure S7 in the SI and indicate that formation of the photoproduct is only significant for excitation wavelength of $\lambda_{\text{pump}} \leq 456$ nm.

4.3.5 Nanosecond time-resolved electronic absorption spectra

Further qualitative information on the possible product formation was obtained by nanosecond TEAS following photoexcitation at $\lambda_{\text{pump}} = 325$ nm. The averaged nanosecond transient absorption spectra recorded for delay times between $\Delta t_3 = 1.6 - 59.6$ ns and $\Delta t_4 = 59.6 - 117.6$ ns are displayed in Figure 7 for *trans*-azoNiPor(LS) (a) and *cis*-azoNiPor(HS) (b). In addition, the femtosecond transient absorption spectra recorded at $\Delta t_1 = 3.7$ ps ($\Delta t_{1'} = 12.4$ ps for *cis*-azoNiPor(HS)) and $\Delta t_2 = 1.6$ ns and the static UV-vis difference spectra expected for formation of the respective photoproduct are displayed. For *trans*-azoNiPor(LS) the spectrum observed at $\Delta t_1 = 3.7$ ps shows the Gaussian derivative shape at maximum amplitude, while the final femtosecond transient absorption spectrum at $\Delta t_2 = 1.6$ ns is devoid of any absorption peaks. However, the averaged nanosecond transient absorption spectra recorded at Δt_3 and Δt_4 again feature clear Gaussian derivative shaped absorption peaks which match the static *trans*-azoNiPor(LS)–*cis*-azoNiPor(HS) difference spectrum. This indicates a delayed formation of the stable spin switching product upon excitation of *trans*-azoNiPor(LS). In case of *cis*-azoNiPor(HS) the shape of the

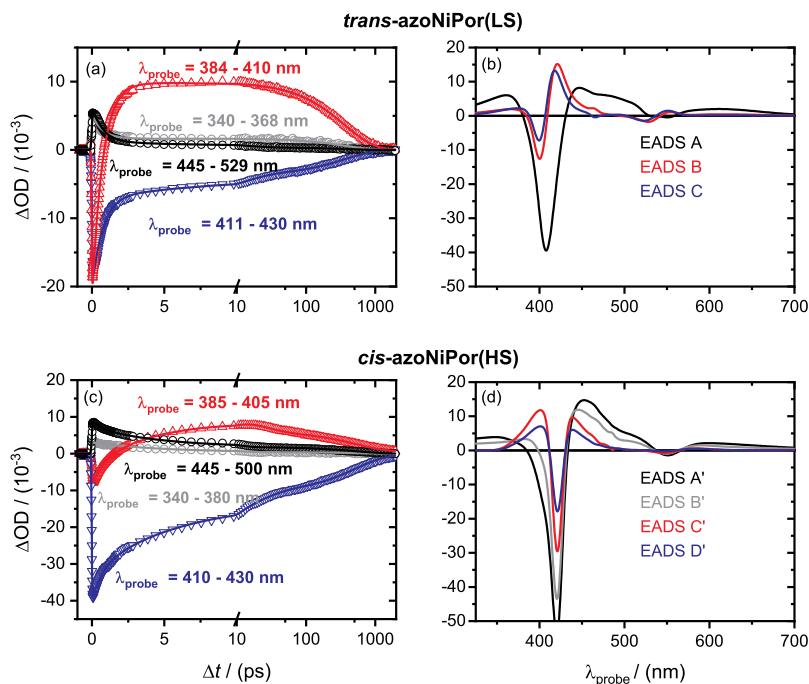


Figure 6: Fitted transient difference absorption vs. delay time traces of different spectral regions (λ_{probe}) as well as evolution-associated difference spectra obtained from a singular value decomposition (SVD) based analysis of *trans*-azoNiPor(LS) (a,b) and *cis*-azoNiPor(HS) (c,d).

femtosecond transient absorption spectrum at $\Delta t_1 = 12.4 \text{ ps}$ resembles a second derivative Gaussian shape and evolves towards the first derivative shaped spectrum observed at $\Delta t_2 = 1.6$ with opposite amplitudes compared to the ones observed following excitation of the *trans*-LS isomer. The same absorption bands with virtually identical amplitudes are observed in the averaged nanosecond spectra recorded at Δt_3 and Δt_4 and are congruent with the static *cis*-azoNiPor(HS)–*trans*-azoNiPor(LS) difference spectrum. Consequently, upon photoexcitation of *cis*-azoNiPor(HS), the sustainable spin switching product is already formed on the timescale of the femtosecond TEAS experiment.

4.4 Discussion

The azoNiPor complex was designed according to the LD-CISSS concept.^[11] This is based on the idea that direct excitation of the PAP ligand leads to its isomerization, (de-)coordination and, ultimately, the SCO. Therefore, the molecule was designed in order to minimize conjugation between the azo and the porphyrin chromophore.^[12] Accordingly, a similar trend of the *trans/cis* PSS ratios in dependency of the irradiation wavelength of the free PAP and the PAP ligand in the azoNiPor complex was expected. However, the actu-

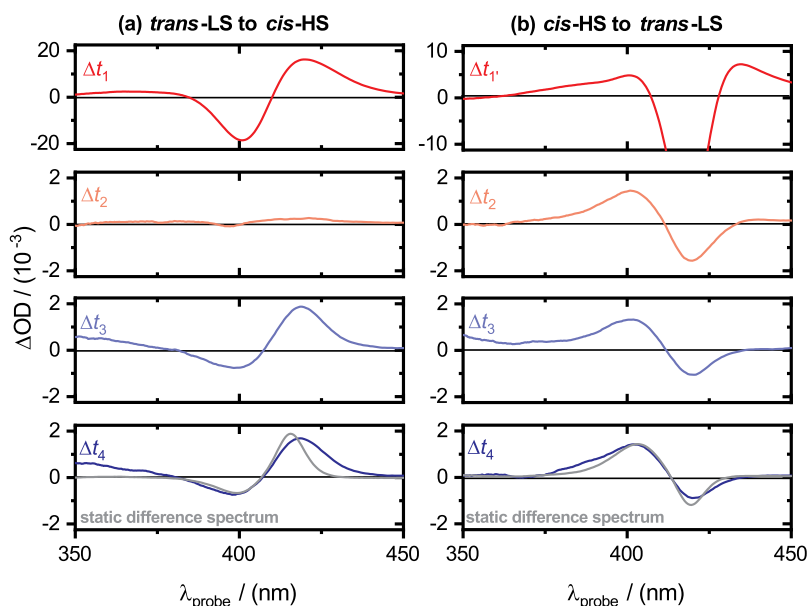


Figure 7: Femtosecond transient absorption spectra recorded at $\Delta t_1 = 3.7$ ps ($\Delta t_{1'} = 12.4$ ps) and $\Delta t_2 = 1.6$ ns and averaged nanosecond transient absorption spectra recorded between $\Delta t_3 = 1.6$ –59.6 ns and $\Delta t_4 = 59.6$ –117.6 ns of *trans*-azoNiPor(LS) (a) and *cis*-azoNiPor(HS) (b). All spectra were recorded following photoexcitation at $\lambda_{\text{pump}} = 325$ nm. Additionally, the *trans*-azoNiPor(LS)–*cis*-azoNiPor(HS) (a) and *cis*-azoNiPor(HS)–*trans*-azoNiPor(LS) (b) difference spectra calculated from the static absorption spectra is displayed in gray. Note the different ΔOD scales of the spectra in the first row.

ally observed PSS ratios exhibited significant deviations between both systems, bringing up questions about the mechanism of the spin switch. In course of this, the excited nickel porphyrin was attributed a major role especially in the *trans*-to-*cis*-isomerization of the PAP ligand in azoNiPor.^[11–13,17] The newly obtained results presented in this study, however, draw a different picture of the spin switching mechanism in the azoNiPor molecule and will be discussed in the following.

4.4.1 Static UV–vis absorption spectroscopy and quantum yield measurements

The static UV–vis absorption results demonstrated that following irradiation with high-power LEDs of different wavelengths, the *trans*/*cis* PSS ratios of PAP in azoNiPor deviate significantly from those of the free PAP and related azo compounds. Owing to the higher absorption coefficient of the $n\pi^*$ band of the *cis*-PAP, the photostationary equilibria obtained upon irradiation at this band are in favor of the *trans*-isomer (cf. Fig. S2). In the azoNiPor complex, however,

a clear turnover from mostly *trans*- to almost exclusively *cis*-species is observed for $\lambda_{\text{irr}} > 470$ nm. Consequently, it has to be discussed why *cis*-azoNiPor(HS) is enriched in this wavelength range. As generally known, the *trans-cis* isomerization of azo compounds takes place in the $S_1(n\pi^*)$ state. Tan *et al.* demonstrated that the 0–0 transition between the ground and the $S_1(n\pi^*)$ state of the parent azobenzene originates at $18\,471.7\text{ cm}^{-1}$ (541.3 nm) in the gas phase with an estimated activation barrier to the reactive part of the potential energy surface of about 2 kcal mol^{-1} .^[16] Considering these findings, it is apparent that the excitation conditions applied in this study of rather broad irradiation bandwidths and the sample molecules being present in solution and at room temperature, are easily sufficient to introduce isomerization of the PAP derivative in this wavelength range. Based on the assumption that the porphyrin macrocycle exerts no strong influence on the spectral position and intensity of the $n\pi^*$ transition of the PAP chromophore in the azoNiPor molecule and that the SCO is driven by PAP isomerization, the quantum yields of the spin switch ($\Phi_{\text{SCO}}(\lambda_{\text{irr}})$) can be estimated according to

$$\Phi_{\text{SCO}}(\lambda_{\text{irr}}) = \frac{\epsilon_{\text{PAP}}(\lambda_{\text{irr}})}{\epsilon_{\text{azoNiPor}}(\lambda_{\text{irr}})} \cdot \Phi_{\text{isom}}(\lambda_{\text{irr}}). \quad (4.5)$$

Here, $\epsilon_{\text{PAP}}(\lambda_{\text{irr}})$ and $\epsilon_{\text{azoNiPor}}(\lambda_{\text{irr}})$ denote the absorption coefficients of the free PAP and azoNiPor at the irradiation wavelength and $\Phi_{\text{isom}}(\lambda_{\text{irr}})$ denotes the quantum yield of the isomerization of the azo unit upon excitation of the $S_1(n\pi^*)$ state. The calculated quantum yields $\Phi_{\text{theo},i}$ are given in Table 2 and agree well with the low experimentally determined quantum yields $\Phi_{\text{exp},i}$ of $\Phi_{LS \rightarrow HS}(505\text{ nm}) = 0.005 \pm 0.001$ and $\Phi_{HS \rightarrow LS}(435\text{ nm}) = 0.023 \pm 0.003$.

Table 2: Parameters used for the theoretical estimation the quantum yields of the spin switch in azoNiPor (Φ_{theo}) based on the assumption that PAP is directly excited.

λ_{irr}	$\epsilon_{t\text{-PAP}}(\lambda_{\text{irr}})$	$\epsilon_{LS-t}(\lambda_{\text{irr}})$	$\Phi_{t-c}(n\pi^*)$	$\Phi_{LS-HS,\text{theo}}(\lambda_{\text{irr}})$
505 nm	0.15 L mmol ⁻¹ cm ⁻¹	3.32 L mmol ⁻¹ cm ⁻¹	0.24 ^α	0.01
λ_{irr}	$\epsilon_{c\text{-PAP}}(\lambda_{\text{irr}})$	$\epsilon_{HS-c}(\lambda_{\text{irr}})$	$\Phi_{c-t}(n\pi^*)$	$\Phi_{HS-LS,\text{theo}}(\lambda_{\text{irr}})$
435 nm	1.1 L mmol ⁻¹ cm ⁻¹	40.93 L mmol ⁻¹ cm ⁻¹	0.55 ^α	0.02

^αValues of the isomerization quantum yields of azobenzene in hexane upon excitation to the $S_1(n\pi^*)$ state.^[53]

Such small quantum yields can be anticipated for this system, considering the fact that the absorption of the PAP moiety is obscured by the porphyrin macrocycle in most of the spectral region. Thus, the elsewhere proposed PAP isomerization via energy transfer from the excited porphyrin Q state^[11,13,17] can be discarded, as it is a redundant assumption for the explanation of the spin switch.

4.4.2 Time-resolved electronic absorption spectroscopy

The photodynamics of azoNiPor derived from TEAS are summarized in the relaxation scheme in Figure 8 and will be discussed separately for *trans*-azoNiPor(LS) and *cis*-azoNiPor(HS). The observed structures and states in part (a) and (b) of Figure 8 are labeled in accordance with the previously extracted EADS.

Photodynamics of *trans*-azoNiPor(LS). The *trans*-azoNiPor(LS) isomer shows virtually identical photodynamics to the nickel porphyrin NiTPPF₂₀ (cf. Fig. S4(b)), which is due to the fact that the porphyrin absorption exceeds that of the PAP at almost all wavelengths. Thus, its photodynamics can be discussed in the context of previous studies on four-coordinate LS nickel porphyrins. Initial photoexcitation of the porphyrin B or Q state, respectively, generates the exact same first transient spectrum in all measurements (cf. Fig. S5). This means that the deactivation of higher lying excited states is faster than the time-resolution of our experiment and therefore generates the initially observed state with high efficiency. Indeed, it was shown that internal conversion between the B and Q states in porphyrins is mediated by a so-called N state in <100 fs.^[21] The origin of the first observable diffuse transient is interpreted differently. Some studies state that it represents a vibrationally highly excited nickel state with ($d_{z^2}, d_{x^2-y^2}$) electron configuration with the initially excited porphyrin already returned to its ground state.^[30] This conclusion is based on the absence of the characteristic stimulated emission at $\lambda_{\text{probe}} > 600$ nm from the macrocycles $^1\pi\pi^*$ states, reported elsewhere.^[22,26] Subsequent processes are consequently assigned to vibrational cooling (VC) and intermolecular vibrational relaxation (IVR) with time components of $\tau_{\text{VC}} \approx 1$ ps and $\tau_{\text{IVR}} \approx 15$ ps, respectively. These are accompanied by spectral narrowing and strong blue shifts of the ESA signals. However, in line with most studies,^[18,22–25,29,54] we clearly assign the spectrum after 100 fs to the lowest excited singlet $^1\pi\pi^*$ state of the porphyrin macrocycle ($^1\text{Por}^*$), (see structure **A** in Figure 8(a)). The shape of the transient shows great similarity to the one of the free porphine base H₂TPPF₂₀ observed after photoexcitation (cf. Fig. S4(a)). Further, the pronounced non-zero isosbestic points indicate the excitation-energy transfer from the porphyrin excited state to a nickel-centered excited state. The derivative-shaped spectra after ~ 5 ps are characteristic for the excited nickel center with ($d_{z^2}, d_{x^2-y^2}$) electron configuration, which can either be a singlet or triplet ($^1,^3\text{Ni}(d,d)^*$) and the porphyrin back in the ground state, which explains the strong GSR observed in this time window. Consequently, the time constant $\tau_1 = 0.7$ ps is assigned to the energy-transfer process that causes the SCO in the Ni(II) ion. This state is formed with some excess energy (structure **B**) and thus undergoes vibrational cooling with the extracted $\tau_3 = 9$ ps. Since the Ni(II) ion is bigger with the $d_{x^2-y^2}$ orbital being singly occupied, the Ni–N bond length is increased and the porphyrin is promoted to the more planar structure **C**. In this state the metal center is highly attractive towards axial coordination of the pyridine ligand. However, since the azo unit is unable to coordinate in the *trans*-configuration,^[17] the data show a

complete GSR of the LS state with a time constant of $\tau_4 = 360$ ps and no observable formation of *cis*-azoNiPor(HS). This deexcitation path is summarized in part (a) of Figure 8.

Thus, the sustainable formation of the HS species inevitably requires the formation of *cis*-PAP which subsequently triggers the SCO process by its coordination to the nickel center, in accordance with the LD-CISSS concept. The straightforward way to obtain the *cis*-PAP isomer is by direct excitation of the PAP moiety, which is illustrated in part (c) of Figure 8. As the isosbestic points observed at any time in the femtosecond transient absorption spectra, indicate exceptional consecutive kinetics, a bifocation of the wave packet can be excluded. Therefore, the elsewhere proposed isomerization pathway via energy transfer from the excited porphyrin Q state to the azo ligand^[11,13,17] is not considered any further.

The photoisomerization of PAP is possible upon direct excitation of either the $S_1(n\pi^*)$ or the $S_2(\pi\pi^*)$ state. Though isomerization of azo compounds through the S_1 state has comparably high quantum yields,^[53] the absorption of this state is weak ($\epsilon_{\text{PAP},n\pi^*,\text{max}}(440\text{ nm}) = 400\text{ L mol}^{-1}\text{cm}^{-1}$) and by far exceeded by the porphyrin absorption ($\epsilon_{\text{trans-azoNiPor(LS)}}(440\text{ nm}) = 12300\text{ L mol}^{-1}\text{cm}^{-1}$). Therefore, the observation of any signature of the small fraction of excited PAP in the femtosecond TEAS experiments is prohibited, since the magnitude of the absorbed photons will lead to the excitation of the porphyrin. Direct excitation of the PAP ligand is facilitated aiming at the S_2 state ($\lambda_{\text{pump}} < 350\text{ nm}$) where the ratio of the molar absorption coefficients is more in favor of the PAP. However, it has to be taken into account that the quantum yield for the isomerization reaction of azo compounds is significantly decreased when excited to the S_2 state,^[53,55–57] resulting in a still small overall yield of *cis*-PAP. As demonstrated, the femtosecond TEAS measurement carried out at $\lambda_{\text{pump}} = 325\text{ nm}$ shows no formation of *cis*-azoNiPor(HS) on the timescale of $\Delta t < 2\text{ ns}$. However, small amounts of the stable *cis*-azoNiPor(HS) product can be observed on the timescale of the nanosecond transient absorption experiment.

These results were interpreted as follows: At $\lambda_{\text{pump}} = 325\text{ nm}$ both the porphyrin as well as the PAP chromophore in azoNiPor are excited. As the contributions of PAP to the excited-state dynamics are superimposed by the more intense and long-lived contributions of the nickel porphyrin, the femtosecond TEAS experiment is blind to the ultrafast isomerization process that leads to the formation of *cis*-PAP. Furthermore, the coordination of the produced *cis*-ligand requires its orientation towards the nickel center. At first, however, the *cis*-PAP will likely point away from the porphyrin illustrated by structure **2** in Figure 8(c). This more favorable configuration was previously demonstrated in STM experiments.^[12,58] The rotation of the azo arm and subsequent coordination-induced SCO consequently occurs on timescales beyond the 2 ns covered by the femtosecond TEAS experiment. Indeed, nanosecond TEAS measurements confirmed the presence of the sustainable spin switching product after no more

than 58 ns.

Photodynamics of *cis*-azoNiPor(HS). In the photodynamics of *cis*-azoNiPor(HS), the first observed transient spectrum has a similar shape compared to the one observed for the diamagnetic species and independent of the excitation wavelength (cf. Fig. S6), suggesting that the lowest excited $^1\pi\pi^*$ state ($^1\text{Por}^*$, structure **A'** in Figure 8(b)) of the macrocycle is formed within the time resolution of the experiment. However, the results of SVD show that this state decays biexponentially with $\tau_1 = 0.7$ ps and $\tau_2 = 5$ ps to the second derivative-shaped spectrum of the excited nickel state, which points to an intermediate state being involved in the energy transfer process. From studies on six-coordinate paramagnetic nickel porphyrins, the presence of a triplet porphyrin $^3\pi\pi^*$ state ($^3\text{Por}^*$, **B'**) is reported.^[38] This state is also formed in the free porphine base,^[59,60] but on a much longer timescale due to the spin-forbidden transition according to the El-Sayed rules. This restriction is presumably lifted considering the spin-orbit coupling introduced by the triplet Ni(II) ion ($^3\text{Ni}(\text{d},\text{d})$). The characteristic absorption of such a triplet state at supposedly $\lambda_{\text{probe}} > 700$ nm lies outside of the detection range of our experiment and thus cannot be excluded. The successor state forms within ~ 12 ps and shows a characteristic absorption blue-shifted to the Soret band bleach. The maximum of the absorption band coincides with the ground state Soret band absorption of the diamagnetic species. Consequently, it is assigned to the formation of an excited state in which the nickel possesses $(\text{d}_{z^2})^2$ configuration, which is likely to be formed with some excess vibrational energy (**C'**). Following vibrational relaxation with $\tau_3 = 21$ ps the relaxed $^1\text{Ni}(\text{d}^2)$ (structure **D'**) is present. This state was shown to be repulsive towards axial ligands and will eject coordinated bases like pyridine.^[30–33,35,37] A time constant $\tau_4 = 600$ ps for the GSR of the HS species was extracted. This process necessarily involves recoordination of the PAP, which is only possible in the *cis* configuration.

Again, as displayed in Figure 8(c), the only path to the formation of the *trans*-azoNiPor(LS) species is via direct excitation of the PAP chromophore. Since the ultrafast *cis*-to-*trans* isomerization of the azo arm directly triggers the decoordination-induced SCO, the sustainable photoproduct **2'** is present virtually immediately. This is indicated by the incomplete recovery of the GSB signals and its stability was further confirmed by the nanosecond TEAS results. Furthermore, the extrapolated time traces of the GSB signal (cf. Fig. S7) indicate that the formation of the LS product is suppressed at increasing excitation wavelengths.

These results offer a plausible explanation why the PSSs at wavelength $\lambda_{\text{irr}} > 470$ nm favor the *cis*-azoNiPor(HS) compound: In *trans*-azoNiPor(LS) the photochromism of the PAP moiety is relatively unaffected by the nickel porphyrin, as it was designed in a way that minimizes conjugation between the two chromophores.^[61] In *cis*-azoNiPor(HS), however, the direct coordination of the *cis*-PAP ligand to the nickel introduces an additional restriction to the isomeriza-

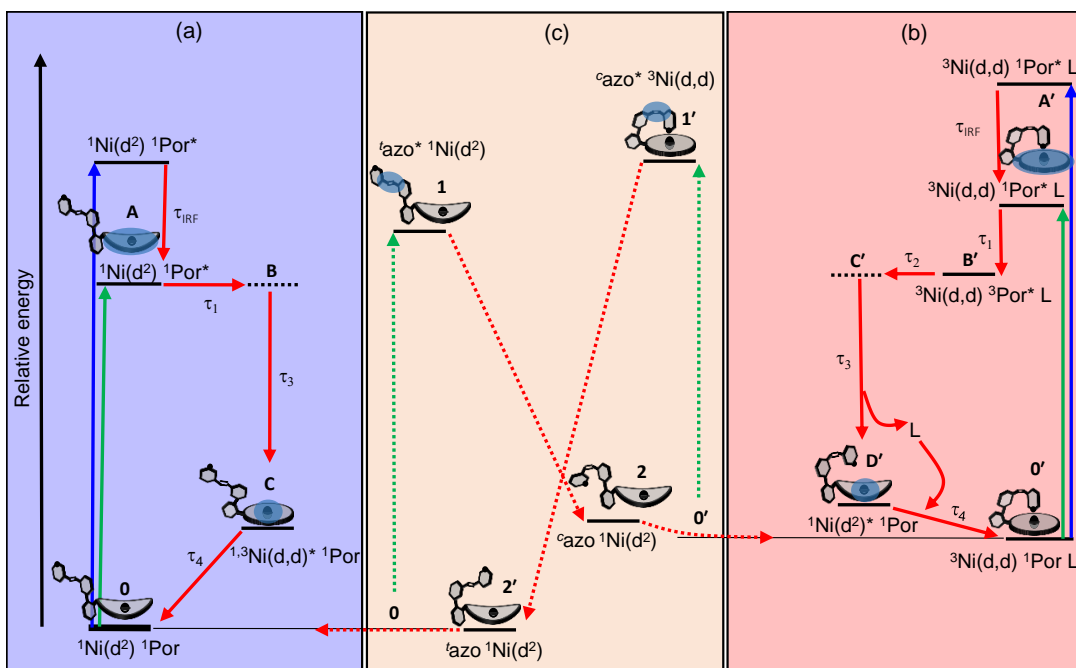


Figure 8: Relaxation scheme summarizing the photodynamics of azoNiPor following photoexcitation of either the porphyrin in the low-spin (a) and high-spin (b) complex or the phenylazopyridine moiety (c). The pictograms and labels display the key structural features identified in the photodynamics of the azoNiPor molecule. Blue spheres together with superscripts * indicate the location of the excitation energy in the respective excited state. Superscripts 1 and 3 denote the spin multiplicity of the respective nickel (Ni) and porphyrin (Por) states. The configuration of the nickel d-electrons and the presence of a coordinated axial ligand (L) is further given. Superscripts *t* and *c* indicate the *trans* and *cis* configuration of the azopyridine (azo). The LD-CISS mechanism in part (c) is displayed with dashed arrows since direct excitation of the azo ligand only has a minor contribution to the overall photodynamics.

tion from *cis*- to *trans*-PAP by the additional coordination energy that has to be overcome. This will likely impede the *cis*-to-*trans* isomerization at lower excitation energies (longer excitation wavelengths) compared to the free PAP and, consequently, shift the photostationary equilibrium at these wavelengths to the *cis*-azoNiPor(HS) form. Furthermore, direct coordination of azopyridines to transition-metal centers can effectively enable energy transfer processes to ligand-field states, which can diminish the extent of photoisomerization.^[62] Thus, in order to explain the deviations of the *trans*/*cis* PSS ratios between free PAP and azoNiPor, it is necessary to consider the influence of the nickel porphyrin on the *cis*-to-*trans* isomerization, rather than on the *trans*-to-*cis* isomerization.

4.5 Conclusion

In summary, the presented results suggest that one has to carefully differentiate between two SCO mechanisms in the azoNiPor molecule: the light-induced SCO on the one hand and the coordination-induced SCO on the other hand. The results of femtosecond TEAS show that excitation of either the B or the Q state of the porphyrin in *trans*-azoNiPor(LS) and *cis*-azoNiPor(HS) generates the same excited state within the time resolution of the experiment. From this state, which is associated with the porphyrin macrocycle, effective energy transfer to the SCO state of the nickel center occurs within a few picoseconds. However, the product of this light-induced SCO is metastable and cannot be trapped, since the configuration of the PAP ligand is preserved and no (de)coordination takes place. Furthermore, the observed consecutive kinetics do not indicate any energy transfer from the excited porphyrin Q state to the PAP moiety that could lead to its isomerization.

Consequently, direct excitation of the PAP chromophore is demanded to complete the spin switch. Indeed, the TEAS measurements carried out at pump wavelengths that excite a larger fraction of the PAP chromophore allowed to observe the formation of the spin-switching product. In the case of *cis*-azoNiPor(HS) the required decoordination occurs practically immediately upon *cis*-to-*trans*-isomerization of the PAP and can be observed by femtosecond TEAS. However, the threshold energy required for the isomerization of the coordinated *cis*-ligand in azoNiPor appears to be somewhat higher compared to the free PAP chromophore. In the case of *trans*-azoNiPor(LS), the coordination process following ultrafast *trans*-to-*cis*-isomerization requires orientation of the azo ligand towards the nickel center, which occurs on longer timescales and was identified by nanosecond TEAS.

Consequently, the presented results suggest that the SCO mechanism of azoNiPor follows the initially proposed LD-CISSS concept and, further, gives rise to the following implications for the improvement of future spin switches: The insight that isomerization of the PAP moiety is caused by direct excitation rather than by energy transfer from the porphyrin Q state should be considered in the recent efforts to achieve switching of the system *in vivo* for medical applications which aim towards shifting the porphyrin Q bands to the biooptical window (650–900 nm).^[61] The design of azoNiPor derivatives with photoswitchable ligands that can be addressed in this spectral region might be more promising. In this course, sensitized azobenzenes that undergo two-NIR-photon triggered isomerization represent viable candidates.^[63] Furthermore, we demonstrated that for the system in its current design the LD-CISSS process takes place with small quantum efficiencies. For applications in, *e.g.*, optical data storage, this drawback needs to be overcome. Since we determined that the poor quantum yields most likely arise from the enormous absorption coefficients of the porphyrin compared to the PAP chromophore, a more selective addressing of the chro-

mophore has to be established. The choice of a less absorbing basic structure than the porphyrin for the complexation of the nickel central ion could allow for the quantum yields of the spin switch to at least approximate those of the free azopyridine. Additionally, employing photoswitches with higher quantum yields such as bridged-azobenzenes^[64,65] could lead to a significant increase in quantum efficiency. Another probably more promising approach, however, would be to exploit the efficient light-induced SCO and high absorption coefficients of nickel porphyrins by using the associated structural change for intramolecular feedback, stabilizing one spin state or the other. This idea is approached by the recently designed “hair clip” molecules, where the axial pyridine ligand is strapped over the nickel center by covalent connections to two opposite *meso*-positions of the porphyrin.^[66] Unfortunately, the energy barrier separating the two species in the ground state is not sufficient in the current designs.^[66] Nevertheless, the high conversion efficiencies reached for azoNiPor, despite its low quantum yield, emphasize the potential of the LD-CISSS concept. Furthermore, the measurements on *cis*-azoNiPor(HS) represent one of the first femtosecond time-resolved absorption studies of an isolated five-coordinate nickel porphyrin and could thus contribute to the better understanding of this class of bio molecules.

Conflicts of interest

There are no conflicts to declare.

Acknowledgements

This work has been supported by the Deutsche Forschungsgemeinschaft within the Sonderforschungsbereich 677 “Function by Switching”.

References

- [1] Bajema, L.; Gouterman, M.; Meyer, B. *J. Mol. Spectrosc.* **1961**, *27*, 225–235.
- [2] Song, N. W.; Cho, H. S.; Yoon, M.-C.; Jeoung, S. C.; Yoshida, N.; Osuka, A.; Kim, D. *Bull. Chem. Soc. Jpn.* **2002**, *75*, 1023–1029.
- [3] Holten, D.; Bocian, D. F.; Lindsey, J. S. *Acc. Chem. Res.* **2002**, *35*, 57–69.
- [4] Lee, T.-H.; Gonzalez, J. I.; Zheng, J.; Dickson, R. M. *Acc. Chem. Res.* **2005**, *38*, 534–41.
- [5] Kullmann, M.; Hipke, A.; Nuernberger, P.; Bruhn, T.; Götz, D. C. G.; Sekita, M.; Guldi, D. M.; Bringmann, G.; Brixner, T. *Phys. Chem. Chem. Phys.* **2012**, *14*, 8038–50.
- [6] Ziegler, C. J. *Handbook of Porphyrin Science*; World Scientific Publishing Co. Pt. Ltd., 2012; Vol. 20; pp 113–238.
- [7] Szacilowski, K.; Macyk, W.; Drzewiecka-Matuszek, A.; Brindell, M.; Stochel, G. *Chem. Rev.* **2005**, *105*, 2647–2694.
- [8] Burdzinski, G.; Kubicki, J.; Maciejewski, A. *ChemInform*; Wiley Online Library, 2006; Vol. 37.
- [9] Nakano, A.; Osuka, A.; Yamazaki, T.; Nishimura, Y.; Akimoto, S.; Yamazaki, I.; Itaya, A.; Murakami, M.; Miyasaka, H. *Chemistry* **2001**, *7*, 3134–51.
- [10] Kumble, R.; Palese, S.; Lin, V. S. Y.; Therien, M. J.; Hochstrasser, R. M. *J. Am. Chem. Soc.* **1998**, *120*, 11489–11498.
- [11] Venkataramani, S.; Jana, U.; Dommaschk, M.; Sönnichsen, F. D.; Tuczek, F.; Herges, R. *Science* **2011**, *331*, 445–449.
- [12] Dommaschk, M.; Schütt, C.; Venkataramani, S.; Jana, U.; Näther, C.; Sönnichsen, F. D.; Herges, R. *Dalt. Trans.* **2014**, *43*, 17395–17405.
- [13] Dommaschk, M.; Peters, M.; Gutzeit, F.; Schütt, C.; Näther, C.; Sönnichsen, F. D.; Tiwari, S.; Riedel, C.; Boretius, S.; Herges, R. *J. Am. Chem. Soc.* **2015**, *137*, 7552–7555.

- [14] Megow, S.; Bahrenburg, J.; Dittner, M.; Kohly, B.; Gripp, J.; Domaschk, M.; Schütt, C.; Herges, R.; Temps, F. *EPJ Web Conf.* **2019**, *05019*, 9–11.
- [15] Bandara, H. M.; Burdette, S. C. *Chem. Soc. Rev.* **2012**, *41*, 1809–1825.
- [16] Tan, E. M.; Amirjalayer, S.; Smolarek, S.; Vdovin, A.; Zerbetto, F.; Buma, W. J. *Nat. Commun.* **2015**, *6*, 1–7.
- [17] Alcover-Fortuny, G.; de Graaf, C.; Caballol, R. *Phys. Chem. Chem. Phys.* **2015**, *17*, 217–225.
- [18] Ryland, E. S.; Zhang, K.; Vura-Weis, J. *J. Phys. Chem. A* **2019**, *123*, 54214–5222.
- [19] Gouterman, M.; Wagnière, G. H.; Snyder, L. C. *J. Mol. Spectrosc.* **1963**, *11*, 108–127.
- [20] Bräm, O.; Cannizzo, A.; Chergui, M. *J. Phys. Chem. A* **2019**, *123*, 1461–1468.
- [21] Falahati, K.; Hamerla, C.; Huix-Rotllant, M.; Burghardt, I. *Phys. Chem. Chem. Phys.* **2018**, *20*, 12483–12492.
- [22] Zamyatin, A. V.; Soldatova, A. V.; Rodgers, M. A. *Inorg. Chim. Acta* **2007**, *360*, 857–868.
- [23] Zamyatin, A. V.; Gusev, A. V.; Rodgers, M. A. J. *J. Am. Chem. Soc.* **2004**, *126*, 15934–15935.
- [24] Drain, C. M.; Kirmaier, C.; Medforth, C. J.; Nurco, D. J.; Smith, K. M.; Holten, D. *J. Phys. Chem.* **1996**, *100*, 11984–11993.
- [25] Drain, C. M.; Gentemann, S.; Roberts, J. A.; Nelson, N. Y.; Medforth, C. J.; Jia, S.; Simpson, M. C.; Smith, K. M.; Fajer, J.; Shelnutt, J. A.; Holten, D. *J. Am. Chem. Soc.* **1998**, *120*, 3781–3791.
- [26] Zhang, X.; Wasinger, E. C.; Muresan, A. Z.; Attenkofer, K.; Jennings, G.; Lindsey, J. S.; Chen, L. X. *J. Phys. Chem. A* **2007**, *111*, 11736–11742.
- [27] Rodriguez, J.; Kirmaier, C.; Holten, D. *J. Am. Chem. Soc.* **1989**, *111*, 6500–6506.
- [28] Rodriguez, J.; Holten, D. *J. Chem. Phys.* **1989**, *91*, 3525.
- [29] Chen, L. X.; Zhang, X.; Wasinger, E. C.; Attenkofer, K.; Jennings, G.; Muresan, A. Z.; Lindsey, J. S. *J. Am. Chem. Soc.* **2007**, *129*, 9616–9618.

- [30] Eom, H. S.; Jeoung, S. C.; Kim, D.; Ha, J. H.; Kim, Y. R. *J. Phys. Chem. A* **1997**, *101*, 3661–3669.
- [31] Retsek, J. L.; Drain, C. M.; Kirmaier, C.; Nurco, D. J.; Medforth, C. J.; Smith, K. M.; Sazanovich, I. V.; Chirvony, V. S.; Fajer, J.; Holten, D. *J. Am. Chem. Soc.* **2003**, *125*, 9787–800.
- [32] Kim, D.; Kirmaier, C.; Holten, D. *Chem. Phys.* **1983**, *75*, 305–322.
- [33] Kim, D.; Holten, D. *Chem. Phys. Lett.* **1983**, *98*, 584–589.
- [34] Chen, L. X.; Zhang, X.; Wasinger, E. C.; Lockard, J. V.; Stickrath, A. B.; Mara, M. W.; Attenkofer, K.; Jennings, G.; Smolentsev, G.; Soldatov, A. *Chem. Sci.* **2010**, *1*, 642.
- [35] Chen, L. X.; Zhang, X.; Lockard, J. V.; Stickrath, A. B.; Attenkofer, K.; Jennings, G.; Liu, D. J. *Acta Crystallogr. Sect. A Found. Crystallogr.* **2010**, *66*, 240–251.
- [36] Uesugi, Y.; Mizutani, Y.; Kitagawa, T. *J. Phys. Chem. A* **1998**, *102*, 5809–5815.
- [37] Chen, L. X.; Zhang, X.; Jäger, W. J. H.; Jennings, G.; Gosztola, D. J.; Munkholm, A.; Hessler, J. P. *Science* **2001**, *292*, 262–264.
- [38] Rodriguez, J.; Holten, D. *J. Chem. Phys.* **1990**, *92*, 5944.
- [39] Megerle, U.; Lechner, R.; König, B.; Riedle, E. *Photochem. Photobiol. Sci.* **2010**, *9*, 1400–1406.
- [40] Hatchard, C. G.; Parker, C. *Proceedings of the Royal Society of London. Series A. Mathematical and Physical Sciences* **1956**, *235*, 518–536.
- [41] Rubin, M. B.; Braslavsky, S. E. *Photochem. Photobiol. Sci.* **2010**, *9*, 670–674.
- [42] Maafi, M.; Brown, R. G. *Photochem. Photobiol. Sci.* **2008**, *7*, 1360–1372.
- [43] Corrie, J. E.; Kaplan, J. H.; Forbush, B.; Ogden, D. C.; Trentham, D. R. *Photochem. Photobiol. Sci.* **2016**, *15*, 604–608.
- [44] Gauglitz, G. *GIT Fachzeitschrift für das Laboratorium* **1982**, *26*, 597–611.
- [45] Wolfram Research, I. Mathematica. 2016.
- [46] Riedle, E.; Beutter, M.; Lochbrunner, S.; Piel, J.; Schenkl, S.; Spörlein, S.; Zinth, W. *Appl. Phys. B* **2000**, *71*, 457–465.

- [47] Röttger, K.; Wang, S.; Renth, F.; Bahrenburg, J.; Temps, F. *Appl. Phys. B Lasers Opt.* **2015**, *118*, 185–193.
- [48] Renth, F.; Siewertsen, R.; Strübe, F.; Mattay, J.; Temps, F. *Phys. Chem. Chem. Phys.* **2014**, *16*, 19556–19563.
- [49] Renth, F.; Foca, M.; Petter, A.; Temps, F. *Chem. Phys. Lett.* **2006**, *428*, 62–67.
- [50] Van Stokkum, I. H.; Larsen, D. S.; Van Grondelle, R. *Biochim. Biophys. Acta - Bioenerg.* **2004**, *1657*, 82–104.
- [51] Cattell, R. B. *Multivariate Behav. Res.* **2010**, *1*, 245–276.
- [52] Wang, S.; Bohnsack, M.; Megow, S.; Renth, F.; Temps, F. *Phys. Chem. Chem. Phys.* **2019**, *21*, 2080–2092.
- [53] Quick, M.; Dobryakov, A. L.; Gerecke, M.; Richter, C.; Berndt, F.; Ioffe, I. N.; Granovsky, A. A.; Mahrwald, R.; Ernsting, N. P.; Kovalenko, S. A. *J. Phys. Chem. B* **2014**, *118*, 8756–8771.
- [54] Musewald, C.; Hartwich, G.; Lossau, H.; Gilch, P.; Pöllinger-Dammer, F.; Scheer, H.; Michel-Beyerle, M. E. *J. Phys. Chem. B* **1999**, *103*, 7055–7060.
- [55] Rau, H.; Lüddecke, E. *J. Am. Chem. Soc.* **1982**, *104*, 1616–1620.
- [56] Fujino, T.; Arzhantsev, S. Y.; Tahara, T. *Bull. Chem. Soc. Jpn.* **2002**, *75*, 1031–1040.
- [57] Nenov, A.; Borrego-Varillas, R.; Oriana, A.; Ganzer, L.; Segatta, F.; Conti, I.; Segarra-Martí, J.; Omachi, J.; Dapor, M.; Taioli, S.; Manzoni, C.; Mukamel, S.; Cerullo, G.; Garavelli, M. *J. Phys. Chem. Lett.* **2018**, *9*, 1534–1541.
- [58] Matino, F.; Schull, G.; Jana, U.; Ko, F.; Herges, R. **2010**, *Chem. Commun.*, 6780–6782.
- [59] Retsek, J. L.; Gentemann, S.; Medforth, C. J.; Smith, K. M.; Chirvony, V. S.; Fajer, J.; Holten, D. *J. Phys. Chem. B* **2000**, *104*, 6690–6693.
- [60] Baskin, J. S.; Yu, H. Z.; Zewail, A. H. *J. Phys. Chem. A* **2002**, *106*, 9837–9844.
- [61] Dommaschk, M.; Thoms, V.; Schütt, C.; Näther, C.; Puttreddy, R.; Rissanen, K.; Herges, R. *Inorg. Chem.* **2015**, *54*, 9390–9392.
- [62] Megow, S.; Fitschen, H. L.; Tuczec, F.; Temps, F. *J. Phys. Chem. Lett.* **2019**, *10*, 6048–6054.

-
- [63] Moreno, J.; Gerecke, M.; Grubert, L.; Kovalenko, S. A.; Hecht, S. *Angew. Chem. Int. Ed.* **2016**, *55*, 1544–1547.
- [64] Siewertsen, R.; Neumann, H.; Buchheim-Stehn, B.; Herges, R.; Näther, C.; Renth, F.; Temps, F. *J. Am. Chem. Soc.* **2009**, *131*, 15594–15595.
- [65] Siewertsen, R.; Schönborn, J. B.; Hartke, B.; Renth, F.; Temps, F. *Phys. Chem. Chem. Phys.* **2011**, *13*, 1054–1063.
- [66] Gutzeit, F.; Dommaschk, M.; Levin, N.; Buchholz, A.; Schaub, E.; Plass, W.; Näther, C.; Herges, R. *Inorg. Chem.* **2019**, *58*, 12542–12546.

Supporting Information

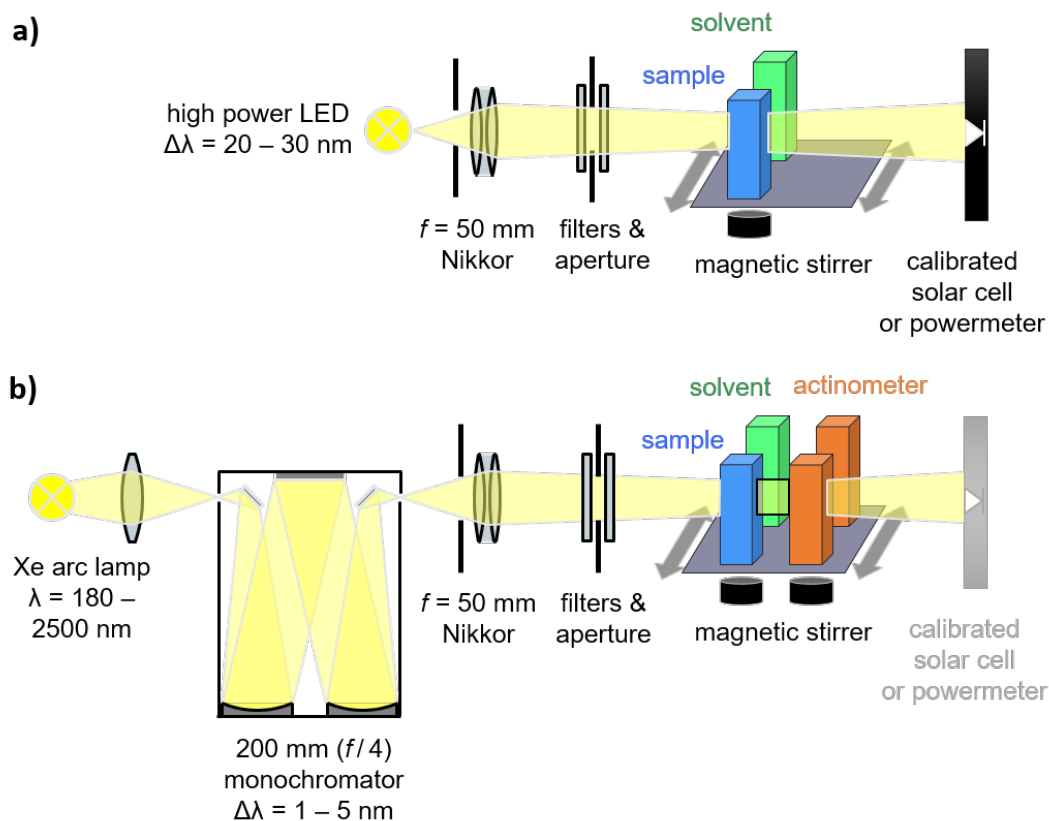


Figure S1: Schematic depiction of the experimental setups for the determination of photoreaction quantum yields using (a) high-power LEDs for irradiation and a calibrated solar cell or powermeter for detection and (b) a xenon arc lamp in combination with a monochromator for narrow bandwidth irradiation and the chemical ferrioxalate actinometer for detection.

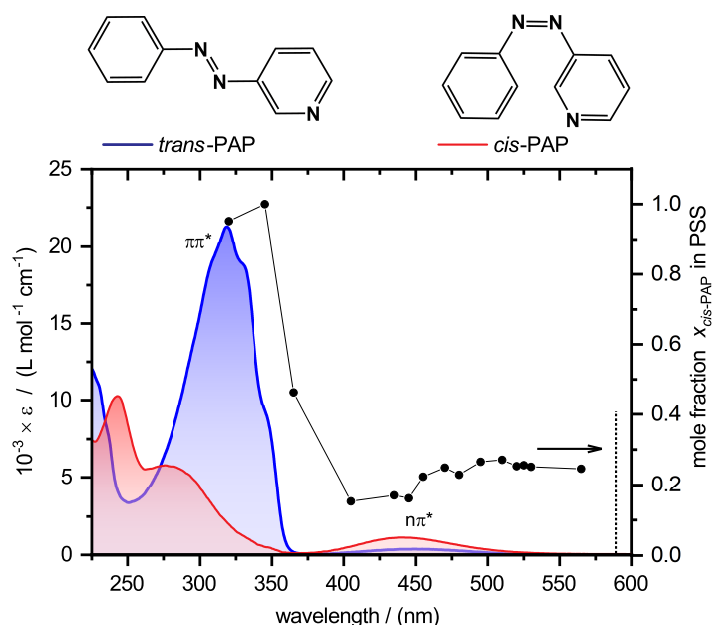


Figure S2: Chemical structures and static UV-vis absorption spectra recorded in cyclohexane of *trans*- and *cis*-3-(phenylazo)pyridine (PAP). The black dots display the fraction of *cis*-PAP in the photostationary state (PSS) that is present upon irradiation with an LED of the respective wavelength. For LED wavelength ≥ 590 nm (vertical dashed line) no photostationary equilibrium could be reached. The UV-vis spectra of *trans*- and *cis*-PAP can be interpreted analogously to the more extensively studied azobenzene.^[1]

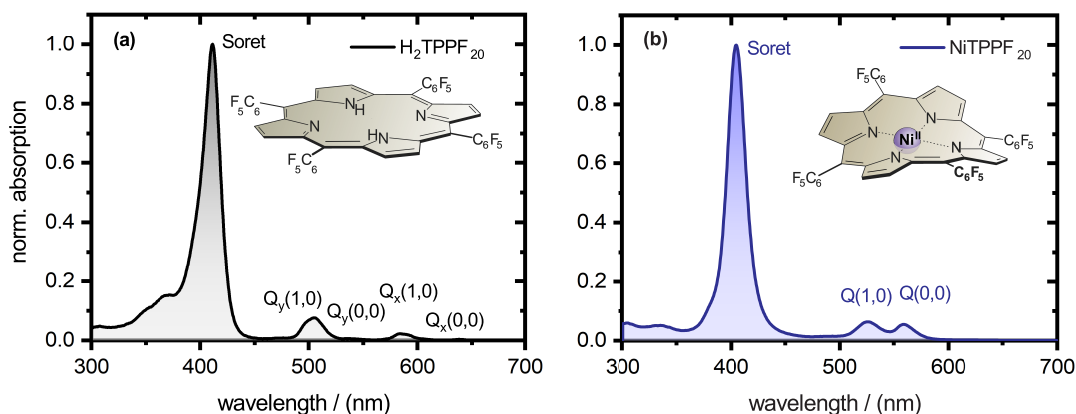


Figure S3: Chemical structures and static UV-vis spectra of the free porphine base $\text{H}_2\text{TPPF}_{20}$ (a) and the nickel porphyrin NiTPPF_{20} (b) recorded in cyclohexane. The D_{4h} symmetry of NiTPPF_{20} leads to the occurrence of two Q bands ($Q(1,0)$ and $Q(0,0)$). In $\text{H}_2\text{TPPF}_{20}$ the two opposite pyrrole protons lower the symmetry to D_{2h} as they lift the degeneracy of the molecular x- and y-axis. This leads to a further splitting of the Q bands into a x- and a y-polarized transition (Q_x and Q_y).^[2–5]

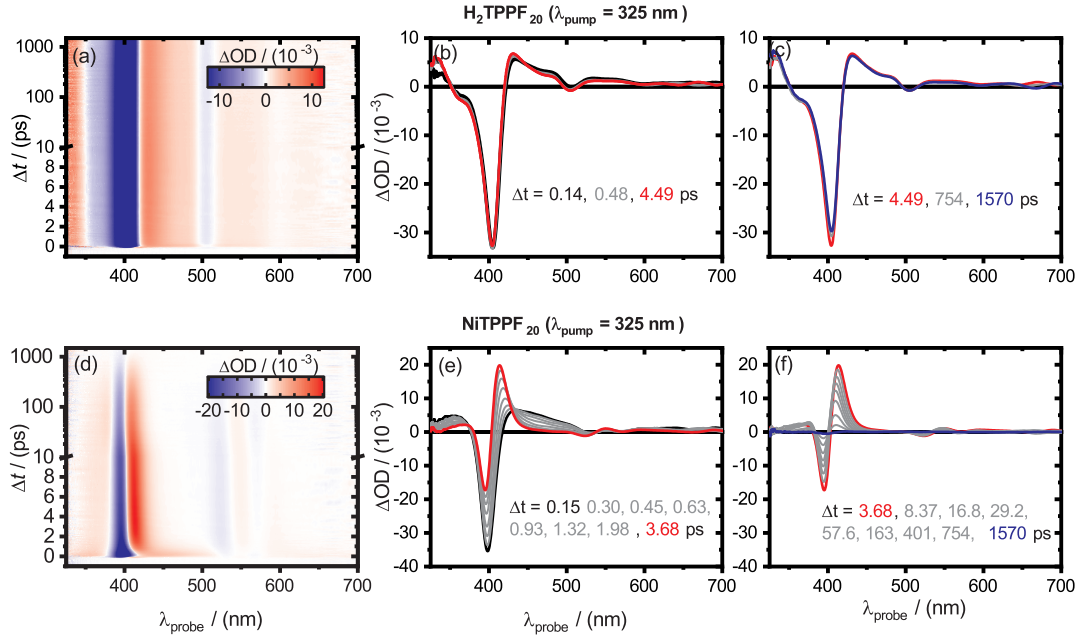


Figure S4: Two-dimensional time-resolved electronic absorption maps and spectra of $\text{H}_2\text{TPPF}_{20}$ (a–c) and NiTPPF_{20} (d–f) in cyclohexane obtained after photoexcitation at $\lambda_{\text{pump}} = 325 \text{ nm}$. $\text{H}_2\text{TPPF}_{20}$ shows virtually no spectral evolution within the recorded time window, which is attributed to a slow deexcitation pathway involving spin-forbidden transitions between porphyrin singlet $^1\pi\pi^*$ and triplet $^3\pi\pi^*$ states, that was identified in other porphines.^[6–13] The vacant d-orbitals of the incorporated Ni(II) ion in NiTPPF_{20} , however, enable rapid deexcitation of the porphyrin macrocycle via energy transfer to ligand-field states of the nickel ion, leading to significant spectral evolution and complete recovery of the ground state, observed in previous studies on four-coordinate nickel porphyrins.^[14–20]

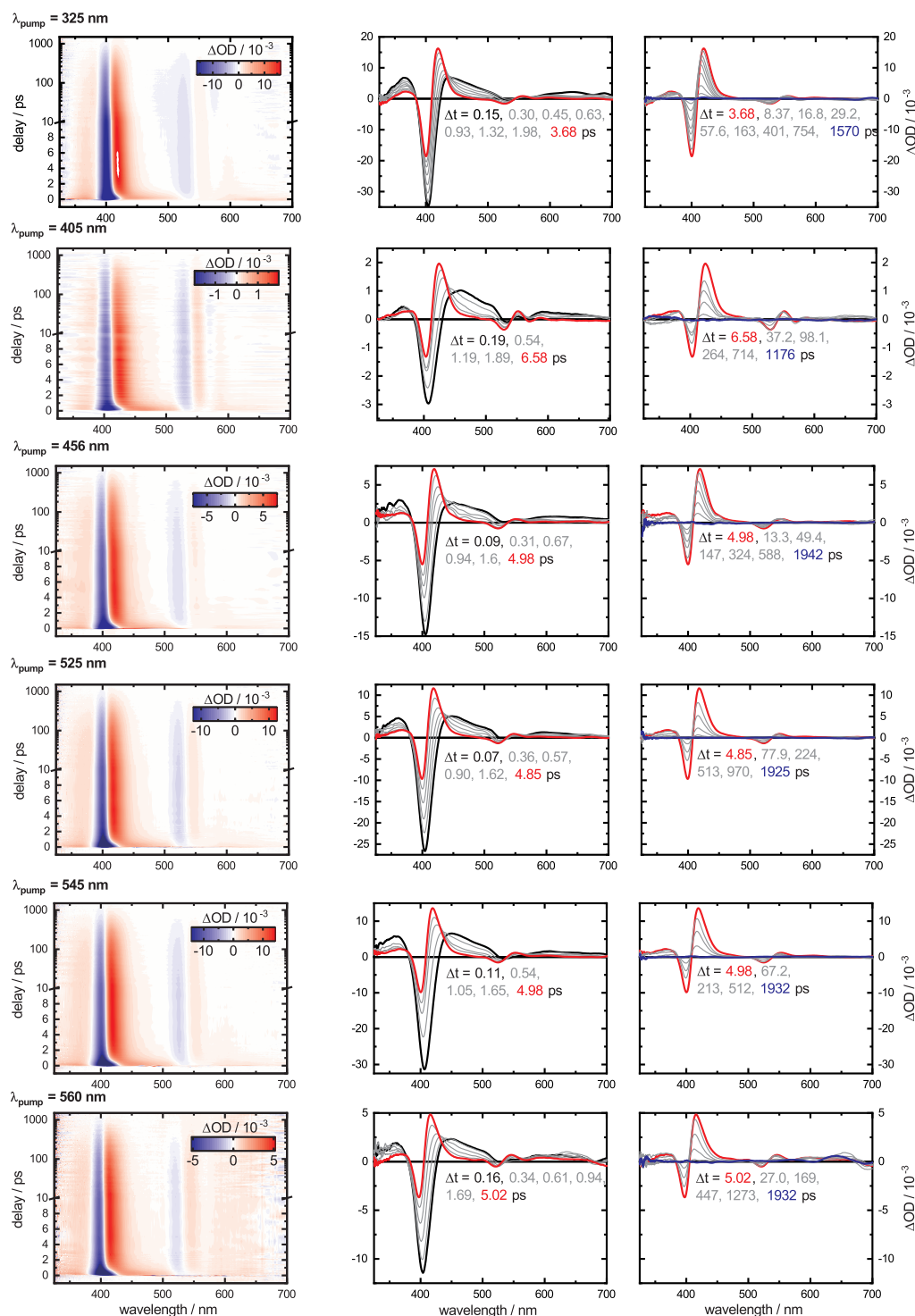


Figure S5: Two-dimensional time-resolved electronic absorption maps and spectra of *trans*-azoniPnPor(LS) obtained after photoexcitation at the respective wavelength λ_{pump} . All data sets exhibit virtually identical photodynamics independent of the excitation wavelength and full recovery of the ground state within the recorded time window.

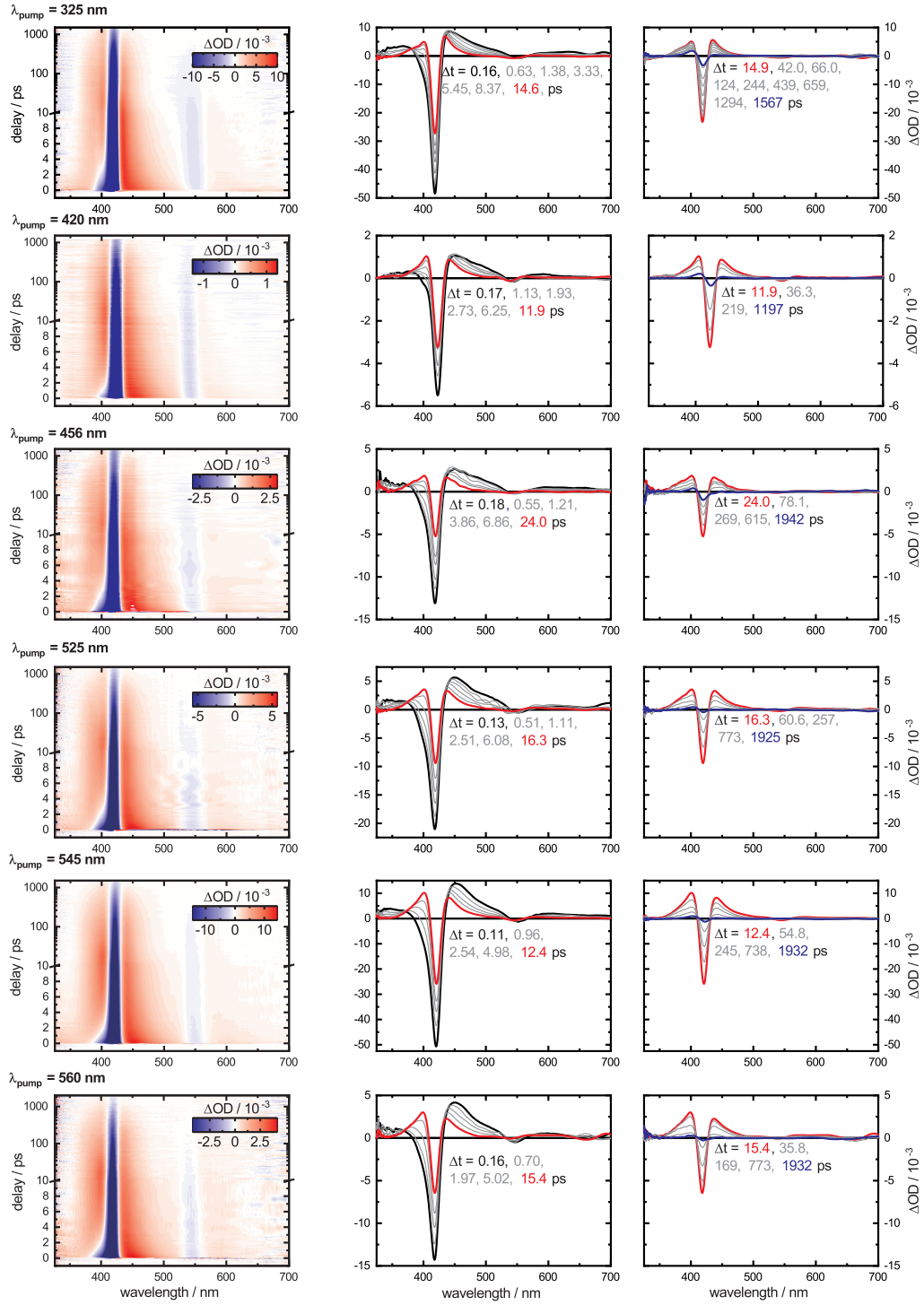


Figure S6: Two-dimensional time-resolved electronic absorption maps and spectra of *cis*-azoNiPor(HS) obtained after photoexcitation at the respective wavelength λ_{pump} . All data sets exhibit virtually identical photodynamics independent of the excitation wavelength. In each case the latest recorded transient spectrum shows some remaining absorption, indicating an incomplete recovery of the ground state within the recorded time window.

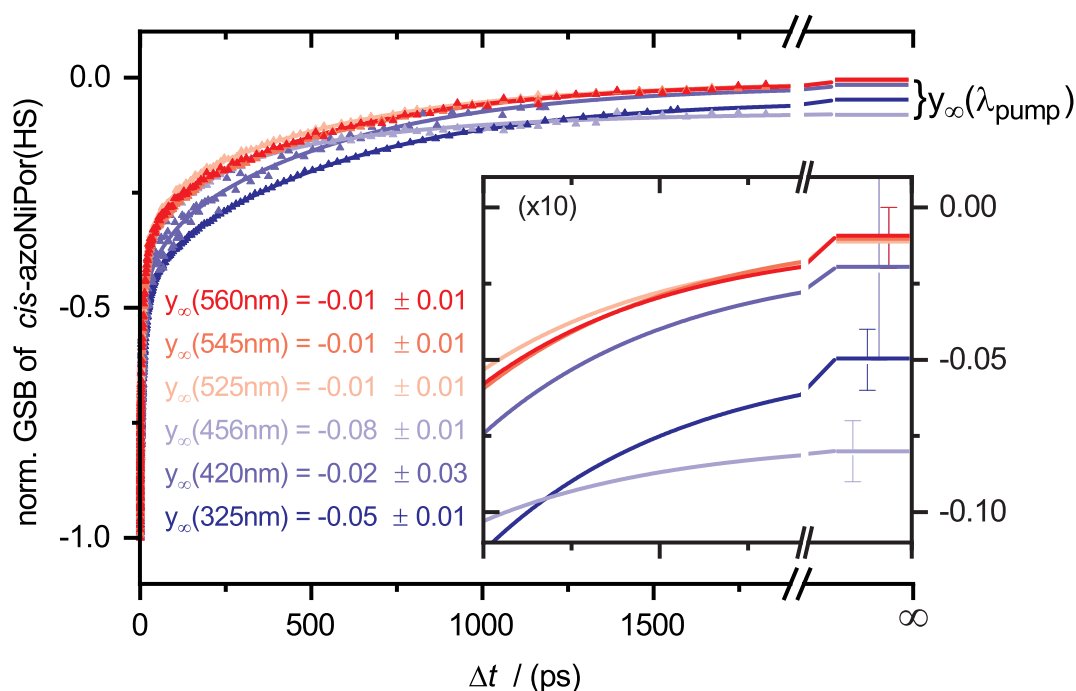


Figure S7: Normalized transient absorption time traces of the GSB signals of *cis*-azoNiPor(HS) at each of the applied excitation wavelength λ_{pump} together with the fitted exponential curves. All traces could be well described with four exponential functions and an offset y_{∞} . Since all GSB signals were normalized to -1 the absolute value of y_{∞} can directly be viewed as an upper limit of the quantum yield for the reaction from the HS to the LS species. The above results indicate that formation of the photoproduct is only significant for excitation wavelength of $\lambda_{\text{pump}} \leq 456$ nm.

References

- [1] Bandara, H. M.; Burdette, S. C. *Chem. Soc. Rev.* **2012**, *41*, 1809–1825.
- [2] Gouterman, M. *J. Chem. Phys.* **1959**, *30*, 1139–1161.
- [3] Bajema, L.; Gouterman, M.; Meyer, B. *J. Mol. Spec.* **1961**, *27*, 225–235.
- [4] Gouterman, M.; Wagnière, G. H.; Snyder, L. C. *J. Mol. Spec.* **1963**, *11*, 108–127.
- [5] Hirao, K. *J. Phys. Chem. A* **1999**, *103*, 1894–1904.
- [6] Pekkarinen, L.; Linschitz, H. *J. Am. Chem. Soc.* **1960**, *82*, 2407–2411.
- [7] Osuka, A.; Li Liu, B.; Maruyama, K. *J. Org. Chem.* **1993**, *58*, 3582–3585.
- [8] Yu, H. Z.; Baskin, J. S.; Steiger, B.; Wan, C. Z.; Anson, F. C.; Zewail, A. H. *Chem. Phys. Lett.* **1998**, *293*, 1–8.
- [9] Yang, S. I.; Lammi, R. K.; Seth, J.; Riggs, J. A.; Arai, T.; Kim, D.; Boccian, D. F.; Holten, D.; Lindsey, J. S. *J. Phys. Chem. B* **1998**, *102*, 9426–9436.
- [10] Gratz, H.; Penzkofer, A. *Chem. Phys.* **2000**, *254*, 363–374.
- [11] Baskin, J. S.; Yu, H. Z.; Zewail, A. H. *J. Phys. Chem. A* **2002**, *106*, 9837–9844.
- [12] Yeon, K. Y.; Jeong, D.; Kim, S. K. *Chem. Commun.* **2010**, *46*, 5572–5574.
- [13] Kim, S. Y.; Joo, T. *J. Phys. Chem. Lett.* **2015**, *6*, 2993–2998.
- [14] Chen, L. X.; Zhang, X.; Wasinger, E. C.; Attenkofer, K.; Jennings, G.; Muresan, A. Z.; Lindsey, J. S. *J. Am. Chem. Soc.* **2007**, *129*, 9616–9618.
- [15] Drain, C. M.; Kirmaier, C.; Medforth, C. J.; Nurco, D. J.; Smith, K. M.; Holten, D. *J. Phys. Chem.* **1996**, *100*, 11984–11993.
- [16] Drain, C. M.; Gentemann, S.; Roberts, J. A.; Nelson, N. Y.; Medforth, C. J.; Jia, S.; Simpson, M. C.; Smith, K. M.; Fajer, J.; Shelnutt, J. A.; Holten, D. *J. Am. Chem. Soc.* **1998**, *120*, 3781–3791.

-
- [17] Musewald, C.; Hartwich, G.; Lossau, H.; Gilch, P.; Pöllinger-Dammer, F.; Scheer, H.; Michel-Beyerle, M. E. *J. Phys. Chem. B* **1999**, *103*, 7055–7060.
- [18] Zamyatin, A. V.; Soldatova, A. V.; Rodgers, M. A. *Inorg. Chim. Acta* **2007**, *360*, 857–868.
- [19] Zamyatin, A. V.; Gusev, A. V.; Rodgers, M. A. J. *J. Am. Chem. Soc.* **2004**, *126*, 15934–15935.
- [20] Ryland, E. S.; Zhang, K.; Vura-Weis, J. *J. Phys. Chem. A* **2019**, *123*.

Additional Results

To gain a more detailed understanding of the composition of the electronic absorption spectra of the azoNiPor molecule and to be able to discriminate between different contributions to its ultrafast photodynamics, its building blocks, the free porphine base $\text{H}_2\text{TPPF}_{20}$, the nickel porphyrin NiTPPF_{20} as well as the 3-(phenylazo)pyridine (PAP) ligand in the *trans*- and *cis*-conformation were further studied individually by static and time-resolved spectroscopy. The analysis of the obtained results is presented and discussed in more detail in the following.

Photodynamics of $\text{H}_2\text{TPPF}_{20}$

The two-dimensional spectro-temporal absorption map showing the change in optical density (ΔOD) as a function of probe wavelength and pump-probe time delay of $\text{H}_2\text{TPPF}_{20}$ in cyclohexane recorded after photoexcitation at $\lambda_{\text{pump}} = 325$ nm is displayed in Figure 4.1(a). The 2D map features a broad and diffuse excited state absorption (ESA) covering almost all the spectral range alongside with some superimposed ground state bleach (GSB) signals. A slight blue shift of the ESA band in the region around 430 nm is observed within the first picosecond. Overall, $\text{H}_2\text{TPPF}_{20}$ shows very little temporal evolution within the recorded time window of ~ 1.6 ns. The transient absorption vs. delay time plot of the ESA band at $\lambda_{\text{probe}} = 435$ nm is shown in Figure 4.1(b). The data are well described by three exponential functions with decay constants $\tau_1 = 1.3 \pm 0.3$ ps, $\tau_2 = 27 \pm 17$ ps and a step function ($\tau_3 \rightarrow \infty$) convoluted with a Gaussian-shaped instrument response function (IRF). Further insight into the excited-state dynamics of $\text{H}_2\text{TPPF}_{20}$ is obtained from fluorescence experiments. Static fluorescence spectra were measured with a Horiba JobinYvon FluoroMax-4 spectrofluorometer. The static fluorescence spectrum in cyclohexane recorded after photoexcitation at $\lambda_{\text{exc.}} = 340$ nm is given in Figure 4.2(a). The shape of the fluorescence spectrum mirrors the shape of the Q_x bands observed in the static absorption spectrum. The fluorescence decay was detected by time-correlated single-photon counting (TCSPC) with a PicoQuant FluoTime 200 modular fluorescence lifetime spectrometer. Fluorescence time traces were recorded following excitation with a laser diode at $\lambda_{\text{exc.}} = 340$ nm for fluorescence wavelengths from $630 \text{ nm} < \lambda_{\text{flu.}} < 730 \text{ nm}$ in 10 nm steps. An exemplary time profile recorded at 640 nm together with the Gaussian-shaped IRF and the global fit of the data points is displayed in Figure 4.2(b). All time traces are well described with a single exponential function with a global decay constant of $\tau_3 = 10.1 \pm 0.2$ ns.

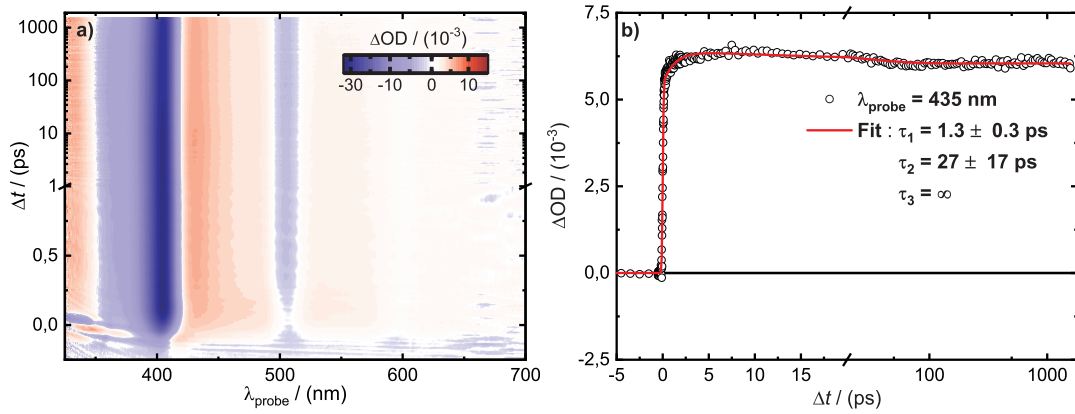


Figure 4.1: Two-dimensional time-resolved electronic absorption map (a) and fitted transient absorption time trace at $\lambda_{\text{probe}} = 435 \text{ nm}$ (b) of $\text{H}_2\text{TPPF}_{20}$ obtained after photoexcitation at $\lambda_{\text{pump}} = 325 \text{ nm}$.

To further map the photocycle of $\text{H}_2\text{TPPF}_{20}$, nanosecond transient absorption spectroscopy using two coupled Ti:Sa amplifiers was employed. The recorded transient absorption spectra at delay times of $0 \text{ ns} < \Delta t < 500 \text{ ns}$ are shown in Figure 4.3(a) and clearly reveal the recovery of the GSB signals as well as the decay of the diffuse ESA bands. The transient absorption vs. delay time profiles of the ESA band at $\lambda_{\text{probe}} = 435 \text{ nm}$ and the GSB $\lambda_{\text{probe}} = 400 \text{ nm}$ in Figure 4.3(b) were fitted simultaneously using a single exponential function with a time constant of $\tau_4 = 335 \pm 29 \text{ ns}$. All together, these results can be

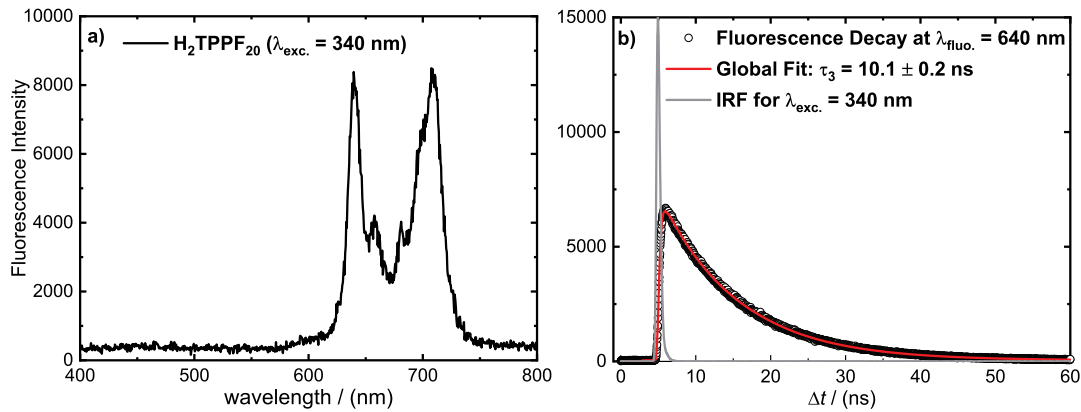


Figure 4.2: Static fluorescence spectrum (a) and fitted fluorescence time trace at $\lambda_{\text{fluo.}} = 640 \text{ nm}$ (b) of $\text{H}_2\text{TPPF}_{20}$ in cyclohexane recorded after photoexcitation at $\lambda_{\text{exc.}} = 340 \text{ nm}$.

interpreted as follows: photoexcitation of a high-lying porphyrin state rapidly generates the lowest lying singlet $^1\pi\pi^*$ state of the macrocycle (Q_x) within $<80 \text{ fs}$ which is the time resolution of our transient absorption experiment. Since the Q_x state is formed very rapidly, it possesses some excess vibrational en-

ergy which is subsequently redistributed to other vibrational modes as well as to the solvent environment being responsible for a slight blue-shift of the ESA bands. This process is associated with the time constants $\tau_1 = 1.3 \pm 0.3$ ps and $\tau_2 = 27 \pm 17$ ps. The lifetime of the relaxed Q_x state was determined by TCSPC to $\tau_3 = 10.1 \pm 0.2$ ns. As no recovery of the ground state is observed in the transient absorption spectra and fluorescence is rarely a major deactivation pathway the depopulation of the Q_x state occurs most likely via ISC to the $^3\pi\pi^*$ state. Ultimately, the ground state is recovered with $\tau_4 = 335 \pm 29$ ns determined by nanosecond TEAS. These results are in agreement with previous studies of other porphine derivatives.^[6–13]

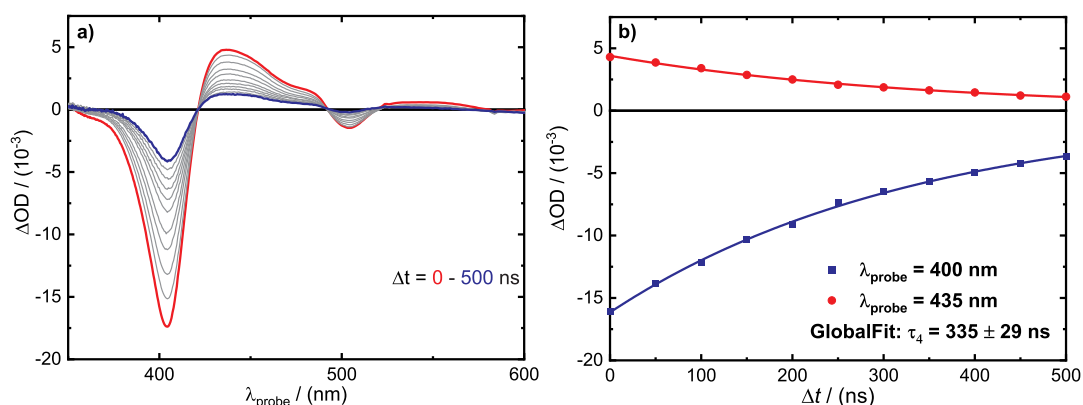


Figure 4.3: Nanosecond transient absorption spectra (a) and ground-state bleach (GSB, blue) and excited-state absorption (ESA, red) time traces with fitted exponentials (b) of H_2TPPF_{20} in cyclohexane recorded after photoexcitation at $\lambda_{exc.} = 325$ nm.

Photodynamics of $NiTPPF_{20}$

When going from the free porphine base H_2TPPF_{20} to the corresponding nickel complex $NiTPPF_{20}$, the photodynamics change drastically. The vacant d-orbitals of the $Ni(II)$ ion enable the porphyrin to undergo relaxation processes involving ligand-field states which manifests itself in the virtual absence of luminescence from the usually emissive porphyrin $\pi\pi^*$ states. The 2D transient absorption map of $NiTPPF_{20}$ in cyclohexane recorded after photoexcitation at $\lambda_{pump} = 325$ nm is shown in Figure 4.4(a). For $NiTPPF_{20}$ a clear temporal evolution of the initially diffuse ESA into a sharp band centered around $\lambda_{probe} = 420$ nm alongside with a pronounced ground state recovery (GSR) are observed within the first picosecond. In the time window $\Delta t > 1$ ps slight spectral shifts and a complete vanishing of all other spectral features occurs. The singular value decomposition (SVD) based global analysis of the time-resolved electronic absorption data was carried out using 3 SVD individual components. The SVD

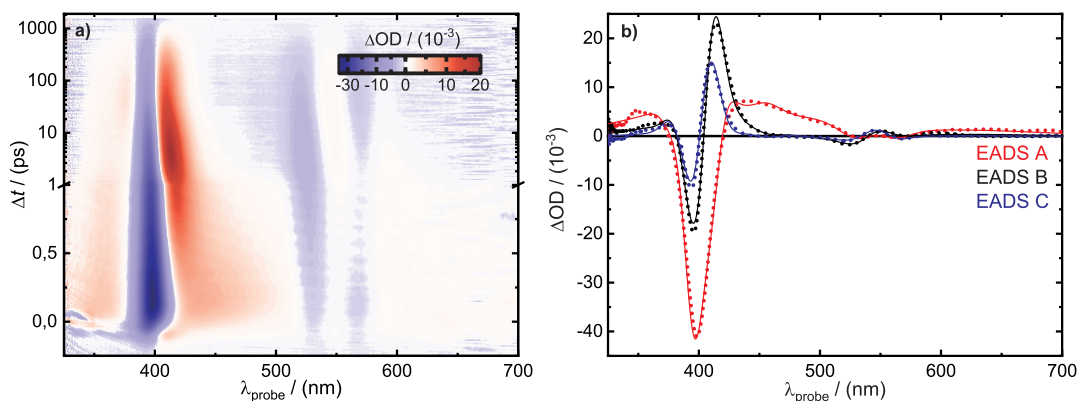


Figure 4.4: Two-dimensional time-resolved electronic absorption map (a) and evolution-associated difference spectra (EADS, b) of NiTPPF₂₀ in cyclohexane obtained after photoexcitation at $\lambda_{\text{pump}} = 325$ nm.

time traces are well described by a sum of 3 exponentials with global decay time constants of $\tau_1 = 0.85 \pm 0.02$ ps, $\tau_2 = 11.8 \pm 0.7$ ps and $\tau_3 = 367 \pm 16$ ps. Application of a sequential kinetic model of the type



where 0 denotes the ground state of NiTPPF₂₀, yielded evolution-associated difference spectra (EADS) that are shown in Figure 4.4(b). While EADS A features a diffuse spectral shape, the ensuing two EADS B and C exhibit the shape of a first derivative Gaussian.

These results lead to the conclusion that photoexcitation of a high-lying porphyrin state rapidly generates the lowest-lying singlet $^1\pi\pi^*$ state of the macrocycle within the time resolution of the experiment. Subsequently, energy transfer to the ligand field $^{1,3}(d,d)$ state of the nickel takes place with the time constant $\tau_1 = 0.85 \pm 0.02$ ps. This state exhibits the characteristic Gaussian derivative-shaped spectrum and undergoes vibrational cooling represented by the averaged time constant $\tau_2 = 11.8 \pm 0.7$ ps and manifesting itself in a pronounced blue shift of the transient absorption signals. The relaxed nickel $^{1,3}(d,d)$ state undergoes ISC to the ground state with the time constant $\tau_3 = 367 \pm 16$ ps. The results are in good agreement with previously reported studies on four-coordinate nickel porphyrin systems.^[14–20]

Photodynamics of *trans*-3-(phenylazo)pyridine

Femtosecond time-resolved electronic absorption spectroscopy was carried out at an excitation wavelength of $\lambda_{\text{pump}} = 312$ nm, which allows for the excitation of both PAP isomers at sufficient optical densities. The 2D transient absorption map of *trans*-3-(phenylazo)pyridine (PAP) in cyclohexane recorded after

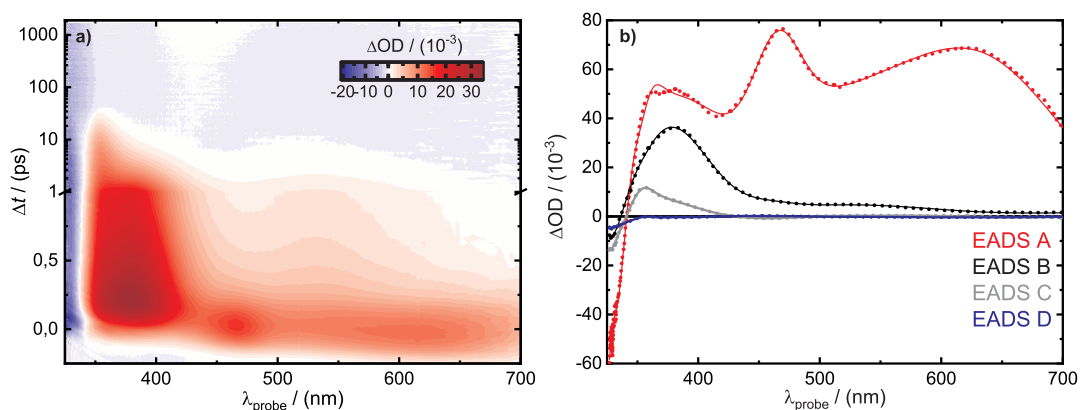
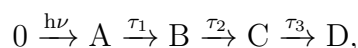


Figure 4.5: Two-dimensional time-resolved electronic absorption map (a) and evolution-associated difference spectra (EADS, b) of *trans*-3-(phenylazo)pyridine (PAP) obtained after photoexcitation at $\lambda_{\text{pump}} = 312$ nm.

photoexcitation at $\lambda_{\text{pump}} = 312$ nm are displayed in Figure 4.5(a). At early delay times the transient absorption map features a broad ESA with a distinct peak around $\lambda_{\text{probe}} = 470$ nm which rapidly evolves to a pronounced ESA band centered at $\lambda_{\text{probe}} = 390$ nm. No apparent recovery of the GSB signal at $\lambda_{\text{probe}} < 350$ nm is observed in this time window. The decay of these ESA features is accompanied by significant GSR. However, the spectra measured at late delay times still feature some sustainable GSB indicating the formation of a photoproduct. The SVD based global analysis of the time-resolved electronic absorption data was carried out using 4 individual SVD components. The SVD time traces are well described by a sum of 3 exponentials with global decay time constants of $\tau_1 = 0.07 \pm 0.01$ ps, $\tau_2 = 1.00 \pm 0.04$ ps and $\tau_3 = 12.0 \pm 0.7$ ps and a step function ($\tau_4 \rightarrow \infty$). The EADS obtained by applying a sequential kinetic model of the type



where 0 denotes the ground state of *trans*-PAP, are given in Figure 4.5(b). The peak at $\lambda_{\text{probe}} = 470$ nm in EADS A is associated with the initially excited S_2 state. However, as this state decays with $\tau_1 = 0.07 \pm 0.01$ ps, which is close to the time resolution of the experiment, EADS A also exhibits some contributions of the subsequently populated S_1 state. The S_1 state is associated with the prominent absorption band around $\lambda_{\text{probe}} = 390$ nm observed in EADS B and C and shows biexponential decay with $\tau_2 = 1.00 \pm 0.04$ ps and $\tau_3 = 12.0 \pm 0.7$ ps. On this timescale the ground state of the *trans*-isomer is recovered. Furthermore, the *cis*-PAP photoproduct is formed to some extent, which is identified by the persistent bleach of *trans*-PAP at $\lambda_{\text{probe}} = 330$ nm in the EADS D. A quantum yield of $\sim 12\%$ for the *trans*-to-*cis*-isomerization was estimated from the ratio of the initial and final bleach. These results are in line with those reported for

the well-studied and structurally related *trans*-azobenzene.^[21–23]

Photodynamics of *cis*-3-(phenylazo)pyridine

The *cis*-isomer of PAP was obtained by continuous irradiation of the sample solution with a high-power LED at 344 nm. The smaller molar attenuation of *cis*-PAP at $\lambda_{\text{pump}} = 312$ nm compared to *trans*-PAP leads to a smaller fraction of excited sample molecules and consequently to smaller ΔOD values in the recorded 2D transient absorption map, which is displayed in Figure 4.6(a). The initially observed broad ESA with a distinct peak around $\lambda_{\text{probe}} = 470$ nm rapidly evolves into a prominent ESA band centered at $\lambda_{\text{probe}} = 390$ nm. The decay of this ESA is accompanied by the build-up of a positive absorption feature at $\lambda_{\text{probe}} < 350$ nm that is persistent until the end of the investigated time window. For the quantitative analysis of the transient absorption data of

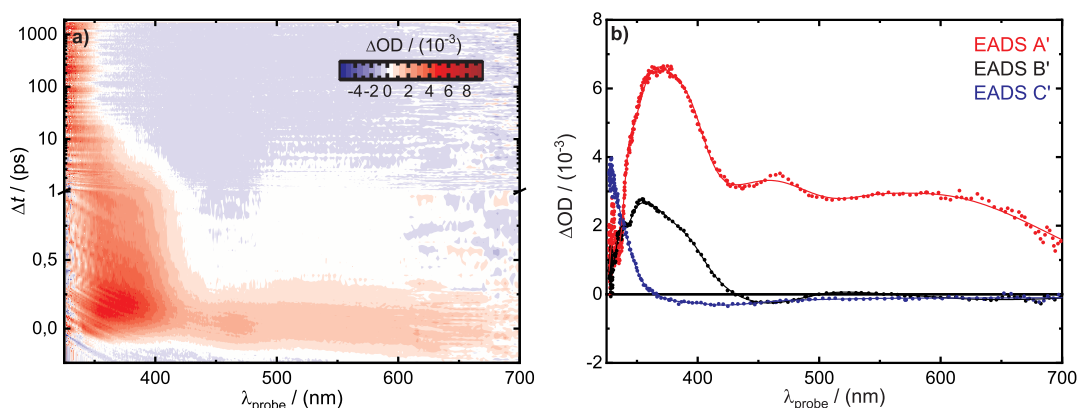
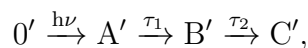


Figure 4.6: Two-dimensional time-resolved electronic absorption map (a) and evolution-associated difference spectra (EADS, b) of *cis*-3-(phenylazo)pyridine (PAP) obtained after photoexcitation at $\lambda_{\text{pump}} = 312$ nm.

cis-PAP it was sufficient to use 3 individual SVD components. The SVD time traces could be well described by a sum of 2 exponentials with global decay time constants of $\tau_1 = 0.32 \pm 0.06$ ps, $\tau_2 = 7 \pm 1$ ps and a step function ($\tau_3 \rightarrow \infty$). The EADS obtained by applying a sequential kinetic model of the type



where $0'$ denotes the ground state of *cis*-PAP, are given in Figure 4.6(b). Both, EADS A' and B' of *cis*-PAP, feature the characteristic absorption peak of the S_1 state at $\lambda_{\text{probe}} = 390$ nm. This indicates that the $S_n \rightarrow S_1$ conversion in *cis*-PAP occurs even faster compared to the *trans*-isomer and is thus completed within the time resolution of the experiment. The decay of the S_1 state proceeds

in a biexponential fashion with $\tau_1 = 0.32 \pm 0.06$ ps and $\tau_2 = 7 \pm 1$ ps and is accompanied by the formation of the ground state of the *trans*-isomer, described by the final EADS C', which features the product absorption of the *trans*-species at $\lambda_{\text{probe}} = 330$ nm and the bleach of the *cis*-species at $\lambda_{\text{probe}} = 440$ nm. Overall, these results are in good agreement with those reported for *cis*-azobenzene.^[21,22,24]

References

- [1] Bajema, L.; Gouterman, M.; Meyer, B. *J. Mol. Spectrosc.* **1961**, *27*, 225–235.
- [2] Gouterman, M.; Wagnière, G. H.; Snyder, L. C. *J. Mol. Spectrosc.* **1963**, *11*, 108–127.
- [3] Gouterman, M. *J. Chem. Phys.* **1959**, *30*, 1139–1161.
- [4] Hirao, K. *J. Phys. Chem. A* **1999**, *103*, 1894–1904.
- [5] Giovannetti, R. *Macro Nano Spectrosc.* **2012**, 87–108.
- [6] Pekkarinen, L.; Linschitz, H. *J. Am. Chem. Soc.* **1960**, *82*, 2407–2411.
- [7] Osuka, A.; li Liu, B.; Maruyama, K. *J. Org. Chem.* **1993**, *58*, 3582–3585.
- [8] Yu, H. Z.; Baskin, J. S.; Steiger, B.; Wan, C. Z.; Anson, F. C.; Zewail, A. H. *Chem. Phys. Lett.* **1998**, *293*, 1–8.
- [9] Yang, S. I.; Lammi, R. K.; Seth, J.; Riggs, J. A.; Arai, T.; Kim, D.; Boccian, D. F.; Holten, D.; Lindsey, J. S. *J. Phys. Chem. B* **1998**, *102*, 9426–9436.
- [10] Gratz, H.; Penzkofer, A. *Chem. Phys.* **2000**, *254*, 363–374.
- [11] Baskin, J. S.; Yu, H. Z.; Zewail, A. H. *J. Phys. Chem. A* **2002**, *106*, 9837–9844.
- [12] Yeon, K. Y.; Jeong, D.; Kim, S. K. *Chem. Commun.* **2010**, *46*, 5572–5574.
- [13] Kim, S. Y.; Joo, T. *J. Phys. Chem. Lett.* **2015**, *6*, 2993–2998.
- [14] Chen, L. X.; Zhang, X.; Wasinger, E. C.; Attenkofer, K.; Jennings, G.; Muresan, A. Z.; Lindsey, J. S. *J. Am. Chem. Soc.* **2007**, *129*, 9616–9618.
- [15] Drain, C. M.; Kirmaier, C.; Medforth, C. J.; Nurco, D. J.; Smith, K. M.; Holten, D. *J. Phys. Chem.* **1996**, *100*, 11984–11993.
- [16] Drain, C. M.; Gentemann, S.; Roberts, J. A.; Nelson, N. Y.; Medforth, C. J.; Jia, S.; Simpson, M. C.; Smith, K. M.; Fajer, J.; Shelnutt, J. A.; Holten, D. *J. Am. Chem. Soc.* **1998**, *120*, 3781–3791.

-
- [17] Musewald, C.; Hartwich, G.; Lossau, H.; Gilch, P.; Pöllinger-Dammer, F.; Scheer, H.; Michel-Beyerle, M. E. *J. Phys. Chem. B* **1999**, *103*, 7055–7060.
- [18] Zamyatin, A. V.; Soldatova, A. V.; Rodgers, M. A. *Inorg. Chim. Acta* **2007**, *360*, 857–868.
- [19] Zamyatin, A. V.; Gusev, A. V.; Rodgers, M. A. J. *J. Am. Chem. Soc.* **2004**, *126*, 15934–15935.
- [20] Ryland, E. S.; Zhang, K.; Vura-Weis, J. *J. Phys. Chem. A* **2019**, *123*, 54214–5222.
- [21] Bandara, H. M.; Burdette, S. C. *Chem. Soc. Rev.* **2012**, *41*, 1809–1825.
- [22] Quick, M.; Dobryakov, A. L.; Gerecke, M.; Richter, C.; Berndt, F.; Ioffe, I. N.; Granovsky, A. A.; Mahrwald, R.; Ernsting, N. P.; Kovalenko, S. A. *J. Phys. Chem. B* **2014**, *118*, 8756–8771.
- [23] Nenov, A.; Borrego-Varillas, R.; Oriana, A.; Ganzer, L.; Segatta, F.; Conti, I.; Segarra-Marti, J.; Omachi, J.; Dapor, M.; Taioli, S.; Manzoni, C.; Mukamel, S.; Cerullo, G.; Garavelli, M. *J. Phys. Chem. Lett.* **2018**, *9*, 1534–1541.
- [24] Nägele, T.; Hoche, R.; Zinth, W.; Wachtveitl, J. *Chem. Phys. Lett.* **1997**, *272*, 489–495.

5 Ultrafast Photodynamics of an Azopyridine-Functionalized Iron(II) Complex: Implications on the Concept of Ligand-Driven Light-Induced Spin Change

Sebastian Megow,[†] Henrike-Leonie Fitschen,[‡] Felix Tuczek^{‡,}
and Friedrich Temps^{†,*}*

[†]Institut für Physikalische Chemie, Christian-Albrechts-Universität,
Olshausenstrasse 40, 24098 Kiel, Germany

[‡]Institut für Anorganische Chemie, Christian-Albrechts-Universität,
Olshausenstrasse 40, 24098 Kiel, Germany

Repinted with permission from
J. Phys. Chem. Lett., **2019**, *10*, 6048-6054
Copyright 2019 American Chemical Society

OWN CONTRIBUTIONS TO THIS MANUSCRIPT:

- Static UV–vis absorption spectroscopy,
- Femtosecond time-resolved electronic absorption spectroscopy (TEAS),
- Analysis of experimental TEAS data,
- Writing of the manuscript.

^{*}To whom correspondence should be addressed. Email: temps@phc.uni-kiel.de, ftuczek@ac.uni-kiel.de

Abstract

We report on the ultrafast photodynamics of an iron(II) complex with a photoisomerizable pentadentate azo-tetrapyridylamino ligand after irradiation with ultraviolet light. The results of femtosecond transient electronic absorption spectroscopy performed on the low-spin (LS) form of the title complex show that initial excitation of the $\pi\pi^*$ state of the azopyridine unit in the ligand at $\lambda_{\text{pump}} = 312$ nm is followed by an ultrafast intersystem crossing (ISC) that leads to the formation of a metal-centered (MC) ^5T state, in competition with the intended photoswitching of the azopyridine unit. Additional measurements carried out upon excitation of the singlet metal-to-ligand charge-transfer ($^1\text{MLCT}$) transition at $\lambda_{\text{pump}} = 455$ nm suggest that this energy transfer occurs via an MLCT state. The resulting high-spin (HS) ^5T state of the complex is metastable and recovers to the LS ground state with a time constant of ~ 3 ns. The implications of these observations on the ligand-driven light-induced spin change concept are discussed.

5.1 Reprint of the Publication

Light-induced spin crossover (SCO) in transition-metal complexes is a phenomenon with application potential as molecular devices for high-density magnetic data storage or medicine.^[1,2] Among many possible candidates, Fe(II) SCO complexes are a very promising class of molecules, because they undergo a doubly spin-forbidden transition upon irradiation with light from the singlet ($S = 0$) low-spin (LS) to a quintet ($S = 2$) high-spin (HS) state. In many experimental^[3–7] and theoretical^[8–10] studies of Fe(II) complexes with polypyridyl ligands, it was shown that excitation of the singlet metal-to-ligand charge-transfer ($^1\text{MLCT}$) transition and higher transitions^[11] is followed by ultrafast intersystem crossing (ISC) leading to the formation of the metal-centered (MC) HS state with a quantum yield of almost unity. The lifetime of the MLCT states has to be increased, if an application of such compounds as photosensitizers is desired. This can be done, using various concepts for the design of the ligands, with the aim to avoid the usually favorable subsequent internal conversion and intersystem crossing processes.^[12–16] In contrast, applications based on spin-crossover demand the formation of the MC state. This HS ^5T state is metastable and may be long-lived at low temperature by virtue of the light-induced excited spin-state trapping (LIESST) effect.^[17] At room temperature, however, the ^5T state relaxes back to the LS ground state on the timescale of several nanoseconds.^[18] The lifetimes increase further with distortion from octahedral symmetry.^[19,20] For most applications, on the other hand, a bi-stability between the HS and LS states and a reversible switchability are desired at room temperature. This, in turn, requires a higher potential energy barrier between the HS and LS states than encountered in classic SCO complexes. In the past, several concepts for

a rational design of such compounds have been developed and explored, e.g. light-driven coordination induced spin state switching (LD-CISSS)^[21–24] and light-driven ligand-induced spin change (LD-LISC).^[25–31] In this work, we focus on the latter. The underlying idea is to introduce a chromophore into the ligand that can undergo a reversible photoreaction and thus change the ligand field strength and thereby the spin state of the transition metal center.

Herein, we present the complex $[\text{Fe}(\text{3AzoN4Py})(\text{MeCN})](\text{BF}_4)_2$ (**1**), where the Fe(II) central ion is surrounded by the photo-isomerizable azo-tetrapyridylamino ligand 3AzoN4Py (**3**) (see Scheme 1). We chose a pentadentate design of the ligand, since complexes with chelating ligands show high thermal stability and are unlikely to undergo decomposition upon irradiation. Our ligand is derived from the N4Py ligand that has been employed by Feringa and coworkers to mimic oxygen activation on non-heme iron centers in biological processes.^[32,33] In the literature-known^[34] parent $[\text{Fe}(\text{N4Py})(\text{MeCN})](\text{BF}_4)_2$ complex **2** (cf. Scheme 1), the free sixth binding site allows for an additional axial coordination of a solvent molecule. This solvent coordination to the complex indeed determines its spin state: in acetonitrile (MeCN) the complex exists in the LS form, but in methanol (MeOH) it switches predominantly to the HS state.^[35] In an attempt to realize a photoswitchable SCO in this system by the LD-LISC effect, we functionalized one of the pyridines of the N4Py ligand with an azo unit that can undergo reversible *trans-cis* isomerization upon irradiation with ultraviolet (UV) or visible (vis) light, respectively. The syntheses and purification of the samples $[\text{Fe}(\text{3AzoN4Py})(\text{MeCN})](\text{BF}_4)_2$ (**1**), $[\text{Fe}(\text{N4Py})(\text{MeCN})](\text{BF}_4)_2$ (**2**) and 3AzoN4Py (**3**) are described in the Supporting Information (SI).

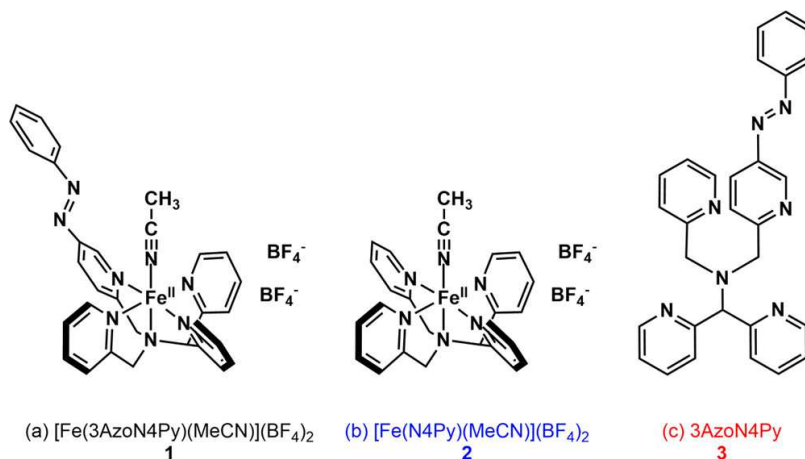


Figure 1: Structural formulas of the azo-functionalized complex $[\text{Fe}(\text{3AzoN4Py})(\text{MeCN})](\text{BF}_4)_2$ (**1**, a) and the reference compounds $[\text{Fe}(\text{N4Py})(\text{MeCN})](\text{BF}_4)_2$ (**2**, b) and 3AzoN4Py (**3**, c).

Since isomerization reactions of azo compounds as well as ISC processes in iron complexes with polypyridyl ligands proceed on ultrafast timescales and are accompanied by large changes in the electronic spectra of the molecules, we

used a combination of static and time-resolved UV–vis absorption techniques to explore the photochemical properties of the new complex **1** and, for comparison, **2** as well as **3** (Scheme 1). The static UV–vis absorption spectra of **1** and the reference compounds **2** and **3** in MeCN are displayed in Fig. 1. The spectrum of **1** shows little differences in the range <350 nm compared to the free ligand **3**. The intense absorption band centered around 325 nm can be assigned to the $\pi\pi^*$ transition of the azopyridine. In the range from 350–550 nm, both **1** and **2** show two significant absorption features compared to **3** that originate mainly from metal-to-ligand charge transfer (MLCT) transitions. The respective absorption spectra in MeOH, where the intensities of the absorption bands at 376 nm and 455 nm are strongly reduced because the complexes are switched predominantly to the HS state,^[35] are given in Figs. S1 and S2 in the SI for comparison.

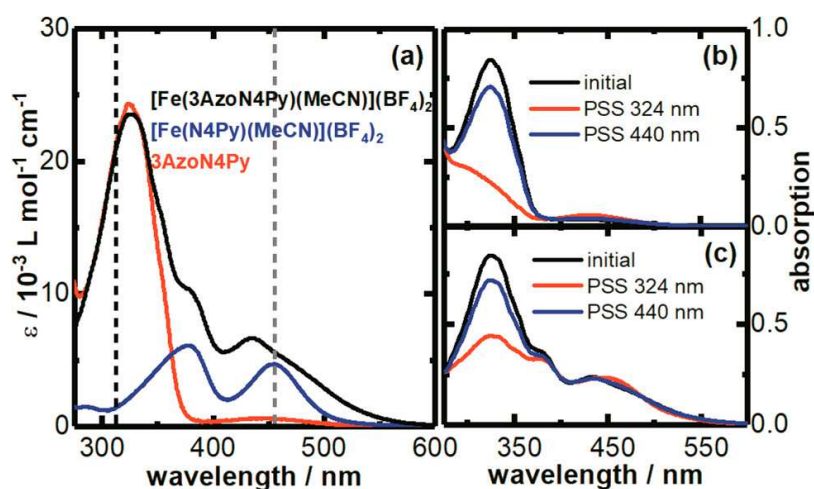


Figure 2: (a) Static UV–vis absorption spectra in MeCN of $[\text{Fe}(\text{3AzoN4Py})(\text{MeCN})](\text{BF}_4)_2$ (**1**) and the reference compounds $[\text{Fe}(\text{N4Py})(\text{MeCN})](\text{BF}_4)_2$ (**2**) and 3AzoN4Py (**3**). The dashed lines indicate the excitation wavelengths $\lambda_{\text{pump}} = 312$ nm and $\lambda_{\text{pump}} = 455$ nm used in the transient electronic absorption experiments. The absorptions are solely due to the $[\text{Fe}(\text{3AzoN4Py})(\text{MeCN})]^{2+}$ resp. $[\text{Fe}(\text{N4Py})(\text{MeCN})]^{2+}$ cations; the BF_4^- counterions do not show any significant absorption in the wavelength range of interest. (b) and (c) Static switching properties of the free ligand **3** (b), and complex **1** (c) upon irradiation with a high-power LED with a center wavelength of 324 nm for *trans*-to-*cis* and 440 nm for *cis*-to-*trans* photoisomerization from the initial states to the respective photostationary states PSS 324 and PSS 440 at the applied wavelength.

Irradiation of the free ligand **3** using a high-power light-emitting diode (LED) with a center wavelength of 324 nm leads to an almost quantitative conversion from the *trans*- to the *cis*-isomer, as can be seen by the strong decrease of the $\pi\pi^*$ band and the slight increase of the $n\pi^*$ band. In contrast, irradiation of **1** under the same conditions leads to significantly less *trans*-to-*cis* isomerization in the

coordinated azoligand. Both isomerization reactions are photo-reversible upon irradiation with a 440 nm LED. Under the present conditions, the configuration of the ligand does not appear to influence the spin state of the complex, since no significant intensity decrease of the MLCT bands is observed when the *cis*-isomer is formed. Such a decrease is expected for the HS state of **1** due to the increased metal-ligand distance that reduces the CT transition intensity, as can be seen from the UV-vis spectra recorded in MeOH (cf. Figs. S1 and S2). Thus, we conclude that the change of the ligand field strength due to the isomerization of the single azo unit in our complex is not sufficient to cause a spin change of the Fe(II) center under the applied conditions. Typically, introduction of a larger number of photoswitchable ligand units has been found necessary for LD-LISC to work.^[27] Nevertheless, as shown in the following, our system provides valuable information about the photo-induced dynamical processes that determine the switching efficiency on the basis of the LD-LISC concept.

In order to shed light on the photochemical mechanisms that affect the switching properties of the ligand in our azo-functionalized complex, we studied the photodynamics of **1** as well as the reference compounds **2** and **3** using femtosecond transient electronic absorption spectroscopy (TEAS). A brief description of the setup and the experimental conditions is given in the SI. The obtained two-dimensional spectro-temporal transient absorption maps showing the change in optical density (ΔOD) after excitation at $\lambda_{\text{pump}} = 312$ nm as function of probe wavelength and pump-probe time delay are displayed in Fig. 2 for all three compounds. Since all measurements were taken under the same experimental conditions but with different sample concentrations, the maps are scaled to the same effective concentrations for comparison. From the static spectra in Fig. 1 (a) it becomes obvious that at the applied pump wavelength both our complex **1** as well as the free ligand **3** are predominantly excited to the azopyridine $\pi\pi^*$ state, whereas only weak MLCT transitions are excited in the case of **2**. The respective transient absorption map for **2** in Fig. 2 (b) immediately shows the negative ground state bleaching (GSB) features of the MLCT bands, which decay only slightly within the recorded time frame of 1500 ps. The weak intensity of the signal is explained by the low absorption coefficient at the excitation wavelength (cf. Fig. 1 (a)). Excitation of the $\pi\pi^*$ transition of the azopyridine in the free ligand **3** (see Fig. 2 (c)) and in **1** (Fig. 2 (a)) give a spectrally broad excited state absorption (ESA) that can be assigned to the initially excited $\pi\pi^*$ (S_2) state of azopyridine. In the map for **3** this feature rapidly evolves within the first 100 fs to the intense and narrow transient ESA feature of the $n\pi^*$ (S_1) state of the azopyridine centered around 390 nm (Fig. 2 (c)). In contrast, the ultrafast decay of the initial ESA in ~ 100 fs in **1** is followed by an intense bleaching in the region of the MLCT bands, which — as in the case of the reference complex **2** — exhibit very slow ground state recovery (GSR) on the nanosecond timescale. The absence of an ESA feature of the azopyridine S_1 state as well as the large degree of bleaching observed for the MLCT bands compared

to **2** indicate that internal conversion within the azopyridine is not the major relaxation pathway in **1**. Rather, the excitation energy is transferred from the initially excited $\pi\pi^*$ state of the azopyridine to a MC excited state of the iron. The facts that the contributions to the transient absorption signals of **1** and **2** at late times are solely due to GSB of the MLCT bands, and that any positive features are absent in the detected spectral range provide clear evidence for a formation of the MC HS iron ^5T state.

To understand the observed dynamics in some detail, Fig. 3 (d) and (e) show the transient absorption spectra at selected delay times after excitation of **1** at $\lambda_{\text{pump}} = 312$ nm compared to respective transient spectra of the free ligand **3** at the same excitation wavelength in Fig. 3 (a) and (b) and to those of **1** after excitation at $\lambda_{\text{pump}} = 455$ nm in Fig. 3 (g) and (h). At 455 nm, mainly MLCT transitions are excited. Considering first and foremost complex **1** excited at 312 nm, the initial transient at $\Delta t = 0.1$ ps in Fig. 3 (d) shows a distinct peak at $\lambda_{\text{probe}} = 460$ nm that is assigned to the $\text{S}_2 \leftarrow \text{S}_\text{n}$ transition of the azopyridine unit (cf. Fig. 3 (a)). This feature vanishes quickly in the following transient ($\Delta t = 0.49$ ps), where the data show great similarity to the spectra observed immediately after direct excitation of the MLCT transitions at 455 nm in Fig. 3 (g), and are therefore assigned to ESA from the MLCT state(s). The latest transients in Fig. 3 (e) and (h), at $\Delta t = 1690$ and 1950 ps, respectively, are due to bleaching of the MLCT transitions, indicating a relaxation to the ^5T HS state. This becomes clear when they are compared to the difference spectrum of the LS and HS states of **1** derived from the static UV–vis spectra in MeCN (Fig. 1) and MeOH (Fig. S1) that are given by the dashed lines in Fig. 3 (e) and (h). Those difference spectra clearly belong to the ^5T HS state. We note further that upon 312 nm excitation of the free ligand (Fig. 3 (a) and (b)), the negative feature around 330 nm belonging to the bleaching of the $\pi\pi^*$ transition of the *trans*-azopyridine does not fully recover owing to the production of the *cis*-isomer. In the case of **1**, on the other hand, the initially strong GSB seems to recover practically completely after the ligand absorption at 312 nm was excited, whereas the *trans*-azopyridine GSB signal is virtually absent in the transient spectra recorded after 455 nm excitation. This means that in both cases the azopyridine’s initial *trans*-configuration is preserved, and shows that not *trans*-to-*cis* isomerization, but energy transfer to the iron center is the dominant relaxation pathway for the initially excited $\pi\pi^*$ state of the azopyridine in **1** at 312 nm.

Quantitative insight into the different states involved in the relaxation process of **1** was gained by a global analysis of the time-zero and solvent corrected transient absorption maps by singular value decomposition (SVD).^[36,37] The SVD analysis of the data for **3** and **1** following excitation at 312 nm required four independent spectral components. The decay-associated difference spectra (DADS) associated with the time constants $\tau_1 - \tau_4$ resulting from simultaneous nonlinear least-squares fitting to the SVD time profiles of a sum of four expo-

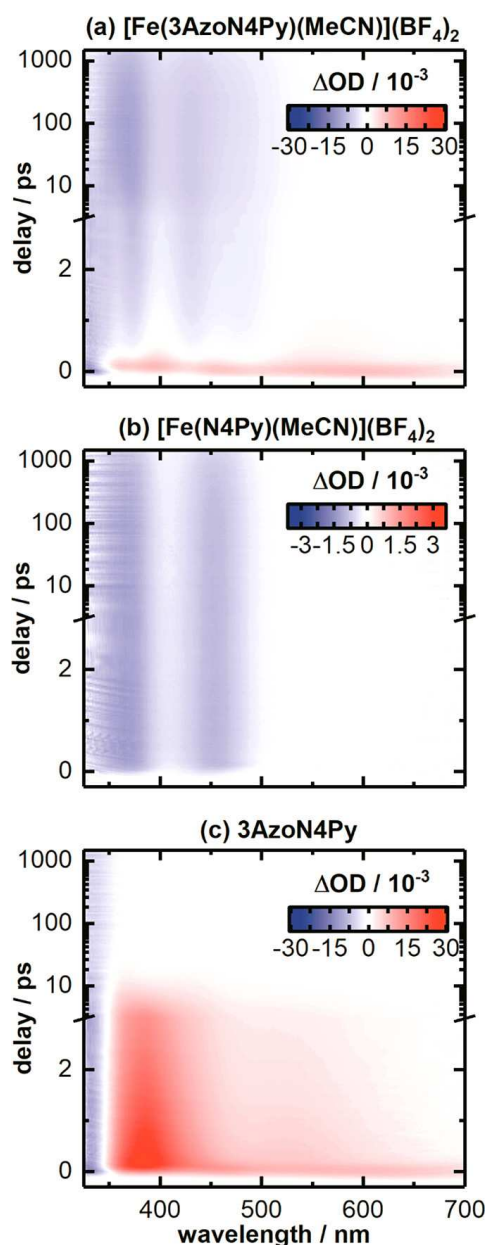


Figure 3: Two-dimensional spectro-temporal transient absorption maps showing the change in optical density ΔOD after photoexcitation at $\lambda_{\text{pump}} = 312$ nm in MeCN for $[\text{Fe}(\text{3AzoN4Py})(\text{MeCN})](\text{BF}_4)_2$ (**1**, a), $[\text{Fe}(\text{N4Py})(\text{MeCN})](\text{BF}_4)_2$ (**2**, b) and 3AzoN4Py (**3**, c) at probe wavelengths between $325 \text{ nm} < \lambda_{\text{probe}} < 700 \text{ nm}$ and pump-probe delays between $-0.3 \text{ ps} < \Delta t < 1500 \text{ ps}$. The results are displayed using a linear timescale for delay times between $-0.3 \text{ ps} < \Delta t < 3 \text{ ps}$ and a logarithmic timescale between $3 \text{ ps} < \Delta t < 1500 \text{ ps}$. Please note the different false-color scale in panel (b) required due to the low absorption coefficient of reference compound **2**. The map for the reference compound **2** in (b) was normalized by applying a scaling factor of 0.29 to obtain the same effective sample concentration as for (a) and (c).

nential decay functions are displayed in Fig. 3 (c) and (f). The data recorded after 455 nm excitation required only three independent spectral components for satisfactory modeling, the associated time constants are given in Fig. 3 (i). The corresponding DADS #1–#3 in Fig. 3 (i) resemble the DADS #2–#4 in Fig. 3 (f) and are thereby assigned to the relaxation of the MLCT state of photoexcited **1** to the MC HS state. However, DADS #1 in Fig. 3 (f) shows great similarity to DADS #1 of the free ligand in Fig. 3 (c), and is consequently assigned to the initially excited $\pi\pi^*$ state of the azopyridine unit, from which the excitation energy is transferred to the MLCT manifold (DADS #2–#4). The remaining DADS #2 and #3 of the free ligand **3** (Fig. 3(c)) represent the bi-exponential relaxation/isomerization process with the time constants τ_2 and τ_3 from the subsequently populated S_1 state to the relaxed S_0 ground state of the *trans*- or *cis*-isomer, respectively. The final DADS #4 that is described as a permanent offset is due to the formation of some amount of *cis*-azopyridine photoproduct. The spectral evolution as well as the timescales are in good agreement with previous results of the relaxation of azo compounds following $\pi\pi^*$ excitation.^[38–44] The described results point out a major intrinsic dilemma of the LD-LISC principle: On the one hand, the natural photoswitching ability of the ligand needs to be preserved upon integration into the complex to ensure the desired bistability and photo-reversibility of the LD-LISC phenomenon. On the other hand, a strong coupling between the ligand and the transition metal center is required to guarantee that small changes of the ligand environment can trigger the SCO in the metal center. This, however, opens additional relaxation channels for the excited states of the photoswitchable ligand which lead to MC and/or MLCT excited states. As shown here for the title complex **1**, these processes can lead to the formation of the desired HS quintet state on the femtosecond timescale, but the obtained transient HS state recovers to the initial ground state via ISC, as no persistent conformational change is created in the ligand environment and no actual bistability is achieved. The observed ultrafast energy transfer is the reason, why the *trans*-to-*cis* switching efficiency of **3** in **1** is much lower than anticipated. A schematic sketch of this mechanism that summarizes the competing dynamics of the *trans*-*cis* photoisomerization of the azopyridine unit after $\pi\pi^*$ excitation and the ultrafast energy transfer from the azopyridine $\pi\pi^*$ state to the MLCT and MC excited states of the iron is shown in Scheme 2. In conclusion, we studied the photodynamics of the azopyridine-functionalized iron(II) complex $[\text{Fe}(\text{3AzoN4Py})(\text{MeCN})](\text{BF}_4)_2$ (**1**), a possible candidate for application of the LD-LISC concept, in comparison to the reference complex $[\text{Fe}(\text{N4Py})(\text{MeCN})](\text{BF}_4)_2$ (**2**) and the free ligand 3AzoN4Py (**3**). Transient electronic absorption spectroscopy after photoexcitation at $\lambda_{\text{pump}} = 312$ nm revealed that the initially populated $\pi\pi^*$ (S_2) state of the azopyridine ligand of the complex rapidly decays to the long-lived HS ^5T MC state. This relaxation pathway competes with the internal conversion of the azopyridine $\pi\pi^*$ state to its $n\pi^*$ (S_1) state and diminishes the yield of the *cis*-

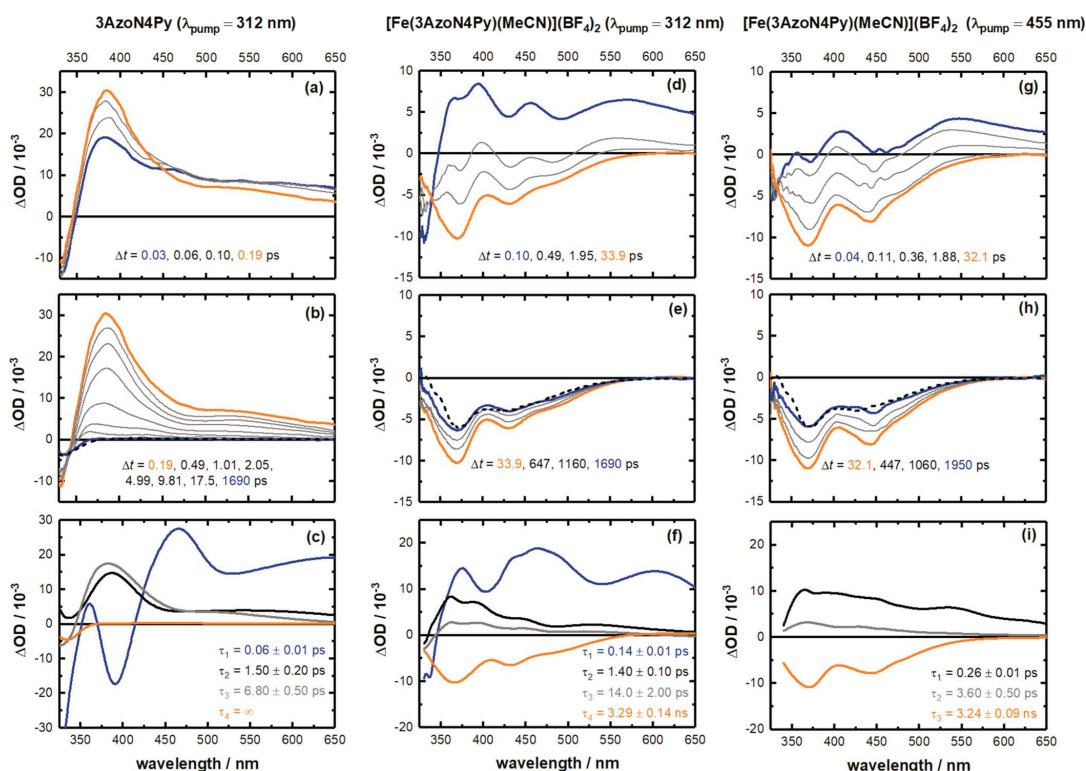


Figure 4: Transient difference absorption spectra (a, b, d, e, g, h) and decay-associated difference spectra (DADS; c, f, i) belonging to the time constants $\tau_1 - \tau_4$ resp. $\tau_1 - \tau_3$ obtained by a singular value decomposition-based global multi-exponential analysis of the data for 3AzoN4Py (**3**) with $\lambda_{\text{pump}} = 312$ nm (a – c) and [Fe(3AzoN4Py)(MeCN)](BF₄)₂ (**1**) with $\lambda_{\text{pump}} = 312$ nm (d – f) and $\lambda_{\text{pump}} = 455$ nm (g – i), respectively. The dashed line in (b) represents the static *trans-cis* difference spectrum of 3AzoN4Py (**3**). The dashed lines in (e) and (h) represent the difference spectrum of the LS and HS forms of **1**.

azopyridine isomer of the complex compared to the dynamics in the free ligand. Additional measurements following excitation of the ¹MLCT transition of the complex at $\lambda_{\text{pump}} = 455$ nm helped to identify an MLCT state as intermediate for this energy-transfer process. SVD-based global analyses of the TEAS data indicate that the HS ⁵T state is metastable and recovers to the LS ground state with a time constant for the ISC process of ~ 3 ns. These results point at an intrinsic contradiction of the LD-LISC concept, which, on the one hand, requires that the natural photochemical properties of the ligand must be preserved, but, on the other hand, demands that the changes in the ligand environment are strong enough to trigger sustainable transition to the SCO product.

To the best of our knowledge, functional LD-LISC systems with quantitative photoswitching between a pure LS and a pure HS state still await realization.^[45] The competing ultrafast energy transfer from the ligand to the MLCT and MC

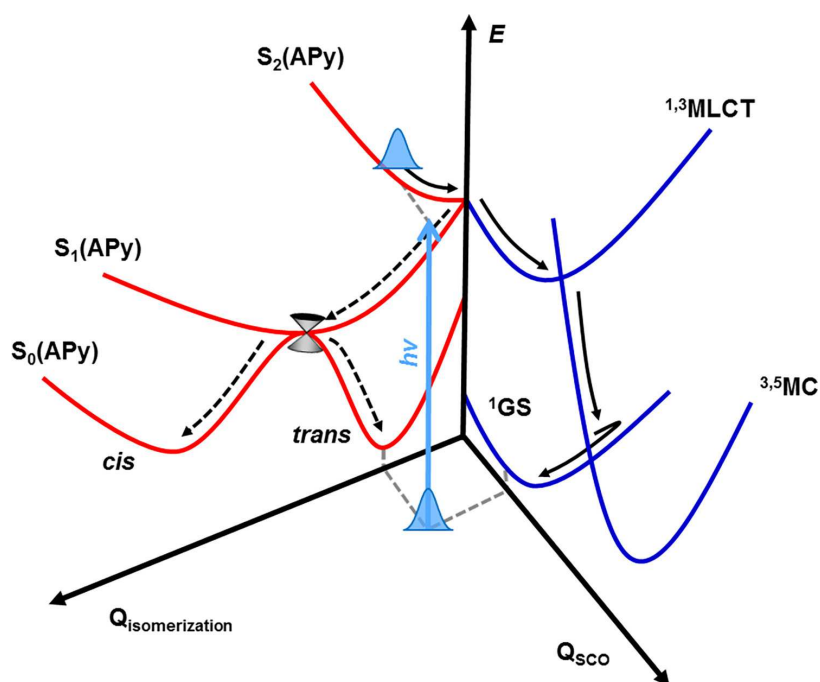


Figure 5: Sketch of the competing relaxation paths of $[\text{Fe}(\text{3AzoN4Py})(\text{MeCN})](\text{BF}_4)_2$ (**1**): Initial excitation of the S_2 state of the *trans*-azopyridine ligand is followed by an energy transfer process leading to the formation of a MC HS state via MLCT states. This process diminishes the yield of the *cis*-azopyridine ligand formed by relaxation via the S_1 state.

states of the $\text{Fe}(\text{II})$, which we identified here, could be one reason for this — besides the still insufficient change of the ligand field strength in our complex. The above results should be taken into consideration for future developments of magnetically bi-stable LD-LISC systems. One useful approach could be to use photochromic ligand units that can be switched at wavelengths to the red of the MLCT bands. Bridged^[46,47] or *ortho*-fluoro^[48–50] azo compounds could meet those demands. Alternatively, LD-LISC complexes could be based on metal-ligand systems that are devoid of MLCT transitions in the UV–vis region.^[51] Finally, the weak change of the ligand field strength evidenced in our case could be overcome by functionalization with two or more photoswitchable azo units or by modifying the complex such that its initial ligand field strength is closer to SCO behavior at room temperature.

Acknowledgements

The authors acknowledge the support of this work by the Deutsche Forschungsgemeinschaft through the Collaborative Research Center 677 “Function by Switching” and the CAU Kiel.

References

- [1] Kahn, O. *Science*. **1998**, *279*, 44–48.
- [2] Dommaschk, M.; Peters, M.; Gutzeit, F.; Schütt, C.; Näther, C.; Sönnichsen, F. D.; Tiwari, S.; Riedel, C.; Boretius, S.; Herges, R. *J. Am. Chem. Soc.* **2015**, *137*, 7552–7555.
- [3] Chergui, M. *Acc. Chem. Res.* **2015**, *48*, 801–808.
- [4] Auböck, G.; Chergui, M. *Nat. Chem.* **2015**, *7*, 629–633.
- [5] Monat, J. E.; McCusker, J. K. *J. Am. Chem. Soc.* **2000**, *122*, 4092–4097.
- [6] Smeigh, A. L.; Creelman, M.; Mathies, R. A.; McCusker, J. K. *J. Am. Chem. Soc.* **2008**, 14105–14107.
- [7] Huse, N.; Cho, H.; Hong, K.; Jamula, L.; De Groot, F. M. F.; Kim, T. K.; McCusker, J. K.; Schoenlein, R. W. *J. Phys. Chem. Lett.* **2011**, *2*, 880–884.
- [8] De Graaf, C.; Sousa, C. *Chem. Eur. J.* **2010**, *16*, 4550–4556.
- [9] Sousa, C.; Alías, M.; Domingo, A.; De Graaf, C. *Chem. Eur. J.* **2019**, *25*, 1152–1164.
- [10] Sousa, C.; De Graaf, C.; Rudavskiy, A.; Broer, R. *J. Phys. Chem. A* **2017**, *121*, 9720–9727.
- [11] Fondell, M. et al. *Struct. Dyn.* **2017**, *4*.
- [12] Zhang, W. et al. *Chem. Sci.* **2017**, *8*, 515–523.
- [13] Kjær, K. S. et al. *Phys. Chem. Chem. Phys.* **2018**, *20*, 4238–4249.
- [14] Wenger, O. S. *Chem. Eur. J.* **2019**, *25*, 6043–6052.
- [15] Zimmer, P.; Burkhardt, L.; Friedrich, A.; Steube, J.; Neuba, A.; Schepfer, R.; Müller, P.; Flörke, U.; Huber, M.; Lochbrunner, S.; Bauer, M. *Inorg. Chem.* **2018**, *57*, 360–373.
- [16] Liu, L.; Duchanois, T.; Etienne, T.; Monari, A.; Beley, M.; Assfeld, X.; Haacke, S.; Gros, P. C. *Phys. Chem. Chem. Phys.* **2016**, *18*, 12550–12556.

- [17] Hauser, A. *Spin Crossover Transit. Met. Compd. II*; Springer, Berlin, Heidelberg, 2004; pp 155–198.
- [18] Brady, C.; Callaghan, P. L.; Ciunik, Z.; Coates, C. G.; Døssing, A.; Hazell, A.; McGarvey, J. J.; Schenker, S.; Toftlund, H.; Trautwein, A. X.; Winkler, H.; Wolny, J. A. *Inorg. Chem.* **2004**, *43*, 4289–4299.
- [19] Jamula, L. L.; Brown, A. M.; Guo, D.; McCusker, J. K. *Inorg. Chem.* **2014**, *53*, 15–17.
- [20] Hong, K.; Cho, H.; Schoenlein, R. W.; Kim, T. K.; Huse, N. *Acc. Chem. Res.* **2015**, *48*, 2957–2966.
- [21] Thies, S.; Bornholdt, C.; Köhler, F.; Sönnichsen, F. D.; Näther, C.; Tuczek, F.; Herges, R. *Chem. Eur. J.* **2010**, *16*, 10074–10083.
- [22] Venkataramani, S.; Jana, U.; Dommaschk, M.; Sönnichsen, F. D.; Tuczek, F.; Herges, R. *Science* **2011**, *331*, 445–449.
- [23] Thies, S.; Sell, H.; Bornholdt, C.; Schütt, C.; Köhler, F.; Tuczek, F.; Herges, R. *Chem. Eur. J.* **2012**, *18*, 16358–16368.
- [24] Dommaschk, M.; Schütt, C.; Venkataramani, S.; Jana, U.; Näther, C.; Sönnichsen, F. D.; Herges, R. *Dalt. Trans.* **2014**, *43*, 17395–17405.
- [25] Zarembowitch, J.; Roux, C.; Boillot, M. L.; Claude, R.; Itie, J. P.; Polian, A.; Bolte, M. *Mol. Cryst. Liq. Cryst. Sci. Technol. Sect. A. Mol. Cryst. Liq. Cryst.* **1993**, *234*, 247–254.
- [26] Roux, C.; Zarembowitch, J.; Gailois, B.; Granier, T.; Claude, R. *Inorg. Chem.* **1994**, *33*, 2273–2279.
- [27] Boillot, M. L.; Chantraine, S.; Zarembowitch, J.; Lallemand, J. Y.; Prunet, J. *New J. Chem.* **1999**, *23*, 179–183.
- [28] Boillot, M.-L.; Roux, C.; Audière, J.-P.; Dausse, A.; Zarembowitch, J. *Inorg. Chem.* **1996**, *35*, 3975–3980.
- [29] Boillot, M.-L.; Zarembowitch, J.; Sour, A. In *Spin Crossover Transit. Met. Compd. II*; Gütlich, P., Goodwin, H. A., Eds.; Springer, Berlin, Heidelberg, 2004; Chapter Ligand-Dri, pp 261–276.
- [30] Brachňáková, B.; Šalitroš, I. *Chem. Pap.* **2018**, *72*, 773–798.
- [31] Bannwarth, A.; Schmidt, S. O.; Peters, G.; Sönnichsen, F. D.; Thimm, W.; Herges, R.; Tuczek, F. *Eur. J. Inorg. Chem.* **2012**, 2776–2783.
- [32] Lubben, M.; Meetsma, A.; Wilkinson, E. C.; Feringa, B.; Que, L. *Angew. Chemie Int. Ed. English* **1995**, *34*, 1512–1514.

- [33] Roelfes, G.; Lubben, M.; Chen, K.; Ho, R. Y. N.; Meetsma, A.; Genseberger, S.; Hermant, R. M.; Hage, R.; Mandal, S. K.; Young, V. G.; Zang, Y.; Kooijman, H.; Spek, A. L.; Que, L.; Feringa, B. L. *Inorg. Chem.* **1999**, *38*, 1929–1936.
- [34] McQuilken, A. C.; Ha, Y.; Sutherlin, K. D.; Siegler, M. A.; Hodgson, K. O.; Hedman, B.; Solomon, E. I.; Jameson, G. N.; Goldberg, D. P. *J. Am. Chem. Soc.* **2013**, *135*, 14024–14027.
- [35] Draksharapu, A.; Li, Q.; Roelfes, G.; Browne, W. R. *Dalt. Trans.* **2012**, *41*, 13180–13190.
- [36] Cattell, R. B. *Multivariate Behav. Res.* **1966**, *1*, 245–276.
- [37] Van Stokkum, I. H.; Larsen, D. S.; Van Grondelle, R. *Biochim. Biophys. Acta - Bioenerg.* **2004**, *1657*, 82–104.
- [38] Quick, M.; Dobryakov, A. L.; Gerecke, M.; Richter, C.; Berndt, F.; Ioffe, I. N.; Granovsky, A. A.; Mahrwald, R.; Ernsting, N. P.; Kovalenko, S. A. *J. Phys. Chem. B* **2014**, *118*, 8756–8771.
- [39] Nenov, A.; Borrego-Varillas, R.; Oriana, A.; Ganzer, L.; Segatta, F.; Conti, I.; Segarra-Martí, J.; Omachi, J.; Dapor, M.; Taioli, S.; Manzoni, C.; Mukamel, S.; Cerullo, G.; Garavelli, M. *J. Phys. Chem. Lett.* **2018**, *9*, 1534–1541.
- [40] Fujino, T.; Arzhantsev, S. Y.; Tahara, T. *Bull. Chem. Soc. Jpn.* **2002**, *75*, 1031–1040.
- [41] Otolski, C. J.; Mohan Raj, A.; Ramamurthy, V.; Elles, C. G. *J. Phys. Chem. Lett.* **2019**, *10*, 121–127.
- [42] Lednev, I. K.; Ye, T.-Q.; Hester, R. E.; Moore, J. N. *J. Phys. Chem.* **1996**, *100*, 13338–13341.
- [43] Schultz, T.; Quenneville, J.; Levine, B.; Toniolo, A.; Martínez, T. J.; Lochbrunner, S.; Schmitt, M.; Shaffer, J. P.; Zgierski, M. Z.; Stolow, A. *J. Am. Chem. Soc.* **2003**, *125*, 8098–8099.
- [44] Bandara, H. M.; Burdette, S. C. *Chem. Soc. Rev.* **2012**, *41*, 1809–1825.
- [45] Khusniyarov, M. M. *Chem. Eur. J.* **2016**, *22*, 15178–15191.
- [46] Siewertsen, R.; Schönborn, J. B.; Hartke, B.; Renth, F.; Temps, F. *Phys. Chem. Chem. Phys.* **2011**, *13*, 1054–1063.
- [47] Siewertsen, R.; Neumann, H.; Buchheim-Stehn, B.; Herges, R.; Näther, C.; Renth, F.; Temps, F. *J. Am. Chem. Soc.* **2009**, *131*, 15594–15595.

-
- [48] Knie, C.; Utecht, M.; Zhao, F.; Kulla, H.; Kovalenko, S.; Brouwer, A. M.; Saalfrank, P.; Hecht, S.; Bléger, D. *Chem. Eur. J.* **2014**, *20*, 16492–16501.
- [49] Bléger, D.; Schwarz, J.; Brouwer, A. M.; Hecht, S. *J. Am. Chem. Soc.* **2012**, *134*, 20597–20600.
- [50] Ahmed, Z.; Siiskonen, A.; Virkki, M.; Priimagi, A. *Chem. Commun.* **2017**, *53*, 12520–12523.
- [51] Hauser, A. *J. Chem. Phys.* **1991**, *94*, 2741–2748.

Supporting Information

Remark: For the sake of briefness, only the part of the Supporting Information directly related to the work of the author of this Thesis, is reprinted here. The full text can be found under the corresponding DOI: 10.1021/acs.jpcclett.9b02083.

Static UV–vis absorption spectra

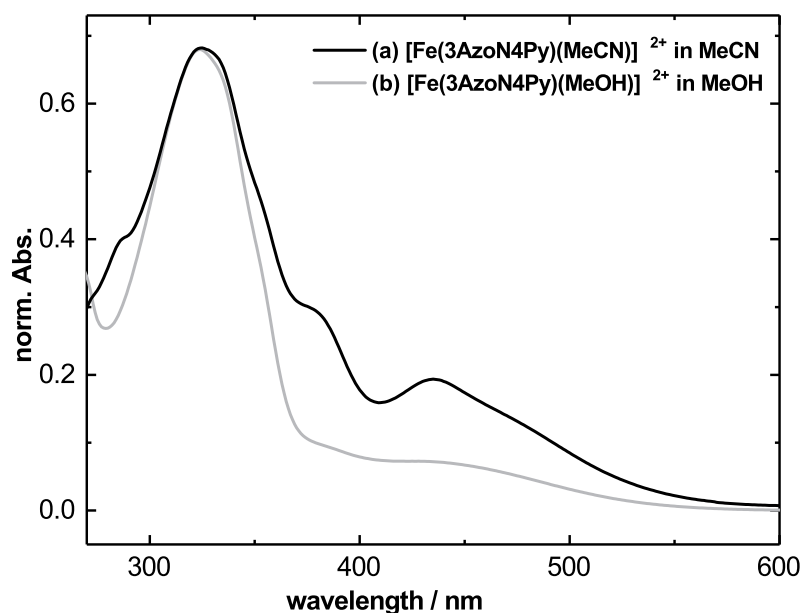


Figure S1: Static UV–vis spectra of [Fe(3AzoN4Py)(MeCN)](BF₄)₂ (1) recorded in (a) acetonitrile (MeCN) (black), where the Fe(II) is present in its low-spin (LS) state and (b) in methanol (MeOH) (grey), where the Fe(II) is present in its high-spin (HS) state.

Transient electronic absorption measurements

The femtosecond transient absorption measurements were performed in spectroscopic grade acetonitrile in a flow cell with 1 mm optical path length. Excitation pulses at $\lambda_{\text{pump}} = 312$ nm were generated using a home-built non-collinear optical parametric amplifier (NOPA) operated at 625 nm equipped with a prism pulse compressor and second harmonic generation (SHG) crystal. Excitation

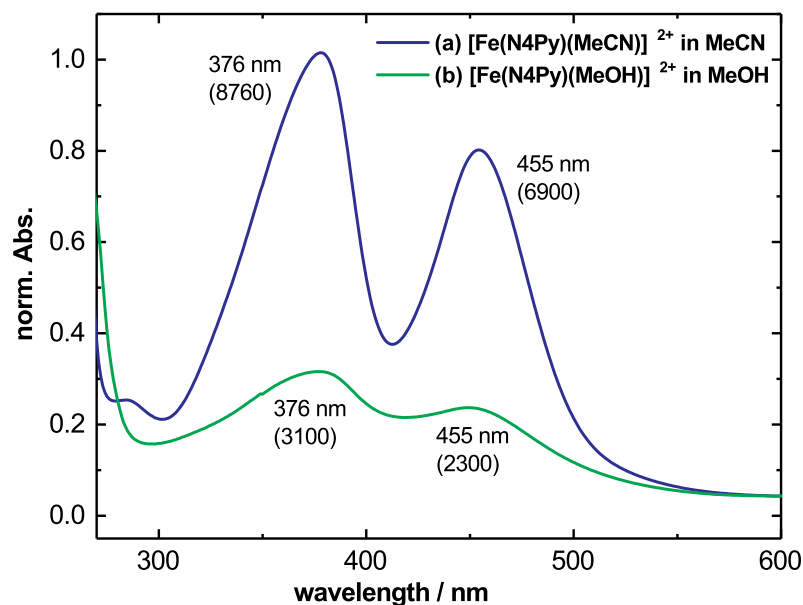


Figure S2: Static UV–vis spectra of $[\text{Fe}(\text{N4Py})(\text{X})](\text{BF}_4)_2$ (**2**) (X = solvent) recorded in (a) acetonitrile (MeCN), where the Fe(II) is present in its low-spin (LS) state (blue), and (b) in methanol (MeOH), where the Fe(II) is present in its high-spin (HS) state (green). The wavelengths of the absorption maxima are given next to the spectra, with the extinction coefficients in parentheses. This phenomenon has already been reported by DRAKSHARAPU et al.^[1]

pulses at $\lambda_{\text{pump}} = 455$ nm where generated directly in the NOPA and compressed as well. Broadband probe pulses in the range of $325 \text{ nm} < \lambda_{\text{probe}} < 700$ nm were obtained by supercontinuum generation (SCG) of the 775 nm Ti:Sa pulses in a 2 mm CaF_2 window, split into probe and reference beam, dispersed in a prism spectrograph and detected by fast frame-transfer CCD cameras.^[2–4] In order to measure background free transient absorption data, a chopper operated at $\frac{1}{4}$ of the laser repetition rate was introduced in the pump beam path, which allowed just two consecutive pump pulses to pass and blocked the next two pulses, while another chopper operated at half the laser repetition rate blocked every other probe pulse. The pump-probe time delay was achieved by a computer-controlled delay stage. For all measurements the pump polarization was set to the magic angle (54.7°) with respect to the probe polarization. UV–vis spectra were taken before and after the measurements to exclude sample degradation.

References

- [1] Draksharapu, A.; Li, Q.; Roelfes, G.; Browne, W. R. *Dalt. Trans.* **2012**, *41*, 13180–13190.
- [2] Röttger, K.; Wang, S.; Renth, F.; Bahrenburg, J.; Temps, F. *Appl. Phys. B Lasers Opt.* **2015**, *118*, 185–193.
- [3] Renth, F.; Siewertsen, R.; Strübe, F.; Mattay, J.; Temps, F. *Phys. Chem. Chem. Phys.* **2014**, *16*, 19556–19563.
- [4] Renth, F.; Foca, M.; Petter, A.; Temps, F. *Chem. Phys. Lett.* **2006**, *428*, 62–67.

Additional Results

In order to further rationalize the processes that lead to the decrease of the efficiency of ligand isomerization in $[\text{Fe}(\text{3AzoN4Py})(\text{MeCN})](\text{BF}_4)_2$ (**1**), the study of derivatives of the complex with different transition-metal ions seems worthwhile. In this course, the Zn(II) analogue $[\text{Zn}(\text{3AzoN4Py})(\text{MeCN})](\text{BF}_4)_2$ (**1'**) was investigated. The molecule was synthesized and supplied by Leonie Fitschen from the Tuzek workgroup. Furthermore, to assess the nature of the excited electronic states of the three compounds, quantum chemical calculations were performed on **1**, **1'** and the 3AzoN4Py ligand (**3**).

Photodynamics of the Zn(II) Analogue

The chemical structures and the proposed photoisomerization of **1'** are displayed in Figure 5.1. Due to its closed-shell electron configuration, Zn(II) is

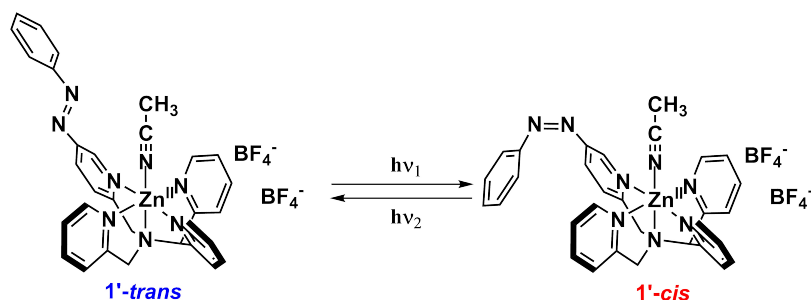


Figure 5.1: Chemical structures and reversible photoisomerization of $[\text{Zn}(\text{3AzoN4Py})(\text{MeCN})](\text{BF}_4)_2$ (**1'**).

devoid of ligand-field states. The static UV–vis absorption spectra of **1'** in acetonitrile are shown in Figure 5.2. Intense metal-to-ligand charge-transfer (MLCT) bands are absent in the visible spectrum of **1'** since it is extremely hard to reduce Zn(II).^[1] Consequently, the UV–vis spectrum is virtually identical to that of **3** and almost quantitative conversion to the *cis*-isomer can be obtained upon continuous irradiation with a high power LED at $\lambda_{\text{LED}} = 344$ nm. However, **1'** represents a more suitable reference compound than **3** as the novel azo-tetrapyrrolylamino ligand possesses the coordinated geometry. Femtosecond time-resolved electronic absorption spectroscopy (TEAS) was carried out on **1'-trans** and **1'-cis** at an excitation wavelength of $\lambda_{\text{pump}} = 314$ nm. The

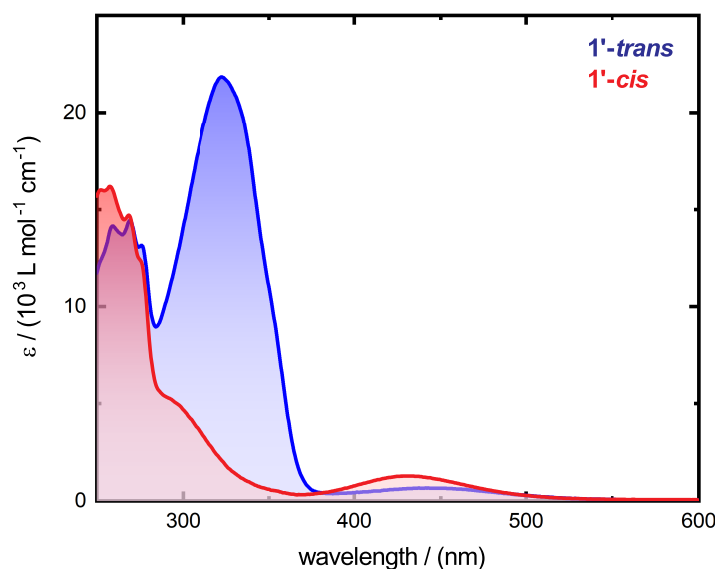
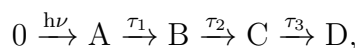


Figure 5.2: Static UV–vis spectra of **1'-trans** (blue) and **1'-cis** (red) recorded in acetonitrile.

two-dimensional spectro-temporal absorption map showing the change in optical density (ΔOD) as a function of probe wavelength (λ_{probe}) and pump-probe delay time (Δt) of **1'-trans** in acetonitrile is given in Figure 5.3(a). The initially broad excited state absorption (ESA) with a distinct peak around $\lambda_{\text{probe}} = 470$ nm associated with the $S_n \leftarrow S_2$ transition from the photo-produced $S_2(\pi\pi^*)$ state of the azopyridine evolves rapidly to the $S_1(n\pi^*)$ state. This state can be identified by the prominent $S_n \leftarrow S_1$ ESA feature centered at $\lambda_{\text{probe}} = 390$ nm. A slight recovery of the ground state bleach (GSB) feature at $\lambda_{\text{probe}} < 350$ nm can be observed in this time frame. The subsequent decay of the $S_n \leftarrow S_1$ ESA features is accompanied by significant ground state recovery (GSR). However, some remaining GSB signal can be observed even at the longest measured delay time due to formation of the *cis*-isomer. The singular value decomposition (SVD) based global analysis of the time-resolved electronic absorption data was carried out using 4 individual SVD components. The SVD time traces could be well described by a sum of 3 exponentials with global decay time constants of $\tau_1 = 0.05 \pm 0.01$ ps, $\tau_2 = 1.29 \pm 0.08$ ps and $\tau_3 = 6.3 \pm 0.3$ ps and a step function ($\tau_4 \rightarrow \infty$). The reconstruction of the 2D map from the 4 SVD components is displayed in Figure 5.3(b). The corresponding evolution-associated difference spectra (EADS), obtained for a sequential kinetic model of the type



where 0 denotes the ground state of **1'-trans**, are given in Figure 5.3(c). The EADS A is associated with the initially excited $S_2(\pi\pi^*)$ state. However, since the decay of this state with a global time constant of $\tau_1 = 0.05 \pm 0.01$ ps is close to

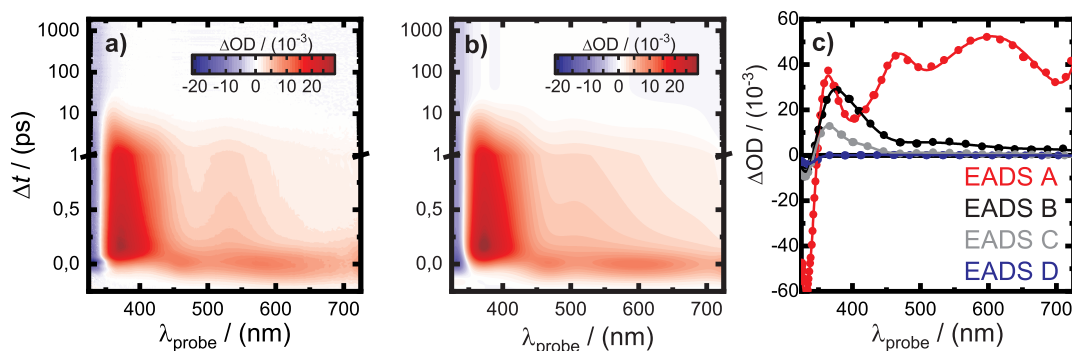


Figure 5.3: Two-dimensional time-resolved electronic absorption map (a) of $1'$ -*trans* obtained after photoexcitation at $\lambda_{\text{pump}} = 314$ nm, reconstructed 2D map (b) and evolution-associated difference spectra (EADS, c) obtained by a singular value decomposition (SVD) based analysis.

the time resolution of the experiment, the spectrum is partially convoluted with the subsequently populated $S_1(n\pi^*)$ state. The EADS B and C are associated with the $S_1S_1(n\pi^*)$ state that shows biexponential decay with $\tau_2 = 1.29 \pm 0.08$ ps and $\tau_3 = 6.3 \pm 0.3$ ps. On this timescale, the ground state of the $1'$ -*trans* is recovered. Furthermore, the $1'$ -*cis* photoproduct is formed to some extent, which is reflected by the persistent bleach of $1'$ -*trans* at $\lambda_{\text{probe}} = 330$ nm in EADS D. The quantum yield of the *trans*-to-*cis*-isomerization was estimated from the ratio of the initial and final bleach to $\sim 20\%$. In summary, the photodynamics of $1'$ -*trans* are virtually identical to those observed for the *trans*-isomer of **3**. Solely the change in geometry between the free and the coordinated form of the novel azo-tetrapyridylamino ligand does not exert an influence on the photoisomerization. Consequently, the diminished yield of the *cis*-isomer observed in the iron analogue **1** results from the identified energy-transfer process. This process is shut down for the zinc analogue $1'$ since it possesses neither ligand-field states nor low-lying MLCT states.

The two-dimensional spectro-temporal absorption map of $1'$ -*cis* in acetonitrile is displayed in Figure 5.4(a). Upon photoexcitation of $1'$ -*cis*, the ESA with the prominent $S_1(n\pi^*)$ absorption peak centered at $\lambda_{\text{probe}} = 390$ nm, is present immediately after photoexcitation. The subsequent decay of this ESA, however, is accompanied by the emergence of another positive absorption band at shorter λ_{probe} , which persists until the longest detected delay time, indicating the formation of a photoproduct. The SVD based global analysis of the time-resolved electronic absorption data was carried out using 3 individual SVD components. The SVD time traces are well described by a sum of 3 exponentials with global decay time constants of $\tau_1 = 0.05 \pm 0.05$ ps, $\tau_2 = 2.7 \pm 0.4$ ps and a step function ($\tau_3 \rightarrow \infty$). The reconstruction of the 2D map from the 3 SVD components is shown in Figure 5.4(b). The corresponding EADS, obtained for a sequential

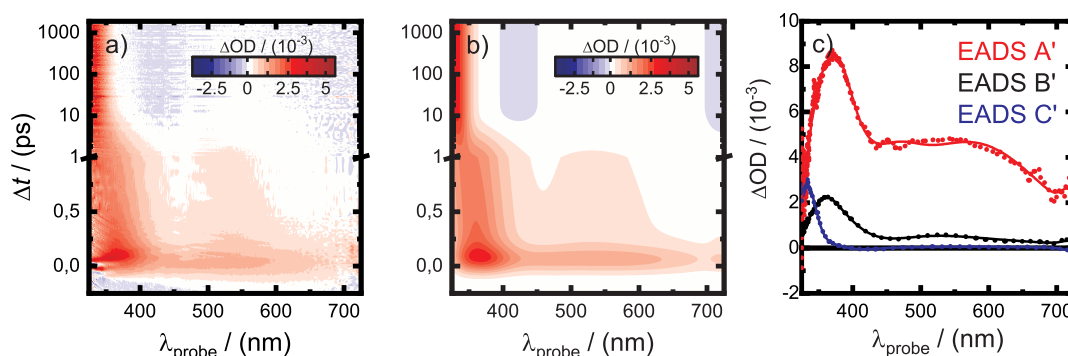
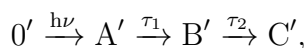


Figure 5.4: Two-dimensional time-resolved electronic absorption map (a) of **1'**-*cis* obtained after photoexcitation at $\lambda_{\text{pump}} = 314$ nm, reconstructed 2D map (b) and evolution-associated difference spectra (EADS, c) obtained by a singular value decomposition (SVD) based analysis.

kinetic model of the type



where $0'$ denotes the ground state of **1'**-*cis*, are given in Figure 5.4(c). The very short lifetime of EADS A' close to the time resolution of the experiment is most likely associated with dynamics in the Franck-Condon region on the $S_1(n\pi^*)$ potential energy surface. EADS B' is also associated with the $S_1(n\pi^*)$ state. The corresponding time constant τ_2 describes the recovery of the ground state of **1'**-*cis* as well as formation of the **1'**-*trans* photoproduct. EADS C' clearly resembles the difference absorption spectrum anticipated for *cis*-to-*trans*-isomerization. Consequently, the photodynamics of *cis*-isomer of **1'** are virtually unaffected by the coordination to the Zn(II) center and show great similarity to those observed for the *cis*-isomer of **3** and plain azobenzene.

Quantum Chemical Calculations

Quantum chemical calculations were employed for the ligand **3** and the complexes **1'** and **1** using the density functional theory (DFT) method.^[2] First a ground state geometry optimization was performed using the B3LYP functional^[3,4] with a def2-TZVP basis set^[5] and a polarized continuum model (PCM) for acetonitrile.^[6–8] Based on these geometries, the first 20 excited electronic singlet states of each compound were calculated by time-dependent DFT (TD-DFT).^[9] All calculations were carried out using the *Gaussian09*, revision D.01. package.^[10] The experimental UV–vis spectra recorded in acetonitrile together with the first 20 calculated excited electronic singlet states of **3**, **1'** and **1** are depicted in Figure 5.5. The respective excitation energies, oscillator strengths and contributing molecular orbitals (MOs) of the relevant transitions in the

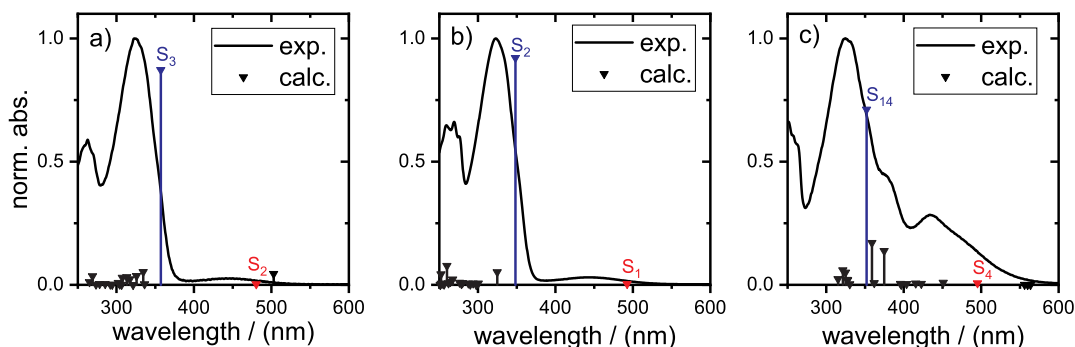


Figure 5.5: UV–vis absorption spectra and first 20 calculated electronic singlet states of 3AzoN4Py (**3**, a), [Zn(3AzoN4Py)(MeCN)]²⁺ (**1'**, b) and [Fe(3AzoN4Py)(MeCN)]²⁺ (**1**, c). The states associated with relevant transitions of the azo moiety are marked red ($n\pi^*$) and blue ($\pi\pi^*$).

wavelength range of $350 \text{ nm} < \lambda < 500 \text{ nm}$ are summarized in Table 5.1.

For the ligand **3**, the experimental UV–vis absorption spectrum features two distinct bands in this wavelength range. From the results of the calculations three electronic states associated with these absorption bands are identified. The contributing molecular orbitals are visualized in Figure 5.6 and suggest that the intense absorption band in the UV originates from a $\pi\pi^*$ transition between the second highest occupied molecular orbital (HOMO–1) and the lowest unoccupied molecular orbital (LUMO) associated with the azopyridine moiety, while the less intense absorption band in the visible range is ascribed to a $n\pi^*$ transition within the azopyridine (HOMO–2→LUMO). These transitions are anticipated for azo compounds. However, the lowest energy HOMO→LUMO transition is exclusively predicted for **3** since it exhibits a charge-transfer (CT)-like character with excitation energy being shifted from the other pyridine moieties of the ligand to the azopyridine chromophore.

The experimental UV–vis spectrum of the zinc complex **1'** is virtually identical to that of **3**. The calculations suggest that for **1'** the weak absorption band in the visible spectral range is associated with the lowest energy HOMO→LUMO transition. In contrast to **3**, however, the calculation predict only a single transition in this wavelength range. Turning to the MOs in Figure 5.7, it can be derived that weak absorption band originates solely from the $n\pi^*$ transition of the azopyridine chromophore and not from CT-like transitions between different parts of the ligand. The intense absorption band in the UV range is again assigned to the $\pi\pi^*$ transition of the azopyridine chromophore. However, it has to be stated that the assignment of the n and the π character of the HOMO and HOMO–1 of **1'** is not as straightforward as for the ligand **3**. While the two aromatic rings of the azopyridine moiety of **3** are almost in the same plane with a C–N–N–C dihedral angle of $\sim 2^\circ$, the azopyridine moiety of **1'** becomes much more distorted with a C–N–N–C dihedral angle of $\sim 16^\circ$ leading to a stronger

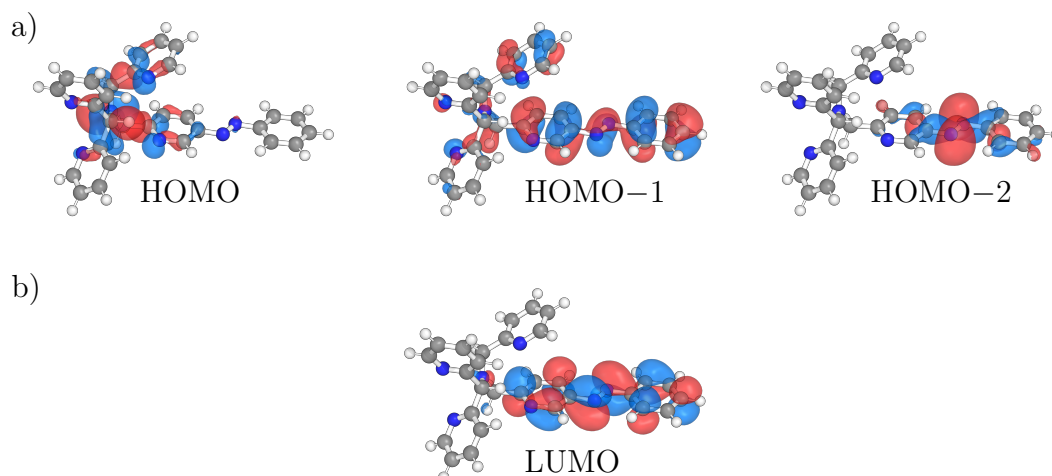


Figure 5.6: B3LYP/def2-TZVP optimized molecular structures together with highest occupied molecular orbitals (HOMOs, a) and the lowest unoccupied molecular orbital (LUMO, b) that contribute predominantly to the relevant electronic transitions in the UV–vis range of 3AzoN4Py (**3**).

mixing of the n and π orbitals. However, the calculated oscillator strengths give a clear indication for the assignment of the transitions to $n\pi^*$ and $\pi\pi^*$.

The exchange from the Zn(II) to the Fe(II) ion leads to drastical changes in the experimental UV–vis spectrum of **1**. The vacant d-orbitals of the iron ion as well as the smaller metal-ligand distances of $\bar{r}_{\text{Fe-N}} = 2.0 \text{ \AA}$ compared to $\bar{r}_{\text{Zn-N}} = 2.2 \text{ \AA}$ lead to strong interactions between the ligand and metal states. The quantum chemical calculations predict several electronic states in the spectral range of $350 \text{ nm} < \lambda < 500 \text{ nm}$, which are listed in Table 5.1. The three lowest energy transitions show up at energies $> 550 \text{ nm}$ and are omitted in Table 5.1 since they mainly arise from d-d transitions between the occupied t_{2g} (Figure 5.8 (b)) and the unoccupied e_g (Figure 5.8 (d)) set of molecular orbitals within the iron(II) center and thus possess vanishingly small oscillator strengths. Apart from these, the lowest energy transition ($S_0 \rightarrow S_4$) occurs between the HOMOs mainly located at the azopyridine chromophore (Figure 5.8 (a)) and the LUMO which is also associated with the azopyridine. The same orbitals, however, with opposite contributions of the respective HOMOs are responsible for the $S_0 \rightarrow S_{14}$ transition. The more pronounced distortion of the planes of the aromatic rings of the azopyridine in **1** compared to **1'** with a C-N-N-C dihedral angle of $\sim 19^\circ$ makes the assignment of the azopyridine HOMOs (Figure 5.8(a)) to the n and π orbitals ambiguous. The significant differences in the calculated oscillator strengths, however, allow for a clear assignment of the S_4 and S_{14} state to $n\pi^*$ and $\pi\pi^*$ transitions of the azopyridine moiety, respectively. The electronic states S_5 – S_7 exhibit MLCT character, since excitation energy is shifted from the Fe(II) HOMOs to the azopyridine LUMO. A further set of d-d transitions gives rise to the electronic states S_8 – S_{10} which are thus also not listed in Table

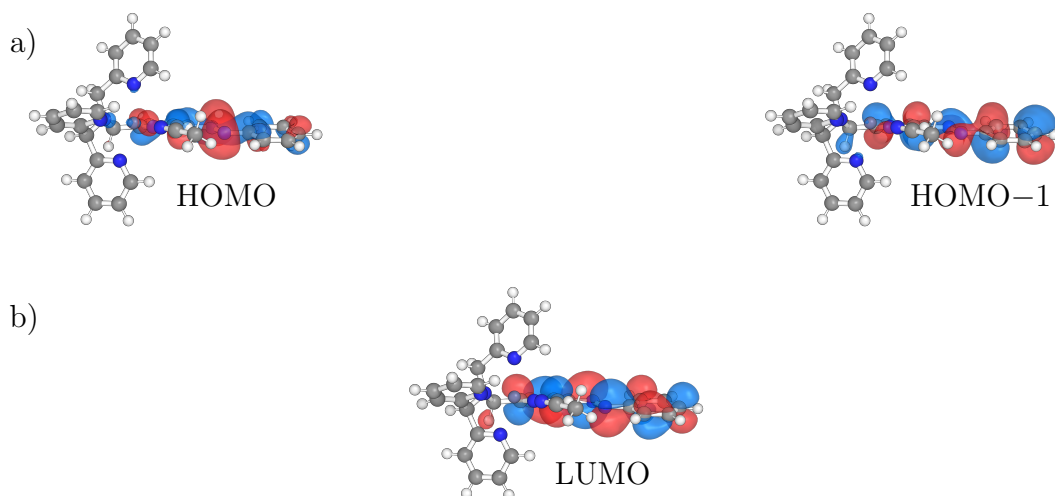


Figure 5.7: B3LYP/def2-TZVP optimized molecular structures together with highest occupied molecular orbitals (HOMOs, a) and lowest unoccupied molecular orbital (LUMO, b) that contribute predominantly to the relevant electronic transitions in the UV–vis range of $[\text{Zn}(\text{3AzoN4Py})(\text{MeCN})]^{2+}$ (**1'**).

5.1. Eventually, the MLCT transitions giving rise to the states S_{11} – S_{13} shift the excitation energy from the Fe(II) HOMOs to the LUMO–1, which is mainly associated with the non-azopyridine part of the ligand.

In summary, the results of the quantum chemical calculations further support the assumption that the applied experimental ($\lambda_{\text{pump}} = 314$ nm, acetonitrile) conditions in the femtosecond TEAS study of **1** initially excite the $\pi\pi^*$ state of the azopyridine ligand, which carries the by far largest oscillator strength of all states in the accessed spectral range. Furthermore, the calculations predict a multitude of MLCT states in a narrow energy range below the photoproduct state, that represent viable candidates for the energy transfer to the identified metal-centered quintet state (^5MC).

For a further systematic investigation of this energy-transfer process, the Ru(II) analogue represents another interesting reference compound for the identification of possible intermediates such as MLCT states. In the ruthenium analogue, the ligand-field states are raised in energy, while the MLCT state remain basically unaffected.^[11] Therefore, possible energy transfer to the MLCT states is preserved whereas their ultrafast deactivation to the low-lying ligand field states, that complicates their identification in the iron complex, is slowed down. Additionally, investigation of the Co(III) analogue could be worthwhile as this system supposedly represents the intermediate case between the Fe(II) and the Zn(II) complex, with the MLCT states shifted to slightly higher energies, while still being in the possession of low-lying ligand-field states that enable a spin-crossover. A systematic investigation of the photoisomerization behavior

of azobenzene-bound Co(II) and Co(III) tris(bipyridine) complexes was already presented by Nishihara and co-workers.^[12] They identified a strong deactivation of the photo-excited azobenzene states depending on the oxidation state of the cobalt ion which was assigned to electron transfer from the azobenzene ligand to the cobalt center.^[12] In general, a previous study of the electrochemical properties of the used ligands and metal ions by cyclic voltammetry provides useful information about the CT states which may help to get to a more rational design of these compounds.

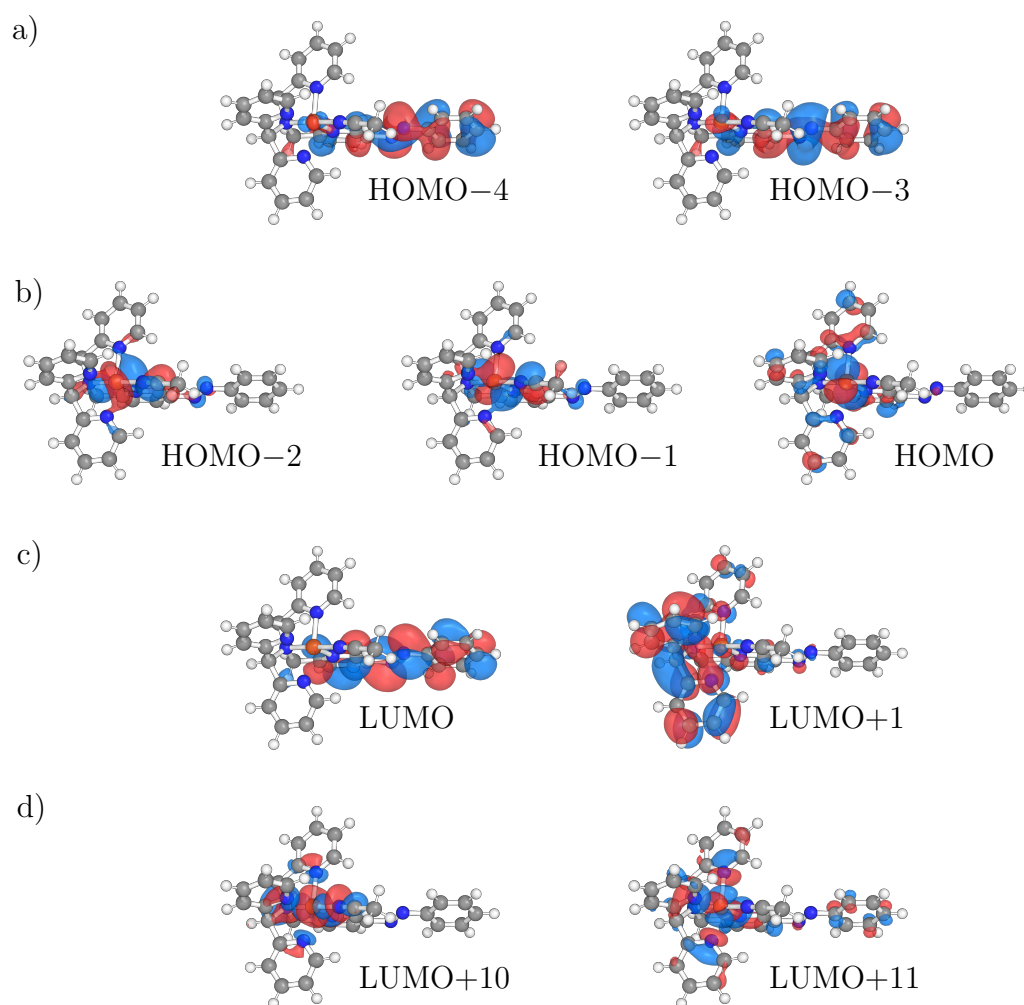


Figure 5.8: B3LYP/def2-TZVP optimized molecular structures together with highest occupied molecular orbitals (HOMOs) and lowest unoccupied molecular orbitals (LUMOs) associated with the ligand (a,c) and the metal center (b,d) that contribute predominantly to the relevant electronic transitions in the UV-vis range of $[\text{Fe}(\text{3AzoN4Py})(\text{MeCN})]^{2+}$ (**1**).

Table 5.1: B3LYP/def2-TZVP calculated excitation energies and oscillator strengths of the of the relevant transitions in the UV – vis range of 3AzoN4Py (**3**), [Zn(3AzoN4Py)(MeCN)]²⁺ (**1'**) and [Fe(3AzoN4Py)(MeCN)]²⁺ (**1**) together with the associated molecular orbitals. Listed are only orbitals that carry a contribution of >10 % to the respective transition. Electronic states S₁–S₃ and S₈–S₁₀ of **1** are not listed as they arise exclusively from d-d transitions and thus carry vanishingly small oscillator strengths.

Compound	State	Transition	Contribution / %	Oscillator Strength	Excitation Energy / eV (nm)
3	S ₁	HOMO → LUMO	97.4	0.0447	2.47 (503)
	S ₂	HOMO–2→ LUMO	93.3	0.0031	2.58 (480)
	S ₃	HOMO–1→ LUMO	95.9	0.8722	3.47 (357)
1'	S ₁	HOMO → LUMO	85.7	0.0038	2.52 (493)
		HOMO–1→ LUMO	14.3		
	S ₂	HOMO–1→ LUMO	85.5	0.9217	3.56 (348)
1		HOMO → LUMO	14.5		
	S ₄	HOMO–3→ LUMO	53.4	0.0072	2.50 (495)
		HOMO–4→ LUMO	35.1		
	S ₅	HOMO → LUMO	100.0	0.0094	2.75 (451)
	S ₆	HOMO–1→ LUMO	91.4	0.0045	2.93 (423)
	S ₇	HOMO–2→ LUMO	88.9	0.0063	2.98 (415)
	S ₁₁	HOMO → LUMO+1	87.9	0.1385	3.31 (375)
		HOMO–2→ LUMO+1	12.1		
	S ₁₂	HOMO–1→ LUMO+1	87.8	0.0079	3.43 (362)
	S ₁₃	HOMO–2→ LUMO+1	75.0	0.1704	3.46 (359)
	S ₁₄	HOMO–4→ LUMO	55.8	0.7119	3.52 (352)
		HOMO–3→ LUMO	33.9		

References

- [1] Geersing, A.; Ségaud, N.; Van Der Wijst, M. G.; Rots, M. G.; Roelfes, G. *Inorg. Chem.* **2018**, *57*, 7748–7756.
- [2] Kohn, W.; Sham, L. J. *Phys. Rev.* **1965**, *140*, A1133–A1138.
- [3] Becke, A. D. *J. Chem. Phys.* **1993**, *98*, 5648–5652.
- [4] Lecklider, T. *EE: Evaluation Engineering* **2011**, *50*, 36–39.
- [5] Weigend, F.; Ahlrichs, R. *Phys. Chem. Chem. Phys.* **2005**, *7*, 3297–3305.
- [6] Barone, V.; Cossi, M.; Tomasi, J. *J. Chem. Phys.* **1997**, *107*, 3210–3221.
- [7] Cossi, M.; Scalmani, G.; Rega, N.; Barone, V. *J. Chem. Phys.* **2002**, *117*, 43–54.
- [8] Tomasi, J.; Mennucci, B.; Cammi, R. *Chem. Rev.* **2005**, *105*, 2999–3093.
- [9] Adamo, C.; Jacquemin, D. *Chem. Soc. Rev.* **2013**, *42*, 845–856.
- [10] Frisch, M. J. Gaussian09. 2009.
- [11] Wenger, O. S. *Chem. Eur. J.* **2019**, *25*, 6043–6052.
- [12] Yamaguchi, K.; Kume, S.; Namiki, K.; Murata, M.; Tamai, N.; Nishihara, H. *Inorg. Chem.* **2005**, *44*, 9056–9067.

6 Ultrafast Intersystem Crossing and Structural Dynamics of $[\text{Pt}(\text{ppy})(\mu\text{-}^t\text{Bu}_2\text{pz})]_2$

Lars Mewes,^{†,*} Rebecca A. Ingle,^{†,*} Sebastian Megow,[‡] Hendrik Böhnke,[‡]
Etienne Baranoff,[§] Friedrich Temps[‡] and Majed Chergui[†]

[†]Laboratoire de spectroscopie ultrarapide and Lausanne Centre for Ultrafast Spectroscopy, Ecole Polytechnique Fédérale de Lausanne, ISIC, FSB Station 6, CH-1015 Lausanne, Switzerland

[‡]Institut für Physikalische Chemie, Christian-Albrechts-Universität, Olshausenstrasse 40, 24098 Kiel, Germany

[§]School of Chemistry, University of Birmingham, Edgbaston, Birmingham B15 2TT, United Kingdom

Reprinted with permission from
Inorg. Chem., **2020**, *59*, 14643-14653
Copyright 2020 American Chemical Society.

OWN CONTRIBUTIONS TO THIS MANUSCRIPT:

- Femtosecond time-resolved fluorescence up-conversion spectroscopy (FIUPS),
- Analysis of experimental FIUPS data.

*To whom correspondence should be addressed. Email: lars.mewes@tum.de, r.ingle@ucl.ac.uk

Abstract

Intersystem crossing (ISC) rates of transition-metal complexes are determined by the complex interplay of a molecule's electronic and structural dynamics. To broaden our understanding of these key factors, we investigate the case of the prototypical d^8-d^8 dimetal complex $[\text{Pt}(\text{ppy})(\mu\text{-}^t\text{Bu}_2\text{pz})]_2$ using broadband transient absorption anisotropy in combination with ultrafast fluorescence up-conversion and ab initio calculations. We find that, upon excitation of the molecule's metal-metal-to-ligand charge-transfer transition, ISC occurs in hundreds of femtoseconds from the lowest excited singlet state S_1 to the triplet state T_2 , from where the energy relaxes to the lowest energy triplet state T_1 . ISC to the T_2 state, rather than T_1 , is further rationalized through supporting arguments. Observed vibrational coherences along the Pt-Pt mode are attributed to the formation of nuclear wavepackets on the ground and excited electronic states that dephase prior to ISC because of the structural flexibility of the complex. Beyond demonstrating the relationship between the energy relaxation and structural dynamics of $[\text{Pt}(\text{ppy})(\mu\text{-}^t\text{Bu}_2\text{pz})]_2$, our results provide new insights into the photoinduced dynamics of d^8-d^8 dimetal complexes more generally.

6.1 Introduction

Understanding the mechanistic details of photoinduced processes relies on disentangling the different energetic relaxation mechanisms within the photoexcited molecule and their interplay with its environment. The main nonradiative intramolecular processes include intramolecular vibrational redistribution (IVR), internal conversion (IC), which is due to an electronic transition between states of the same spin, and intersystem crossing (ISC), involving states of different spin multiplicity. All of these processes may be accompanied by significant changes of the molecular structure, as well as dynamics of the molecule's solvation shell, which is due to the solvent molecules rearranging in response to an electronic redistribution in the solute. The hierarchy of time scales derived from organic photophysics is that IVR occurs in a few to tens of picoseconds, IC in tens of picoseconds to nanoseconds, and ISC in tens of picoseconds to tens of nanoseconds. The latter can typically be accelerated by the presence of "heavier" atoms with large spin-orbit coupling (SOC) constants, the so-called "heavy-atom effect". However, a body of evidence has emerged in the past 20 years that shows significantly different scenarios in the case of inorganic molecular complexes. Specifically, all nonradiative processes are accelerated to the picosecond-femtosecond time domain and show comparable rates.^[1,2] Furthermore, the ISC rates no longer scale with the SOC constant of the metal center(s) as, for example, complexes containing a single metal atom, such as ruthenium,^[3] iron,^[4,5] or rhenium^[6,7] exhibit ultrashort ISC times ($<50\text{--}150$ fs), while complexes with two heavy metals such as the diplatinum complex $[\text{Pt}_2(\text{P}_2\text{O}_5\text{H}_2)_4]^{4-}$

(commonly known as Ptpop) exhibit ISC rates ranging from hundreds of femtoseconds to tens of picoseconds depending on the solvent.^[8–12] As discussed in the literature,^[13] it was concluded that while a large SOC constant is a necessary condition for ultrafast ISC in these systems, it is not a sufficient one, and factors such as the structural dynamics of the system and its density of states also play a crucial role. Disentangling and quantifying these processes is non-trivial because of the electronic and structural complexity of metal complexes. In our previous studies on rhenium carbonyl-polypyridine complexes,^[6,14,15] and on corroles,^[16] this was achieved using time-resolved fluorescence spectroscopy in combination with the substitution of one of the ligands by various halogen atoms, and especially from the former studies, it was concluded that the structural and solvent dynamics play an important role. The influence of the density of states on the ISC can be observed in many bimetallic compounds such as the above-mentioned Ptpop, the more rigid Ptpop-BF₂, and the structurally similar [Ir₂(1,8-diisocyanomethane)₄]²⁺, Ir-(dimen), which undergo significantly slower ISC than would be anticipated based on the large SOC constant of the metal atoms alone. For Ptpop, the solvent-dependent ISC time ranges from 0.7 to 30 ps,^[8,12] for Ptpop-BF₂, it increases to nanoseconds,^[17] and for Ir(dimen), it is on the order of 70 ps.^[18] This quite clearly illustrates the subtle distinction between the metal atoms' SOC constants and the effective SOC, determining the ISC rate.^[13] Despite the impressive 4000 cm⁻¹ SOC constant of the Pt 5d electrons,^[19] the slow ISC in the above Pt₂ complexes was associated with the low density of states and the fact that coupling between the S₁ and T₁ states, which have the same electronic character, is small because of the symmetry-forbidden nature of the transition. Furthermore, the nearly parallel shape of the S₁ and T₁ potential energy surfaces (PESs) along the Pt–Pt bond coordinate, and their large energetic separation (0.5 eV) results in a low probability of crossings between the states and, consequently, a slow ISC rate. The dramatic acceleration of the ISC rate of Ptpop in acetonitrile (0.7 ps) was attributed to the strong stabilization of an energetically higher-lying ligand-to-metal–metal charge-transfer (LMMCT) triplet state with different electronic character, and therefore a stronger coupling to S₁, playing the role of an intermediate state for ISC from S₁ to T₁.^[10]

Because the electronic structure of a molecule strongly determines its underlying nuclear dynamics, the latter is expected to have a strong influence on the ISC rates. This is exemplified by the structurally more rigid Ptpop-BF₂, whose ISC is much slower compared to Ptpop, as mentioned above.^[17] A similar trend was observed for very rigid isocyanide-bridged complexes of rhodium(I) and iridium(I) that, again, undergo ISC more slowly than the 70 ps reported for Ir(dimen).^[18,20] The reason is that structural rigidity may hinder the ability to explore specific regions of the PESs where couplings between electronic states of different spin multiplicity can occur. Conversely, structural changes may also reduce the overall symmetry of a complex, leading to an increase in the

ISC rate. The latter was demonstrated by gas-phase studies on deprotonated Ptpop, which reported an ISC time scale of 0.7 ps, similar to that of Ptpop in acetonitrile.^[21,22] While it is possible that microsolvation could stabilize a higher-lying intermediate state, analogous to the acetonitrile solvation case, the authors argued that a more probable reason is a reduction in symmetry, leading to the observed enhancement of the ISC rate.^[21]

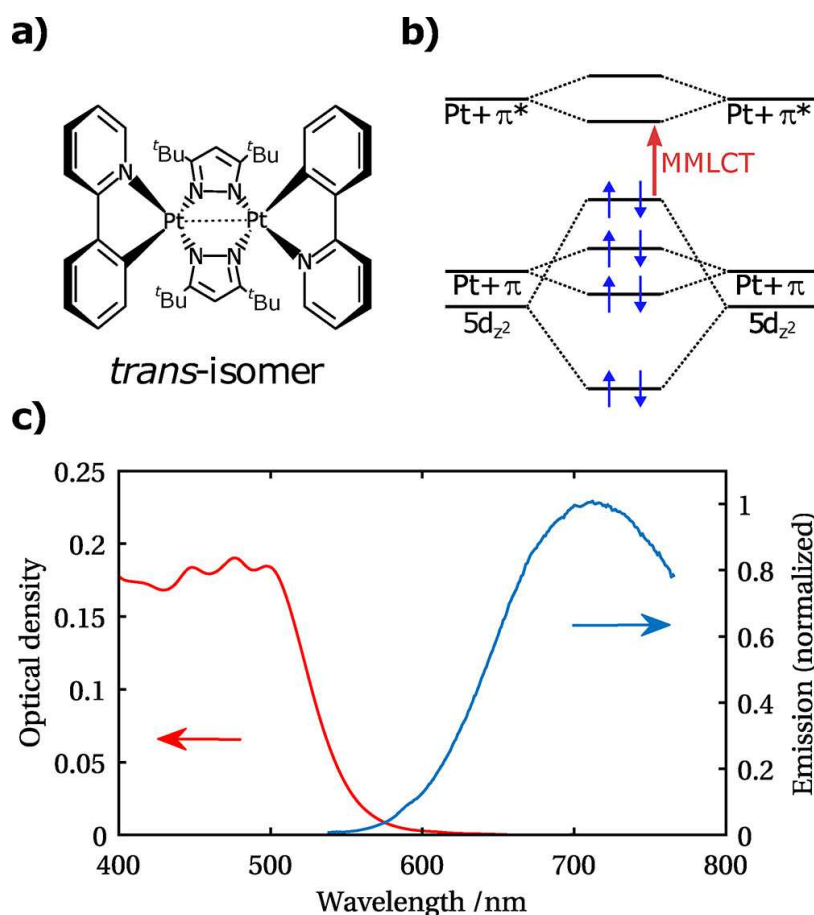


Figure 1: (a) Pseudo-3D molecular structure of the trans isomer of Ptppy and (b) molecular energy level scheme showing a linear combination between the Pt 5d_{z²}, Pt + π , and Pt + π^* molecular orbitals from each half of the complex. In the latter, Pt denotes the orbital contribution from the metal atom, while the π and π^* orbitals are located on the ppy ligands. (c) Absorption spectrum (red) and instrument-response-corrected (see the Supporting Information for details) emission spectrum (blue) of [Pt(ppy)(μ -*t*Bu₂pz)]₂ in toluene.

The above discussion underscores the importance of disentangling the various factors determining the ISC rates in (bi)metallic complexes. Pursuing our previous efforts in this respect,^[8–10] here we investigate the photophysics of [Pt(ppy)(μ -*t*Bu₂pz)]₂ (Ptppy; ppy = 2-phenylpyridine; *t*Bu₂pz = 3,5-ditertbutyl-

pyrazolate; Figure 1a). While the character of its central Pt–Pt bond is reminiscent of Ptpop ($R_{\text{Pt-Pt}}$ 2.97 Å vs $R_{\text{Pt-Pt}}$ 2.93 Å in Ptpop), Ptppy exhibits a more “open” and flexible structure because the ppy ligands are nonbridging.^[12,23–28] Excitation of the lowest-energy transition of Ptppy promotes an electron from a $d\sigma^*$ orbital to one delocalized over the two metals and ppy ligands ($\text{Pt} + \pi^*$; Figure 1b). This metal–metal-to-ligand charge-transfer (MMLCT) transition results in a decreased Pt–Pt bond order and contraction of the interatomic distance in the excited state, with distances of 2.83 Å being reported for the lowest triplet state (vs 2.97 Å for the ground state).^[12,23–25] The ligand–ligand interactions and their dependence on the Pt–Pt distance in Ptppy have initially raised interesting questions about the possibility of electronic coherences, i.e., population of a superposition of electronic states being formed upon electronic excitation, because transient absorption anisotropy (TAA) measurements with monochromatic detection showed an antiphase oscillation of the parallel and perpendicular polarization components, which was attributed to the electronic density hopping back and forth between the ligands.^[29] The transition from a high-frequency (320 cm^{-1}) to a low-frequency (110 cm^{-1}) oscillation within 60 fs was interpreted as being due to ISC.^[29] However, later calculations indicated that the energy gap between the electronic states that need to be populated coherently for an electronic coherence to occur would correspond to an oscillatory period of 10–20 fs, and, consequently, the observed oscillations were reassigned to vibrational coherences.^[30–34] In the description by Chen and co-workers, excitation of the MMLCT transition leads to ISC in less than 150 fs, and it was suggested that the initially prepared vibrational coherence is preserved during the ISC process and evolves on the triplet PES, where it eventually undergoes damping on a ~ 670 fs time scale. The subsequent subpicosecond to a few picosecond dynamics observed in these experiments were attributed to IC and energetic relaxation in the triplet manifold of states. From the lowest-energy triplet state, the molecule then undergoes nonradiative relaxation and phosphorescence on a $0.95\text{ }\mu\text{s}$ time scale.^[24,25,35] Therefore, in the spirit of this special issue on “Light Controlled Reactivity of Metal Complexes”, d^8 – d^8 complexes offer an ideal playground based on previous optical and X-ray studies.^[15,17,21,22,24–28,30,32–36] Control of their reactivity can be exerted via (a) solvent effects (e.g., the case of Ptpop in acetonitrile), (b) increased rigidity (e.g., Ptpop- BF_2), (c) substitution of the metal center (Pt, Ir, and Rh), and (d) engineering of ligands, which affects both the energetics and density of states of the systems. However, in the case of lightcontrolled reactivity, one additional parameter is the light field itself, which can impart its coherence to the system via the generation of vibrational wavepackets. This effect has already been observed in metal complexes^[37] and other systems^[38,39] but its success rests on a detailed understanding of the relaxation pathways and the dissipation processes alongside. Thus, following our studies^[8–10,26–28,36] and those by others^[11,12,21,22,25,30,32–35,40] on diplatinum complexes, here we investigate the nature and character of the ISC in Ptppy

in more detail, using a combination of fluorescence upconversion spectroscopy (FIUPS), transient absorption (TA), and broad-band TAA, as well as *ab initio* calculations. Through characterization of the transient spectral signatures, we determine that ISC occurs with a detection-energy-dependent time constant of 0.5–0.8 ps, significantly longer than previously reported. Therefore, vibrational dephasing occurs prior to ISC, shedding new light on the ultrafast photophysics of Ptpy.

6.2 Experimental Section

Sample Preparation and Characterization. Ptpy was synthesized according to the procedure of ref 35, yielding two geometrical isomers with a *cis/trans* ratio of $\sim 1:2$. The structure of the *trans* isomer is shown in Figure 1a, and the corresponding *cis* isomer has the relative orientation of the ppy ligands reversed. Because the isomers are experimentally inseparable, *ab initio* calculations have been used to assess the differences in their absorption spectra and subsequent photophysics. From the computational results presented in this work, no significant deviation in the excited-state photophysics of the two isomers is expected. Absorption and emission spectra of Ptpy in toluene have been measured on $\leq 15 \mu\text{M}$ solutions inside a 1 cm cuvette and are shown in Figure 1c. The absorption spectrum was recorded on a Shimadzu UV-3600 UV–vis spectrometer and is in good agreement with previously published data,^[29,35] with three bands centered at 499, 476, and 447 nm and a molar absorption coefficient of $\sim 6000 \text{ M}^{-1} \text{ cm}^{-1}$ at 499 nm. The $\sim 100\text{-nm}$ -wide emission band, recorded on a Shimadzu RF-5301PC spectrometer, is centered at 710 nm and has been corrected for the spectral response of the fluorometer.^[41] Details can be found in the Supporting Information. In order to achieve an optical density (OD) sufficient for the TA and FIUPS measurements with a 1 mm path length, a saturated solution was prepared by first dissolving Ptpy in toluene until a solid residue was observed. Sonication of the suspension was performed to further increase the Ptpy concentration. Filtration and subsequent evaporation of the solvent by sparging the solution with argon or evaporation of the solvent under vacuum (23 °C, 30 mbar) yielded a supersaturated solution with an OD between 0.15 and 0.2 at 499 nm for a path length of 1 mm. Under these conditions, the solution remained stable for 2–3 days, after which aggregate formation was observed via the appearance of a characteristic broadening on the red side of the absorption spectrum, as well as via the increase of scattering and the precipitation of a solid residue. This is discussed in more detail in Figure S1.

FIUPS. The single-color-detected femtosecond FIUPS setup was described previously in ref 42. Briefly, a Ti:Sa laser (Clark MXR CPA-2001) provides femtosecond laser pulses (150 fs, 775 nm, 1 kHz) that are used to generate 480 nm excitation pulses using a home-built noncollinear optical parametric ampli-

fier (NOPA). A prism compressor is used to achieve a pulse duration of < 50 fs. The sample is circulated inside a 1 mm flow cell with 0.2-mm-thin fused-silica windows, and a beam stop in combination with a Schott WG glass filter is used to block the transmitted and scattered pump light. A large-aperture, 90° off-axis parabolic mirror ($f = 119$ mm; 63.5 mm aperture) is used to collect the fluorescence, which is refocused into a β -barium borate (BBO) crystal, where it is time-gated with the 775 nm fundamental pulse using sum-frequency generation under type I phase-matching conditions. The 100 μ J gate pulses are delayed by a computer-controlled translation stage and focused into the BBO at an angle of $\sim 14^\circ$ with respect to the fluorescence. The up-converted fluorescence signal is monochromatized using a $f = 0.1$ m double monochromator and detected by a photomultiplier (Hamamatsu R1527P) in combination with a preamplifier (Stanford Research SR 445), which records the signal intensity for each time delay. The measurement is repeated for a fixed excitation wavelength over a range of emission wavelengths by rotating the grating of the monochromator, but the wavelength dependences of the upconversion process and of the monochromator are not corrected. The temporal width of the impulsive Raman response of the solvent below 580 nm quantifies the instrument response function (IRF) of the experiment, which is approximately constant for all detection wavelengths with $\sigma \approx 115$ fs. The monochromatic fluorescence decay curves are individually fit with a biexponential function convoluted with a Gaussian function to account for the IRF (Table S1).

TA Spectroscopy. The TA setup was previously described in refs 43 and 44. Briefly, the output (795 nm, 1 kHz, 600 mW) of an amplified femtosecond Ti:Sa laser system (Spectra Physics) is split by a 90/10 (T/R) beamsplitter into a pump and a probe beam. The 500 nm pump pulse is generated using a home-built NOPA and compressed to its Fourier limit of 25–30 fs using a prism compressor, as quantified using second-harmonic-generation frequency-resolved optical gating at the sample position. The polarization of the pump pulse is controlled by a broad-band $\lambda/2$ waveplate and is set to the magic angle at 54.7° , relative to the probe polarization. For anisotropy measurements, the polarization of the pump pulse is set parallel (\parallel) and perpendicular (\perp) with respect to the probe and TAA data are calculated according to

$$r(\lambda, t) = \frac{I_{\parallel}(\lambda, t) - I_{\perp}(\lambda, t)}{I_{\parallel}(\lambda, t) + 2I_{\perp}(\lambda, t)} \quad (6.1)$$

where the signal intensity I depends on the wavelength λ and time delay t . The probe beam is delayed and focused into a 4 mm calcium fluoride (CaF_2) crystal, generating a white-light continuum from 380 to 900 nm. The 750–850 nm region is blocked by a bandstop filter to decrease the average power of the probe pulse on the sample. The pump and probe beams are overlapped at the sample position with full-width half-maximum (fwhm) foci diameters of ~ 150 and 20 μm , respectively, to guarantee a homogeneous excitation across

the probe volume, and the pump pulse energy is adjusted to ~ 200 nJ. After the sample, the probe beam is focused onto the entrance of a multimode optical fiber and coupled into a grating spectrograph. The dispersed white light is imaged onto a home-built line charge-coupled device (CCD) sensor, which is read out using in-house data acquisition software. The temporal resolution of the experiment is on the order of 190 fs (fwhm), as determined by fitting the strong coherent artifact^[45–48] of the Ptpy measurement and of an auxiliary solvent-only measurement. The coherent artifact resembles the one observed in an auxiliary solvent-only measurement (Figure S7), and no contribution is observed that could be associated with the Ptpy dynamics or kinetics convoluted with it. Time constants and decay-associated spectra (DAS) are extracted from the raw data by global analysis according to refs 49 and 50, the details of which are included in the Supporting Information.

Computational Methodology. Ground- and excited-state geometries of both Ptpy isomers were optimized in vacuo using density functional theory (DFT) with the PBE0 functional.^[51,52] A 6-31G(d) basis set was used for C, H, and N atoms and an effective core potential (ECP) and a LANL2DZ basis set for the Pt atom.^[53,54] These calculations were carried out using the *Gaussian09*, revision D.01, package.^[55] Natural transition orbitals (NTOs) were generated using *THEODORE v1.7.2* and are included in Figure S9.^[56] To investigate the contribution of the low-lying singlet states to the absorption spectrum and examine possible differences between the absorption properties of the cis and trans isomers, 80 molecular geometries were sampled from an approximate Wigner distribution for uncoupled harmonic oscillators. The sampling was performed at the LR-TDDFT/PBE0/6-31G(d) level of theory with a LANL2DZ ECP and corresponding basis set for Pt, starting from a ground-state equilibrium geometry for each isomer. Full-linear-response timedependent DFT (TDDFT) was used unless otherwise stated. The same set of sampled geometries with the same level of theory were used to calculate both the gas-phase absorption spectrum and the absorption spectrum with an implicit solvent mimicking the dielectric response of toluene. The sampling and subsequent excited-state excitation energy calculations were carried out using *NEWTON-X V2.0*^[57,58] interfaced with *Gaussian09*.^[55] The SOC matrix elements are calculated using a perturbative approach to the zeroth-order relativistic approximation (ZORA) relativistic Hamiltonian,^[59,60] as implemented in *ADF 2017.113*.^[61–63] Calculations were carried out on the optimized ground-state geometry using the PBE0^[51,52] exchange-correlation functional with a DZP basis set on the light atoms and an TZP basis set on Pt, with scalar relativistic effects included using ZORA. The magnitudes of the SOC matrix elements between the first singlet state (S_1) and first two triplet states (T_1 and T_2) are calculated as $|H_{S_1T_n}^{\text{SOC}}| = \sqrt{|H_{S_1T_n,x}^{\text{SOC}}|^2 + |H_{S_1T_n,y}^{\text{SOC}}|^2 + |H_{S_1T_n,z}^{\text{SOC}}|^2}$.

6.3 Results and Discussion

Time-Resolved Fluorescence. Given the complexity of the TA signal reported in refs 29, 30, and 32, we perform FLUPS to unambiguously identify the lifetime and spectral shape of the transient fluorescence upon 480 nm excitation. For a range of detection wavelengths, the fluorescence time traces in Figure 2 show an IRF-limited rise, implying that the fluorescing state is promptly populated. This can also be seen from the normalized fluorescence traces in Figure S2. Below ~ 580 nm, the signal is dominated by the impulsive Raman response of toluene, while above ~ 580 nm, the IRF-limited rise is followed by a subpicosecond decay, which becomes increasingly longer as a function of the emission wavelength. An additional few to tens of picosecond decay with low amplitude (5-10%) is observed at longer wavelengths, and the full results are summarized in Table S1. Even though the signal has not been corrected for the spectral response of the experiment, the subpicosecond emission band is clearly situated between the first absorption band and the phosphorescence spectrum (Figure 1c); i.e., it corresponds to the fluorescence from a singlet state. These results show that the ISC time constant is longer than the previously reported ≤ 150 fs.^[29,30,33] The increase of the time constant from 0.5 to 0.8 ps between 570 and 650 nm with a standard error of 20–50 fs is not accompanied by a delayed rise of the signal at longer wavelengths (cf. the normalized fluorescence decay traces in Figure S2), as is typically observed for dynamical Stokes shifts, vibrational cooling, or relaxation among excited singlet states. Furthermore, additional electronic states are not found in this energy region, according to our computational results (vide infra). Instead, the fact that the higher-energy components of the fluorescence decay more rapidly hints at an activation barrier of the energy relaxation pathway, for which the rate of crossing is enhanced when the initial state possesses higher internal energy. This observation provides deeper insight into the mechanistic picture of the energy relaxation pathway, as will be discussed below. The few to tens of picosecond decay component of the transient fluorescence has low amplitude and is difficult to assign to a specific transition or energy relaxation mechanism at this point, but it might be due to part of the population being trapped in the singlet state or it reflects the relaxation within the triplet manifold of states.

Magic-Angle TA. The magic-angle TA of Ptpy at 500 nm is shown as a time-wavelength plot in Figure 3a and as fixed delay time transients in Figure 3b. In TA, negative signals correspond to a ground-state bleach (GSB) or stimulated emission (SE) and positive ones to excited-state absorption (ESA). Beyond the coherent artifact that is observed as a second-order Gaussian derivative at early times, the signal is entirely positive, decays below 500 nm, stays approximately constant around 530 nm, and grows-in above 600 nm, resembling the data by Chen and co-workers.^[30] A global analysis of the TA kinetics shows that it can be described by two exponential decays with a subpicosecond and a

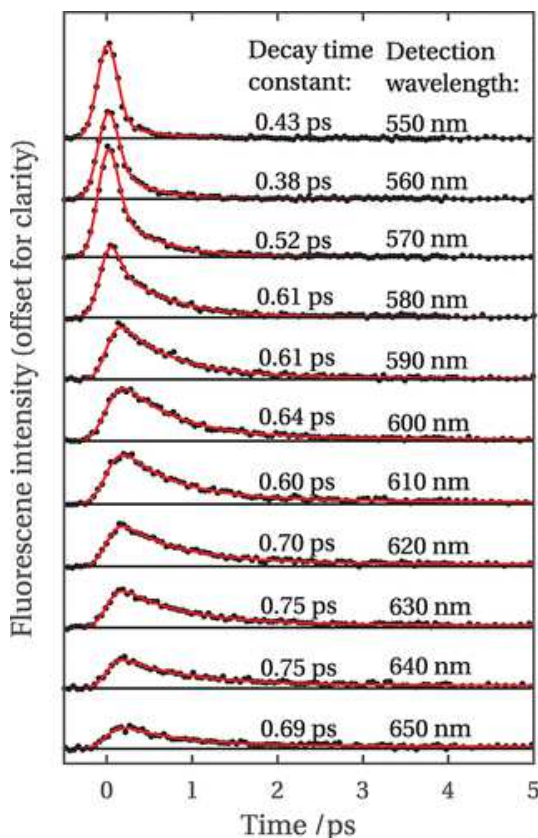


Figure 2: Transient fluorescence time traces after excitation at 480 nm, monochromatically detected between 550 and 650 nm in steps of 10 nm with perpendicular relative polarization of the pump and gate pulses. The time constants for the subpicosecond decay increase with increasing detection wavelength (standard error: 20–50 fs). A second exponential decay with time constants of a few tens of picoseconds is required for fitting of the data, but its amplitude is low. See the text for details.

~ 20 ps time constant, respectively, and a constant offset corresponding to the previously reported $0.95 \mu\text{s}$ decay of the long-lived triplet state.^[35] The DAS are shown in Figure 4 and serve as a guide to determine the time scales involved in the photoinduced kinetics. Beyond the assignment of time scales, the fact that the transient signal is dominated by ESA does not allow a simple kinetic analysis based on the DAS alone, and we thus prefer to discuss the TA signal directly, in combination with the anisotropy and fluorescence observables. In addition to the exponential kinetics, two distinctly different oscillations with frequencies of 100 and 136 cm^{-1} , centered at 540 and 630 nm (highlighted by blue and red vertical lines in Figure 3a), and damping times of 0.2–0.5 ps are observed. These are not observed in FLUPS because the temporal resolution of the fluorescence experiment is not sufficient. Because the signal is entirely positive, the GSB, SE, and ESA components cannot be differentiated by virtue of their sign. This

difficulty is due to a broad and intense ESA that is present immediately after excitation and overlaps with any negative GSB and SE contributions, comparable to the TA data of ref 30. From the steady-state absorption spectrum in Figure 1c, the GSB is expected in the 400–500 nm wavelength region, and the time-resolved fluorescence data in Figure 2 suggest that SE is found in the region between 550 and 650 nm. In order to discuss the TA data and distinguish between the GSB, SE, and ESA signal contributions, we note the occurrence of negative (positive)-*going* transient bands, which are defined as tending toward negative (positive) values regardless of their positive (or negative) amplitude.

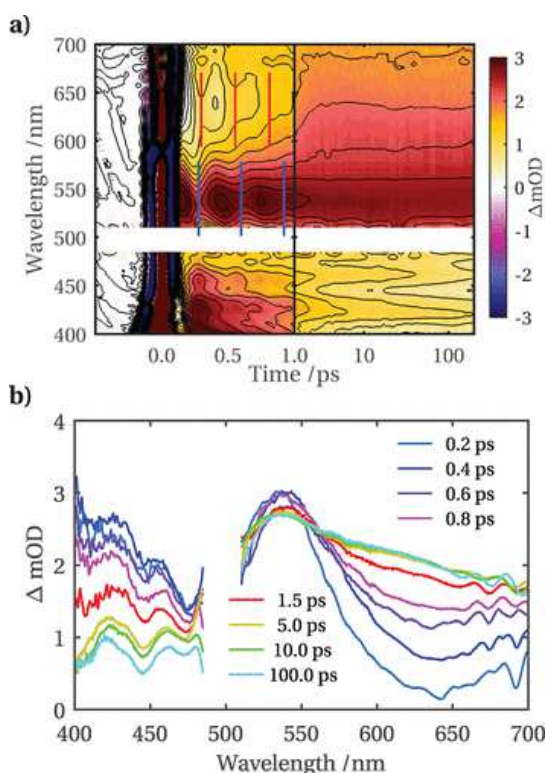


Figure 3: Chirp-corrected, magic-angle TA measurement of Ptpy in toluene excited at 500 nm. (a) Time-wavelength representation that reveals two distinct oscillatory components of the signal during the first 1 ps, highlighted by red and blue vertical lines. (b) Transient spectra at indicated delay times show a strong and broad ESA prohibiting the distinction of GSB, SE, and ESA via the sign of the transient spectrum.

Because the transient fluorescence appears in the 580–630 nm region and has a similar time constant, the TA in this spectral region can be decomposed into a negative-going SE band that is overlapped with the positive ESA signal. This spectral region has previously been interpreted as a “broad band centered at 560 nm” that appears within a few picoseconds,^[30] rather than a decaying SE signal that leaves behind the ESA, as we interpret it here. Congruent to the FLUPS results, we observe an energy dependence of the SE decay within the first

1 ps, which is apparent from the time-wavelength plot in Figure 3a. Additional support for decomposition of the TA spectrum into SE + ESA comes from analysis of its anisotropy (*vide infra*), which, in addition, allows us to identify the GSB contribution below 550 nm. The latter is expected to manifest itself as a negative-going signal at the spectral positions of the absorption bands (447, 476, and 499 nm). The transient feature at 499 nm cannot be observed because the spectral region around 500 nm is obscured by the scattered excitation light. In the spectral region of the GSB + ESA (<550 nm), we observe an additional 20 ps decay component, which is absent in the SE + ESA region (>550 nm), and although it is reminiscent of the one observed in FIUPS, both signals are weak and cannot be identified unambiguously. As was already mentioned, wavepacket oscillations are observed with frequencies of $\sim 100 \text{ cm}^{-1}$ around 540 nm and $\sim 136 \text{ cm}^{-1}$ around 630 nm (indicated by red and blue vertical lines in Figure 3a). Because they are damped within $\sim 0.2\text{--}0.5 \text{ ps}$, a Fourier analysis fails to unambiguously resolve their frequencies, which are instead extracted by analysis of individual time traces (Figure S6). On the basis of the ensuing assignment of all spectral features and identification of the energy relaxation channels, it will become clear that these wavepackets evolve on the ground- and excited-state singlet PESs.

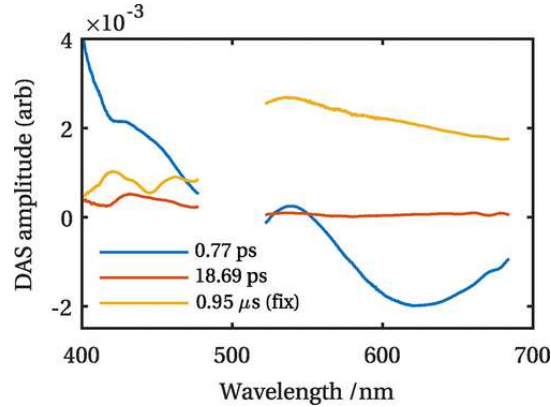


Figure 4: Global fit of the magic-angle data (400–680 nm, excluding the pump wavelength region, as well as delay times of <0.15 ps) revealing three time constants and their DAS.

TAA. The anisotropy of the TA features helps to assign the transient spectral features observed in the magic-angle TA data. Figure 5 shows TAA spectra at a series of time delays that are calculated according to eq 1 from the transient spectra measured with (a) parallel and (b) perpendicular relative polarization of the pump and probe beams (Figure 6). The values of the anisotropy do not necessarily fall in the conventional range of -0.2 to $+0.4$, as, e.g., in time-resolved fluorescence experiments, because, according to

$$r = \frac{\Delta I_{\text{GSB}}}{\Delta I} r_{\text{GSB}} + \frac{\Delta I_{\text{ESA}}}{\Delta I} r_{\text{ESA}} + \frac{\Delta I_{\text{SE}}}{\Delta I} r_{\text{SE}} \quad (6.2)$$

the TAA of each spectral feature (r_x) is scaled by the intensity of its isolated transient signal (ΔI_x) divided by the total intensity of the TA spectrum (ΔI).^[64] In the present case, the latter is negative over the entire detection wavelength region and temporal window, and, consequently, the factors $\frac{\Delta I_{\text{GSB}}}{\Delta I}$ and $\frac{\Delta I_{\text{SE}}}{\Delta I}$ in eq 2 are negative and, by extension, $\frac{\Delta I_{\text{ESA}}}{\Delta I}$ is positive. As an example, let us consider the contribution of the GSB anisotropy to the total TAA. Because the pumped and probed transition dipole moments are parallel, the anisotropy of a GSB prior to molecular rotation is 0.4. Were the GSB band isolated in the transient data ($\Delta I_{\text{GSB}} = \Delta I$), we would indeed obtain $\Delta I_{\text{GSB}} r_{\text{GSB}} = 1 \times 0.4 = 0.4$. However, if $\Delta I > 0$ due to a spectrally overlapping ESA with $|\Delta I_{\text{ESA}}| > |\Delta I_{\text{GSB}}|$, the observed total TAA becomes negative. Takaya et al. elegantly show how it is possible to decompose a TAA spectrum, for a maximum of two overlapping spectral components.^[65] In the present case, however, the TAA spectrum is too congested for such an analysis, but it is still possible to obtain useful, qualitative information about the electronic relaxation of Ptpy. Below 500 nm, the TAA in Figure 5a shows two negative bands at 447 and 475 nm, matching the spectral positions of the absorption bands (Figure 1c) and negative-going TA bands (Figure 3). When the pump pulse is polarized parallel to the probe (Figure 6a), these bands are enhanced in intensity and have negative amplitude. Together these observations help to assign these transient signals to the negative-going GSB. Above 500 nm, the TAA features a single, ~ 50 nm broad band centered at 620 nm that decays from a value of -0.2 (at 200 fs) to 0 within 1 ps. Its defined shape and the observation of a transient fluorescence signal in the same spectral region suggest that it is due to the SE rather than the ESA, which is much broader and featureless. The larger, negative amplitude of the anisotropy at earlier times is clearly overlapped and modulated (in time and in wavelength) by a combination of the coherent artifact and observed coherences. The temporal evolution of the anisotropy is shown for selected wavelengths in Figure 5b. During the first ~ 10 ps, the anisotropy at 447 and 475 nm (and generally below 500 nm) increases from -0.1 and -0.4 to -0.8 . Note that, in this spectral region, we also observe a slow decay of the magic-angle TA signal on a similar time scale. Above ~ 550 nm, the TAA decays within the first 1 ps to a constant value, before the entire TAA decays to $r = 0$ beyond 10 ps because of rotation of the molecules. A rough calculation confirms that the rotational diffusion time constant^[66] for Ptpy in toluene is on the order of 160 ps. The oscillations of the TAA during the first 1 ps correspond predominantly to a Raman mode of toluene with a frequency of 220 cm^{-1} , and more details of the solvent contribution to the TAA signal can be found in the Supporting Information.

Computational Analysis. To assess the nature of the initially excited state of Ptpy, we perform *ab initio* calculations for both isomers. The computed wavelength-dependent photoabsorption cross sections in Figure S8 show a very broad $S_0 \rightarrow S_1$ transition with significantly higher cross section than that of the $S_0 \rightarrow S_2$ transition at wavelengths of > 475 nm. This implies that optical

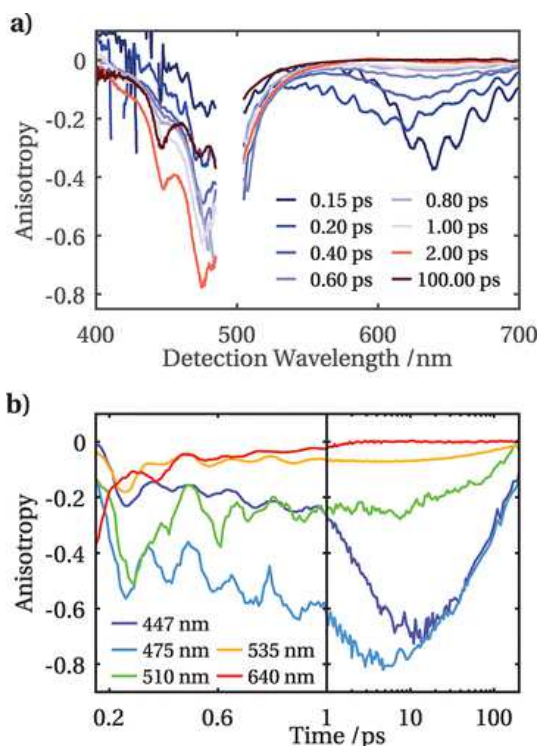


Figure 5: (a) TAA spectra of Ptpy excited at 500 nm. The pump wavelength region is omitted for clarity. (b) Temporal evolution of the anisotropy at selected wavelengths. See the text for details.

excitation at 480–500 nm predominantly populates the S_1 state, thus precluding the formation of a possible electronic coherence with S_2 .^[29,31,33] A detailed description of the calculations, including a comparison of isomers and solvent effects can be found in the Supporting Information.

Figure 7 shows a potential energy cut (PEC) for both Ptpy isomers from the Franck–Condon (FC) region to the S_1 minimum-energy geometry. Calculation of the singlet and triplet vertical excitation energies along the linear interpolation in internal coordinates (LIIC) between the S_0 and S_1 minimum-energy geometries provides insight into potential differences in the reaction pathways for the isomers and the nature of the electronic states involved in the energetic deactivation process. A more detailed description of the LIIC scan can be found in ref 67, but in summary, the LIIC involves an interpolation (in internal coordinates) between two critical geometries on the PES. No reoptimization of the geometries is carried out on this path, so while this does not represent a minimum-energy pathway between two points, these scans offer a clear picture of potential pathways between the selected critical points on the PES and therefore insight into the potential photophysical and photochemical processes that a molecule can undergo. Along the LIIC coordinate, which predominantly involves a contraction of the Pt–Pt distance and deformation of the surrounding

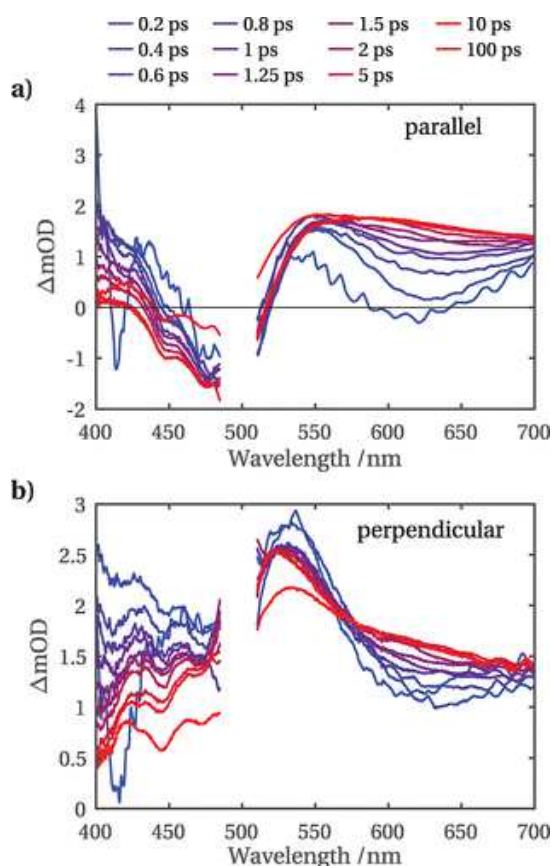


Figure 6: Transient spectra under (a) parallel and (b) perpendicular relative polarization of pump and probe pulses at selected time delays. The pump wavelength region has been omitted for clarity, and the narrow-band, negative-going peaks below 450 nm are due to the coherent artifact.

ligands, the low-lying singlet and triplet states are energetically close, in particular if we focus on the S_1 and T_2 states. Throughout the evolution of the S_1 state along the LIIC coordinate, T_2 is always in close energetic proximity and crosses S_1 close to the FC region. The parallel behavior of the S_1 and T_1 PECs along the LIIC coordinate, on the other hand, attests to their similar electronic character. This can also be seen by inspection of the NTOs in the FC region (Figure S9), which shows that both the $S_0 \rightarrow S_1$ and $S_0 \rightarrow T_1$ transitions are characterized by nearly identical excitations, where the donating orbital of σ^* character is localized on the two metal centers and the accepting orbital is composed of a linear combination of the π^* orbitals located on both ppy ligands, characteristic of a MMLCT excitation. In contrast to this, the $S_0 \rightarrow T_2$ transition is characterized by the same donating orbital as the $S_0 \rightarrow T_1$ transition with an additional contribution from nonbonding Pt 5d orbitals, as well as a larger contribution from the ligand π orbitals. The accepting orbital on the ppy ligand further has a different phase relationship, compared to the accepting

orbital of the $S_0 \rightarrow T_1$ transition, implying a change in the angular momentum that accompanies the energy relaxation from S_1 to T_2 .

The calculated SOC strengths for the trans isomer of 75 cm^{-1} between S_1 and T_2 and 32 cm^{-1} between S_1 and T_1 , in combination with the close energy proximity of S_1 and T_2 in the FC region and the change in orbital angular momentum, imply that ISC will occur between S_1 and T_2 more efficiently than between S_1 and T_1 . Subsequent to ISC, the energy relaxes via IC within the triplet manifold of states from T_2 to T_1 .

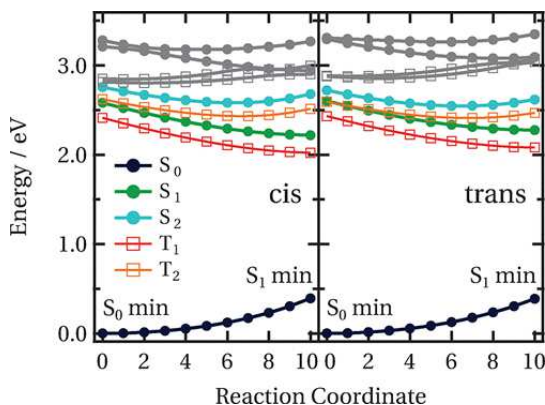


Figure 7: LIICs between the S_0/S_1 minimum-energy geometries for the cis (left) and trans (right) isomers of Ptpy. The filled circles denote singlet states, and the open squares denote triplet states. Excited-state energies were calculated at each point on the LIIC at the TDDFT/PBE0 level of theory within the Tamm–Dancoff approximation. Full details can be found in the Computational Methodology.

Discussion. To discuss the photophysics of Ptpy upon MMLCT excitation, it is crucial to establish a thorough understanding of the nature and number of initially populated electronic states. When including non-Condon effects via the nuclear ensemble approach, our computational results indicate that the $S_0 \rightarrow S_1$ transition is significantly broader and more intense than the $S_0 \rightarrow S_2$ transition (Figure S8) and, therefore, the initial excitation at 480 or 500 nm is expected to predominantly populate the S_1 state. Only little, if any, population is transferred to the S_2 state, precluding the efficient generation of a previously predicted^[29] electronic coherence between S_1 and S_2 . We further consult the computational results to understand whether or not the presence of two isomers influences the experimentally observed photophysics because this is not possible experimentally.^[35] The character of states populated by the excitation, PECs, and ground- and excited-state minimum-energy geometries suggest no major, i.e., observable, differences between their photophysics. However, all time constants extracted from this work should, strictly speaking, be considered combinations of the kinetics of both isomers, bearing in mind the 1:2 cis/trans ratio and differences in the photoexcitation yields of each isomer.

The decay of the fluorescence and SE signals allows us to assign a lifetime of 0.5–0.8 ps to the S_1 state, and considering the fact that Ptpy shows a long-lived phosphorescence (0.95 μ s) with a quantum yield of 0.032 in an argon-saturated toluene solution,^[29] we conclude that the predominant relaxation channel is ISC. The ISC times we report are significantly different from the previously reported sub-150-fs.^[29,30,32] The faster decay of the fluorescence and SE at higher energies, indicated by the range of S_1 lifetimes, is not matched by a commensurate rise of the lower-energy fluorescence components (Figure S2). It thus appears from our experimental results that the ISC is faster from a vibrationally “hot” S_1 state, and the larger amount of internal energy means the system is more likely to reach the S_1/T_n crossing region. The computational results support this hypothesis and strongly indicate that the initial S_1/T_n crossing occurs between S_1/T_2 rather than directly to T_1 . This is because for $S_1 \rightarrow T_2$ the spin change is accompanied by a change in the orbital angular momentum (Figure S9). In addition, the calculated SOC for the trans isomer between S_1 and T_2 is 75 cm^{-1} compared to 32 cm^{-1} between S_1 and T_1 .

Finally, the PECs of S_1 and T_1 along the LIIC coordinate suggest that ISC is most likely near the FC region. The fact that the observed lifetime of the S_1 state exceeds the period of the vibrational coherence, however, implies that ISC does not happen with unity quantum yield immediately after the initial excitation. Instead, the created nuclear wavepacket on S_1 departs from the FC region and, when it returns, a larger internal energy in the form of vibrational energy facilitates the ISC, thus explaining the observed energy-dependent rate.

Subsequently, the energy relaxes to the T_1 minimum via IC and vibrational relaxation within tens of picoseconds, as potentially witnessed by the ~ 20 ps spectral evolution of the ESA below 500 nm (Figures 3 and 4). On a longer time scale, the TA spectrum remains constant, which is attributed to the remaining GSB, as well as the ESA of the phosphorescent triplet electronic ground state, which has a lifetime of $\sim 0.95 \mu\text{s}$.^[29,35]

On the basis of the complete assignment of the transient spectral features and energy relaxation channels, we conclude that the vibrational coherences observed in the magic-angle TA with $\sim 100 \text{ cm}^{-1}$ at 540 nm and $\sim 136 \text{ cm}^{-1}$ at 630 nm occur on the ground and excited states of Ptpy, respectively. The higher frequency of the excited-state vibrational coherence is due to the increase of the Pt–Pt bond order and the associated increase in stiffness of the Pt–Pt vibrational mode, similar to the case of Ptpop.^[8–10] Because the excited-state vibrational coherence is present from time zero and is damped, it is created by exciting a superposition of vibrational eigenstates on the S_1 state with the pump laser field, which has a Fourier-limited bandwidth of $\sim 400 \text{ cm}^{-1}$. Compared to the ~ 2 ps dephasing time observed in Ptpop and Ptpop-BF₂, which is explained by a pure dephasing mechanism allowing the vibrational coherence to be transferred to the triplet manifold of states when the ISC time is shorter,^[8–10] the observed 0.2–0.5 ps dephasing time of the Pt–Pt vibrational coherence in

Ptppy is faster than the ISC time. This is due to the greater structural flexibility of the system, which leads to a wider distribution of initial geometries and, consequently, a greater variability of initial conditions after optical excitation, as well as the availability of low-frequency vibrational modes without a major Pt–Pt component into which excess vibrational energy can be redistributed. Although it is a priori not possible from the TA to distinguish between S_1 and T_2/T_1 vibrational coherences during the first 1 ps, we conclude, from the above, that the coherences occur on the S_1 state and cannot be transferred to the triplet state because their damping is faster than the ISC time.

To answer the question on the importance of the charge-transfer (CT) character of the intermediate state, it is enlightening to identify the differences and similarities between Ptppy and Ptpop, Ptpop- BF_2 , and the gas-phase diprotonated $[\text{Ptpop} + 2\text{H}^+]^{2-}$ complex.^[21,22] A summary of the ISC times of these complexes can be found in Table 2 of ref 10. The initial $S_0 \rightarrow S_1$ excitation in Ptpop and its derivatives populates a metal-centered excited state, whereas in Ptppy, it is of CT character. Depending on the solvent, ISC in Ptpop happens on a subpicosecond to 30 ps time scale, which is notably slow considering the large SOC due to the presence of heavy Pt atoms. This is explained by the fact that the PESs are nested and harmonic and that spin transitions between S_1 and T_1 are symmetry-forbidden.^[9] In the gas phase, the diprotonated complex, $[\text{Ptpop} + 2\text{H}^+]^{2-}$, shows a fast ISC with a time constant of ~ 0.7 ps, which was explained by a symmetry-breaking structural distortion that becomes more accessible without the retaining solvent environment.^[21,22] The importance of structural distortions is supported by studies of perfluoroborated Ptpop, in which the O atoms of different pop ligands are linked by BF_2 groups, yielding a significantly more rigid system with qualitatively similar photophysics, Ptpop- BF_2 . The increased rigidity, higher symmetry, and electron-withdrawing effect of the BF_2 groups of Ptpop- BF_2 lead, however, to a significant decrease of the ISC rate and a lifetime of the S_1 state of 1.6 ns.^[10,17] On the other hand, ISC in Ptpop solvated in acetonitrile, in which the ISC time is reduced to ~ 0.7 ps, demonstrates the relevance of the nature and energetics of intermediate states that mediate the ISC. In this case, higher energy triplet CT states are stabilized by the solvent environment such that they come close to resonance with S_1 , opening an energetic channel for ISC to T_1 .^[10] In the present study, we find that, in Ptppy, ISC happens on a comparable 0.5–0.8 ps time scale from the initially excited CT state, S_1 , to the T_2 state, highlighting the importance of the CT intermediate state in ISC. However, the greater conformational flexibility of the complex also enhances the probability that the system will be able to sample regions of configuration space necessary for efficient ISC.^[1]

6.4 Conclusion

Using TA and TAA in conjunction with FLUPS and *ab initio* calculations, we provide a thorough analysis and interpretation of the dominant energy relaxation channels in Ptpy upon optical excitation of the MMLCT transition, in which an electron is transferred from an antibonding Pt–Pt orbital to the ligand-centered orbitals, forming the S_1 state. The 0.5–0.8 ps decay of the initial singlet ESA and SE signals in TA, concomitant with the decay of the transient fluorescence signal, is due to depopulation of the initially excited S_1 state by an energy-dependent ISC. Vibrational coherences in the ground and excited electronic states dephase within 0.2–0.5 ps because of the flexibility of Ptpy, in which the Pt atoms are only linked by two $t\text{Bu}_2\text{pz}$ groups. Together with the additional conformational degrees of freedom of the ppy ligands, this structural “flexibility” results in an efficient redistribution of the vibrational energy and a loss of the system’s vibrational coherence. *Ab initio* calculations allow us to identify the states involved in the energetic relaxation and their character, which leads to the conclusion that ISC happens from S_1 to T_2 because of the symmetry-forbidden nature of the S_1/T_1 crossing. The observable evolution of the triplet ESA is a weak 20 ps contribution below 500 nm, which is associated with the IC within the triplet manifold of states. Together, the spectroscopic methods and theoretical techniques used in this work help us to disentangle complex optical TA and identify the role of specific electronic states, nuclear motions, and resulting vibrational coherences in the energetic deactivation mechanisms. We show this for the case of Ptpy and anticipate that the methodology in our study will help to analyze and understand the photophysics of other complex systems.

Acknowledgements

This work was supported by the Swiss National Science Foundation via Grants 200020_155893, 200020_169914, and 200021_175649 and via the NCCR:MUST and by the Deutsche Forschungsgemeinschaft through the Collaborative Research Center 677 “Function by Switching”.

References

- [1] Chergui, M. *Dalt. Trans.* **2012**, *41*, 13022–13029.
- [2] Chergui, M. *Acc. Chem. Res.* **2015**, *48*, 801–808.
- [3] Tarnovsky, A. N.; Gawelda, W.; Johnson, M.; Bressler, C.; Chergui, M. *J. Phys. Chem. B* **2006**, *110*, 26497–26505.
- [4] Kjær, K. S. et al. *Chem. Sci.* **2019**, *10*, 5749–5760.
- [5] Auböck, G.; Chergui, M. *Nat. Chem.* **2015**, *7*, 629–633.
- [6] Cannizzo, A.; Blanco-Rodríguez, A. M.; El Nahhas, A.; Šebera, J.; Zális, S.; Vlček, A. J.; Chergui, M. *J. Am. Chem. Soc.* **2008**, 8967–8974.
- [7] Harabuchi, Y.; Eng, J.; Gindensperger, E.; Taketsugu, T.; Maeda, S.; Daniel, C. *J. Chem. Theory Comput.* **2016**, *12*, 2335–2345.
- [8] Van Der Veen, R. M.; Cannizzo, A.; Van Mourik, F.; Vlček, A.; Chergui, M. *J. Am. Chem. Soc.* **2011**, *133*, 305–315.
- [9] Monni, R.; Auböck, G.; Kinschel, D.; Aziz-Lange, K. M.; Gray, H. B.; Vlček, A.; Chergui, M. *Chem. Phys. Lett.* **2017**, *683*, 112–120.
- [10] Monni, R.; Capano, G.; Auböck, G.; Gray, H. B.; Vlček, A.; Tavernelli, I.; Chergui, M. *Proc. Natl. Acad. Sci. U. S. A.* **2018**, *115*, E6396–E6403.
- [11] Biasin, E. et al. *J. Synchrotron Radiat.* **2018**, *25*, 306–315.
- [12] Haldrup, K. et al. *Phys. Rev. Lett.* **2019**, *122*, 63001.
- [13] Turro, N. J.; Ramamurthy, V.; Scaiano, J. C. *Principles of molecular photochemistry: an introduction*; University Science Books, 2009.
- [14] El Nahhas, A.; Cannizzo, A.; Mourik, F. V.; Blanco-Rodríguez, A. M.; Zális, S.; Vlček, A.; Chergui, M. *J. Phys. Chem. A* **2010**, *114*, 6361–6369.
- [15] El Nahhas, A.; Consani, C.; Blanco-Rodríguez, A. M.; Lancaster, K. M.; Braem, O.; Cannizzo, A.; Towrie, M.; Clark, I. P.; Zális, S.; Chergui, M.; Vlček, A. *Inorg. Chem.* **2011**, *50*, 2932–2943.
- [16] Pomarico, E.; Pospíšil, P.; Bouduban, M. E.; Vestfrid, J.; Gross, Z.; Zális, S.; Chergui, M.; Vlček, A. *J. Phys. Chem. A* **2018**, *122*, 7256–7266.

- [17] Durrell, A. C.; Keller, G. E.; Lam, Y. C.; Sýkora, J.; Vlček, A.; Gray, H. B. *J. Am. Chem. Soc.* **2012**, *134*, 14201–14207.
- [18] Pižl, M.; Hunter, B. M.; Greetham, G. M.; Towrie, M.; Zális, S.; Gray, H. B.; Vlček, A. *J. Phys. Chem. A* **2017**, *121*, 9275–9283.
- [19] Piepho, S. B.; Schatz, P. N.; McCaffery, A. J. *J. Am. Chem. Soc.* **1969**, *91*, 5994–6001.
- [20] Gray, H. B.; Zális, S.; Vlček, A. *Coord. Chem. Rev.* **2017**, *345*, 297–317.
- [21] Winghart, M. O.; Yang, J. P.; Vonderach, M.; Unterreiner, A. N.; Huang, D. L.; Wang, L. S.; Kruppa, S.; Riehn, C.; Kappes, M. M. *J. Chem. Phys.* **2016**, *144*.
- [22] Kruppa, S. V.; Nosenko, Y.; Winghart, M. O.; Walg, S. P.; Kappes, M. M.; Riehn, C. *Int. J. Mass Spectrom.* **2016**, *395*, 7–19.
- [23] Ma, B.; Li, J.; Djurovich, P. I.; Yousufuddin, M.; Bau, R.; Thompson, M. E. *J. Am. Chem. Soc.* **2005**, *127*, 28–29.
- [24] Lockard, J. V.; Rachford, A. A.; Smolentsev, G.; Stickrath, A. B.; Wang, X.; Zhang, X.; Atenkoff, K.; Jennings, G.; Soldatov, A.; Rheingold, A. L.; Castellano, F. N.; Chen, L. X. *J. Phys. Chem. A* **2010**, *114*, 12780–12787.
- [25] Haldrup, K.; Dohn, A. O.; Shelby, M. L.; Mara, M. W.; Stickrath, A. B.; Harpham, M. R.; Huang, J.; Zhang, X.; Møller, K. B.; Chakraborty, A.; Castellano, F. N.; Tiede, D. M.; Chen, L. X. *J. Phys. Chem. A* **2016**, *120*, 7475–7483.
- [26] Van Der Veen, R. M.; Milne, C. J.; Nahhas, A. E.; Lima, F. A.; Pham, V. T.; Best, J.; Weinstein, J. A.; Borca, C. N.; Abela, R.; Bressler, C.; Chergui, M. *Angew. Chem., Int. Ed.* **2009**, *48*, 2711–2714.
- [27] Van Der Veen, R. M.; Milne, C. J.; Pham, V. T.; El Nahhas, A.; Weinstein, J. A.; Best, J.; Borca, C. N.; Bressler, C.; Chergui, M. *Chimia* **2008**, *62*, 287–290.
- [28] Penfold, T. J.; Curchod, B. F.; Tavernelli, I.; Abela, R.; Rothlisberger, U.; Chergui, M. *Phys. Chem. Chem. Phys.* **2012**, *14*, 9444–9450.
- [29] Chen, L. X.; Castellano, F. N.; Rachford, A. A.; Lockard, J. V.; Wang, X.; Mara, M. W.; Cho, S. *J. Phys. Chem. A* **2011**, *115*, 3990–3996.
- [30] Brown-Xu, S. E.; Kelley, M. S.; Fransted, K. A.; Chakraborty, A.; Schatz, G. C.; Castellano, F. N.; Chen, L. X. *J. Phys. Chem. A* **2016**, *120*, 543–550.

- [31] Lingerfelt, D. B.; Lestrangle, P. J.; Radler, J. J.; Brown-Xu, S. E.; Kim, P.; Castellano, F. N.; Chen, L. X.; Li, X. *J. Phys. Chem. A* **2017**, *121*, 1932–1939.
- [32] Kim, P.; Kelley, M. S.; Chakraborty, A.; Wong, N. L.; Van Duyne, R. P.; Schatz, G. C.; Castellano, F. N.; Chen, L. X. *J. Phys. Chem. C* **2018**, *122*, 14195–14204.
- [33] Radler, J. J.; Lingerfelt, D. B.; Castellano, F. N.; Chen, L. X.; Li, X. *J. Phys. Chem. A* **2018**, *122*, 5071–5077.
- [34] Valentine, A. J.; Radler, J. J.; Mills, A.; Kim, P.; Castellano, F. N.; Chen, L. X.; Li, X. *J. Chem. Phys.* **2019**, *151*.
- [35] Rachford, A. A.; Castellano, F. N. *Inorg. Chem.* **2009**, *48*, 10865–10867.
- [36] Van Der Veen, R. M.; Kas, J. J.; Milne, C. J.; Pham, V.-T.; El Nahhas, A.; Lima, F. A.; Vithanage, D. A.; Rehr, J. J.; Abela, R.; Chergui, M. *Phys. Chem. Chem. Phys.* **2010**, *12*, 5503–5513.
- [37] Bergt, M.; Brixner, T.; Kiefer, B.; Strehle, M.; Gerber, G. *J. Phys. Chem. A* **1999**, *103*, 10381–10387.
- [38] Wurzer, A. J.; Lochbrunner, S.; Riedle, E. *Appl. Phys. B Lasers Opt.* **2000**, *71*, 405–409.
- [39] Rafiq, S.; Dean, J. C.; Scholes, G. D. *J. Phys. Chem. A* **2015**, *119*, 11837–11846.
- [40] Levi, G.; Pápai, M.; Henriksen, N. E.; Dohn, A. O.; Møller, K. B. *J. Phys. Chem. C* **2018**, *122*, 7100–7119.
- [41] Pfeifer, D.; Hoffmann, K.; Hoffmann, A.; Monte, C.; Resch-Genger, U. *J. Fluoresc.* **2006**, *16*, 581–587.
- [42] Schwalb, N. K.; Michalak, T.; Temps, F. *J. Phys. Chem. B* **2009**, *113*, 16365–16376.
- [43] Helbing, J.; Bonacina, L.; Pietri, R.; Bredenbeck, J.; Hamm, P.; Van Mourik, F.; Chaussard, F.; Gonzalez-Gonzalez, A.; Chergui, M.; Ramos-Alvarez, C.; Ruiz, C.; Lopez-Garriga, J. *Biophys. J.* **2004**, *87*, 1881–1891.
- [44] Schenkl, S.; Van Mourik, F.; Friedman, N.; Sheves, M.; Schlesinger, R.; Haacke, S.; Chergui, M. *Proc. Natl. Acad. Sci. U. S. A.* **2006**, *103*, 4101–4106.
- [45] Ekvall, K.; Van Der Meulen, P.; Dhollande, C.; Berg, L. E.; Pommeret, S.; Naskrecki, R.; Mialocq, J. C. *J. Appl. Phys.* **2000**, *87*, 2340–2352.

- [46] Lorenc, M.; Ziolek, M.; Naskrecki, R.; Karolczak, J.; Kubicki, J.; Maciejewski, A. *Appl. Phys. B Lasers Opt.* **2002**, *74*, 19–27.
- [47] Lebedev, M. V.; Misochko, O. V.; Dekorsy, T.; Georgiev, N. *J. Exp. Theor. Phys.* **2005**, *100*, 272–282.
- [48] Dietzek, B.; Pascher, T.; Sundström, V.; Yartsev, A. *Laser Phys. Lett.* **2007**, *4*, 38–43.
- [49] Fita, P.; Luzina, E.; Dziembowska, T.; Radzewicz, C.; Grabowska, A. *J. Chem. Phys.* **2006**, *125*.
- [50] Slavov, C.; Hartmann, H.; Wachtveitl, J. *Anal. Chem.* **2015**, *87*, 2328–2336.
- [51] Adamo, C.; Barone, V. *J. Chem. Phys.* **1999**, *110*, 6158–6170.
- [52] Perdew, J. P.; Burke, K.; Ernzerhof, M. *Phys. Rev. Lett.* **1996**, *77*, 3865–3868.
- [53] Hay, P. J.; Wadt, W. R. *J. Chem. Phys.* **1985**, *82*, 299–310.
- [54] Wadt, W. R.; Hay, P. J. *J. Chem. Phys.* **1985**, *82*, 284–298.
- [55] Frisch, M. J. Gaussian09. 2009.
- [56] Plasser, F. THEODORE 1.7.2: A Package for Theoretical Density, Orbital Relaxation, and Exciton Analysis. 2018.
- [57] Barbatti, M.; Ruckebauer, M.; Plasser, F.; Pittner, J.; Granucci, G.; Persico, M.; Lischka, H. *WIREs Comput. Mol. Sci.* **2014**, *4*, 26–33.
- [58] Barbatti, M.; Granucci, G.; Ruckebauer, M.; Plasser, F.; Crespo-Otero, R.; Pittner, J.; Persico, M.; Lischka, H. NEWTON-X: A Package for Newtonian Dynamics Close to the Crossing Seam. 2016.
- [59] Van Lenthe, E.; Van Leeuwen, R.; Baerends, E. J.; Snijders, J. G. *Int. J. Quantum Chem.* **1996**, 281–293.
- [60] Wang, F.; Ziegler, T. *J. Chem. Phys.* **2005**, *123*.
- [61] te Velde, G.; Bickelhaupt, F. M.; Baerends, E. J.; Fonseca Guerra, C.; van Gisbergen, S. J.; Snijders, J. G.; Ziegler, T. *J. Comput. Chem.* **2001**, *22*, 931–967.
- [62] Baerends, E. J. ADF2017. 2017.
- [63] Fonseca Guerra, C.; Snijders, J. G.; Baerends, E. J. *Theor. Chem. Acc.* **1998**, *99*, 391–403.

- [64] Wallin, S.; Davidsson, J.; Modin, J.; Hammarström, L. *J. Phys. Chem. A* **2005**, *109*, 4697–4704.
- [65] Takaya, T.; Hamaguchi, H.-o.; Iwata, K. *J. Chem. Phys.* **2009**, *130*, 014501.
- [66] Lee, H. B.; Cong, A.; Leopold, H.; Currie, M.; Boersma, A. J.; Sheets, E. D.; Heikal, A. A. *Phys. Chem. Chem. Phys.* **2018**, *20*, 24045–24057.
- [67] Hudock, H. R.; Levine, B. G.; Thompson, A. L.; Satzger, H.; Townsend, D.; Gador, N.; Ullrich, S.; Stolow, A.; Martínez, T. J. *J. Phys. Chem. A* **2007**, *111*, 8500–8508.

7 A Setup for Multi-Timescale Pump-Supercontinuum Probe Spectroscopy: Full Photocycle of 7-Hydroxyquinoline-8-Carbaldehyde

Sebastian Megow,¹ Ole Hüter,¹ Sebastian Schatz,¹ and Friedrich Temps^{1,}*

¹Institute of Physical Chemistry, Christian-Albrechts-University Kiel,
Max-Eyth-Str. 1, 24098 Kiel, Germany

Manuscript

OWN CONTRIBUTIONS TO THIS MANUSCRIPT:

- Setup of the experiment,
- Characterization of the experimental parameters,
- Pico- to Microsecond transient electronic absorption spectroscopy (TEAS),
- Analysis of the experimental TEAS data,
- Writing of the manuscript.

*To whom correspondence should be addressed. Email: temps@phc.uni-kiel.de

Abstract

A setup consisting of two synchronized femtosecond amplifiers seeded by free-running oscillators is presented, that allows for broadband transient electronic absorption spectroscopy with delay times up to 1 ms. The method is based on *a posteriori* determination of the pump-probe delay using a time-correlated single-photon counting (TCSPC) board with 25 ps base resolution. Its implementation in a preexisting femtosecond transient absorption experiment is straightforward and possible without any changes to the optical setup. As demonstrated for the proposed excited-state proton-transfer switch 7-hydroxyquinoline-8-carbaldehyde, the combined experiments allow for a seamless tracking of the photodynamics of systems that exhibit a distribution of time constants on multiple timescales.

7.1 Introduction

Femtosecond pump-probe spectroscopy is the most common technique for studying the ultrafast dynamics of physically, chemically or biologically relevant systems. The basic principle is to split the beam of a single pulsed laser system into two beams of which one, the pump, triggers a certain photo-induced process in the sample, while the other, the probe, monitors the molecular response. A relative temporal delay between the pump and the probe pulse can be controlled by introducing a variable optical delay to the pump resp. probe beam path. Such techniques usually make use of a mechanical stage with a mounted retroreflector whose position can be precisely set to a certain delay time. Thus, the time resolution associated with the response times of the photodetector is overcome and is ultimately limited to the duration of the employed laser pulses. Practically the length of the delay line limits the maximum accessible time delay to a few nanoseconds as the scanning times increase and variation in beam pointing and defocussing effects have to be considered. However, the photodynamics of many relevant systems such as complex biomolecules do not exclusively take place on ultrafast timescales as they exhibit a distribution of time constants on multiple time scales ranging from just a few femtoseconds up to seconds.^[1–3]

Concepts for turning femtosecond pump-probe into multi-timescale pump-probe experiments have been subject of research for several decades. Most methods make use of two laser systems with one laser acting as pump and the other as probe. One approach, namely asynchronous optical sampling (ASOPS) is a stroboscopic method exploiting slight differences in the repetition rates f_{pump} and f_{probe} of two phase-locked laser oscillators, by generating a pump-probe pulse train with linearly-increasing time delays.^[4–9] As in femtosecond pump-probe spectroscopy, the time delays are predetermined, since after initial

coincidence the evolution of the delays obeys the known law

$$\Delta t_n = n(T_{\text{probe}} - T_{\text{pump}}) \quad (7.1)$$

with the probe pulse number n and the oscillation periods of the pump $T_{\text{pump}} = 1/f_{\text{pump}}$ and the probe $T_{\text{probe}} = 1/f_{\text{probe}}$ laser. This method allows for high scanning rates with sub-picosecond time resolution. However, the maximum accessible delay times are restricted to the period of the reference oscillator, which is typically in the range of 10 ns. Another successful approach relies on using two femtosecond amplifiers seeded by two phase-locked oscillators of identical repetition rates.^[10–12] In this setup fine tuning of the delay can be achieved by shifting the relative phase between the oscillators, while coarse tuning is achieved through electronic control of the amplifier delays. Thus, the ultimate delay time was extended to the amplifier period, which is in the range of milliseconds for typical kHz systems. However, as this approach requires a piezo ring actuator acting on the probe oscillator cavity to match the round trip periods ($T_{\text{pump}} = T_{\text{probe}}$), its implementation is not straightforward. Joffre and co-workers impressively presented a new variant of the ASOPS method, coined arbitrary detuning ASOPS (ADASOPS), applicable to any pair of independent free-running femtosecond oscillators.^[13] In contrast to previous methods, here, the pump-probe delays are determined *a posteriori* with sub-picosecond time resolution. This concept was subsequently applied to femtosecond amplifiers allowing for a multiscale pump-probe application ranging from sub-picoseconds to milliseconds.^[14] Further improvements on the scanning speed and control over the time delays, which usually follows a uniform distribution owing to the timing jitter between the oscillators, as well as coincidence detection were recently reported.^[15–17] Other than the randomly-interleaved-pulse-train (RIPT) method,^[18] that purely relies on *a posteriori* electronic detection of the delays and thus exhibits poorer time resolution, ADASOPS exploits the great clock stability of femtosecond oscillators.^[17]

In contrast to the aforementioned conceptional methods our approach is a rather practical one, aiming for the extension of the timescales of an existing femtosecond pump-probe experiment working with predetermined mechanical delays by introduction of a second laser system. The delays in the nano- to microsecond range are obtained by an electronic delay generator introduced between the two coupled femtosecond amplifiers, which are seeded by two independent oscillators. Delays in the pico- to nanosecond range are obtained by *a posteriori* determination of the pump-probe delays using a time-correlated single-photon counting (TCSPC) board and subsequent recovery of the time axis. The combination of all techniques allows for the seamless detection of broadband time-resolved electronic absorption spectra from a few femtoseconds up to a millisecond.

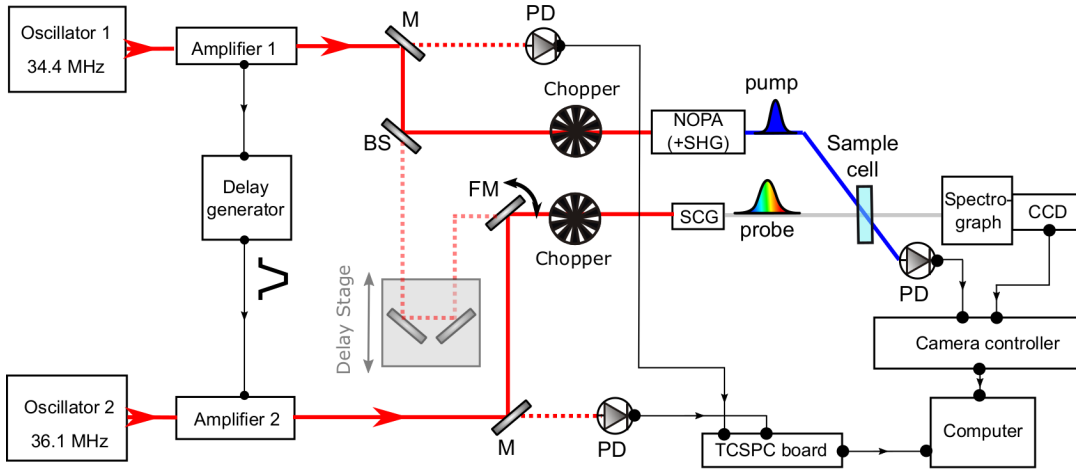


Figure 1: Sketch of the nanosecond time-resolved electronic absorption (TEAS) setup. The beam path for the corresponding femtosecond TEAS setup is displayed in pale colors. BS: beamsplitter; CCD: FFT-CCD camera; FM: Flipping mirror; M: mirror; NOPA: noncollinear optical parametric amplifier; PD: photodiode; SCG: supercontinuum generation; SHG: second-harmonic generation; TCSPC: time-correlated single-photon counting.

7.2 Experimental Setup

A sketch of the experimental setup is given in Fig. 1. A detailed depiction of every single optical element is omitted for the sake of clarity. It consists of two technically almost identical laser systems (Clark MXR CPA) each comprising a 1 kHz Ti:Sa regenerative amplifier seeded by a passively mode-locked Erbium-doped fiber (ErF) oscillator operating at ~ 35 MHz. The difference repetition frequency of the two oscillators is 1.7 MHz.

7.2.1 Femtosecond Time-Resolved Electronic Absorption Spectroscopy

The femtosecond time-resolved electronic absorption spectroscopy setup has been described previously.^[19–21] In brief, a Clark MXR CPA 2001 Ti:Sa regenerative amplifier with 1 W output performance supplies pulses at a center wavelength of 775 nm with 150 fs (sech^2) duration (full width at half maximum, fwhm) at a repetition rate of 1013 Hz. Most of the laser fundamental is used to operate a home-built noncollinear optical parametric amplifier (NOPA) with subsequent pulse compression. If pulses in the UV were required the compressed output was frequency doubled by second-harmonic generation (SHG). After passing through the sample flow-cell the pump status is detected by a photodiode. Another small fraction of the laser fundamental passes an computer-controlled optical delay line with a maximum displacement of 30 cm allowing to introduce pump-probe delays up to 2 ns. To obtain broadband detection

the probe beam is subsequently sent through a CaF_2 plate for supercontinuum generation (SCG), split into probe and reference beam, dispersed by a prism spectrograph and detected using fast frame-transfer CCD cameras. An optical chopper in the probe beam path, operated at half the repetition rate, blocks every second probe pulse, while another chopper in the pump beam path, operated at a quarter the repetition rate, allows two consecutive pump pulses to pass while blocking the next two. This way it is possible to record transient absorption difference spectra corrected for potential background such as scattered pump light. The time resolution of the experiment is ~ 50 fs, depending on the pump wavelength.

7.2.2 Nanosecond Time-Resolved Electronic Absorption Spectroscopy

Broadband transient absorption spectra on the nano- to millisecond timescale are recorded using another laser, namely a Clark MXR CPA 2011 with 880 mW output performance that supplies pulses at a center wavelength of 775 nm with 150 fs (sech^2) duration (fwhm) at a repetition rate of 1015 Hz, as probe laser. For that a flipping mirror is used to bring the beam into the supercontinuum generation of the femtosecond transient absorption experiment and to adjust it to the same optical pathway described previously. Only minor additions to the setup have to be made which is displayed in the sketch of the experiment in Fig. 1. The generation of the pump and probe pulses as well as the detection and optical elements used, remain the same as for the femtosecond transient absorption experiment. As the laser beams provided by the two systems exhibit almost identical spatio-temporal properties and spectra, the generation of the probe supercontinuum from the second laser is straightforward. Additionally, two photodetectors (THORLABS PDA10A2) are used to detect a fraction of the pump and the probe beam, respectively. Both photodetectors are connected to a time-correlated single-photon counting (TCSPC) board with 25 ps base resolution (PicoQuant TH260). Temporal relation between the two lasers is achieved by using the operation frequency of the pump laser (1013 Hz) to trigger the pockels cell of the amplifier of the probe laser. Due to technical restrictions, the assignment of the pump (Clark MXR CPA 2001) and probe (Clark MXR CPA 2011) laser cannot be altered. To achieve coupling, the Sync 3 output at the internal delay control unit (DT-505) of the Clark MXR CPA2001 system is connected to the Delay In channel at the DT-505 unit of the Clark MXR CPA2011 system with a coaxial cable. The thus obtained relation between the two laser systems becomes obvious by looking at the oscilloscope signals of the pump and the probe photodetectors displayed in Fig. 2. Owing to the slight deviation in the oscillatory frequencies and thus in the operation frequencies of both systems the probe pulse is provided with a temporal jitter of 58 ns with respect to the pump pulse. That jitter reflects the time window of the pockels

cell opening.

The DT-505 unit allows to control the delay between the pump pulse and the 58 ns window, in which the arrival of the probe pulse train occurs, with a precision of 400 ps. A more precise and facile control of the electronic delay is achieved by an interstage delay generator (Stanford Research Systems Model DG535) with a delay resolution of 5 ps. In principal, an electronic delay of up to 1000 s can be achieved, however, the longest reasonable delay is restricted to 1 ms by the repetition rate and further by the diffusion of the excited sample molecules out of the probe volume which takes at least 50 μ s. To calibrate the delay, detected by the TCSPC board, to the coincidence of the pump and the probe pulse in the sample cell, the distances between the photodetectors and the sample cell, as well as the lengths of the coaxial cables that transmit the signals were adjusted accordingly and the pump and probe pulses were shifted by monitoring the rising edges of photodiode signals with a 500 MHz digital phosphor oscilloscope (Tektronix TDS3054).

7.2.3 Measurement Schemes

Using the TCSPC board it is possible to resolve the photodynamics within the 58 ns window determined by the pump-probe jitter. For that, the photodiode detecting the pump pulses is connected to the sync channel of the TCSPC board, while the photodiode detecting the probe pulses is connected to one of the detection channels of the TCSPC board. The input voltage of the photodiodes have to be checked in advance for stability and to make sure they do not exceed the damage level of the board of ± 1500 mV. A stable trigger input of at least 600 mV was experimentally found to be necessary. The electronic delay is set such that the probe pulse arrives within $0 \text{ ns} < \Delta t < 58 \text{ ns}$ with respect to the pump pulse. A *LabView* routine is used to time-tag every single transient spectrum with the respective pump-probe delay time at a fixed time resolution. In a postprocessing procedure all spectra recorded at the same delay are averaged and ordered to recover the time axis. The exact value of the time resolution can be set to a value between 25 ps and 52.42 μ s. Since fast time components are already resolved in preceding femtosecond TEAS measurements it is sufficient to choose a value in the magnitude of the biggest delay step of the femtosecond TEAS measurement. This also helps to reduce data since less single-shot transient spectra have to be recorded for the same signal-to-noise ratio. Subsequently the electronic delay is increased such that the next 58 ns window is covered and the time resolution might be adjusted to a higher value. Furthermore, coarse scanning of the delay time is possible by measuring the transient absorption spectrum averaged over the 58 ns at every electronic delay. In this mode the time-resolution is principally limited to 58 ns, however, it can still be sufficient to investigate molecules with photodynamics that extend from several hundred nanoseconds to microseconds and allows for a rapid scanning

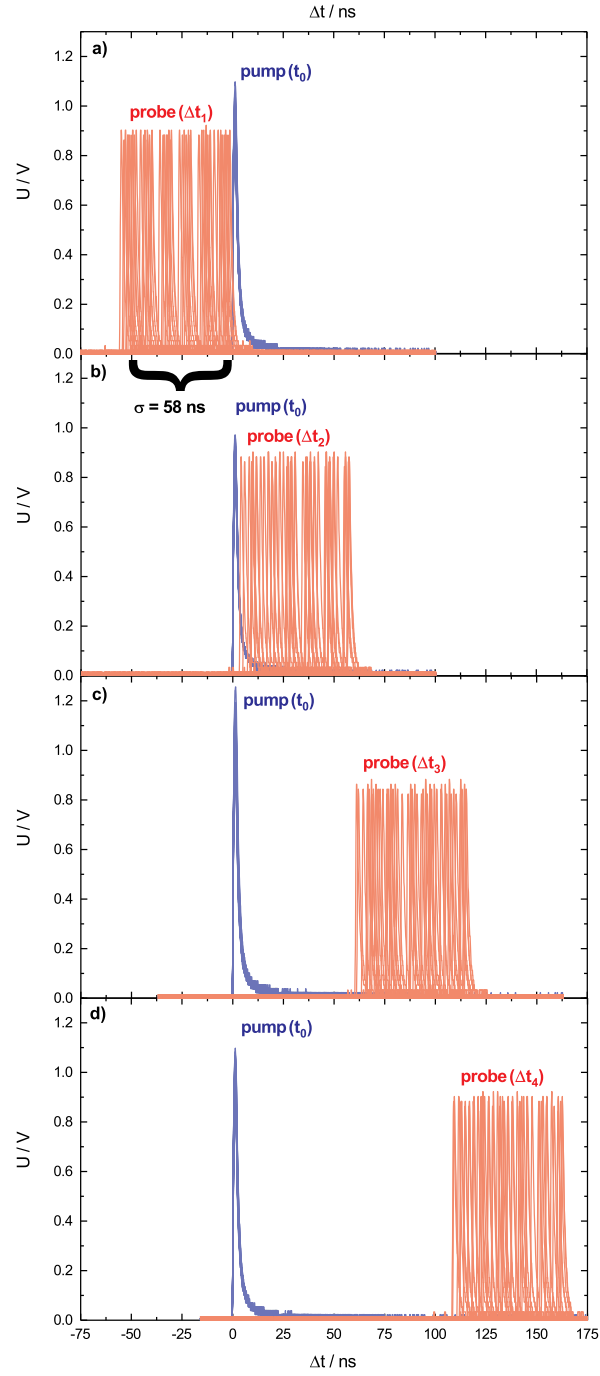


Figure 2: Pump-probe jitter induced by the coupling of the two Ti:Sa laser systems. The probe pulse (red) arrives within a 58 ns window with respect to the pump pulse (blue). The relative delay time (Δt) between the probe pulse window and the pump pulse (t_0) can be controlled using an electronic delay generator. From a–d the delay was increased by 58 ns each.

of the time delays.

7.3 Results for 7-Hydroxyquinoline-8-Carbaldehyde

The first molecule investigated by this setup is the proposed excited-state intramolecular proton-transfer (ESIPT) switch 7-hydroxyquinoline-8-carbaldehyde (7-HQC).^[22] The chemical structural formulas of the proposed tautomeric forms that share a solvent dependent equilibrium are displayed in Fig. 3. A detailed discussion of the chemical and physical properties as well as the nature of the observed dynamical processes omitted at this point. It only serves as a reference molecule to proof the principle of the experiment.

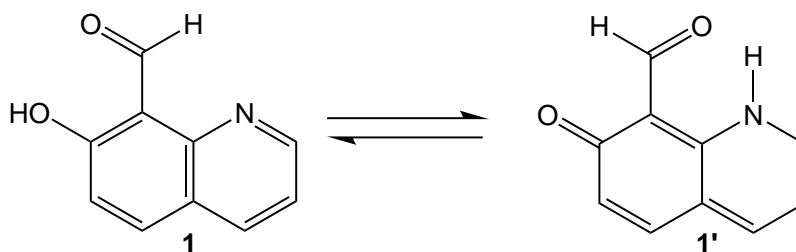


Figure 3: Chemical structural formulas of the OH- (**1**) and the NH-tautomer (**1'**) of 7-HQC.

7.3.1 Static UV–vis Absorption Spectroscopy

The static UV–vis absorption spectra of 7-HQC in spectroscopic-grade methanol (MeOH) are displayed in Fig. 4. In this solvent, the ratio between the OH- (**1**) and the NH-form (**1'**) is estimated to be 1:1 from the room temperature NMR studies.^[22] However, the employed excitation wavelength of $\lambda_{\text{pump}} = 387$ nm leads to an almost exclusive excitation of **1'** as the low-energy absorption band centered at 400 nm is associated with the lowest $^1\pi\pi^*$ state of the NH-tautomer.^[22]

7.3.2 Time-Resolved Electronic Absorption Spectroscopy

Time-resolved electronic absorption spectroscopy (TEAS) of 7-HQC was performed in methanol upon photoexcitation at $\lambda_{\text{pump}} = 387$ nm. The transient absorption difference spectra at selected delay times displaying the different phases of spectro-temporal evolution are displayed in Figure 5a–b.

The transient absorption difference spectra at delay times $0.38 \text{ ps} < \Delta t < 1525 \text{ ps}$ (blue to black, Fig. 5a) were recorded by femtosecond TEAS. At wavelengths of $425 \text{ nm} < \lambda_{\text{probe}} < 550 \text{ nm}$ these spectra evolve from negative ΔOD

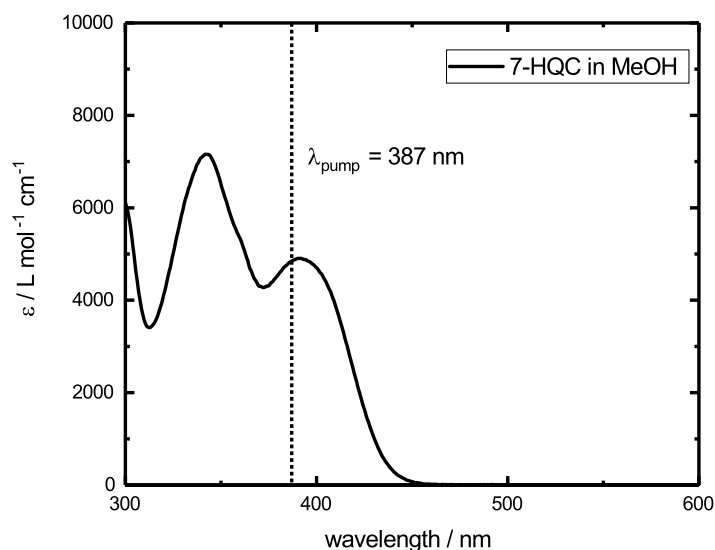


Figure 4: Static UV–vis absorption spectrum of 7-HQC recorded in methanol.

values that are attributed to stimulated emission (SE) towards positive ΔOD values, while the positive excited-state absorption (ESA) in the range $\lambda_{\text{probe}} \geq 550$ nm decreases. Apparently, at the longest recorded delay of 1.5 ns the temporal evolution of the system is not completed and no significant recovery of the ground state bleach (GSB) at $400 \text{ nm} < \lambda_{\text{probe}} \leq 425$ nm is observed. From these data alone it cannot be stated whether a stable photoproduct is formed or the photodynamics recover the ground state of the educt.

Therefore, nanosecond TEAS measurements provide useful information about the 7-HQC system. The transient absorption data were recovered with a time resolution of 400 ps for delay times from $1.1 \text{ ns} < \Delta t < 109.9 \text{ ns}$ by two consecutive measurements with different electronic delay settings. The representative transient absorption difference spectra (green to black, Fig. 5a and b) obtained by this method connect seamlessly to those from the fs TEAS measurements. Apparently, the transient absorption signal at $425 \text{ nm} < \lambda_{\text{probe}} < 550$ nm reaches its maximum after 6.6 ns (cf. Fig. 5a) and is associated with the complete decay of the ESA band at $\lambda_{\text{probe}} \geq 550$ nm, as indicated by the isosbestic point at 550 nm. Again, no recovery of the GSB signal is observed in this time frame. The subsequent decay of all transient absorption signals and a significant recovery of the GSB signal up to 110 ns can be observed in the spectra in Figure 5b. In this time frame the spectra exhibit a clear isosbestic point at 425 nm. Therefore, the absorption band centered at 470 nm is attributed to ESA rather than absorption of a ground state photoproduct.

Ultimately, measurements were taken by coarse scanning of the electronic delay up to $1.2 \mu\text{s}$ with a time resolution of 58 ns. The representative transient absorption difference spectra (red to black, Fig. 5b) unambiguously show that the ground state of the educt is recovered completely.

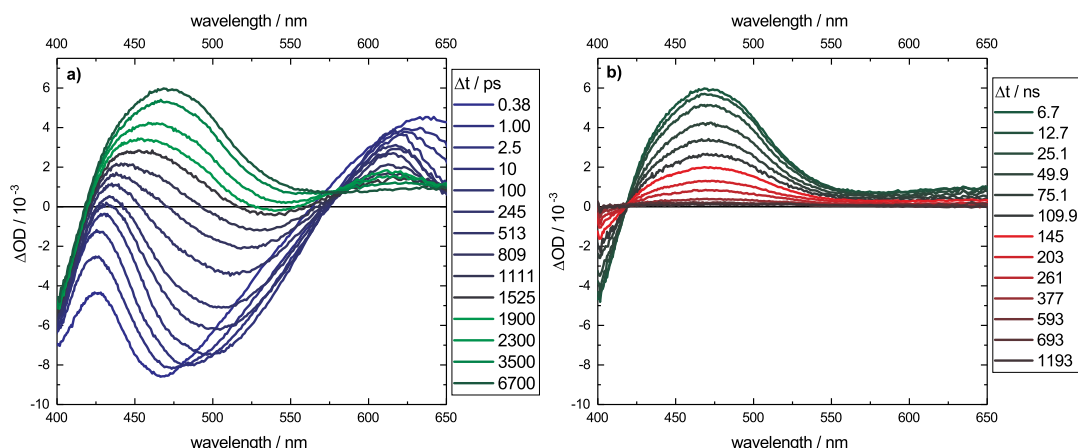


Figure 5: Transient difference absorption spectra of 7-HQC in methanol obtained by time-resolved electronic absorption spectroscopy (TEAS) upon photoexcitation at $\lambda_{\text{pump}} = 387$ nm. The spectra at delay times $0.38 \text{ ps} < \Delta t < 1525 \text{ ps}$ (blue to black) were recorded by femtosecond TEAS. The spectra at delay times $1.9 \text{ ns} < \Delta t < 109.9 \text{ ns}$ (green to black) were recovered from the nanosecond TEAS measurements using the TCSPC board with a set time resolution of 400 ps. The spectra at delay times $145 \text{ ns} < \Delta t < 1193 \text{ ns}$ (red to black) were recorded by coarse scanning of the electronic delay with a time resolution of 58 ns. The panels a) and b) display the different phases of the spectro-temporal evolution.

In order to ensure that the method also allows to obtain quantitative insight into photodynamics, the excited-state kinetics of 7-HQC were further analyzed. The transient absorption vs. delay time traces of the GSB signal ($\lambda_{\text{probe}} = 405$ nm) the short-lived ESA ($\lambda_{\text{probe}} = 615$ nm) and the long-lived ESA ($\lambda_{\text{probe}} = 470$ nm) are displayed in Figure 6.

The time trace obtained from femtosecond TEAS (Fig. 6a) could be well described by simultaneous least-square fitting of a sum of three exponential convoluted with a Gaussian-shaped instrument response function (IRF) with decay time constants of $\tau_1 = 0.7 \pm 0.1 \text{ ps}$ and $\tau_2 = 8.8 \pm 0.9 \text{ ps}$ as well as a long component of $\tau_3 = 1.48 \pm 0.07 \text{ ns}$. The time resolution was determined from the width of the IRF to $\sim 160 \text{ fs}$. This value is comparably long owing to the fact that the pump pulses of $\lambda_{\text{pump}} = 387 \text{ nm}$ were generated directly from SHG of the laser fundamental and used without further compression.

The respective time traces obtained from nanosecond TEAS (Fig. 6b) with a set time resolution of 400 ps were simultaneously fitted with a sum of two exponentials. The thus obtained decay time constant $\tau_3 = 1.33 \pm 0.06 \text{ ns}$ corresponds to the longest time constant extracted from the femtosecond TEAS measurements and is apparently associated with the formation of the metastable excited-state species. Additionally, the longer decay time constant $\tau_4 = 120 \pm 6 \text{ ns}$ could be extracted and is associated with the decay of this species and the

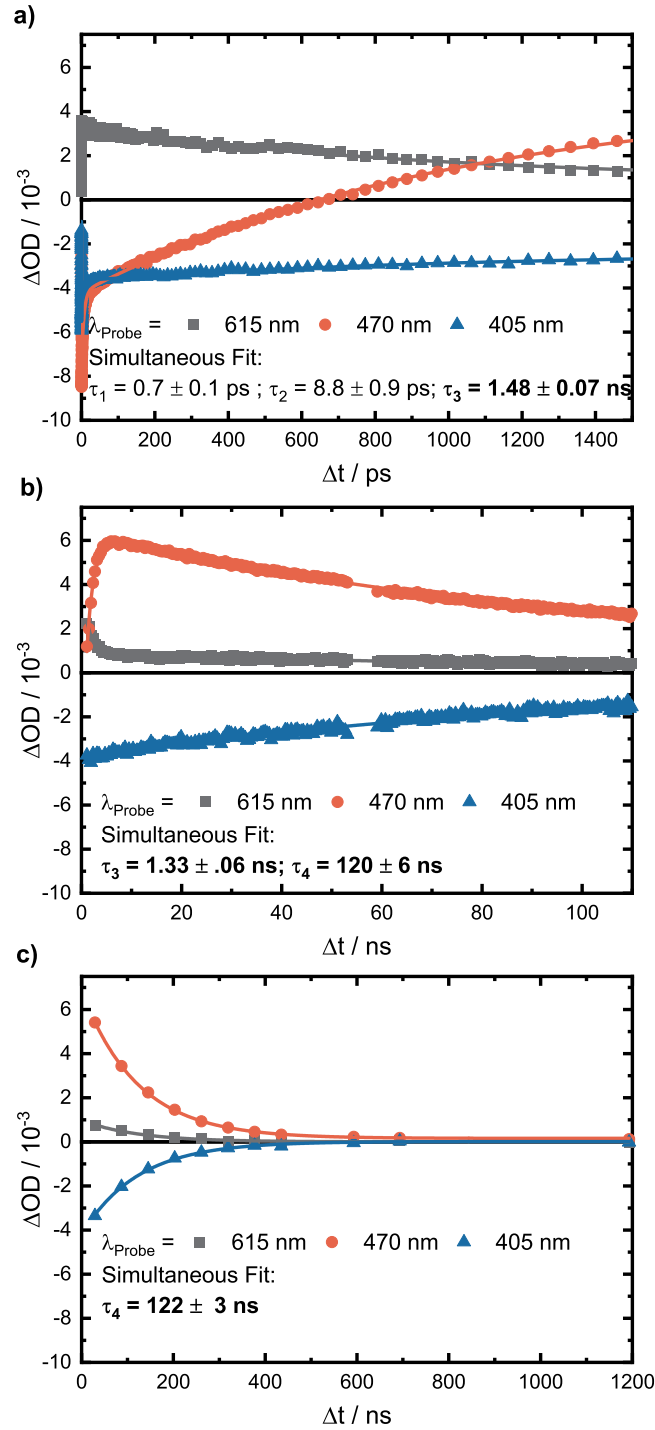


Figure 6: Transient absorption vs. delay time traces with simultaneously fitted exponential functions of 7-HQC in methanol excited at $\lambda_{\text{pump}} = 387 \text{ nm}$ a) obtained by femtosecond time-resolved electronic absorption spectroscopy (TEAS) b) recovered from the nanosecond TEAS measurements using the TCSPC board with a set time resolution of 400 ps and c) recorded by coarse scanning of the electronic delay with a time resolution of 58 ns.

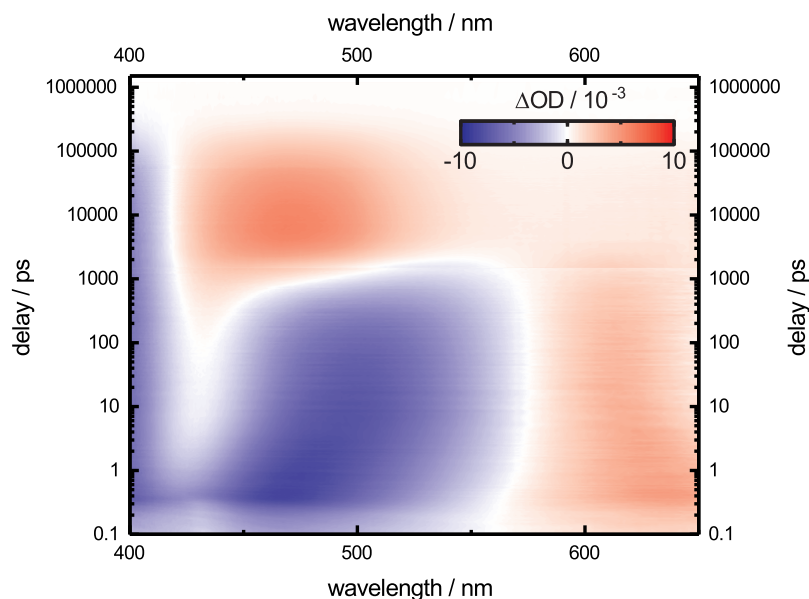


Figure 7: Combined two-dimensional spectro-temporal absorption map displaying the photodynamics of 7-HQC in methanol excited at $\lambda_{\text{pump}} = 387$ nm for delay times of $0.1 \text{ ps} < \Delta t < 1500000 \text{ ps}$ and wavelengths of $400 \text{ nm} < \lambda_{\text{probe}} < 650 \text{ nm}$.

recovery of the ground state. Congruently, fitting of the respective kinetic traces obtained from coarse scanning of the electronic delay with a time resolution of 58 ns (Fig. 6c) yielded a single decay time constant of $\tau_4 = 122 \pm 3$ ns reproducing the one determined in the preceding nanosecond measurements. From the combined two-dimensional transient absorption maps in Fig. 7 it becomes clear that this method is sufficient to seamlessly resolve photodynamical processes on timescales longer than those accessible with conventional femtosecond transient absorption experiments.

7.4 Conclusion

In summary, the presented method offers a facile approach for the realization of transient electronic absorption spectroscopy on multiple timescales. Since the basis of the setup is formed by a conventional femtosecond pump-probe spectrometer the advantage of the high time resolution, achieved by the mechanical delays, is preserved. The implementation of a second laser system that provides the probe pulses for measurements on longer timescales requires no rearrangements of the optics and the beam paths of the femtosecond TEAS experiment. As the nanosecond TEAS experiment is based purely on the *a posteriori* determination of the randomly distributed pump-probe delays between the two synchronized femtosecond Ti:Sa amplifiers with a TCSPC board,

its implementation into preset experiments is straightforward and requires no costly modifications to match the frequencies of both oscillators such as piezoring actuators.^[10–12] The temporal resolution of this electronic detection of 25 ps is adequate on the considered timescales as faster dynamical processes are resolved in preceding femtosecond TEAS measurements. Furthermore, coarse scanning is possible by electronically delaying the trigger signal between the two amplifiers. This way rapid scanning of the pump-probe delay up to 1 ms is facilitated with 58 ns time resolution, which is again sufficient if the photodynamics extend to the microsecond regime. As demonstrated, the combination of these methods allowed to seamlessly resolve the full photocycle of the 7-HQC system. It was shown that under the applied experimental conditions the photoexcitation of this molecule does not lead to the formation of a stable photoproduct from an excited-state proton-transfer process but to the population of a long-lived excited state from which the ground state of the educt is completely recovered.

Acknowledgements

The authors acknowledge the support of this work by the Deutsche Forschungsgemeinschaft through the Collaborative Research Center 677 “Function by Switching” and the CAU Kiel.

References

- [1] Bredenbeck, J.; Helbing, J.; Kumita, J. R.; Woolley, G. A.; Hamm, P. *Proc. Natl. Acad. Sci. U. S. A.* **2005**, *102*, 2379–2384.
- [2] Leonova, M. M.; Fufina, T. Y.; Vasilieva, L. G.; Shuvalov, V. A. *Biochem.* **2011**, *76*, 1465–1483.
- [3] Antonucci, L.; Bonvalet, A.; Solinas, X.; Jones, M. R.; Vos, M. H.; Joffre, M. *Opt. Lett.* **2013**, *38*, 3322.
- [4] Elzinga, P. A.; Lytle, F. E.; Jian, Y.; King, G. B.; Laurendeau, N. M. *Appl. Spectrosc.* **1987**, *41*, 2–4.
- [5] Kafka, J. D.; Pieterse, J. W.; Watts, M. L. *Opt. Lett.* **1992**, *17*, 1286.
- [6] Sucha, G.; Fermann, M. E.; Harter, D. J.; Hofer, M. *IEEE J. Sel. Top. Quantum Electron.* **1996**, *2*, 605–620.
- [7] Takagi, Y.; Adachi, S. *Rev. Sci. Instrum.* **1999**, *70*, 2218–2224.
- [8] Keilmann, F.; Gohle, C.; Holzwarth, R. *Opt. Lett.* **2004**, *29*, 1542–1544.
- [9] Gebbs, R.; Klatt, G.; Janke, C.; Dekorsy, T.; Bartels, A. *Opt. Express* **2010**, *18*, 5974.
- [10] Bredenbeck, J.; Helbing, J.; Hamm, P. *Rev. Sci. Instrum.* **2004**, *75*, 4462–4466.
- [11] Yu, A.; Ye, X.; Ionascu, D.; Cao, W.; Champion, P. M. *Rev. Sci. Instrum.* **2005**, *76*, 1–8.
- [12] Bartels, A.; Hudert, F.; Janke, C.; Dekorsy, T.; Köhler, K. *Appl. Phys. Lett.* **2006**, *88*, 1–3.
- [13] Antonucci, L.; Solinas, X.; Bonvalet, A.; Joffre, M. *Opt. Express* **2012**, *20*, 17928.
- [14] Antonucci, L.; Bonvalet, A.; Solinas, X.; Daniault, L.; Joffre, M. *Conf. Lasers Electro-Optics Eur. - Tech. Dig.* **2015**, *2015-Augus*, 27931–27940.
- [15] Solinas, X.; Antonucci, L.; Bonvalet, A.; Joffre, M. *Opt. Express* **2017**, *25*, 17811.

-
- [16] Antonucci, L.; Solinas, X.; Bonvalet, A.; Joffre, M. *Opt. InfoBase Conf. Pap.* **2017**, *Part F82-C*, 91128.
 - [17] Antonucci, L.; Solinas, X.; Bonvalet, A.; Joffre, M. *Opt. Express* **2020**, *28*, 18251.
 - [18] Nakagawa, T.; Okamoto, K.; Hanada, H.; Katoh, R. *Opt. Lett.* **2016**, *41*, 1498.
 - [19] Röttger, K.; Wang, S.; Renth, F.; Bahrenburg, J.; Temps, F. *Appl. Phys. B* **2015**, *118*, 185–193.
 - [20] Renth, F.; Siewertsen, R.; Strübe, F.; Mattay, J.; Temps, F. *Phys. Chem. Chem. Phys.* **2014**, *16*, 19556–19563.
 - [21] Renth, F.; Foca, M.; Petter, A.; Temps, F. *Chem. Phys. Lett.* **2006**, *428*, 62–67.
 - [22] Vetokhina, V.; Nowacki, J.; Pietrzak, M.; Rode, M. F.; Sobolewski, A. L.; Waluk, J.; Herbich, J. *J. Phys. Chem. A* **2013**, *117*, 9127–9146.

8 Conclusion and Outlook

The first goal of this Thesis was the investigation of the ultrafast photodynamics of transition-metal complexes that were designed to undergo photo-induced spin crossover (SCO) at room temperature in solution using femtosecond time-resolved pump-probe spectroscopy. These complexes have been functionalized with photochromic molecular switches in order to achieve control over and actual bi-stability of the two spin states. Although the investigated complexes were designed with the same goal and make use of azopyridines as photoswitches, the underlying SCO concepts exhibit principal differences. The presented studies contribute fundamental insights into the underlying working principle of these paradigmatic systems. From the obtained results, implications on the SCO concepts were determined and guidelines for a more rational design of such compounds were made. These are summarized in the following.

8.1 Photodynamics of Azo-Porphyrin Nickel(II)

The azopyridine nickel porphyrin (azoNiPor, Figure 8.1) was designed as a light-driven coordination-induced spin-state switch (LD-CISSS). The basic idea is that the coordination number of the central ion determines its spin state and that control over the coordination number can be achieved by a photo-induced configurational change of the ligand. The azoNiPor molecule is the first molecule to show magnetic bi-stability in solution and at room temperature. The spin state of the Ni(II) ion can be reversibly photo-switched between the diamagnetic low-spin (LS) state ($S = 0$) and the paramagnetic (HS) state ($S = 1$). This process is accompanied by the isomerization of the attached phenylazopyridine (PAP) unit that acts as an axial ligand in the *cis*-configuration, while it is unable to coordinate in the *trans*-configuration. The mismatch between the experimentally determined best switching wavelength and those expected on the basis of the LD-CISSS concept brought up questions about the actual mechanism of the spin switching. Although the system was designed to avoid conjugation between the PAP and the porphyrin chromophores, energy transfer from the porphyrin to the PAP was assumed to play a major role especially in the *trans*-to-*cis*-isomerization of the ligand.

In the course of this Thesis, the quantum yields of the spin switch at the best switching wavelength were determined. The values for the *trans*-azoNiPor(LS)

to *cis*-azoNiPor(HS) direction upon irradiation with $\lambda_{\text{irr}} = 505$ nm and the *cis*-azoNiPor(HS) to *trans*-azoNiPor(LS) direction upon irradiation at $\lambda_{\text{irr}} = 435$ nm were established to

$$\Phi_{\text{LS} \rightarrow \text{HS}}(505 \text{ nm}) = 0.005 \pm 0.001.$$

$$\Phi_{\text{HS} \rightarrow \text{LS}}(435 \text{ nm}) = 0.023 \pm 0.003$$

Surprisingly, despite such low quantum yields, the azoNiPor molecule reaches almost quantitative conversion efficiencies. In order to elucidate the switching mechanism, both azoNiPor isomers as well as the reference compounds, namely the free PAP, the free porphine base $\text{H}_2\text{TPPF}_{20}$ and the nickel porphyrin NiTPPF_{20} (cf. Figure 8.1), were studied using time-resolved electronic absorption spectroscopy (TEAS) and stationary spectroscopic techniques.

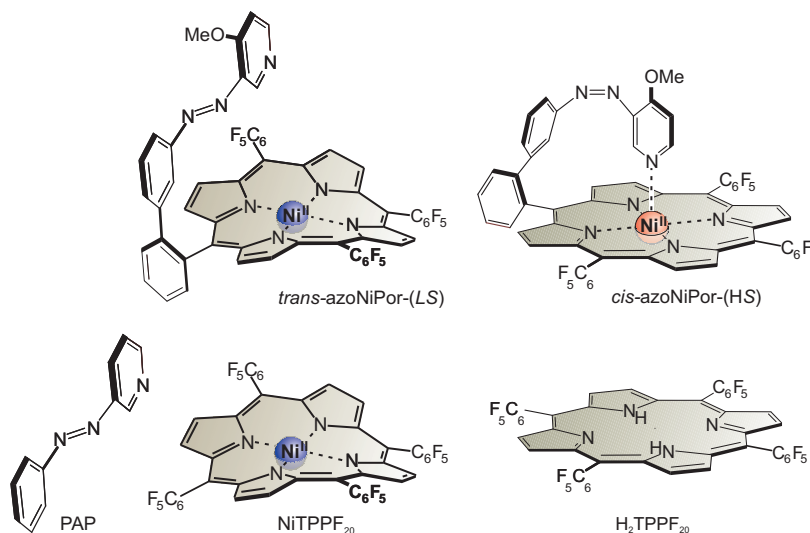


Figure 8.1: Chemical structures of the record player isomers *trans*-azoNiPor(LS) and *cis*-azoNiPor(HS) and the building blocks the phenylazopyridine (PAP), the nickel porphyrin (NiTPPF_{20}) and the free porphine base $\text{H}_2\text{TPPF}_{20}$.

The results of femtosecond TEAS measurements on *trans*-azoNiPor(LS) show that photoexcitation of either the B or the Q states of the porphyrin generates the same state within the time resolution of the experiment. From this state, which is associated with a $^1\pi\pi^*$ the porphyrin macrocycle, effective energy transfer to the nickel (d,d) state occurs with a time constant of

$$\tau_1 = 0.7 \pm 0.02 \text{ ps}$$

and subsequent vibrational cooling with

$$\tau_2 = 9 \pm 1 \text{ ps}.$$

In this SCO state, the Ni(II) ion possesses the desired HS electron configuration

however, it can only be preserved by coordination of an axial ligand. Since in the case of porphyrin excitation the PAP ligand remains in its *trans*-configuration, it has no chance to bind to the nickel center and the LS ground state is recovered with

$$\tau_3 = 360 \pm 13 \text{ ps.}$$

For *cis*-azoNiPor(HS), excitation of the B or Q states also results in the rapid formation of the same porphyrin excited state. Congruently, the subsequent energy transfer occurs to the nickel (d^2) state exhibiting more complex dynamics with

$$\begin{aligned}\tau_1 &= 0.7 \pm 0.02 \text{ ps,} \\ \tau_2 &= 5 \pm 1 \text{ ps}\end{aligned}$$

and subsequent vibrational cooling with

$$\tau_3 = 21 \pm 3 \text{ ps.}$$

This energy transfer process presumably involves an intermediate which is likely to be associated with a $^3\pi\pi^*$ state of the porphyrin macrocycle. Again, the formation of the SCO state with the desired LS electron configuration at the nickel center is not sustainable since the PAP ligand, still in the *cis*-configuration, will recoordinate to form the HS ground state with

$$\tau_4 = 600 \pm 30 \text{ ps.}$$

In summary, the femtosecond transient absorption measurements showed no indications for the supposed energy transfer from the excited porphyrin Q state to the PAP moiety that could lead its isomerization. Consequently, direct excitation of the PAP chromophore was identified to be demanded for sustainable spin switching. Indeed, the TEAS measurements carried out at pump wavelengths that excite a larger fraction of the PAP chromophores allowed us to observe small fractions of the spin switching product. In the case of *cis*-azoNiPor(HS) the required decoordination occurs immediately upon ultrafast *cis*-to-*trans*-isomerization of PAP and can be observed by femtosecond TEAS. However, in the case of *trans*-azoNiPor(LS) the coordination process following ultrafast *trans*-to-*cis*-isomerization requires orientation of the azo ligand towards the nickel center, which occurs on longer timescales and was identified by nanosecond TEAS. These results show that we carefully have to differentiate between two SCO mechanism in the azoNiPor molecule: on the one hand light-induced SCO occurs upon photoexcitation of the porphyrin with high efficiency, but the product of this process is metastable and, eventually, the original ground state is recovered. On the other hand, coordination-induced SCO yields the sus-

tainable photoproduct although excitation as well as isomerization of the PAP is required which gives rise to the low quantum yields. Additional reliable calculations seem mandatory to complete the picture especially for the identification of a potential barrier or charge-transfer states arising from the coordination *cis*-PAP the nickel center that could hinder the *cis*-to-*trans*-isomerization in azoNiPor and thus cause the unanticipated switching wavelengths of azoNiPor.

Based on the finding that the SCO mechanism of azoNiPor follows the initially proposed LD-CISSS concept, several suggestions for improving future LD-CISSS systems were made. Recent efforts made by the Herges workgroup to realize *in vivo* switching of azoNiPor for medical applications by irradiation through skin tissue should focus on shifting the absorption bands of the photoswitch towards the biooptical window (650–900 nm) rather than that of the porphyrin. In this course sensitized azobenzenes that undergo two-NIR-photon triggered isomerization might be interesting. For the application of such compounds in the field of optical data storage, the poor quantum yields of the system in its current design need to be overcome. For that, a more selective addressing of the photoswitch has to be established. As porphyrins exhibit enormous absorption over a broad spectral range, the choice of a less absorbing basic structure for the complexation of the Ni(II) ion could be worthwhile. Furthermore, employing photoswitches with higher quantum yields such as bridged-azobenzenes represents a feasible solution. Probably the most promising approach would be to exploit the efficient light-induced SCO and high absorption coefficients of nickel porphyrins by using the associated structural change as intramolecular feedback, stabilizing one spin state or the other. This approach has already been tackled by the so-called “hair clip” molecules, recently designed in the Herges workgroup, where the axial pyridine ligand is strapped over the nickel center by covalent connections to two opposite *meso*-positions of the porphyrin. Hitherto, however, the current designs suffer from insufficient energy barriers separating the two species in the ground state.

8.2 Photodynamics of Azo-N4Py Iron(II)

In the novel complex $[\text{Fe}(\text{3AzoN4Py})(\text{MeCN})](\text{BF}_4)_2$ (**1**, Figure 8.2), the realization of a photoswitchable SCO was attempted on the basis of the concept of ligand-driven light-induced spin change (LD-LISC). The underlying idea is to introduce a chromophore into the ligand that can undergo a reversible photoreaction, which changes the ligand-field strength and thereby the spin state of the transition-metal center.

In this system, the Fe(II) central ion is surrounded by a pentadentate tetrapyridylamino ligand functionalized with an azo unit (3AzoN4Py, **3**, Figure 8.2). The pentadentate design of the ligand was chosen, since complexes with chelating ligands show high thermal stability and are unlikely to undergo decomposition upon irradiation. The ligand is derived from the N4Py ligand that has

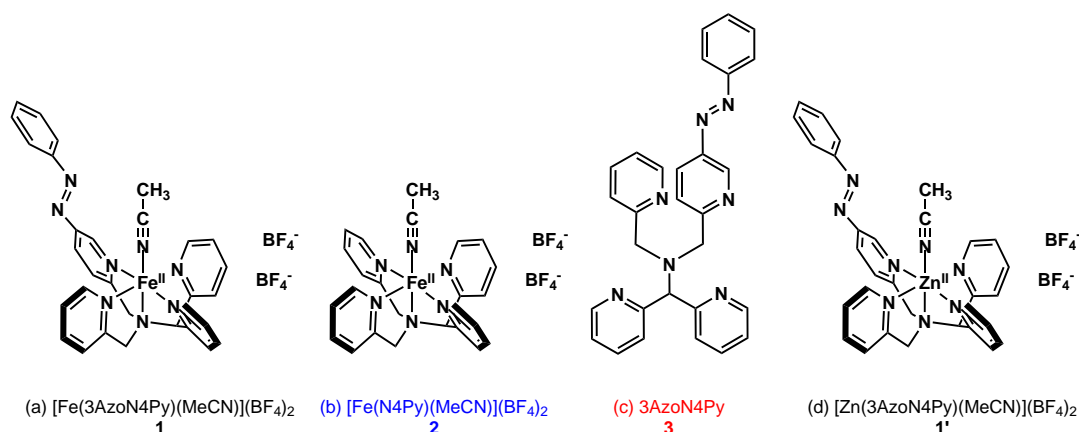


Figure 8.2: Structural formulas of the azo-functionalized complex $[\text{Fe}(\text{3AzoN4Py})(\text{MeCN})](\text{BF}_4)_2$ (**1**, a) and the reference compounds $[\text{Fe}(\text{N4Py})(\text{MeCN})](\text{BF}_4)_2$ (**2**, b), **3AzoN4Py** (**3**, c) and $[\text{Zn}(\text{3AzoN4Py})(\text{MeCN})](\text{BF}_4)_2$ (**1'**, d).

been employed to mimic oxygen activation on non-heme iron centers in biological processes. In the parent $[\text{Fe}(\text{N4Py})(\text{MeCN})](\text{BF}_4)_2$ complex **2** (cf. Figure 8.2), the free sixth binding site allows for an additional axial coordination of a solvent molecule. This solvent coordination to the complex determines its spin state: in acetonitrile (MeCN) the complex exists in the LS form, but in methanol (MeOH) it switches predominantly to the HS state. The complex **1** as well as the reference complex **2**, the free ligand **3** were first characterized by static UV–vis absorption spectroscopy. The UV–vis spectra show that the free ligand **3** can undergo reversible *trans-cis* isomerization upon irradiation. In contrast, irradiation of **1** under the same conditions leads to significantly less *trans-to-cis* isomerization in the coordinated azo-ligand. Furthermore, it was concluded that the change of the ligand field strength due to the isomerization of the single azo unit in the complex is not sufficient to cause a spin change of the Fe(II) center under the applied conditions, since no significant intensity decrease of the metal-to-ligand charge-transfer (MLCT) bands is observed when the *cis*-isomer is formed. Such a decrease is expected for the HS state of **1** due to the increased metal-ligand distance that reduces the CT transition intensity. Nevertheless, the study of the ultrafast photodynamics of **1** in comparison to that of its reference compounds using femtosecond TEAS provided valuable information about the photo-induced dynamical processes that determine the switching efficiency on the basis of the LD-LISC concept. Transient electronic absorption spectroscopy revealed that in complex **1** the decay of the photo-produced $\pi\pi^*$ state, localized at the azopyridine, leads to the subsequent population of the energetically lowest metal-centered (MC) HS state ($^5\text{T}_2$). As this energy transfer competes with relaxation dynamics involving purely ligand-centered (LC) states, it diminishes the yield of the *trans-to-cis*-isomerization of

complex **1** compared to the free ligand **3**. Additional measurements following excitation of the $^1\text{MLCT}$ transition of the complex indicate that MLCT states supposedly mediate the energy-transfer process. The decay of the metastable HS $^5\text{T}_2$ state to the LS ground state occurs *via* intersystem crossing with a time constant of

$$\tau_4 = 3290 \pm 140 \text{ ps.}$$

These results point at an intrinsic contradiction of the LD-LISC concept, which, on the one hand, requires that the natural photochemical properties of the ligand must be preserved, but, on the other hand, demands that the changes in the ligand environment are strong enough to trigger sustainable transition to the SCO product. The identified competing ultrafast energy transfer from the ligand to the MLCT and MC states of the Fe(II) could be one reason for the fact that functional LD-LISC systems with quantitative photoswitching between a pure LS and a pure HS state still await realization.

The obtained results should be taken into consideration for future developments of magnetically bi-stable LD-LISC systems. For that, a systematic investigation of the energy-transfer process is mandatory. The synthesis and study of derivatives with different metal ions could be worthwhile. The ruthenium analogue could help to identify the intermediate steps in the relaxation from the azopyridine $\pi\pi^*$ state to the ligand-field $^5\text{T}_2$ state. In the ruthenium analogue, the ligand-field states are raised in energy while the MLCT state remain basically unaffected. Therefore, possible energy transfer to the MLCT states is preserved while their ultrafast deactivation to the low-lying ligand-field states that complicates their identification in the iron complex is slowed down. Further, the coupling between the azopyridine and the MLCT states can be varied using other fourth row transition metals. The Zn(II) analogue $[\text{Zn}(\text{3AzoN4Py})(\text{MeCN})](\text{BF}_4)_2$ (**1'**, Figure 8.2d) was already synthesized in the Tuzek workgroup and investigated in the course of this Thesis. Due to its closed-shell electron configuration, Zn(II) is devoid of ligand-field states. Furthermore, the UV–vis spectra of **1'** show that the MLCT states are shifted out of the visible spectrum to much higher energies and are thus inaccessible upon excitation of the $\pi\pi^*$ state of the azopyridine ligand. Therefore, **1'** exhibits the perfect reference compound to study the photophysical and -chemical properties of the novel ligand **3** in its coordinated geometry. The static absorption spectra resemble that of the free ligand **3** and an efficient interconversion between the *trans*- and the *cis*-isomer was observed. Consequently, the ultrafast photodynamics and the extracted time constants are virtually identical to those obtained for the free ligand **3**, indicating that the geometric change upon coordination does not exert an influence on the photochemical properties of the ligand. Additional quantum chemical calculations were carried out in order to assess the nature of the excited electronic states in **1**, **1'** and **3**. These calculations support the assumption that low-lying MLCT states are the most viable candidates to

promote the energy transfer from the photoproduct azopyridine $\pi\pi^*$ state to the MC 5T_2 state. Future LD-LISC complexes could be based on metal-ligand systems that are devoid of MLCT transitions in the UV–vis region. In this course, the investigation of the Co(III) analogue could be worthwhile as this system supposedly represents the intermediate case between the Fe(II) and the Zn(II) complex, with the MLCT states shifted to slightly higher energies, while still being in the possession of low-lying ligand-field states. Alternatively, photochromic ligands that can be switched at wavelengths to the red of the MLCT bands could be employed. Bridged- or *ortho*-fluoro-azo compounds could meet those demands. Finally, the weak change of the ligand-field strength encountered in complex **1** have to be overcome. First derivatives of **1** functionalized with two photoswitchable azo units have already been synthesized in the Tuzcek workgroup. Furthermore, attempts to modify the complex such that its initial ligand-field strength is closer to SCO behavior at room temperature, by replacing some of the pyridines units by benzimidazoles, are underway. In general, previously studying the used ligands and metal ions by cyclic voltammetry can provide useful information about their redox properties which can help to get to a more rational design of these compounds.

8.3 Multiscale Pump-Probe Spectroscopy

Most of the results presented in this Thesis were obtained by femtosecond time-resolved electronic absorption spectroscopy (TEAS) which represents a well established method in the Temps workgroup. This setup allows for broadband detection in the wavelength range of $310\text{ nm} < \lambda_{\text{probe}} < 750\text{ nm}$ with a time resolution of $\sim 50\text{ fs}$ at best. However, the initial events following photoexcitation of transition-metal coordination compounds as well as photochromic molecular switches were shown to take place on much shorter timescales. In order to be able to resolve the fastest photophysical and -chemical events it is always desired to increase the time resolution of the current experiments. The generation of shorter pump pulses using broadband NOPA pulses in combination with a double-chirped mirror compressor has been explored in the course of a bachelor Thesis and the implementation into the femtosecond time-resolved electronic absorption setup is underway.

Moreover, the current setup makes use of a computer-controlled stage with a mounted retroreflector to introduce the temporal delay between the pump and the probe pulses. Therefore, the maximum accessible time delay is limited by the length of the stage. However, as demonstrated, the photodynamics of transition-metal complexes, and other systems of interest, do not exclusively take place on ultrafast timescales. Especially if transitions between different spin states or (de)coordination processes are involved, the photodynamics can extend from only a few femtoseconds to hundreds of nanoseconds or even microseconds. In this Thesis, further efforts on the development of an experiment

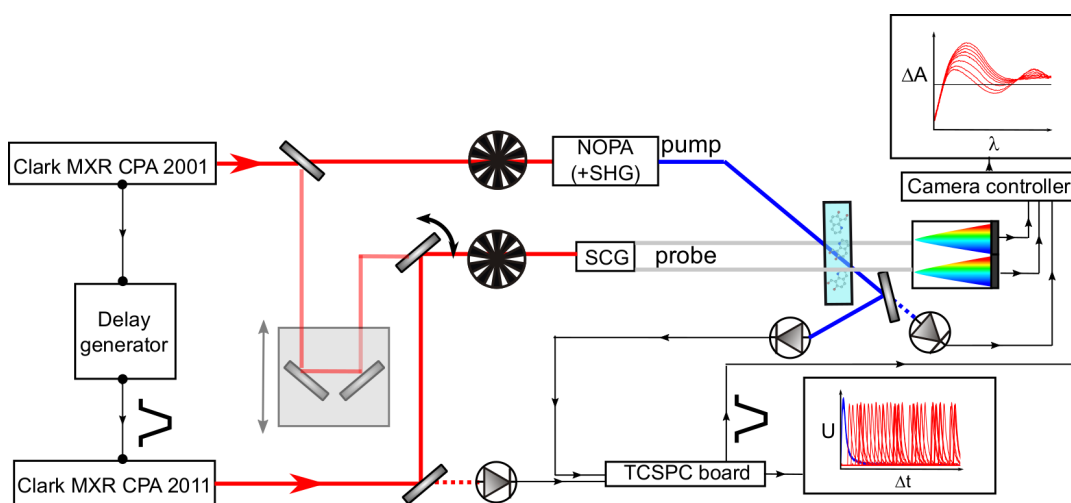


Figure 8.3: Sketch of the nanosecond time-resolved electronic absorption spectroscopy (TEAS) setup. The beam path for the corresponding femtosecond TEAS setup is displayed in pale colors.

allowing for the observation of the photodynamics on timescales of several picoseconds up to micro- or even milliseconds were made. For that, a pair of two technically identical Ti:Sa amplifiers seeded by two independent free-running oscillators was used. In this experimental combination one laser supplies the pump pulses, while the other supplies the probe pulses. Temporal relation between the two lasers is achieved by using the operation frequency of the amplifier of the pump laser to trigger the amplifier of the probe laser. Owing to slight deviations in the oscillation frequencies of both systems, which are determined by the cavity roundtrip times, the probe pulses are provided with a temporal jitter of 58 ns with respect to the pulses, that reflects the time window of the pockels cell opening. The delay between the pump pulse and the 58 ns window in which the arrival of the probe pulse occurs can be controlled by an interstage delay generator. A second computer with an integrated time-correlated single-photon counting (TCSPC) board with 25 ps base resolution is used to simultaneously detect the respective pump-probe delays during the transient absorption measurement. In order to account for a more accurate delay calibration, additional efforts have to be put into the setup of a device that allows for coincidence detection between the two laser beams. One possibility is to detect the nonlinear interaction of the pump and the probe beam by *e.g.* sum-frequency generation (SFG). However, as both laser systems exhibit almost identical spectra linear methods for coincidence detection such as interferometry are facilitated. The assignment pump-probe delays to the respective single-shot transient absorption spectra occurs *a posteriori*. The time-axis is recovered by subsequent averaging of all spectra recorded at the same delay time and ordering of the arbitrarily distributed delays. As demonstrated for the proposed excited-state proton-transfer

switch 7-hydroxyquinoline-8-carbaldehyde (7-HQC), the photo-induced dynamics for delay times of $0 \text{ ps} < \Delta t < 116 \text{ ps}$ could be mapped with 400 ps time resolution yielding two additional decay time constants of

$$\tau_3 = 1.4 \pm 0.1 \text{ ns and } \tau_4 = 120 \pm 6 \text{ ns.}$$

While the shorter component τ_3 could be reproduced from an earlier femtosecond TEAS experiment, the determination of the longer component τ_4 was only possible by means of the novel nanosecond TEAS measurements. The associated process is the decay of long lived excited state which is a finding that contributes fundamentally to the understanding of the photodynamics of 7-HQC and related systems. The current setup, however, requires very stable experimental conditions since delays and spectra are recorded on different devices neither can get lost in order to account for an adequate assignment. Combination of the TCSPC board and the transient absorption measurement program on the same computer will facilitate the operation of the experiment and data analysis as an on-the-fly assignment and averaging of the spectra will be possible and data sets can be drastically reduced which, in turn, allows to increase the set time resolution of the TCSPC board to 25 ps if necessary. Additionally, coarse scanning of the photodynamics is possible by electronically delaying the trigger signal between the two amplifiers. This way rapid scanning of the pump-probe delay up to 1 ms is facilitated with 58 ns time resolution. Despite the poor time resolution, this measurement mode is sufficient to resolve, *e.g.*, the decay of triplet states of organic molecules, as was successfully demonstrated for the porphine $\text{H}_2\text{TPPF}_{20}$. A new time constant of

$$\tau_4 = 335 \pm 29 \text{ ns}$$

was extracted for the triplet state decay.

In the future, the improved experimental setup can prove valuable in the investigation of the photodynamics of possible SCO systems as it allows for the monitoring of full photocycles. Thus, unwanted relaxation channels, *i.e.* vibrational modes that mediate the ground-state recovery (GSR) of the desired SCO state can be identified and shut down by proper design of the complexes. Additional improvements to the time-resolved electronic absorption experiment could be made by extending the detection range further into the near-infrared region, where excited-state absorption (ESA) features of possibly formed triplet states can occur. The required probe pulses can be provided by supercontinuum generation in sapphire or yttrium aluminum garnet (YAG). Ultimately, recent developments in the ultrafast spectroscopy with free-electron laser sources and magneto-optical methods allow one to directly probe the spin dynamics in SCO materials.

Danksagung

Mein größter Dank gebührt Herrn Prof. Dr. Friedrich Temps dafür, dass ich diesem vielfältigen, interessanten und für die Arbeitsgruppe auch recht neuen Thema, mit allen dafür benötigten Freiheiten und Ressourcen nachgehen durfte. Seine engagierte Betreuung und Begeisterung haben in mir das nachhaltige Interesse an der Forschung in diesem Themengebiet geweckt. Außerdem danke ich ihm für die Unterstützung dabei, meine Forschung auf zahlreichen Fachkonferenzen präsentieren zu dürfen.

Ein weiteres Riesen-Dankeschön geht an die aktuelle und ehemaligen Weggefährtinnen und Weggefährten in der Arbeitsgruppe: Rebecca, Birthe, Vivian, Simone, Pascal, Schatzi, Malte, Hendrik, meinem HSV Leidensgenossen Dennis, meinem 304er Jonas, meinem Part-time-flatmate Shuangqing, sowie Ole, Henrik, Mahmoud, Uta, Thrun, Anja und Julia. Vielen Dank für die immer positive Arbeitsatmosphäre, die grenzenlose Hilfsbereitschaft und gegenseitige Unterstützung bei wissenschaftlichen und privaten Problemen, für gemeinsame Hochzeits-, Geburtstags-, Einweihungs- und Chemikerpartys, Schrottwichteleien, Kanu-Touren, Schaftherapien, Sternstunden, MTB Unterricht in den Rockys, etc.

Ein spezielles Dankeschön geht an Dr. Joachim Gripp für einen stets gefüllten Chemikalienschrank, das Instandhalten der Spektrometer und Pumpen sowie die unvergesslichen Exkursionen in die Astronomie und Dr. Falk Renth (aka Rant) für das Schreiben und Zurverfügungstellen von Notebooks und Experimenten-Steuerungssoftware sowie für die interessanten wissenschaftlichen Gespräche.

Außerdem möchte ich mich bei dem gesamten technischen Personal des Instituts stellvertretend Timo, Andreas, Sina, Birgit, Klaus, Uwe, Michael, Carsten, Frank, Mark und Haxhi für die unkomplizierte, schnelle und stets kompetente Hilfe bedanken. Ganz besonders danke ich dabei Klaus, Mark und Haxhi für die Anfertigung von LEDs und Reparaturen am Laser-Netzteil, Andreas für die ununterbrochene Versorgung mit dermatologischer Handcreme und Tipps zum MeeFo-Angeln sowie Timo für seinen wesentlichen Beitrag zur Quantenausbeutenapparatur.

Tanja Stojic, Sonja Ehmke und Claudia Kurz danke ich für ihre schnelle und stets freundliche Hilfe bei bürokratischen Problemen aller Art.

Ein weiterer großer Dank gebührt meinen Kooperationspartner:innen aus der anorganischen Chemie allen voran Prof. Dr. Felix Tuczek sowie Leonie Fitschen für die großartige Zusammenarbeit an den Polypyridyl-Komplexen.

Meinen Kooperationspartnern aus der organischen Chemie - Prof. Dr. Rainer Herges und Dr. Marcel Dommaschk - sei für die Unterstützung und das Zurverfügungstellen der Porphyrin-Komplexe gedankt.

Außerdem danke ich Dr. Lars Mewes, Dr. Rebecca Ingle und Prof. Majed Cherqui für die fruchtbare Kooperation an den Di-Platin Komplexen.

Allen Bachelor- und Masterstudentinnen/studenten, die ich betreuen durfte - allen voran Birthe, Simone, Swantje und Malte - danke ich für ihr herausragendes Engagement und die angenehme Zusammenarbeit. Viel Erfolg auf eurem weiteren Weg!

Ein besonderer Dank geht an Dr. Alexander Schlimm und Sebastian Schatz für den gemeinsamen Weg durch die Höhen und Tiefen des Studiums von Tag 1 im Hörsaal bis zum Korrekturlesen der Dissertation und natürlich für die unzähligen Donnerstage bei Milan.

Nicht zuletzt danke ich meinen Kommilitoninnen und Kommilitonen Alex, Jan-tje, Schatzi, Jana, Lars, Tobi, Eike, Fynn, den Mädels und Jungs rund um den PTSK Futsal und dem Wobbler Squad für lange Nächte im Luna, unzählige erfolglose Stunden mit der Angel am NOK und die Zeit an und auf der Ostsee. Ihr habt Kiel zu einem echten zu Hause gemacht!

Großer Dank geht außerdem raus an meine Hansebembles aus Buxtehude für die langjährige Freundschaft und alle gemeinsamen Erlebnisse, die für Abwechslung vom wissenschaftlichen Alltag gesorgt haben.

Zu guter Letzt danke ich meiner Familie für ihre unendliche Geduld, den bedingungslosen Rückhalt und ein permanentes zu Hause, in das ich jedes mal gerne zurückkehre.

“Scientific discovery and scientific knowledge have been achieved only by those who have gone in pursuit of it without any practical purpose whatsoever in view.”

– Max Planck, *Where is Science Going?*

